Photodisintegration of Lithium Isotopes

A Thesis Submitted to the
College of Graduate Studies and Research
in Partial Fulfillment of the Requirements
for the degree of Doctor of Philosophy
in the Department of Physics and Engineering Physics
University of Saskatchewan
Saskatoon

By
Ward Andrew Wurtz

©Ward Andrew Wurtz, August 2010. All rights reserved.

Permission to Use

In presenting this thesis in partial fulfilment of the requirements for a Postgraduate degree from the University of Saskatchewan, I agree that the Libraries of this University may make it freely available for inspection. I further agree that permission for copying of this thesis in any manner, in whole or in part, for scholarly purposes may be granted by the professor or professors who supervised my thesis work or, in their absence, by the Head of the Department or the Dean of the College in which my thesis work was done. It is understood that any copying or publication or use of this thesis or parts thereof for financial gain shall not be allowed without my written permission. It is also understood that due recognition shall be given to me and to the University of Saskatchewan in any scholarly use which may be made of any material in my thesis.

Requests for permission to copy or to make other use of material in this thesis in whole or part should be addressed to:

Head of the Department of Physics and Engineering Physics
116 Science Place
University of Saskatchewan
Saskatoon, Saskatchewan
Canada
S7N 5E2

Abstract

We have performed a measurement of the photodisintegration of the lithium isotopes, ^{6}Li and ^{7}Li, using a monochromatic, polarised photon beam and a segmented neutron detector array which covers approximately $\frac{1}{4}$ of 4π srad. Using time-of-flight and scintillator light-output spectra we separate the data into individual reaction channels. This work is motivated by the need to compare with recent theoretical predictions and to provide data for future theoretical work.

For the photodisintegration of ^{6}Li we took data at 12 photon energies between 8 and 35 MeV. We describe the data using a model consisting of two-body reaction channels and obtain angular distributions and absolute cross sections for many of these reaction channels. We compare our results with a recent Lorentz integral transform calculation (Bacca *et al.* Phys. Rev. C **69**, 057001 (2004)). Our results are in reasonable agreement with the calculation, in contradiction with previous experimental results.

For the photodisintegration of ^{7}Li, we took data at 9 photon energies between 10 and 35 MeV. We obtain cross sections for the reaction channel $^7\mathrm{Li} + \gamma \rightarrow n + {}^6\mathrm{Li}$(g.s.) at all photon energies with angular distributions at all but the highest energy. We obtain angular distributions and total cross sections for reaction channels involving excited states of the daughter nucleus, ^{6}Li, at select energies. We hope that these measurements will provide incentive for new theoretical calculations.

We observe neutrons that can only be described by the reaction channel $^7\mathrm{Li} + \gamma \rightarrow n + {}^6\mathrm{Li}(10.0)$ which necessitates an excited state of ^{6}Li with excitation energy $E_x = 10.0 \pm 0.5$ MeV that is not in the standard tables of excited states.

Acknowledgements

I would like to begin by thanking NSERC for their support in funding this work through the post graduate scholarships granted to me and through their support of my group's research through equipment and discovery grants. I would also like to thank the University of Saskatchewan and the Department of Physics and Engineering Physics; not only have they made this work possible through financial support but the moral support and encouragement that I have received from the faculty and staff has been tremendous. The simulations performed in this thesis would not have been possible without access to WestGrid computing facilities; I have run nearly a thousand simulations on the Glacier cluster, each one lasting more than a day of computer time. The production of my targets would not have been possible without the assistance of Johannes Vogt and the staff of the Canadian Light Source. The staff of HIGS must be credited for their collaboration, assistance and the superb operation of the accelerator systems.

I would like to thank Rob Pywell for being my supervisor these years. You helped me when I needed help and you let me discover on my own when I needed to find my own way. I am eternally grateful for both. I would also like to thank Ru Igarashi for many interesting and entertaining discussions and Norm Kolb for getting me started.

There are too many people who have influenced me over the years to list everyone here; this thesis is too long already and it would double in length if I were to give everyone their proper acknowledgements. Let me instead single out my parents, Bryan and Gerri, who brought me into this world along with my brother Mark, and my wife Melissa who shares it with me. To those who were my friends in Melfort, those who studied with me though my undergraduate days, those who were my fellow graduate students, those who I have found adventure with, those who are part of my new career at the Canadian Light Source, and those who I have met through the random nature of life, thank you all.

For Melissa. Without your love and support I could never have achieved all that I dreamed.

Contents

List of Tables

List of Figures

List of Abbreviations

ADC	Analogue to Digital Converter
CAMAC	Computer Automated Measurement And Control
DFELL	Duke Free Electron Laser Laboratory
FEL	Free Electron Laser
Flash-eng	Flasher System Enable
Flash-trig	Flasher System Trigger
G-win	Gamma Window
HIGS	High Intensity Gamma Source
HIγS	High Intensity Gamma Source (Alternate Abbreviation)
LED	Light Emitting Diode
LIT	Lorentz Integral Transform
Mon-en	Monitor Enable
Mon-trig	Monitor Trigger
N+G-win	Neutron/Gamma Window
NIM	Nuclear Instrumentation Module
N-OR	Neutron OR
N-trig	Neutron Trigger
N-win	Neutron Window
OK	Optical Klystron
Out-win	Out Window
PCI	Peripheral Component Interconnect
P-en	Pedestal Enable
PMT	Photomultiplier Tube
PSD	Pulse-Shape Discrimination
P-trig	Pedestal Trigger
QDC	Charge-to-Digital Converter
RF	Radio Frequency
RTEMS	Real-Time Executive for Multiprocessor Systems
SAL	Saskatchewan Accelerator Laboratory
TDC	Time to Digital Converter
TUNL	Triangle Universities Nuclear Laboratory
VME	VersaModule Eurocard

Chapter 1

Introduction

1.1 Few-Body Problems in Nuclear Physics

> "Few-body systems are both technically relatively simple and physically non-trivial enough to test theories quantitatively. For instance the He-atom played historically an important role in verifying predictions of QED. A similar role is contributed nowadays to the three-nucleon system as a testing ground for nuclear dynamics and maybe in the near future to few-quark systems. They are also often the basic building blocks for many-body systems like to some extent nuclei, where the *real many-body* aspect is not the dominant feature."
>
> – Walter Glöckle, 1983 [Glö83]

Since 1983 the testing ground for nuclear dynamics has expanded to include four, six and seven-nucleon systems.[1] However, this fact does not change the spirit of what Glöckle has said. Few-body systems in nuclear physics can be studied with the Schrödinger equation making them technically simple. The results are certainly physically non-trivial and provide deep insight into the forces that hold the nucleus together. It is the nuclear dynamics themselves that make the nuclear few-body problem difficult to solve. In 1983 calculations with more than three bodies were intractable and in 2010, even with 27 years of advances in computer technology, calculations with more than seven bodies remain intractable. It is only through insightful and creative theoretical and computational techniques that nuclear physicists are able to perform any few-body calculations.

The nuclear system consists of protons and neutrons which are together called nucleons. Nucleons are made out of quarks with a proton consisting of two up quarks and a down quark while a neutron consists of two down quarks and an up quark. Up quarks have electric charge $+\frac{2}{3}e$ while down quarks have an electric charge $-\frac{1}{3}e$, where e is the positive, elementary charge. This gives the proton a charge of $+e$ while the neutron has no electric charge.

The force between quarks is mediated by gluons and described by the theory of quantum chromodynamics (QCD). Gluons are able to bind together three quarks to form the nucleons but they are also able to bind together quarks and anti-quarks to form mesons. It is these mesons that mediate the force that binds the nucleons together.

[1] There do not exist any particle-stable five nucleon systems due to the tightly bound alpha particle. A particle stable state is one which does not decay through the emission of protons or neutrons, although it may undergo beta decay.

The massless photon is the gauge boson responsible for electrodynamics and leads to potential $V(r) \sim \frac{1}{r}$. Likewise we expect the nuclear force to have a Yukawa potential [Sak67]

$$V(r) \sim \frac{e^{-m_\pi c r/\hbar}}{r} \tag{1.1}$$

where m_π is the mass of the lightest meson, the pion. Unfortunately, using this simple potential is not sufficient for few-body calculations. We therefore must resort to models of the nuclear potential which typically have forms justified by theory and parameters fit to data.

One advanced model of the nuclear potential is the Argonne V18 (AV18) which has 18 operators [Wir95]. "The potential has been fit directly to the Nijmegen *pp* and *np* scattering database, low-energy *nn* scattering parameters, and deuteron binding energy. With 40 adjustable parameters it gives a χ^2 per datum of 1.09 for 4301 *pp* and *np* data in the range 0-350 MeV" [Wir95]. With 18 operators and 40 adjustable parameters, the AV18 is a highly detailed potential model. Calculations that use it require substantial resources.

There is another class of potential, the semi-realistic nuclear potentials, which compromise detail in order to make computations tractable. One such potential is the Malfliet-Tjon I-III (MTI-III) [Mal69] which uses a superposition of an attractive and repulsive Yukawa potential

$$V(r) = -\lambda_A \frac{e^{-\mu_A r}}{r} + \lambda_R \frac{e^{-\mu_R r}}{r} \tag{1.2}$$

where λ_A, λ_R, μ_A and μ_R are adjustable parameters. It is important to note that these fitting parameters vary depending on how the nucleons are bound. If they are bound in a singlet state, one set of parameters is used. If they are bound in a triplet state, another set is used. It is this kind of dependence that makes calculations with the nuclear potential a much more formidable challenge than the electric potential.

When the number of nucleons in the problem becomes too great we can no longer perform calculations based on nucleons interacting through a potential. Instead we must form models in order to abstract away the details of the nuclear force and enter the realm of many-body calculations. It is one of the goals of research into few-body problems to expand the calculations to nuclei with more-and-more nucleons. However, there is a long way to go before few-body methods can encroach on many-body problems.

This thesis represents an attempt to aid theoretical physicists pushing the boundaries of few-body problems by providing much needed experimental data. Lithium is at the frontier of few-body research as its isotopes contain six and seven nucleons. The lithium isotopes are studied through the process of photodisintegration which is described in detail in the next section.

1.2 Photodisintegration of Nuclei

The photodisintegration of a nucleus is simply the breaking apart of a nucleus by photons. Nuclear systems are in many ways similar to atomic systems in that they have ground states, excited states and can have constituent particles ejected from them, given enough energy. Let us begin our discussion by looking at some examples to better understand nuclear systems.

Take a volume of matter, say a cylinder of natural lithium 12.7 cm long and 4.1 cm in diameter.[2] Now place that volume in a beam of gamma-ray photons with energy E_γ. If $E_\gamma = 478$ keV we can promote a ^{7}Li nucleus to its first excited state. After a moment,[3] that nucleus will decay back to the ground state and emit a photon with the same energy. This is analogous to an atomic system being promoted to a higher energy level and then decaying to the ground state by emitting a photon. This is an example of nuclear photoabsorption and we now change it slightly to examine photodisintegration.

Let us increase the energy of our example photon to $E_\gamma = 3.00$ MeV. This photon now has enough energy to break a ^{7}Li nucleus in two. To compute the minimum energy required to break apart a nucleus, also known as the reaction threshold, we use the binding energy of the nucleus. The binding energy is the amount of energy required to remove all the nucleons from the nucleus and take them infinitely far away. Table 1.1 lists a number of isotopes of interest to the photodisintegration of lithium isotopes and gives their binding energies along with their half-lives and decay modes. The binding energy of ^{7}Li is 39.24 MeV while the binding energies for ^{3}H and ^{4}He are 8.48 and 28.30 MeV respectively. The sum of the ^{3}H and ^{4}He binding energies is 36.78 MeV. With the addition of 2.46 MeV of energy, we can destruct the ^{7}Li nucleus and build ^{3}H and ^{4}He nuclei. We say that the threshold for the $^7\mathrm{Li} + \gamma \rightarrow {}^3\mathrm{H} + {}^4\mathrm{He}$ reaction is 2.46 MeV. Our 3.00 MeV photon can break apart the ^{7}Li nucleus and the ^{3}H and ^{4}He reaction products will have 0.54 MeV of kinetic energy to share between them.

The photodisintegration of a nucleus can proceed though several different reaction channels. We have already discussed the $^7\mathrm{Li} + \gamma \rightarrow {}^3\mathrm{H} + {}^4\mathrm{He}$ reaction channel. Other important reaction channels include the photoneutron reaction channel, $^7\mathrm{Li} + \gamma \rightarrow n + {}^6\mathrm{Li}$, and the photoproton reaction channel, $^7\mathrm{Li} + \gamma \rightarrow p + {}^6\mathrm{He}$. Each of these reaction channels will have its own threshold. The reaction channels of relevance to the photodisintegration of lithium will be discussed further in section 1.5. Now we discuss how to quantify the study of these reaction channels.

The physical observable we will study in the photodisintegration of nuclei is the cross section. Theoretical physicists predict the cross section and experimental physicists measure it. The cross section is essentially the probability of a photodisintegration reaction occurring with the geometrical

[2] These are the dimensions of the lithium volumes used in this thesis as targets.
[3] The 0.478 MeV state of ^{7}Li has a half life of 105±3 fs [Til02].

Table 1.1: Isotopes of interest. Only ground states are considered. Binding energies listed without error are known to more decimal places than recorded here [Aud03, Til87, Til92, Til02]. Half-lives and decay widths are related by the relationship $t_{\frac{1}{2}}\Gamma = \hbar \ln 2$ [Sak94] and only the most sensible values are reported.

Isotope	Binding energy (MeV)	Spin/parity	Half life/ Decay width	Decay mode
^{7}Li	39.24	$\frac{3}{2}^{-}$	stable	
^{6}Li	31.99	1^{+}	stable	
^{6}He	29.27	0^{+}	806.7 ± 1.5 ms	beta decay
^{5}Li	26.33 ± 0.05	$\frac{3}{2}^{-}$	1.23 MeV	proton emission
^{5}He	27.41 ± 0.05	$\frac{3}{2}^{-}$	0.648 MeV	neutron emission
^{5}H	6.7 ± 0.1	$\left(\frac{1}{2}^{+}\right)$	n/a	neutron emission
^{4}Li	4.6 ± 0.2	2^{-}	6.03 MeV	proton emission
^{4}He	28.30	0^{+}	stable	
^{4}H	5.6 ± 0.1	2^{-}	5.42 MeV	neutron emission
^{3}He	7.72	$\frac{1}{2}^{+}$	stable	
^{3}H	8.48	$\frac{1}{2}^{+}$	12.32 ± 0.03 y	beta decay
^{2}H	2.22	1^{+}	stable	

aspects removed. In this thesis we are concerned with the angular dependence of the differential cross section. The number of particles per unit time incident on a detector with infinitesimal solid angle $d\Omega$ at polar angle θ and azimuthal angle ϕ, is given by

$$\frac{dN_{scat}}{d\Omega}(\theta,\phi) = \Phi N \ell \frac{d\sigma}{d\Omega}(\theta,\phi) \tag{1.3}$$

where Φ is the number of incident photons per unit time, N is the number density of the target and ℓ is the length of the target in units of length (as opposed to mass thickness units) and $\frac{d\sigma}{d\Omega}$ is the differential cross section, which has units of length squared per steradian.[4] Figure 1.1 shows the geometry of a photodisintegration reaction. If an experiment or calculation is not sensitive to

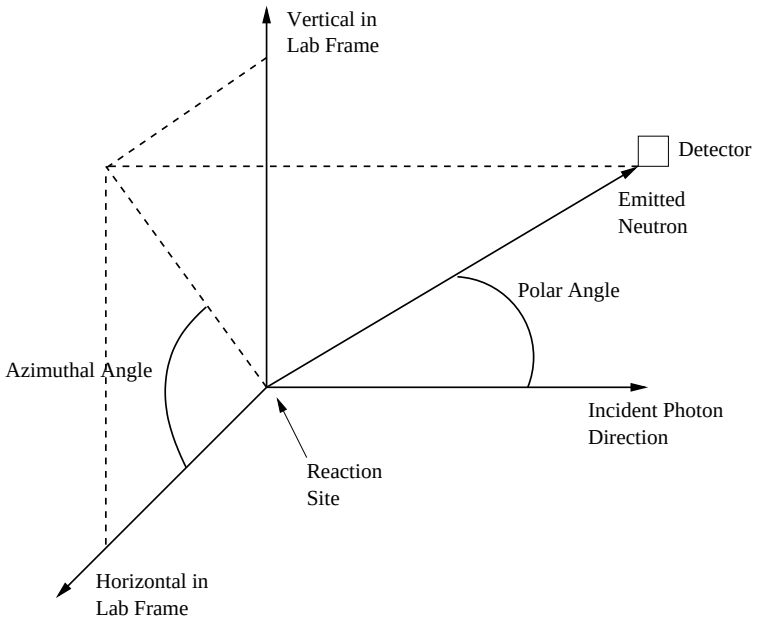

Figure 1.1: Geometry of a photodisintegration reaction

the angular dependence of the differential cross section then only the total cross section, σ, may be found. The cross section is calculated from the differential cross section by integrating over all angles

$$N_{scat} = \Phi N \ell \sigma. \tag{1.4}$$

The cross section contains all of the information related to the interaction with the nucleus, since Φ and ℓ are set by the experimenters while N is simply a density. The challenge for theoretical physicists is to compute this quantity from physical models, while experimental physicists measure it by measuring Φ, N, ℓ and the number of particles produced by the reaction.

We will now apply the principles discussed in this section to the photodisintegration of a specific element, lithium.

[4] We define the unit barn so that 1 barn = 10^{-24} cm^2. Typically cross sections discussed in this thesis will be milli or micro barns: mb or μb.

1.3 Photodisintegration of Lithium

The name lithium is derived from the Greek word for stone, $\lambda\iota\theta o\varsigma$ or lithos, since it was first observed to exist only in minerals. Lithium was first discovered in petalite, $LiAl(Si_2O_5)_2$, and was first found to be an element by the Swedish mineralogist Johan August Arfwedson in 1818 [DeL03]. There are two stable isotopes of lithium, ^{6}Li and ^{7}Li, with relative abundances of 7.59 $\pm$ 0.04 % and 92.42 $\pm$ 0.04 % [DeL03].

The first experiment concerning the photodisintegration of lithium occurred in 1947 [Bec47]. Since then there has been great interest in lithium as it is more complex than the alpha particle but still relatively simple. Until recently, models of the lithium nuclei typically involved cluster models. Researchers have investigated whether ^{6}Li is better modelled by an alpha particle bound to a deuteron (αd) or by a ^{3}He nucleus bound to a ^{3}H nucleus (τt). Sometimes the researchers conclude that it is more αd [Bur89] and other times they conclude it is more τt [Shi75]. Other researchers treat the ^{6}Li nucleus as a superposition of αd and τt models and attempt to weight the relative importance of the two [You70a]. Unfortunately, it appears that no consensus was ever forged on the cluster structure of either lithium isotope.

Rather than using cluster models, physicists desire to calculate cross sections from more fundamental models. Ideally we would like to be able to use the nuclear potential as the sole input to our calculation. The Lorentz Integral Transform (LIT) [Efr94, Efr07] is a technique developed for just that purpose. It takes a reaction with final states in the continuum and transforms it into a bound-state problem. The inputs to the LIT are a model of the nuclear potential and the electric dipole transition operator. The LIT technique is further discussed in section 2.1 and we look at some of its results here.

The LIT has been applied to nuclei with $A \leq 7$, including the lithium isotopes. Figure 1.2 shows the LIT calculation for the total cross section compared with some experimental data for the photodisintegration of ^{6}Li. The lines correspond to the theoretical predictions using the semi-realistic potentials Argonne V4' (AV4') [Wir02], Malfliet-Tjon I-III (MTI-III) [Mal69] and Minnesota (MN) [Rei70, Tho77]. The dots with error bars represent experimental data. The data of Berman *et al.* (solid squares) [Ber65b] were taken using BF_3 proportional counters and therefore represents all reaction channels that produce neutrons. Up to 15.8 MeV all reaction channels do produce neutrons and the data is the total cross section. Above 15.8 MeV the $^6\mathrm{Li} + \gamma \rightarrow {}^3\mathrm{He} + {}^3\mathrm{H}$ reaction channel comes into play and the data of Berman *et al.* no longer measures the total cross section. Shin *et al.* [Shi75] and Junghans *et al.* [Jun79] measured this reaction channel and their data has been added to the data of Berman in order to compare it with the calculation. The data in figure 1.2 labelled 'Shin' (solid triangles) and 'Junghans' (open circles) is actually their data summed with the data of Berman *et al.* It is clear that new experimental results are needed to compare with the

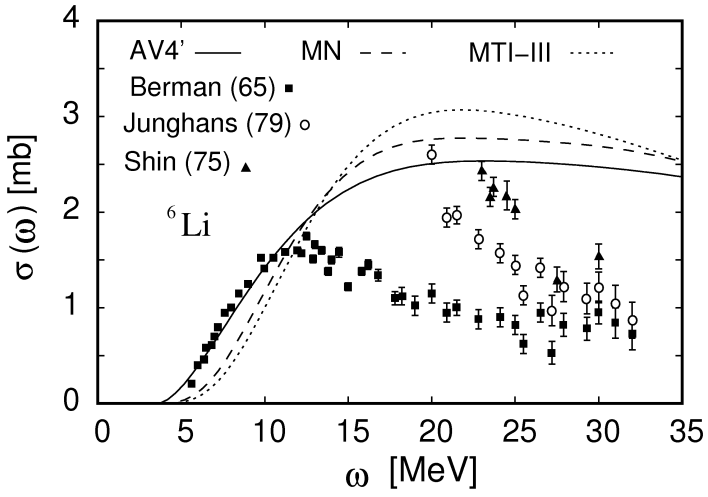

Figure 1.2: Most recent comparison between the theory and experiment of the total photodisintegration cross section of ^{6}Li taken from figure 4 of [Bac04a] (ω is photon energy).

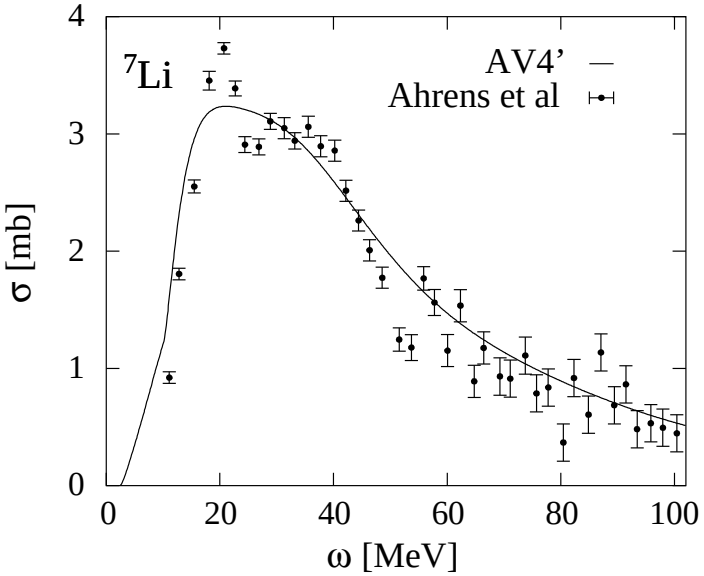

Figure 1.3: Most recent comparison between the theory and experiment of the total photodisintegration cross section of ^{7}Li taken from figure 3 of [Bac04b] (ω is photon energy).

LIT calculation.

A similar LIT calculation has been made for ^{7}Li which is shown in figure 1.3. The lines correspond to the theoretical predictions using the Argonne V4' (AV4') potential while dots with error bars represent the experimental data [Ahr75].

It is clear that there is little agreement between measurement and theory in the ^{6}Li case above 10 MeV. The ^{7}Li case appears to fare better. We will provide new experimental data to compare with these calculations in order to help verify the theoretical methods employed.

While the cross sections determined for ^{6}Li and ^{7}Li so far are for all reaction channels, the LIT does have the ability to produce cross sections for individual reaction channels. This has already been done for ^{4}He [Qua04]. There is little incentive for such a calculation to be performed for the lithium isotopes as there is insufficient experimental data to make a meaningful comparison. This thesis aims to change that by providing cross sections for individual reaction channels.

1.4 The Experiment

Several tools are needed in order to perform a photodisintegration of lithium experiment: a gamma-ray source, a detector arrangement and a quantity of lithium. These components are introduced here and examined in greater detail in chapter 4.

The gamma-ray source is the High Intensity Gamma-Ray Source (HIGS) located at Duke University in Durham, NC, USA. Through the process of Compton backscattering ultra-violet photons from a free-electron laser off storage ring electrons, HIGS can produce monoenergetic, highly polarised gamma-ray photons. HIGS and gamma-ray production are discussed further in section 4.2.

The detector system utilised is the Blowfish Neutron Detector Array, shown in figure 1.4. Blowfish is a general-purpose, segmented neutron detector array that covers approximately $\frac{1}{4}$ of 4π steradians. It consists of 88 neutron detectors mounted 40.6 cm from the target centre. The photon beam travels unimpeded though the array from the right end of the array to the left end, as it is shown in figure 1.4. Blowfish will be discussed in greater detail in section 4.3.

A quantity of lithium, called the target, can be placed in the centre of the array. Figure 1.5 shows two computer generated views of the target. Since lithium reacts with oxygen, the target is housed within a sealed container. The target, its container and its construction are described in more detail in section 4.7.

Since the target is the only solid piece of material in the photon beam, the photon beam will pass through Blowfish and interact with the target. A number of outcomes can result for any one photon. The most likely is that it will pass through the target unhindered. It is possible for the photon to interact with an atomic electron and this is much more probable than it interacting

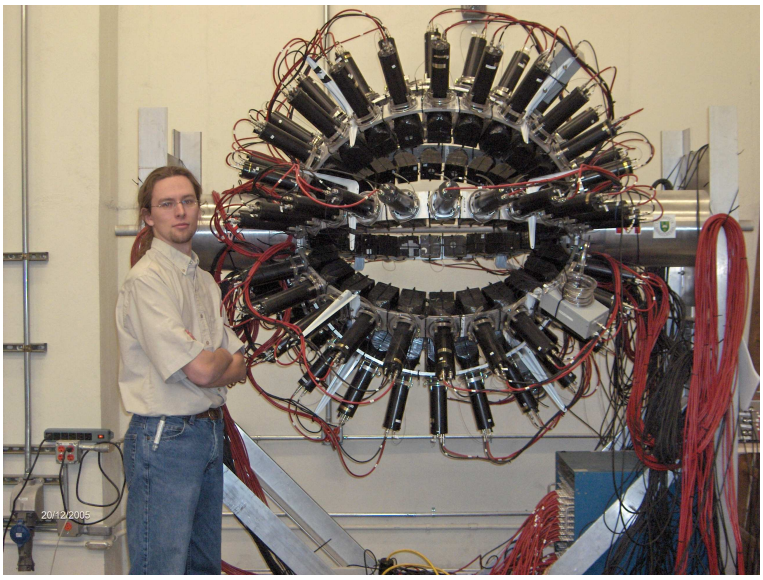

Figure 1.4: The Blowfish Neutron Detector Array

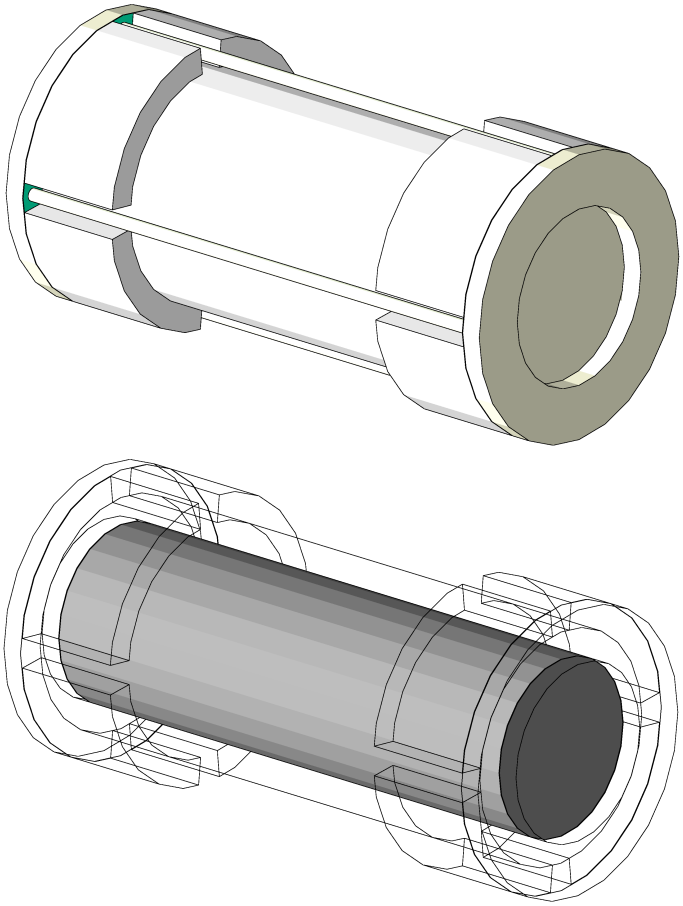

Figure 1.5: Computer generated images of the lithium target in its container (top) and with the container cut away (bottom).

with a nucleus. The processes of pair production, Compton scattering and photoelectric effect are all possible, with pair production and Compton scattering dominating at the energies of interest [Kno00, Leo94]. These processes can scatter gamma-rays into the neutron detectors where they can be detected, and must therefore be separated from detected neutrons. It is also possible for the photon to interact with the nucleus, breaking it apart in a photodisintegration reaction. When a lithium nucleus breaks apart, there are several reaction channels through which the breakup can proceed. These are discussed in the next section.

1.5 Reaction Channels

When a nucleus breaks up, it usually does not disintegrate into only protons and neutrons. In fact, this will not be energetically possible for the measurements performed in this thesis with the exception of the ^{6}Li target in a photon beam with energy 35 MeV. Instead, the target nucleus breaks into two-or-more reaction products. These reaction products may be protons, neutrons, deuterons, ground-state nuclei or nuclei in excited states. We refer to each possible breakup as a reaction channel. All possible reaction channels for ^{6}Li are enumerated in table 1.2, while the same is done for ^{7}Li in table 1.3. It is also possible for the final state nuclei to end in higher-energy, excited states. Some excited states of relevance are listed in table 1.4.

We can determine which reaction channels will be observable in our data by taking the basic reaction channels that produce neutrons from tables 1.2 and 1.3 and adding excited final states. The most relevant of these are listed in table 1.5.

We model our experimental data by assuming that the photodisintegration reactions proceed through these reaction channels. We model photodisintegration reaction channels as proceeding directly from a photon incident on a target nucleus in its ground state to the final continuum state, with the reaction products travelling away from the interaction site with momentum and kinetic energy. The kinematics for these models, derived from the conservation of energy and momentum, are discussed in detail in section 5.3. Reactions where the target nucleus is promoted to a higher energy level before breaking apart are ignored as they do not affect the kinematics of the reaction. We also do not consider reactions where energy is lost to an intermediate photon.

It is through these reaction channels that we will understand our data. Many experiments, such as those of Berman *et al.* [Ber65b] already discussed, used methods of detection which are not sensitive to individual reaction channels. The detectors they used are based on BF_3 proportional counters which are sensitive to neutrons of all energies. The result of such an experiment is a cross section that is the sum of the cross sections of all reaction channels that produce neutrons. In the case of ^{6}Li below 15.8 MeV this is, interestingly enough, the total cross section since all reaction channels below this energy produce neutrons. These historic experiments will be discussed in detail

in chapter 3.

The measurements in this thesis use neutron detectors which operate on different principles and are from the general category of fast neutron detectors. The neutron detectors in Blowfish use the principle of neutron-proton scattering rather than the neutron capture reactions used in BF_3 proportional counters. The Blowfish detectors are not sensitive to neutrons of all energies. The efficiency of the Blowfish detectors (the number of neutrons detected for each neutron that passes through the detector) is a strong function of energy. There is a cutoff, below which the efficiency drops to zero, and no neutrons with energy lower than this threshold will be detected.

It is therefore critical to know which reaction channels are being detected in order to say anything about the data reported in this thesis. It is possible that there will be copious numbers of neutrons produced below the efficiency cutoff of the neutron detectors and that these neutrons will go completely undetected. A good example is the reaction channel $^6\mathrm{Li} + \gamma \rightarrow p + {}^5\mathrm{He(g.s.)} \rightarrow n + p + {}^4\mathrm{He(g.s.)}$. The neutrons produced have too low energy for this reaction channel to be adequately measured by us.

The objective of this thesis is to measure the differential and absolute cross sections for as many reaction channels as possible.

Table 1.2: Possible reactions for ^{6}Li, their thresholds and their lowest order process. Excited states of the final products are neglected.

Reaction		Threshold (MeV)	Process
$^6\mathrm{Li} + \gamma \rightarrow d + {}^4\mathrm{He}$		1.5	E2 [She68]
$^6\mathrm{Li} + \gamma \rightarrow n + p + {}^4\mathrm{He}$		3.7	E1
$^6\mathrm{Li} + \gamma \rightarrow p + {}^5\mathrm{He}$	$\rightarrow n + p + {}^4\mathrm{He}$	4.6	E1
$^6\mathrm{Li} + \gamma \rightarrow n + {}^5\mathrm{Li}$	$\rightarrow n + p + {}^4\mathrm{He}$	5.7	E1
$^6\mathrm{Li} + \gamma \rightarrow {}^3\mathrm{H} + {}^3\mathrm{He}$		15.8	E1 [She68]
$^6\mathrm{Li} + \gamma \rightarrow p + d + {}^3\mathrm{H}$		21.3	E1 [She68]
$^6\mathrm{Li} + \gamma \rightarrow n + d + {}^3\mathrm{He}$		22.1	E1 [She68]
$^6\mathrm{Li} + \gamma \rightarrow n + 2p + {}^3\mathrm{H}$		23.5	n/a
$^6\mathrm{Li} + \gamma \rightarrow 2n + p + {}^3\mathrm{He}$		24.3	n/a
$^6\mathrm{Li} + \gamma \rightarrow 3d$		25.3	E2 [She68]
$^6\mathrm{Li} + \gamma \rightarrow 2p + {}^4\mathrm{H}$	$\rightarrow n + 2p + {}^3\mathrm{H}$	26.4	n/a
$^6\mathrm{Li} + \gamma \rightarrow 2n + {}^4\mathrm{Li}$	$\rightarrow 2n + p + {}^3\mathrm{He}$	27.4	n/a
$^6\mathrm{Li} + \gamma \rightarrow n + p + 2d$		27.5	n/a
$^6\mathrm{Li} + \gamma \rightarrow 2n + 2p + d$		29.8	n/a
$^6\mathrm{Li} + \gamma \rightarrow 3n + 3p$		32.0	n/a

Table 1.3: Possible reactions for ^{7}Li and their thresholds. Excited states of the final products are neglected.

Reaction		Threshold (MeV)
$^7\mathrm{Li} + \gamma \rightarrow {}^3\mathrm{H} + {}^4\mathrm{He}$		2.5
$^7\mathrm{Li} + \gamma \rightarrow n + {}^6\mathrm{Li}$		7.3
$^7\mathrm{Li} + \gamma \rightarrow n + d + {}^4\mathrm{He}$		8.7
$^7\mathrm{Li} + \gamma \rightarrow d + {}^5\mathrm{He}$	$\rightarrow n + d + {}^4\mathrm{He}$	9.6
$^7\mathrm{Li} + \gamma \rightarrow p + {}^6\mathrm{He}$		10.0
$^7\mathrm{Li} + \gamma \rightarrow 2n + p + {}^4\mathrm{He}$		10.9
$^7\mathrm{Li} + \gamma \rightarrow n + p + {}^5\mathrm{He}$	$\rightarrow 2n + p + {}^4\mathrm{He}$	11.8
$^7\mathrm{Li} + \gamma \rightarrow 2n + {}^5\mathrm{Li}$	$\rightarrow 2n + p + {}^4\mathrm{He}$	12.9
$^7\mathrm{Li} + \gamma \rightarrow p + 2{}^3\mathrm{H}$		22.3
$^7\mathrm{Li} + \gamma \rightarrow n + {}^3\mathrm{H} + {}^3\mathrm{He}$		23.0
$^7\mathrm{Li} + \gamma \rightarrow {}^3\mathrm{He} + {}^4\mathrm{H}$	$\rightarrow n + {}^3\mathrm{He} + {}^3\mathrm{H}$	25.9
$^7\mathrm{Li} + \gamma \rightarrow 2d + {}^3\mathrm{H}$		26.3
$^7\mathrm{Li} + \gamma \rightarrow n + p + d + {}^3\mathrm{H}$		28.5
$^7\mathrm{Li} + \gamma \rightarrow 2n + d + {}^3\mathrm{He}$		29.3
$^7\mathrm{Li} + \gamma \rightarrow 2n + 2p + {}^3\mathrm{H}$		30.8
$^7\mathrm{Li} + \gamma \rightarrow p + d + {}^4\mathrm{H}$	$\rightarrow n + p + d + {}^3\mathrm{H}$	31.4
$^7\mathrm{Li} + \gamma \rightarrow 3n + p + {}^3\mathrm{He}$		31.5
$^7\mathrm{Li} + \gamma \rightarrow 2p + {}^5\mathrm{H}$	$\rightarrow 2n + 2p + {}^3\mathrm{H}$	32.5
$^7\mathrm{Li} + \gamma \rightarrow n + 3d$		32.6
$^7\mathrm{Li} + \gamma \rightarrow n + 2p + {}^4\mathrm{H}$	$\rightarrow 2n + 2p + {}^3\mathrm{H}$	33.6
$^7\mathrm{Li} + \gamma \rightarrow 3n + {}^4\mathrm{Li}$	$\rightarrow 3n + p + {}^3\mathrm{He}$	34.6
$^7\mathrm{Li} + \gamma \rightarrow 2n + p + 2d$		34.8
$^7\mathrm{Li} + \gamma \rightarrow 3n + 2p + d$		37.0
$^7\mathrm{Li} + \gamma \rightarrow 4n + 3p$		39.2

Table 1.4: States of interest to the analysis below 16 MeV [Til02]. Half-lives and decay widths are related by the relationship $t_{\frac{1}{2}}\Gamma = \hbar \ln 2$ [Sak94].

Isotope	Excitation Energy (MeV)	Spin/Parity	Decay Width or Half Life	Decay Mode
^{6}Li	0.0	1^+	stable	
^{6}Li	2.186 ± 0.002	3^+	24 ± 2 keV	γ, d, α
^{6}Li	3.56288 ± 0.00010	0^+	8.2 ± 0.2 eV	γ
^{6}Li	4.312 ± 0.022	2^+	1.30 ± 0.10 MeV	γ, d, α
^{6}Li	5.366 ± 0.015	2^+	0.541 ± 0.020 MeV	γ, n, d, α
^{6}Li	5.65 ± 0.050	1^+	1.5 ± 0.2 MeV	d, α
^{6}He	0.0	0^+	806.7 ± 1.5 ms	β^-
^{6}He	1.797 ± 0.025	2^+	0.113 ± 0.020 MeV	n, α
^{5}Li	0.0	$\frac{3}{2}^-$	1.23 MeV	p, α
^{5}Li	1.49	$\frac{1}{2}^-$	6.60 MeV	p, α
^{5}He	0.0	$\frac{3}{2}^-$	0.648 MeV	n, α
^{5}He	1.27	$\frac{1}{2}^-$	5.57 MeV	n, α

Table 1.5: Reaction channels to consider in the analysis below 16 MeV.

Label	Reaction		Threshold (MeV)
6n0	$^6\mathrm{Li} + \gamma \rightarrow n + {}^5\mathrm{Li}$(g.s.)		5.7
6n1	$^6\mathrm{Li} + \gamma \rightarrow n + {}^5\mathrm{Li}(1.49)$		7.0
6p0	$^6\mathrm{Li} + \gamma \rightarrow p + {}^5\mathrm{He}$(g.s.)	$\rightarrow n + p + {}^4\mathrm{He}$(g.s.)	4.6
6p1	$^6\mathrm{Li} + \gamma \rightarrow p + {}^5\mathrm{He}(1.27)$	$\rightarrow n + p + {}^4\mathrm{He}$(g.s.)	5.9
6np	$^6\mathrm{Li} + \gamma \rightarrow n + p + {}^4\mathrm{He}$(g.s.)		3.7
7n0	$^7\mathrm{Li} + \gamma \rightarrow n + {}^6\mathrm{Li}$(g.s.)		7.3
7n1	$^7\mathrm{Li} + \gamma \rightarrow n + {}^6\mathrm{Li}(2.19)$		9.5
7n2	$^7\mathrm{Li} + \gamma \rightarrow n + {}^6\mathrm{Li}(3.56)$		10.9
7n3	$^7\mathrm{Li} + \gamma \rightarrow n + {}^6\mathrm{Li}(4.31)$		11.6
7n4	$^7\mathrm{Li} + \gamma \rightarrow n + {}^6\mathrm{Li}(5.37)$		12.7
7n5	$^7\mathrm{Li} + \gamma \rightarrow n + {}^6\mathrm{Li}(5.65)$		12.9
7p1	$^7\mathrm{Li} + \gamma \rightarrow p + {}^6\mathrm{He}(1.78)$	$\rightarrow p + 2n + {}^4\mathrm{He}$(g.s.)	11.8
7d0	$^7\mathrm{Li} + \gamma \rightarrow d + {}^5\mathrm{He}$(g.s.)	$\rightarrow n + d + {}^4\mathrm{He}$(g.s.)	9.6
7d1	$^7\mathrm{Li} + \gamma \rightarrow d + {}^5\mathrm{He}(1.27)$	$\rightarrow n + d + {}^4\mathrm{He}$(g.s.)	10.9
7nd	$^7\mathrm{Li} + \gamma \rightarrow n + d + {}^4\mathrm{He}$(g.s.)		8.7
7np0	$^7\mathrm{Li} + \gamma \rightarrow n + p + {}^5\mathrm{He}$(g.s.)	$\rightarrow 2n + p + {}^4\mathrm{He}$(g.s.)	11.8
7np1	$^7\mathrm{Li} + \gamma \rightarrow n + p + {}^5\mathrm{He}(1.27)$	$\rightarrow 2n + p + {}^4\mathrm{He}$(g.s.)	13.1
7nn0	$^7\mathrm{Li} + \gamma \rightarrow 2n + {}^5\mathrm{Li}$(g.s.)	$\rightarrow 2n + p + {}^4\mathrm{He}$(g.s.)	12.9
7nn1	$^7\mathrm{Li} + \gamma \rightarrow 2n + {}^5\mathrm{Li}(1.49)$	$\rightarrow 2n + p + {}^4\mathrm{He}$(g.s.)	14.4

Chapter 2

Theory

In this chapter we look at two distinct theoretical topics: The Lorentz Integral Transform which is used to compute cross sections and a useful parameterisation of the differential cross section.

2.1 Lorentz Integral Transform

We have already discussed some of the results of the Lorentz Integral Transform (LIT) and we now take a look at its basic formalism. Typically, papers that utilise the LIT begin with equations (2.15) and (2.16), which are taken to be the starting point for calculations of cross sections. Before we consider the LIT itself, we will begin with a discussion of how these equations are derived starting from a basic result of time-dependent perturbation theory.

2.1.1 Absorption of Radiation

We begin our discussion with Fermi's golden rule for a harmonic perturbation. A harmonic perturbation adds a time-dependent potential to the Hamiltonian with the form

$$V(t) = \Lambda e^{i\omega t} + \Lambda^\dagger e^{-i\omega t} \tag{2.1}$$

where Λ is a quantum-mechanical operator and ω is a frequency. This perturbation is understood to be turned on at $t = 0$ so $V(t < 0) = 0$. Using time-dependent perturbation techniques, Fermi's golden rule for absorption is found to be [Sak94]

$$w_{0\to n} = \frac{2\pi}{\hbar}|\langle\Psi_n|\Lambda^\dagger|\Psi_0\rangle|^2\delta(E_n - E_0 - \hbar\omega) \tag{2.2}$$

and is interpreted as the transition rate from state $|\Psi_0\rangle$ with energy E_0 to final state $|\Psi_n\rangle$ with energy E_n. In the case that the perturbation is due to the absorption of electromagnetic radiation we recognise that ω is the frequency of the absorbed photon with gamma-ray energy $E_\gamma = \hbar\omega$.

Equation (2.2) requires some modifications for our use. In photodisintegration experiments, enough energy is absorbed to convert the nuclear ground state, $|\Psi_0\rangle$, into a final continuum of states, $|\Psi_f\rangle$, where parts of the nucleus are no longer bound. In photodisintegration, we have a continuous set of final states. To fix equation (2.2), we need to change the single state index, n,

to the continuum, $[f]$, and integrate over all final states.[1] We also need to include the incident photons, $|n\rangle$, and photons after an interaction, $|n-1\rangle$,

$$w_{0\to[f]} = \frac{2\pi}{\hbar}\int \mathrm{d}f |\langle \Psi_f; n-1|\Lambda^\dagger|\Psi_0; n\rangle|^2 \delta(E_f - E_0 - E_\gamma). \tag{2.3}$$

We make a semi-classical treatment of the photon. The electromagnetic vector potential is given by [Sak67]

$$\mathbf{A}(\mathbf{x},t) = \sum_{\lambda=1}^{2}\int \mathrm{d}^3\mathbf{k} c\sqrt{\frac{2\pi\hbar^2}{VE_\gamma}}\left(a_\lambda(\mathbf{k})\hat{\epsilon}_\lambda(\hat{k})e^{i\mathbf{k}\cdot\mathbf{x}-i\omega t} + a_\lambda^\dagger(\mathbf{k})\hat{\epsilon}_\lambda^*(\hat{k})e^{-i\mathbf{k}\cdot\mathbf{x}+i\omega t}\right) \tag{2.4}$$

where $a_\lambda(\mathbf{k})$ and $a_\lambda^\dagger(\mathbf{k})$ are the boson annihilation and creation operators for photons with wave vector $\mathbf{k}$ and polarisation $\hat{\epsilon}_\lambda(\hat{k})$. These operators annihilate and create photon states $|n(\mathbf{k},\hat{\epsilon}_\lambda)\rangle$ which have $n(\mathbf{k},\hat{\epsilon}_\lambda)$ photons with wave vector $\mathbf{k}$ and polarisation $\hat{\epsilon}_\lambda(\hat{k})$. The polarisation has dependence on the direction of $\mathbf{k}$, denoted $\hat{k}$, because we require these vectors to be orthogonal. The variable V represents the volume of a box with sides $V^{1/3}$. The boundary conditions for $\mathbf{A}(\mathbf{x},t)$ are periodic over this box and $k_i = 2n_i\pi/V^{1/3}$ which becomes continuous as $V\to\infty$ [Sak67]. In any calculation of an observable quantity, the volume will cancel.[2] Notice that we are dealing with the Coulomb gauge, $\nabla\cdot\mathbf{A} = 0$ since $\mathbf{k}$ and $\hat{\epsilon}_\lambda(\hat{k})$ are perpendicular.

Polarisation vectors are an important part of equation (2.4). We want to write a state with $n(\mathbf{k},\hat{\epsilon})$ photons in an arbitrary polarisation, $\hat{\epsilon}$, in terms of two polarisation vectors, $\hat{\epsilon}_1(\hat{k})$ and $\hat{\epsilon}_2(\hat{k})$ that form an orthonormal basis with $\hat{k}$. We can use the creation operator to build such states by $|n(\mathbf{k},\hat{\epsilon})\rangle = \frac{1}{\sqrt{n!}}a^\dagger(\mathbf{k})^n|0\rangle$ where $a^\dagger(\mathbf{k})$ is the creation operator with wave vector $\mathbf{k}$ and polarisation $\hat{\epsilon}$, and $|0\rangle$ is the vacuum state. We can write the annihilation and creation operators[3]

$$a(\mathbf{k}) = (\hat{\epsilon}_1(\hat{k})\cdot\hat{\epsilon}^*)a_1(\mathbf{k}) + (\hat{\epsilon}_2(\hat{k})\cdot\hat{\epsilon}^*)a_2(\mathbf{k}) \tag{2.5}$$

$$a^\dagger(\mathbf{k}) = (\hat{\epsilon}_1^*(\hat{k})\cdot\hat{\epsilon})a_1^\dagger(\mathbf{k}) + (\hat{\epsilon}_2^*(\hat{k})\cdot\hat{\epsilon})a_2^\dagger(\mathbf{k}) \tag{2.6}$$

where we note that $\hat{\epsilon}$ need not be real. Note the special case where

$$\hat{\epsilon}_\pm(\hat{k}) = \mp\frac{1}{\sqrt{2}}(\hat{\epsilon}_1(\hat{k}) \pm i\hat{\epsilon}_2(\hat{k})) \tag{2.7}$$

corresponds to circularly polarised photons [Sak67].

[1] We denote the integration of final states by $\int \mathrm{d}f$ as a shorthand version of $\int \mathrm{d}\Psi_f$.

[2] Notice that reference [Sak67] sums over $\mathbf{k}$ instead of integrating over it as I do here. This is because $\mathbf{k}$ is only continuous in the limit where $V\to\infty$. However, since V will cancel when we compute the cross section, this limit becomes trivial. I have decided to use an integral because, from an experimental point of view, $\mathbf{k}$ is continuous.

[3] To derive this form of the creation and annihilation operators, consider the vector potential with two different sets of polarisation basis vectors, $\hat{\epsilon}_\lambda(\hat{k})$ and $\hat{\epsilon}'_\ell(\hat{k})$. Both forms of the vector potential must be equal giving $\sum_{\lambda=1}^2 a_\lambda(\mathbf{k})\hat{\epsilon}_\lambda(\hat{k})e^{i\mathbf{k}\cdot\mathbf{x}-i\omega t} = \sum_{\ell=1}^2 a'_\ell(\mathbf{k})\hat{\epsilon}'_\ell(\hat{k})e^{i\mathbf{k}\cdot\mathbf{x}-i\omega t}$ which simplifies to $\sum_{\lambda=1}^2 a_\lambda(\mathbf{k})\hat{\epsilon}_\lambda(\hat{k}) = \sum_{\ell=1}^2 a'_\ell(\mathbf{k})\hat{\epsilon}'_\ell(\hat{k})$. Multiplying $\hat{\epsilon}'^*_1(\hat{k})$ with the dot product gives $\sum_{\lambda=1}^2 a_\lambda(\mathbf{k})\hat{\epsilon}_\lambda(\hat{k})\cdot\hat{\epsilon}'^*_1(\hat{k}) = \sum_{\ell=1}^2 a'_\ell(\mathbf{k})\hat{\epsilon}'_\ell(\hat{k})\cdot\hat{\epsilon}'^*_1(\hat{k}) = \sum_{\ell=1}^2 a'_\ell(\mathbf{k})\delta_{\ell 1} = a'_1(\mathbf{k})$.

The electromagnetic Hamiltonian for multiple nucleons with charges q_i has the form [Sak67]

$$\begin{aligned} H_{EM} &= \frac{1}{2m}\sum_{i=1}^{N+Z}\left(\mathbf{p}_i - \frac{q_i\mathbf{A}(\mathbf{x}_j,t)}{c}\right)^2 + \sum_{i=1}^{N+Z} q_i\phi(\mathbf{x}_i) \\ &= \sum_{i=1}^{N}\frac{\mathbf{p}_i^2}{2m} + \sum_{j=1}^{Z}\left[\frac{\mathbf{p}_j^2}{2m} + e\phi(\mathbf{x}_j) + \frac{e^2}{2mc^2}\mathbf{A}^2(\mathbf{x}_j,t) - \frac{e}{mc}\mathbf{A}(\mathbf{x}_j,t)\cdot\mathbf{p}_j\right] \end{aligned} \tag{2.8}$$

where we adopt the convention that a sum from 1 to Z is over all protons and 1 to N is over all neutrons. We see that the $\mathbf{A}^2(\mathbf{x}_j,t)$ term does not contribute to single-photon absorption since it only contains two-photon terms $a_{\lambda''}(\mathbf{k}'')a_{\lambda'}(\mathbf{k}')$, $a_{\lambda''}(\mathbf{k}'')a^\dagger_{\lambda'}(\mathbf{k}')$, $a^\dagger_{\lambda''}(\mathbf{k}'')a_{\lambda'}(\mathbf{k}')$ and $a^\dagger_{\lambda''}(\mathbf{k}'')a^\dagger_{\lambda'}(\mathbf{k}')$ which cannot take a photon state $|n(\mathbf{k},\hat{\epsilon})\rangle$ to $|(n-1)(\mathbf{k},\hat{\epsilon})\rangle$. The perturbing part is

$$-\sum_{j=1}^{Z}\frac{e}{mc}\mathbf{A}(\mathbf{x}_j,t)\cdot\mathbf{p}_j \tag{2.9}$$

$$= -\frac{e}{m}\sqrt{\frac{2\pi\hbar^2}{VE_\gamma}}\sum_{j=1}^{Z}\sum_{\lambda=1}^{2}\int \mathrm{d}^3\mathbf{k}c\left(a_\lambda(\mathbf{k})e^{i\mathbf{k}\cdot\mathbf{x}_j - i\omega t}\hat{\epsilon}_\lambda(\hat{k})\cdot\mathbf{p}_j + a^\dagger_\lambda(\mathbf{k})e^{-i\mathbf{k}\cdot\mathbf{x}_j + i\omega t}\hat{\epsilon}^*_\lambda(\hat{k})\cdot\mathbf{p}_j\right)$$

which is the harmonic perturbation of equation (2.1). We can therefore write

$$\Lambda^\dagger = -\frac{e}{m}\sqrt{\frac{2\pi\hbar^2}{VE_\gamma}}\sum_{j=1}^{Z}\sum_{\lambda=1}^{2}\int \mathrm{d}^3\mathbf{k}a_\lambda(\mathbf{k})e^{i\mathbf{k}\cdot\mathbf{x}_j}\hat{\epsilon}_\lambda(\hat{k})\cdot\mathbf{p}_j \tag{2.10}$$

which can be used in Fermi's golden rule, equation (2.3). The absorption rate is given by

$$\begin{aligned} w_{0\to[f]} &= \frac{2\pi}{\hbar}\int \mathrm{d}f\left|\langle\Psi_f;(n-1)(\mathbf{k},\hat{\epsilon})|\frac{e}{m}\sqrt{\frac{2\pi\hbar^2}{VE_\gamma}}\sum_{j=1}^{Z}\sum_{\lambda=1}^{2}\int \mathrm{d}^3\mathbf{k}'a_\lambda(\mathbf{k}')e^{i\mathbf{k}'\cdot\mathbf{x}_j}\hat{\epsilon}_\lambda(\hat{k}')\cdot\mathbf{p}_j|\Psi_0;n(\mathbf{k},\hat{\epsilon})\rangle\right|^2 \\ &\quad\times\delta(E_f - E_0 - E_\gamma) \\ &= \frac{2\pi}{\hbar}\left(\frac{e}{m}\right)^2\frac{2\pi\hbar^2}{VE_\gamma}\int \mathrm{d}f\left|\sum_{j=1}^{Z}\sum_{\lambda=1}^{2}\int \mathrm{d}^3\mathbf{k}'\langle(n-1)(\mathbf{k},\hat{\epsilon})|a_\lambda(\mathbf{k}')|n(\mathbf{k},\hat{\epsilon})\rangle\right. \\ &\quad\left.\times\langle\Psi_f|e^{i\mathbf{k}'\cdot\mathbf{x}_j}\hat{\epsilon}_\lambda(\hat{k}')\cdot\mathbf{p}_j|\Psi_0\rangle\right|^2\delta(E_f - E_0 - E_\gamma) \\ &= \frac{4\pi^2\alpha}{VE_\gamma}\frac{\hbar^2c}{m^2}n(\mathbf{k},\hat{\epsilon})\int \mathrm{d}f|\langle\Psi_f|\sum_{j=1}^{Z}e^{i\mathbf{k}\cdot\mathbf{x}_j}\hat{\epsilon}\cdot\mathbf{p}_j|\Psi_0\rangle|^2\delta(E_f - E_0 - E_\gamma) \end{aligned} \tag{2.11}$$

for a photon with wave vector $\mathbf{k} = \frac{E_\gamma}{\hbar c}\hat{k}$ and polarisation $\hat{\epsilon}$. The dimensionless fine structure constant $\alpha = \frac{e^2}{\hbar c} \backsimeq \frac{1}{137}$ appears in equation (2.11).

In words, the equation for the photon absorption cross section of a single scattering centre can be written

$$\sigma(E_\gamma) = \frac{\text{Photons absorbed per unit time}}{\text{Photon flux per unit time}} \tag{2.12}$$

where the numerator is given by Fermi's golden rule. To motivate the form of the denominator, consider the volume element V which I promised would cancel. The density of photons with wave vector, $\mathbf{k}$ and polarisation, $\hat{\epsilon}$ is simply the number of photons, $n(\mathbf{k},\hat{\epsilon})$ divided by the volume, V.

In order to obtain the flux, the density must be multiplied by the velocity, c. The photon flux per unit time is $cn(\mathbf{k},\hat{\epsilon})/V$, giving

$$\begin{aligned}\sigma(E_\gamma) &= \frac{w_{0\to[f]}}{cn(\mathbf{k},\hat{\epsilon})/V} \\ &= 4\pi^2\alpha E_\gamma \int \mathrm{d}f |\langle\Psi_f|\frac{\hbar}{E_\gamma m}\sum_{j=1}^{Z} e^{i\mathbf{k}\cdot\mathbf{x}_j}\hat{\epsilon}\cdot\mathbf{p}_j|\Psi_0\rangle|^2\delta(E_f-E_0-E_\gamma). \end{aligned} \tag{2.13}$$

Using the definitions

$$\hat{O} \equiv \frac{\hbar}{E_\gamma m}\sum_{j=1}^{Z} e^{i\mathbf{k}\cdot\mathbf{x}_j}\hat{\epsilon}\cdot\mathbf{p}_j \tag{2.14}$$

and

$$R(E_\gamma) \equiv \int \mathrm{d}f |\langle\Psi_f|\hat{O}|\Psi_0\rangle|^2\delta(E_f-E_0-E_\gamma) \tag{2.15}$$

we obtain

$$\sigma(E_\gamma) = 4\pi^2\alpha E_\gamma R(E_\gamma) \tag{2.16}$$

as our final form of the cross section.

2.1.2 Discussion of the Lorentz Integral Transform

Calculating $R(E_\gamma)$ gives us the total cross section. However, calculating $R(E_\gamma)$ can be difficult since the nuclear potential is complicated and $|\Psi_f\rangle$ is a continuum of states and is not bounded. The LIT now comes into play as it is a method for converting unbound problems into bound ones. The LIT is defined by [Efr94, Efr07]

$$\Phi(s_R+is_I) \equiv \int_{E_{th}}^{\infty}\mathrm{d}E_\gamma \frac{R(E_\gamma)}{(E_\gamma-s_R)^2+s_I^2} \tag{2.17}$$

with the complex number $s = s_R + is_I$. The integration is from the threshold energy for the reaction, E_{th}, over all energies above threshold.

To better understand the transform, substitute the response of equation (2.15) into the LIT, equation (2.17).

$$\begin{aligned}\Phi(s) &= \int_{E_{th}}^{\infty}\mathrm{d}E_\gamma \frac{R(E_\gamma)}{(E_\gamma-s_R)^2+s_I^2} \\ &= \int_{E_{th}}^{\infty}\mathrm{d}E_\gamma \frac{1}{(E_\gamma-s_R)^2+s_I^2}\int \mathrm{d}f|\langle\Psi_f|\hat{O}|\Psi_0\rangle|^2\delta(E_f-E_0-E_\gamma) \\ &= \int \mathrm{d}f \frac{\langle\Psi_0|\hat{O}^\dagger|\Psi_f\rangle\langle\Psi_f|\hat{O}|\Psi_0\rangle}{((E_f-E_0-s_R)-is_I)((E_f-E_0-s_R)+is_I)} \\ &= \langle\Psi_0|\hat{O}^\dagger\frac{1}{H-E_0-s_R-is_I}\int \mathrm{d}f|\Psi_f\rangle\langle\Psi_f|\frac{1}{H-E_0-s_R+is_I}\hat{O}|\Psi_0\rangle \\ &= \langle\Psi_0|\hat{O}^\dagger\frac{1}{H-E_0-s_R-is_I}\frac{1}{H-E_0-s_R+is_I}\hat{O}|\Psi_0\rangle \end{aligned} \tag{2.18}$$

Where $\int \mathrm{d}f|\Psi_f\rangle\langle\Psi_f| = 1$ is the completeness relation and $H|\Psi_f\rangle = E_f|\Psi_f\rangle$. We now define $|\tilde{\Psi}\rangle$ by the Schrödinger-like equation

$$(H-E_0-s_R+is_I)|\tilde{\Psi}\rangle = \hat{O}|\Psi_0\rangle. \tag{2.19}$$

We then have

$$\begin{aligned}\Phi(s) &= \langle\Psi_0|\hat{O}^\dagger \frac{1}{H-E_0-s_R-is_I}\frac{1}{H-E_0-s_R+is_I}\hat{O}|\Psi_0\rangle \\ &= \langle\tilde{\Psi}|\tilde{\Psi}\rangle. \end{aligned} \tag{2.20}$$

We have changed the problem from solving for $R(E_\gamma)$ to solving for $\langle\tilde{\Psi}|\tilde{\Psi}\rangle$. The reason for this transformation is the boundary conditions of the two problems. The conditions for computing $R(E_\gamma)$ with traditional methods are very complicated since the states $|\Psi_f\rangle$ are unbounded. However, $\langle\tilde{\Psi}|\tilde{\Psi}\rangle$ is finite through its relationship with the finite $\Phi(s)$. The state $|\tilde{\Psi}\rangle$ must be bounded for its inner product to be finite. We can apply the boundary condition that $|\tilde{\Psi}\rangle$ must vanish at large distances and can find it using several methods, such as correlated hyperspherical harmonics or effective interaction hyperspherical harmonics [Efr07].

Once we have computed $\langle\tilde{\Psi}|\tilde{\Psi}\rangle$ the LIT must be inverted using an expansion of the response function [Efr94, Efr07]. This expansion is then substituted into the definition of the LIT, equation (2.17). The coefficients of the expansion are then determined by curve fitting.

As it appears above, the LIT allows for calculations of the total cross section, taking into consideration all reaction channels. In other words, it calculates the cross section for inclusive processes. The examples given in section 1.3, and shown in figures 1.2 and 1.3, use this calculation technique. In order to separate the reaction channels, the exclusive processes version of the LIT is required [LaP00, Efr07].

To compute the cross section of a single, two-body photodisintegration reaction channel we can no longer use the completeness relation $\int \mathrm{d}f|\Psi_f\rangle\langle\Psi_f| = 1$. Instead the matrix element $\langle\Psi_f|\hat{O}|\Psi_0\rangle$ is broken into a Born approximation term and a final-state interaction term. The Born term can be computed with conventional means, where the final-state interaction term requires the use of the LIT. The evaluation of the matrix elements in the final-state interaction term proceeds similarly to the inclusive LIT discussed above with the exception that we obtain two Schrödinger-like equations that must be solved. Once the equations have been solved, the transform can be inverted to recover the cross section.

We have outlined how the LIT can be used to compute both inclusive and exclusive cross sections for the photodisintegration of the lithium isotopes. The inclusive calculations have already been performed and were discussed in section 1.3. It is hoped that our measurements of the cross sections of individual reaction channels will prompt exclusive calculations, especially for the $^7\mathrm{Li} + \gamma \rightarrow n + {}^6\mathrm{Li}$(g.s.) reaction channel.

2.2 Parameterisation of the Cross Section

In order to communicate our results we desire to parameterise our differential cross sections. Welton [Wel63] derived general formulae concerning nuclear reactions involving polarised beams and

targets. Weller *et al.* took the general formulae of Welton and applied them to photonuclear physics with linearly polarised [Wel92] and circularly polarised [Wel94] photon beams.

We begin our discussion in the same place as Weller *et al.* by taking the results of Welton's scattering-theory calculations and write the differential cross section as

$$\frac{d\sigma}{d\Omega}(\theta,\phi) = \sum_{kqKQ} A_{kqKQ} t_{kq} T_{KQ} \tag{2.21}$$

where t_{kq} and T_{KQ} are respectively the tensor moments associated with the gamma-ray beam and target polarisations. We can write

$$A_{kqKQ} = \frac{\lambda}{24\pi^2} \sum_{tt'k'q'} B^{k'q'}_{kqKQ} R_t R'_{t'} P^{|q'|}_{k'}(\cos\theta) \tag{2.22}$$

where λ is the photon wavelength, R_t and $R'_{t'}$ are related to the reduced matrix elements of the transition, $P^{|q'|}_{k'}(\cos\theta)$ are the associated Legendre functions, and $B^{k'q'}_{kqKQ}$ is a coefficient. Equation (2.21) can be simplified by noting that, for an unpolarised target, $T_{00} = 1$ and $T_{KQ} = 0$ for all other K and Q [Wel63, Wel94].

We can further simplify (2.21) by finding the beam tensor moments. They are given by [Wel63, Wel92, Wel94]

$$\begin{aligned} t_{00} &= 1 \\ t_{10} &= \frac{f_c}{\sqrt{2}} \\ t_{20} &= \frac{1}{\sqrt{10}} \\ t_{2(\pm 2)} &= -\frac{f_\ell}{2}\sqrt{\frac{3}{5}} e^{\pm 2i\phi} \end{aligned} \tag{2.23}$$

where f_ℓ is the fraction of linear polarisation, ϕ is the angle from the linear polarisation vector and f_c is the fraction of circular polarisation using the convention that right-handed polarisation is positive and left-handed polarisation is negative.

We can use these simplifications to write equation (2.21) as

$$\frac{d\sigma}{d\Omega}(\theta,\phi) = A_{0000}t_{00} + A_{2000}t_{20} + A_{1000}t_{10} + A_{2200}t_{22} + A_{2(-2)00}t_{2(-2)}. \tag{2.24}$$

Furthermore, we can use the relation [Wel94]

$$A_{k(-q)K(-Q)} = (-1)^{k+K+q+Q} A_{kqKQ} \tag{2.25}$$

to show that $A_{1000} = 0$ and $A_{2(-2)00} = A_{2200}$. It is interesting to note that since $A_{1000} = 0$ we have no dependence on the polarisation of a circularly polarised photon beam. The circular polarisation comes into play only if we have a polarised target which can give us non-zero T_{10} and T_{11} terms. We can further simplify equation (2.24) to read

$$\frac{d\sigma}{d\Omega}(\theta,\phi) = A_{0000} + \frac{1}{\sqrt{10}}A_{2000} - f_\ell\sqrt{\frac{3}{5}}\cos(2\phi)A_{2200}. \tag{2.26}$$

While it is possible to examine the cross section in great detail and obtain information about the transition matrix elements, as was done in the thesis of Blackston [Bla07], we will simply try to determine the dependence of the differential cross section on the polar and azimuthal angles, θ and ϕ. It is our goal to obtain a form that we can fit to our data in order to better communicate our results. There are currently no theoretical predictions to compel a transition matrix element analysis at this time.

We note that $B_{kq00}^{k'q'} \sim \delta_{qq'}$ [Wel92] so we can write $A_{0000} \sim P_k^0(\cos\theta)$, $A_{2000} \sim P_k^0(\cos\theta)$ and $A_{2200} \sim P_k^2(\cos\theta)$. We also take $f_c = 1$ when using a linearly polarised beam due to the excellent polarisation of the HIGS beam. Using these results, with equation (2.26), we can obtain the final form of our cross section. The associated Legendre function expansion of the cross section is

$$\frac{d\sigma}{d\Omega}(\theta,\phi) = \frac{\sigma}{4\pi}\left[1 + \sum_{k=1}^{\infty} a_k P_k^0(\cos\theta) + \sum_{k=2}^{\infty} e_k P_k^2(\cos\theta)\cos 2\phi\right] \tag{2.27}$$

for linearly polarised photons and

$$\frac{d\sigma}{d\Omega}(\theta) = \frac{\sigma}{4\pi}\left[1 + \sum_{k=1}^{\infty} a_k P_k^0(\cos\theta)\right] \tag{2.28}$$

for circularly polarised photons. The parameters a_k and e_k are fitting coefficients, σ is the absolute cross section, and the associated Legendre functions up-to-and-including $k = 4$ are

$$\begin{aligned}
P_0^0(\cos\theta) &= 1 \\
P_1^0(\cos\theta) &= \cos\theta \\
P_2^0(\cos\theta) &= \frac{1}{2}\left(3\cos^2\theta - 1\right) \\
P_3^0(\cos\theta) &= \frac{1}{2}\left(5\cos^3\theta - 3\cos\theta\right) \\
P_4^0(\cos\theta) &= \frac{1}{8}\left(35\cos^4\theta - 30\cos^2\theta + 3\right) \\
P_2^2(\cos\theta) &= 3\left(1 - \cos^2\theta\right) \\
P_3^2(\cos\theta) &= 15\cos\theta\left(1 - \cos^2\theta\right) \\
P_4^2(\cos\theta) &= \frac{15}{2}\left(7\cos^2\theta - 1\right)\left(1 - \cos^2\theta\right).
\end{aligned} \tag{2.29}$$

Note that θ is the polar angle in the centre-of-momentum (CM) frame while the azimuthal angle, ϕ, is the same in both the laboratory and CM frames.

We can find the differential cross section for unpolarised photons from equation (2.27) by averaging over polarisations

$$\frac{d\sigma}{d\Omega}(\theta) = \frac{1}{2\pi}\int_0^{2\pi}\left[\frac{d\sigma}{d\Omega}(\theta,\phi)\right]d\phi = \frac{\sigma}{4\pi}\left[1 + \sum_{k=1}^{\infty} a_k P_k(\cos\theta)\right] \tag{2.30}$$

and it is the same as the differential cross section for circularly polarised photons, equation (2.28). For the purposes of this thesis, let it be understood that $\frac{d\sigma}{d\Omega}(\theta,\phi)$ refers to the differential cross

section for a polarised gamma-ray beam while $\frac{d\sigma}{d\Omega}(\theta)$ refers to the differential cross section for an unpolarised gamma-ray beam. It is also interesting to note that $\frac{d\sigma}{d\Omega}(\theta, 45^\circ) = \frac{d\sigma}{d\Omega}(\theta)$.

A useful and often measured parameter is the cross section asymmetry.[4] The cross section asymmetry is defined to be

$$\Sigma(\theta) \equiv \frac{\frac{d\sigma}{d\Omega}(\theta, 0^\circ) - \frac{d\sigma}{d\Omega}(\theta, 90^\circ)}{\frac{d\sigma}{d\Omega}(\theta, 0^\circ) + \frac{d\sigma}{d\Omega}(\theta, 90^\circ)} \tag{2.31}$$

and substituting our associated Legendre polynomial expansion into this equation we obtain

$$\Sigma(\theta) = \frac{\sum_{k=0}^{\infty} e_k P_k^2(\cos\theta)}{1 + \sum_{k=1}^{\infty} a_k P_k(\cos\theta)} = \frac{\sigma}{4\pi \frac{d\sigma}{d\Omega}(\theta)} \sum_{k=0}^{\infty} e_k P_k^2(\cos\theta). \tag{2.32}$$

[4] This quantity is often called the analysing power.

Chapter 3

History of the Photodisintegration of Lithium

3.1 Introduction

There is a long history of experiments studying the photodisintegration of the lithium isotopes. Hundreds of papers have been published and it is the duty of every experimenter to ensure that any new experiment adds new information to the pool of knowledge. The literature is filled with results passed from one generation to the next, with each generation refining its experiments and producing results with smaller uncertainties and richer information.

It is impossible to construct a complete history of this field as the literature does not tell the story of the people behind the experiments and the trials they faced for each publication. Nor is it possible to find every paper written on the subject, with many of them going unreferenced by others, existing only in journals which are no longer published and rarely remembered. The language barrier also causes problems. While many journals have been translated, such as many of the Soviet journals, many others have not and are inaccessible to those who do not know the language in question. However, a reasonable attempt can be made to construct a history of the photodisintegration of lithium. The purpose of such a construction is to enhance our current results by showing how they stand upon the results of those who came before us. Even now we can find guidance and wisdom in such studies.

The story of the photodisintegration of lithium begins in 1947. The first known published result appeared in a short note in Physical Review [Bec47]. In this paper Becker, Hanson and Diven examined the reaction $^{7}\mathrm{Li}(\gamma, p)^{6}\mathrm{He}$ with gamma-rays from a 20 MeV betatron, and found a threshold of 9.5 ± 0.3 MeV. From table 1.3 we see that the threshold is actually 10.0 MeV. They detected the reaction by observing the beta decay of the ^{6}He product. The threshold was reported along with those of five other nuclei.

It is from these humble beginnings that we start to build our knowledge of the photodisintegration of the lithium isotopes.

3.2 Experiments from 1950 to 1958

From 1950 to 1954 Titterton and Brinkley performed a number of experiments at different facilities [Tit50a, Tit50b, Tit51, Tit52, Tit53a, Tit53b, Tit54a, Tit54b, Tit55]. Using the technique of nuclear emulsion, they observed many different photodisintegration reactions for both ^{6}Li and ^{7}Li. Gamma rays for the experiment were usually produced from the $^7\mathrm{Li}(p,\gamma)^8\mathrm{Be}, ^8\mathrm{Be}^*$ reaction which produces gamma rays of energies 14.8 and 17.6 MeV, although an accelerator was occasionally used [Tit53a]. It is somewhat ironic that the photodisintegration of lithium isotopes was studied using gamma rays from the inverse reaction. Highlights of these experiments include the first observation of the two-body reaction $^7\mathrm{Li}(\gamma,t)^4\mathrm{He}$ and the absence of the $^6\mathrm{Li}(\gamma,d)^4\mathrm{He}$ reaction which, if we examine table 1.2, cannot proceed by the electric-dipole transition. Of special interest to our photoneutron work is their observation of the $^6\mathrm{Li}(\gamma,n)^5\mathrm{Li}$ reaction, for which they found 70 events and estimated a cross section of (0.5 ± 0.2) mb averaged over the two gamma rays produced by the $^7\mathrm{Li}(p,\gamma)^8\mathrm{Be}, ^8\mathrm{Be}^*$ reaction [Tit51].

While Titterton and Brinkley were performing their experiments, a number of other groups were performing similar measurements. In 1951 Sher, Halpern and Mann used BF_3 proportional counters to detect the neutrons produced by both the $^6\mathrm{Li}(\gamma,n)^5\mathrm{Li}$ and $^7\mathrm{Li}(\gamma,n)^6\mathrm{Li}$ reactions [She51]. The thresholds of these reactions were found to be 5.35 ± 0.20 MeV and 7.15 MeV (uncertainty estimate not given) respectively. These can be compared with the accepted values of 5.7 and 7.3 MeV respectively. Glenn, in 1952, also failed to observe the $^6\mathrm{Li}(\gamma,d)^4\mathrm{He}$ reaction using 2.76 MeV gamma rays and a ^{6}Li loaded emulsion [Gle52]. Tucker and Gregg, in 1953, measured the cross section of $^7\mathrm{Li}(\gamma,p)^6\mathrm{He}$ from 10 to 19 MeV by detecting the beta ray emitted by the decay of the ^{6}He reaction product [Tuc53]. Nabholz, Stoll and Wäffler studied the $^7\mathrm{Li}(\gamma,\alpha)^3\mathrm{H}$ reaction in 1952 with 6 MeV gamma rays [Nab52]. Later Erdös, Stoll, Wächter and Wataghin studied the same reaction and measured its cross section from threshold to 9 MeV [Sto53, Erd54, Sto54].

In 1953 the first results from the University of Saskatchewan concerning the photodisintegration of lithium were published. Goldemberg and Katz studied the $^7\mathrm{Li}(\gamma,n)$ reaction from threshold to 23 MeV using the University of Saskatchewan Betatron [Gol53, Gol54a, Gol54b]. Figure 3.1 shows the apparatus used with the betatron. The electron beam from the betatron was incident on the X-ray target and photons were produced though bremsstrahlung. This produced a continuous spectrum of photons with energy less than a maximum bremsstrahlung energy. This photon beam was monitored using an ionisation chamber and collimated by lead. The photon beam travelled through an aperture in a concrete wall and entered the detector where it was incident on the natural lithium target. Neutrons could be produced in the target and would be moderated by the surrounding paraffin. Once the neutrons were brought to thermal energy levels, they could be detected by the two BF_3 proportional counters. Figure 3.2b shows the cross section found by Goldemberg and Katz. It was

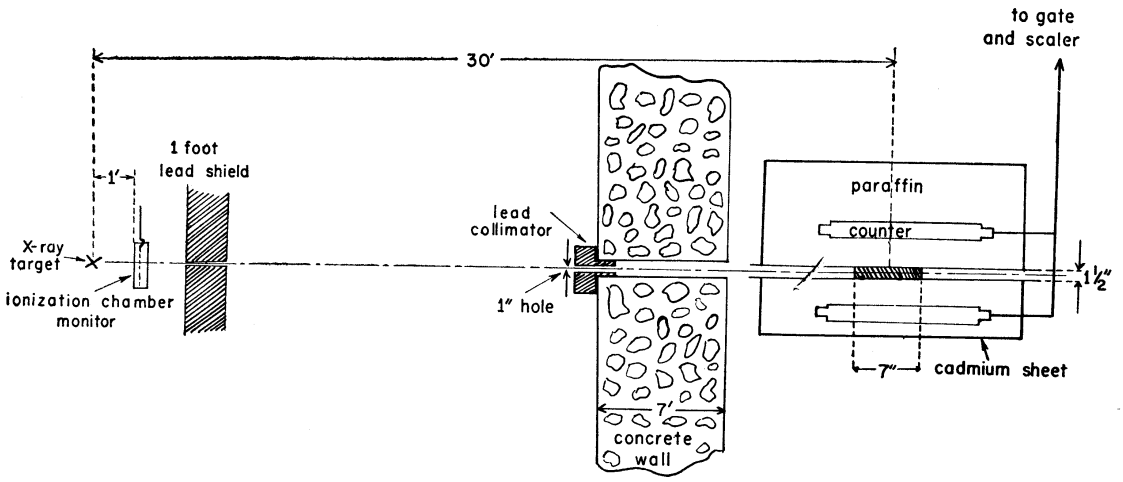

Figure 3.1: The apparatus used with the University of Saskatchewan betatron in 1953, from figure 1 of [Gol54b]

computed using the neutron yield curve for various maximum betatron energies shown in figure 3.2a. Note that the yield curve is the result of photons with a bremsstrahlung spectrum which is a

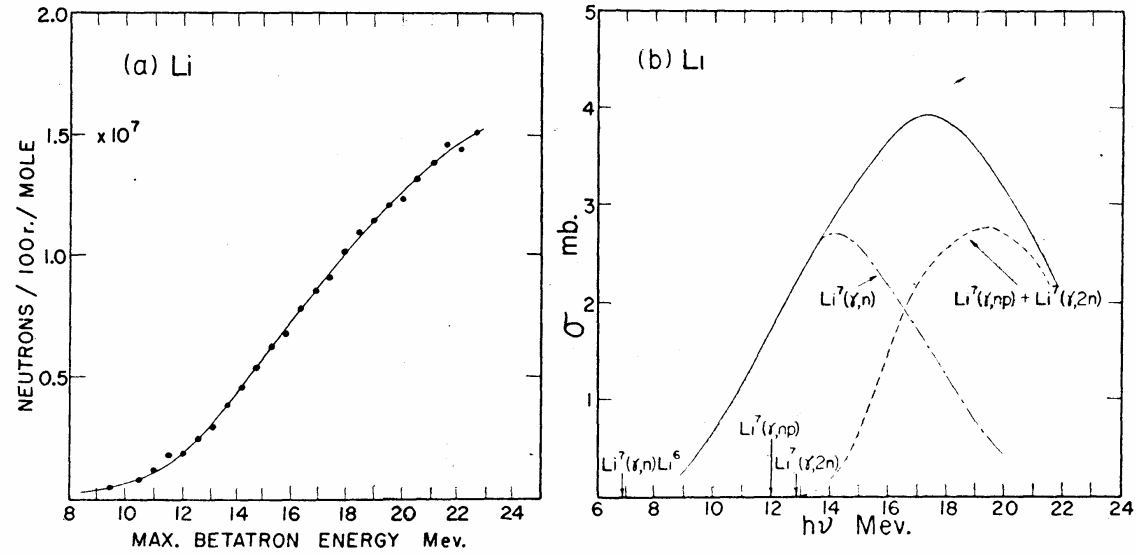

Figure 3.2: The neutron yield curve and lithium photoneutron cross section of Goldemberg and Katz, from figure 1 of [Gol54a]

continuous photon spectrum that is certainly not monochromatic. A deconvolution is required to extract the cross section from the yield curve.

Barton and Smith published experiments in 1954 and later in 1958 concerning the quasideuteron disintegration of natural lithium [Bar54, Bar58]. The quasideuteron effect was first proposed by Levinger [Lev51] and relates the cross section of the photodisintegration of nuclei to that of the deuteron for gamma-ray energies greater than $\sim$ 100 MeV. The formula for the reaction can be

written as ^{7}Li$(\gamma, np)^5$He, noting that ^{5}He will immediately decay into ^{4}He by emitting a proton. Barton and Smith studied this reaction using bremsstrahlung photons up to 280 MeV. In the same time period, the quasideuteron disintegration of natural lithium was also studied by an MIT group with bremsstrahlung photons up to 340 MeV [Odi56, Wat56]. A group from Oxford performed a lower energy measurement of this reaction with bremsstrahlung up to 110 MeV and concluded that even at lower energies, the quasideuteron effect is a major contribution [Whi58].

Other reactions were studied in this time period. Miwa found the total cross section for the ^{6}Li$(\gamma, t)^4$He reaction from threshold to 19 MeV [Miw55]. Edge measured the ^{6}Li(γ, n) cross section at 6.2 MeV to be (0.3 ± 0.2) mb [Edg56]. Rubin and Walter measured the cross sections of ^{7}Li$(\gamma, p)^6$He from 10 to 30 MeV [Rud54] and Heinrich and Rubin measured ^{7}Li(γ, n) from 13 to 31 MeV [Hei55].

Rybka and Katz used the University of Saskatchewan Betatron again in 1958 to measure the cross section of the ^{7}Li(γ, n) reaction. They used a target of LiH and four BF_3 detectors in arrangement similar to the previous experiment shown in figure 3.1. Their results are plotted in figure 3.3 against those of Heinrich and Rubin [Hei55]. The disagreement is significant.

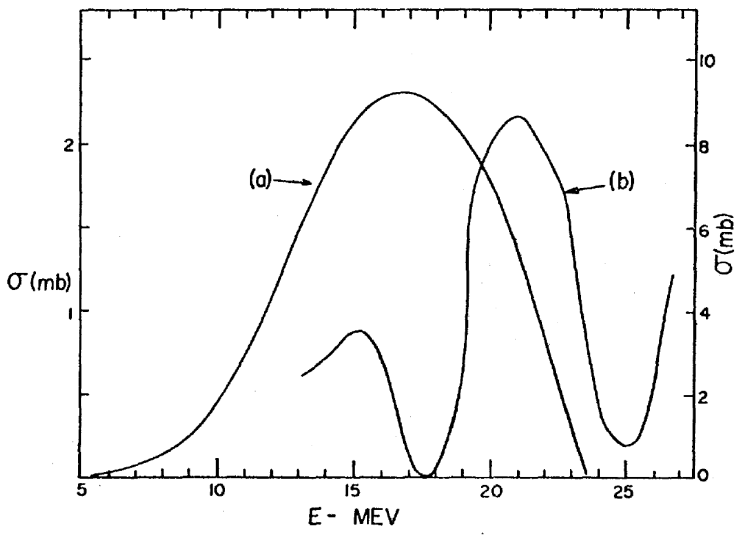

Figure 3.3: The ^{7}Li(γ, n) cross sections of Rybka and Katz (a) and Heinrich and Rubin (b), from figure 2 of [Ryb58]

3.3 Experiments from 1959 to 1963

Until 1959 most research had concentrated on the direct reaction where the input was a photon and the output were ions, protons and neutrons. The inverse reaction ^{3}H$(\alpha, \gamma)^7$Li was studied by two groups around 1960. Griffiths, Morrow, Riley and Warren published preliminary results in 1958 [Ril58] and more detailed cross sections in 1961 for α-particle energies between 0.5 and 1.9 MeV

[Gri61]. They were interested in studying possible cluster models of ^{7}Li consisting of a ^{3}H nucleus bound to an α-particle. Holmgren and Johnson produced a cross section for this reaction using α-particles of energy between 0.48 and 1.32 MeV [Hol59]. Miwa and Yamanouchi measured the cross section of the forward reaction $^7\mathrm{Li}(\gamma,t)^4\mathrm{He}$ [Miw60]. Kohler and Austin studied the inverse reaction on ^{6}Li, $^3\mathrm{H}(^3\mathrm{He},\gamma)^6\mathrm{Li}$ [Koh63].

Two experiments came from the Case Institute of Technology in 1959 and 1960. Romanowski and Voelker found the cross section of both the $^7\mathrm{Li}(\gamma,n)$ reaction and $^6\mathrm{Li}(\gamma,n)$ using BF_3 proportional counters, a betatron and targets consisting of natural lithium and enriched ^{6}Li [Rom59]. Their results are presented in figure 3.4. For the case of $^6\mathrm{Li}(\gamma,n)$, Romanowski and Voelker were

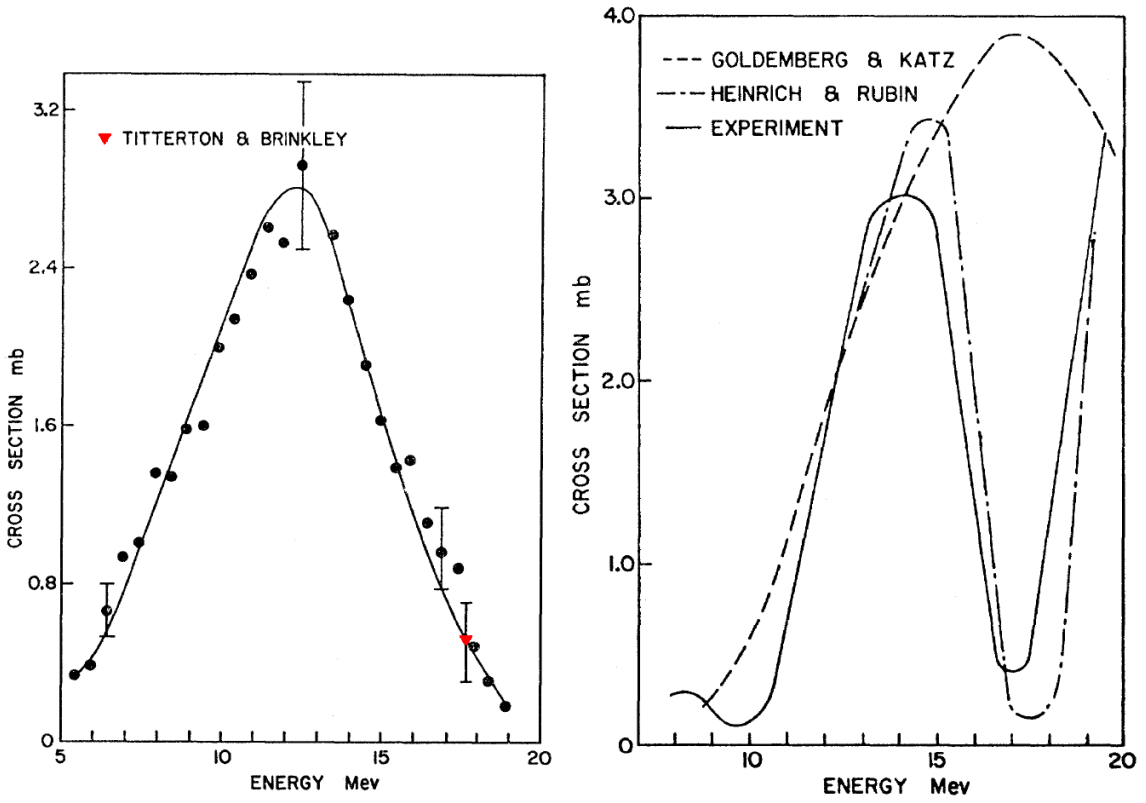

Figure 3.4: The cross sections of Romanowski and Voelker for $^6\mathrm{Li}(\gamma,n)$ (left, colour added for clarity) and $^7\mathrm{Li}(\gamma,n)$ (right), from figures 5 and 7 of [Rom59]

the first to publish a cross section over an energy interval. They also plot the datum of Titterton and Brinkley [Tit51]. For the case of ^{7}Li they plot their results against Goldemberg and Katz [Gol54a] and Heinrich and Rubin [Hei55]. While it would appear that their results agree with those of Heinrich and Rubin, the uncertainties, which are not displayed on this particular graph but are discussed in the paper, are much too large to allow conclusions. Later at the Case Institute of Technology, Proctor and Voelker would study the photodisintegration of ^{6}Li with bremsstrahlung photons with maximum energy 17.3 MeV [Pro60]. They were looking for correlated pairs of neutrons and protons emitted from this reaction, but did not find any. From this they concluded that

a deuteron-alpha model of ^{6}Li may not be appropriate.

The ^{7}Li(γ, n) and ^{6}Li(γ, n) reactions were studied over a wider energy range by groups from the University of Virginia and the Universita di Torino respectively. The Virginia group of Fast, Flournoy, Tickle and Whitehead studied the ^{7}Li(γ, n) reaction using nine BF_3 proportional chambers and a natural lithium target. The cross section they obtained is shown in figure 3.5, along with the integrated cross section [Fas60]. The Torino group of Costa, Ferroni, Wataghin and Malvano

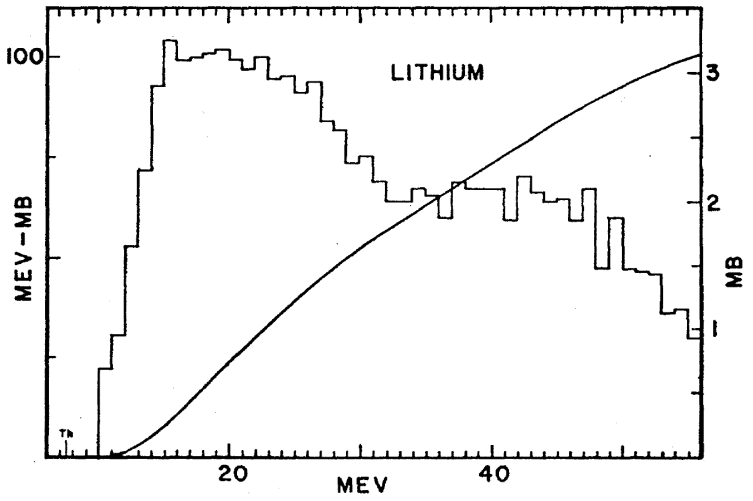

Figure 3.5: The cross section (histogram, right axis) and integrated cross section (line, left axis) of Fast *et al.*, from figure 7 of [Fas60]

studied the ^{6}Li(γ, n) reaction with an enriched ^{6}Li target [Cos63]. Their cross section is shown in figure 3.6 with the previous measurements made at lower energies by Romanowski and Voelker [Rom59] and the datum of Titterton and Brinkley [Tit51].

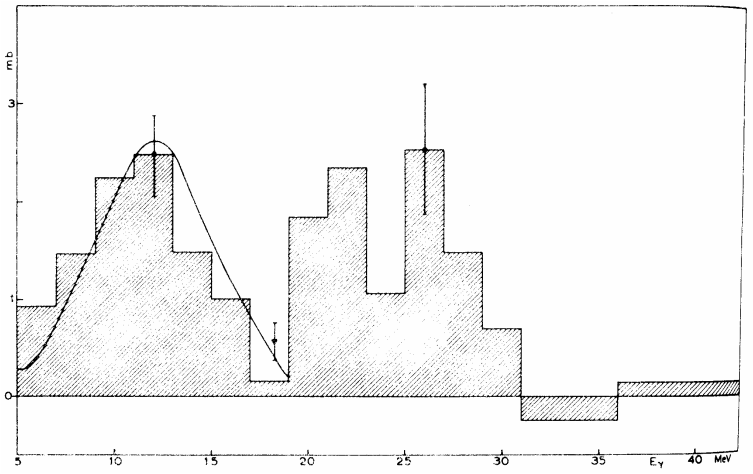

Figure 3.6: The ^{6}Li(γ, n) cross section of Costa *et al.* (histogram), from figure 2 of [Cos63], with the measurements of Romanowski and Voelker (line) and the datum of Titterton and Brinkley (point near 18 MeV)

In 1962-3 several groups studied the production of a proton by the photodisintegration of ^{7}Li. Shardanov and Shevchenko produced a cross section for the $^7\mathrm{Li}(\gamma, p)$ reaction from threshold to 16 MeV [Sha62]. The β-decay of ^{6}He was used by Gregory, Sherwood and Titterton [Gre62] and independently by Clikeman, Bureau, McConnell, Stewart and Tripp [Cli63] to measure the cross section of the $^7\mathrm{Li}(\gamma, ^6\mathrm{He})p$ reaction.

Reactions involving the electrodisintegration of lithium were studied by Bishop and Bernheim. They obtained inelastic scattering form factors for both the total electrodisintegration of ^{6}Li [Ber63a, Bis63] and ^{7}Li [Ber63b, Bis64].

3.4 The 1960-69 USSR Academy of Sciences Experiments

During the 1960's the USSR Academy of Sciences performed several experiments concerning the photodisintegration of lithium. These experiments were generally performed at the A. F. Ioffe Physico-Technical Institute synchrotron in Leningrad, now St. Petersburg. This group of researchers published a number of papers which mostly concern the production of charged reaction products, although some neutron work was done on both isotopes of lithium. The results from this group were mostly published in Soviet journals that were later translated into English.[1]

The first Soviet experiments concerning the photodisintegration of lithium were published in 1960, both studying the $^6\mathrm{Li}(\gamma, p)$ reaction. Komar and Makhnovskiĭ used a nuclear emulsion [Kom60] while Bazhanov and Kul'chitskiĭ used scintillation counters [Baz60]. Later, Volkov and Kul'chitskiĭ would find the cross section per effective quanta for six reactions: ^{6}Li(γ,p), ^{6}Li(γ,d), ^{6}Li(γ,t), ^{7}Li(γ,p), ^{7}Li(γ,d) and ^{7}Li(γ,t) [Vol62]. These two researchers later built upon this foundation and performed more extensive experiments on the ^{7}Li(γ,p) and ^{7}Li(γ,t) reactions [Kul63]. Chizhov *et al.* performed studies on the photoproduction of deuterons from both ^{6}Li and ^{7}Li [Chi62]. This four year period of rapid charged-particle experiments ended with Komar and Makhnovskiĭ publishing measurements on the ^{6}Li(γ,p), ^{6}Li(γ,d) and ^{6}Li(γ,t) reactions [Kom64, Mak64, Baz65].

Charged particle studies momentarily gave way to photoneutron studies. Bazhanov, Komar and Kulikov studied photoneutrons from both isotopes using BF_3 proportional counters. In 1964 they reported a cross section for the $^6\mathrm{Li}(\gamma, n)$ reaction [Baz64, Baz65] which can be seen in figure 3.7, along with the results of Costa *et al.* [Cos63]. In 1966 they reported the results of a subsequent experiment studying the $^7\mathrm{Li}(\gamma, n)$ reaction using an enriched target [Baz66]. Their reported cross section can be seen in figure 3.8, along with the data of Fast *et al.* [Fas60].

After publishing these two photoneutron results these researchers returned their attention to

[1] The spelling of Russian names often vary from paper-to-paper depending on how they are translated into the Roman alphabet. I have tried to maintain consistency in my discussion by choosing one spelling for each name, usually that used in the Soviet Journal of Nuclear Physics. All spellings in the reference section are taken from the individual references.

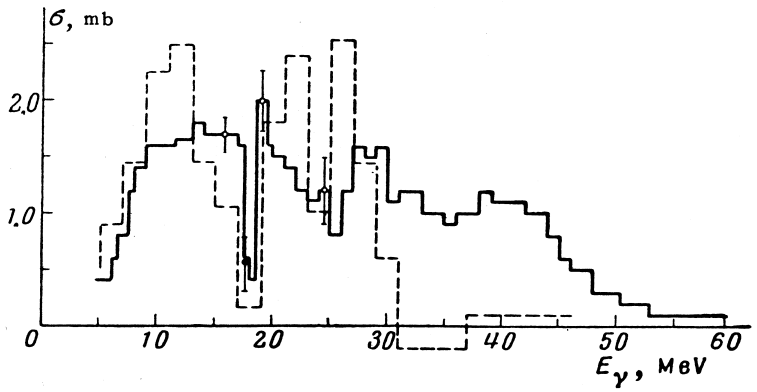

Figure 3.7: The $^{6}\mathrm{Li}(\gamma, n)$ cross section of Bazhanov, Komar and Kulikov (solid line) with the results of Costa *et al.* (dotted line), from figure 1 of [Baz64]

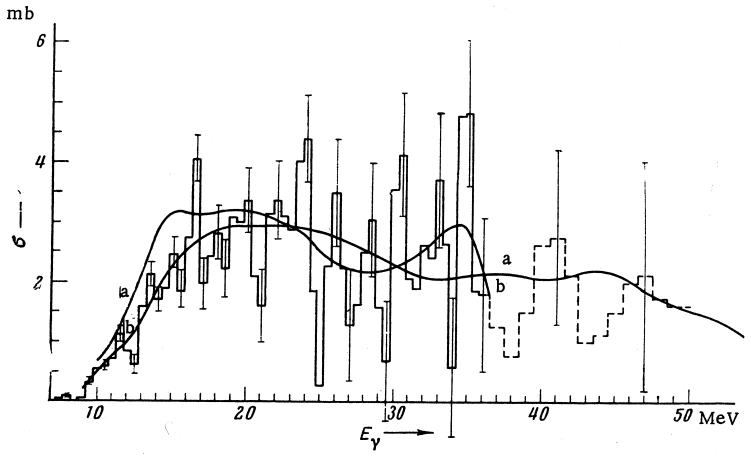

Figure 3.8: The $^{7}\mathrm{Li}(\gamma, n)$ cross section of Bazhanov, Komar and Kulikov both raw (histogram) and smoothed (line b) with the results of Fast *et al.* (line a), from figure 1 of [Baz66]

charged-particle reactions. Denisov and Kul'chitskiĭ studied many different reactions on ^{7}Li resulting in the production of proton and tritons and published cross sections for some reactions [Den67a]. Denisov, Komar, Kul'chitskiĭ and Makhnovskiĭ produced cross sections for ^{6}Li(γ,p), ^{6}Li(γ,d) and ^{6}Li(γ,t) [Den67b].

The last result concerning the photodisintegration of lithium to come out of the A. F. Ioffe Physico-Technical Institute synchrotron came in 1969. Denisov, Komar, Kul'chitskiĭ and Chubukov studied the reaction $^7\mathrm{Li}(\gamma,\gamma')^7\mathrm{Li}^* \rightarrow {}^4\mathrm{He} + {}^3\mathrm{H}$ by detecting both the triton and photon emitted from the reaction [Den69]. In this reaction, the ^{7}Li nucleus is excited to a higher state and then decays into a triton and an alpha particle. This experiment was the first to detect a recoil photon from a lithium nucleus; inverse reactions produce photons, but they use ions as the beam particles.

These researchers published no further results concerning the photodisintegration of lithium isotopes until the mid to late 1970's. During 1960-69 many groups outside of the USSR were publishing results and we now turn our attention to their works.

3.5 Experiments from 1964 to 1966

The short time period from 1964 to 1966 saw many published results describing the production of photoneutrons from the lithium isotopes. These results include the seminal experiments performed at the Ernest O. Lawrence Laboratory in Livermore, California, which will be examined in detail in the next section due to their historic importance. This section covers other experiments performed at this time which are less well-known than the Livermore experiments, but no less important for our historical understanding of the photodisintegration of lithium.

Green and Donahue studied photoneutrons from both lithium isotopes using BF_3 proportional counters and monoenergetic gamma rays produced by thermal neutron capture on several isotopes: Al, Cu, Cl, N, Ni, Cr, Fe, Pb, S, Ti, Mn and Zn [Gre64]. These capture reactions can produce gamma rays with many energies up to 10.8 MeV. Eight measurements were produced from ^{7}Li and ten were produced for ^{6}Li. These measurements can be seen in figure 3.9 along with those of Romanowski and Voelker [Rom59] and Goldemberg and Katz [Gol54a].

Howard and Stovall also used BF_3 proportional counters but used a continuous bremsstrahlung spectrum of photons to study the photoneutrons from both lithium isotopes [How65]. They published two cross sections for each isotope, using two different analysis parameters: one using a $\Delta E = 1$ MeV and the other using a $\Delta E = 0.5$ MeV grid. The cross sections produced with the $\Delta E = 1$ MeV grid are shown in figure 3.10 since these cross sections better resemble more modern cross section measurements.

Two other groups made measurements using BF_3 proportional counters and bremsstrahlung photons. Allum, Crawley and Spicer studied the $^7\mathrm{Li}(\gamma, n)$ reaction [All64] and Costa, Ferrero,

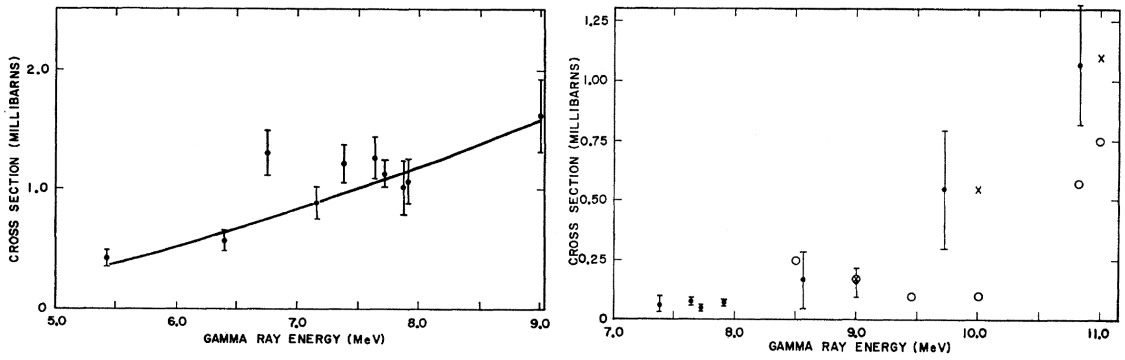

Figure 3.9: The photoneutron cross sections for ^{6}Li (left, data points) and ^{7}Li (right, solid points) by Green and Donahue, with the data from Romanowski and Voelker (line on left and crosses on right) and Goldemberg and Katz (circles on right), from figures 3 and 4 of [Gre64]

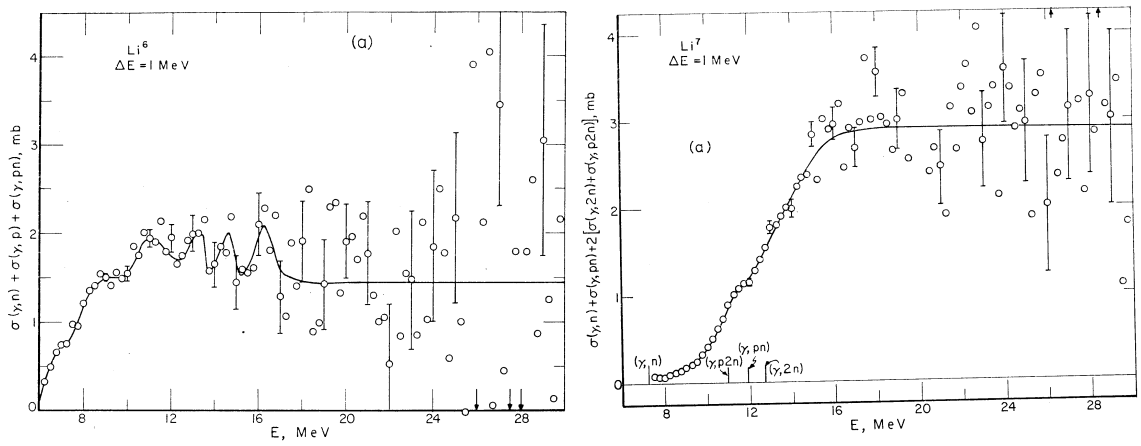

Figure 3.10: The ^{6}Li (left) and ^{7}Li (right) photoneutron cross sections of Howard and Stovall, from figures 3 and 4 of [How65]

Manfredotti, Pasqualini and Roasio made a second measurement of the ^{6}Li(γ, n) reaction from Torino [Cos66]. Their cross sections can be found in figure 3.11.

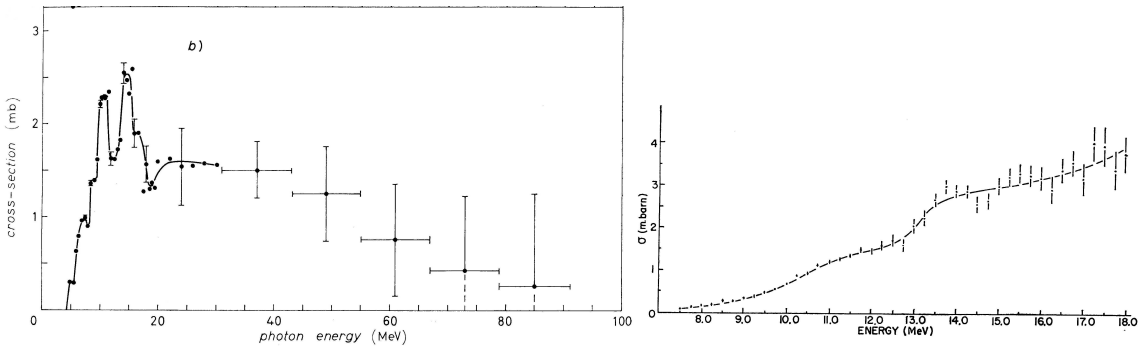

Figure 3.11: The ^{6}Li(γ, n) cross section of Costa *et al.*, from figure 1 (b) of [Cos66] (left), and the ^{7}Li(γ, n) cross section of Allum *et al.* from figure 3 of [All64]

A number of papers came out of Genova with Manuzio, Malvano, Ricco and Sanzone publishing the energy spectra of charged reaction products from both the photodisintegration of ^{6}Li and ^{7}Li [Man65, Man66]. Also from Genova, Wataghin, Scotto and Paoli published the complimentary energy spectra of neutrons from the photodisintegration of both lithium isotopes. They used bremsstrahlung photons and nuclear emulsion [Wat65, Pao66]. None of these papers report a cross section.

There were two other sets of experiments that studied the production of charged reaction products. Dallimore, Lam and Thies studied the reactions ^{6}Li(γ, d) and ^{7}Li(γ, t) below 4 MeV and determined that the reactions are very weak in this energy range by setting upper limits on the cross sections [Dal65]. Sherman, Stewart, Morrison, Baglin and Owens began a multi-year campaign to measure the ^{6}Li$(\gamma, t)^3$He reaction in 1965. They measured the cross section initially from 19 to 24 MeV but then extended their measurements to 35 MeV [She65, She66a, She68, She66b, She67]. Nüsslin, Werner and Zimmerer measured the cross section of the inverse reaction ^{3}H$(^3$He$, \gamma)^6$Li [Nüs66].

The period in time between 1964 to 1966 saw a number of publications concerning the photodisintegration of lithium with special emphasis on the photoneutron reactions. However, the most historic experiments from this time period are the Livermore experiments which we now consider in greater detail.

3.6 The Livermore Experiments

Researchers at the Ernest O. Lawrence Laboratory in Livermore, California performed a campaign of experiments to measure the photoneutron cross section of many different isotopes. Their focus was to use a monochromatic photon beam created by the annihilation of positrons. This was a

very novel technique since previous measurements were made only with continuous bremsstrahlung photon spectra or photons with small energies from radioactive decays and reactions. This group studied a great number of isotopes, including ^{6}Li and ^{7}Li. Their work is presented in summary in the review by Berman and Fultz [Ber75].

While the Livermore photon beam was billed as being monochromatic, this statement requires some interpretation. Figure 3.12 shows the spectra of photons produced when a positron beam is incident on a 0.13 mm beryllium target, as measured by a 20 cm × 20 cm NaI crystal detector. This spectrum is far from monochromatic; there is a monochromatic peak but there is also a large

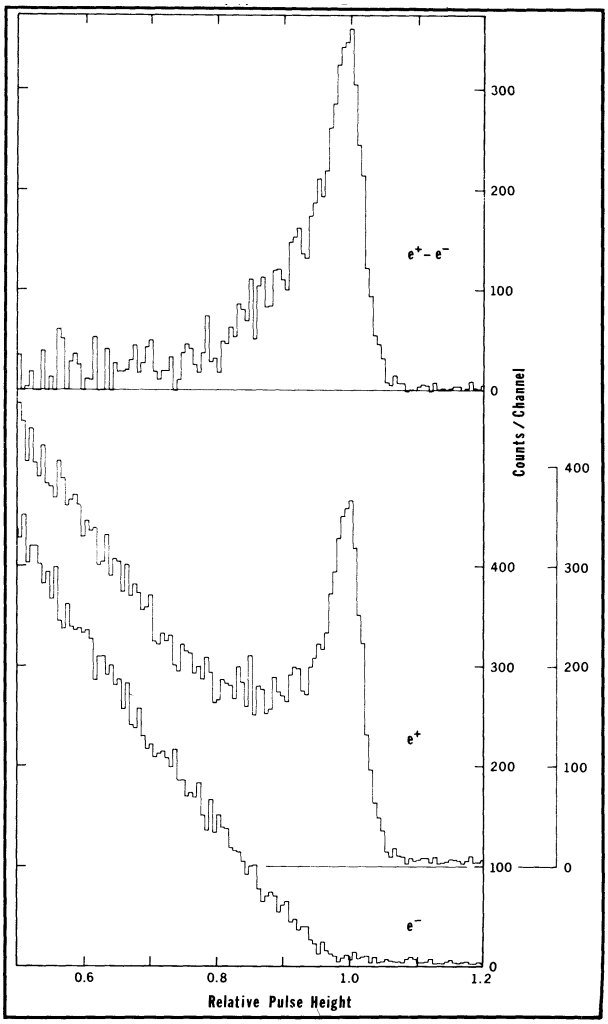

Figure 3.12: Spectra of photons produced using electrons and positrons (bottom) and the subtracted spectrum (top), as measured with a 20 cm × 20 cm NaI detector, from figure 1 of [Ful73]

bremsstrahlung component. However, the researchers measured the effect of this bremsstrahlung component by repeating the experiment using electrons rather than positrons. The bremsstrahlung spectrum due to electrons and the resulting subtraction can also be seen in figure 3.12. The

subtracted photon spectrum is essentially monochromatic. The broadening of the peak in figure 3.12 is mainly due to the resolution of the NaI detector and the Livermore group claimed that they could achieve an energy resolution on the order of 1% [Ber75]. This beam was complimented by an array of BF_3 neutron detectors.

The Livermore group measured the cross sections for both ^{6}Li [Ber65a, Ber65b] and ^{7}Li [Bra66, Bra73]. These cross sections are shown in figure 3.13. The Livermore results became the gold standard for photoneutron cross sections. Forty years later, these cross sections for lithium are still referred to as being worthy of comparison.

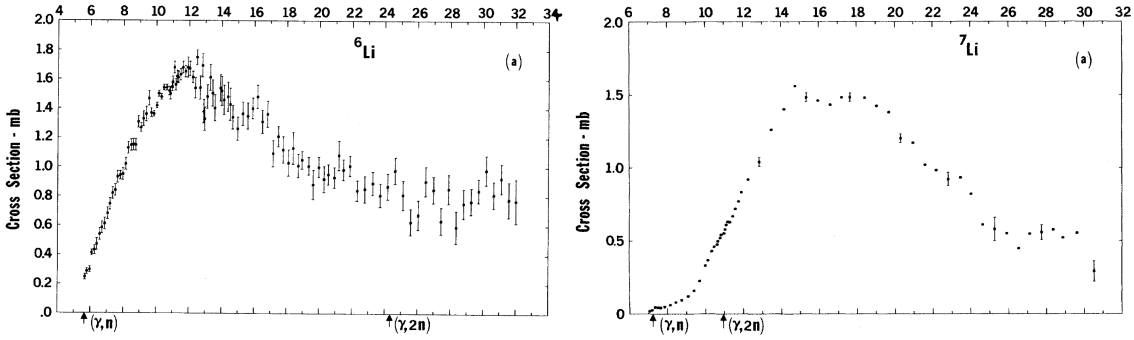

Figure 3.13: The ^{6}Li(γ, n) (left) and ^{7}Li(γ, n) (right) cross sections from the Livermore group, from figures 11 (a) and 12 (a) of [Ber75]

3.7 Experiments from 1967 to 1976

After a rather prolific few years that saw many experiments studying photoneutrons from the lithium isotopes, including the Livermore experiments, the period of 1967 to 1976 saw no new neutron results. There were a number of results published examining charged particle photodisintegration and electrodisintegration which we will quickly review.

Electrodisintegration uses a beam of electrons instead of a photon beam. Electrodisintegration experiments are included in this review since they can be related to photodisintegration because both reactions are electromagnetic and are described by quantum electrodynamics. In fact, some researchers have used the virtual photon spectrum of an electron to convert an electrodisintegration cross section into a photodisintegration cross section [Won70].

Several experiments looked at recoil electrons only. The Saskatchewan experimenters Hutcheon, Drake, Stobie, Beer and Caplan [Hut67, Hut68, Hut69] studied the ^{6}Li(e, e') and ^{7}Li(e, e') inelastic reactions, while Neuhausen [Neu69] and Eigenbrod [Eig69] studied ^{6}Li(e, e'). Later, Neuhausen and Hutcheon returned to study the ^{6}Li(e, e') inelastic reaction [Neu71].

A number of groups looked at the recoil electrons in coincidence with a charged ion produced in the reaction. The group from the Ukrainian Academy of Sciences of Antuf'ev *et al.* reported several

results on the ^{6}Li$(e,e'p)$ reaction [Ant72a, Ant72b, Ant72c, Ant75] and published one paper on the ^{7}Li$(e,e'p)$ reaction [Ant73]. Hiramatsu *et al.* also studied the ^{6}Li$(e,e'p)$ and ^{7}Li$(e,e'p)$ reactions [Hir73], while Heimlich *et al.* examined ^{6}Li$(e,e'p)$ and ^{6}Li$(e,e'd)$ [Hei74] and Genin, Julien *et al.* looked at ^{6}Li$(e,e'd)$, and ^{6}Li$(e,e'\alpha)$ [Gen72, Jul73, Gen74]. Skopik, Tomusiak, Dressler, Shin and Murphy found the energy distribution of deuterons from the electrodisintegration of ^{6}Li [Sko76].

The group of Wong, Hutcheon, Shin and Caplan from the Saskatchewan Accelerator Laboratory used a hybrid method to study the ^{6}Li(γ,p) and ^{7}Li(γ,p) reactions [Won70]. They used an electron beam and found the photoproton cross sections by unfolding the virtual photon spectrum. The method was checked by finding the cross section of ^{6}Li(γ,p) at one energy using real photons. They also studied the ^{6}Li(γ,t) and ^{6}Li$(\gamma,{}^3$He$)$ reactions with real photons [Won70]. The virtual photon method was also employed by Shin, Skopik and Murphy to study ^{6}Li(γ,t) [Shi75] and by Leung *et al.* to study ^{7}Li(γ,t) [Leu77, Sko79a].

There were a number of measurements made concerning photoprotons using bremsstrahlung photons. Matthews, Bertozzi, Kowalski, Sargent and Turchinetz looked at the photoproduction spectra of ^{6}Li(γ,p) and ^{7}Li(γ,p) [Mat68]. Sanzone, Ricco, Costa and Ferrero found the photoproton cross section at 45° for both isotopes of lithium [San70]. Gardiner, Matthews, Owens and Findlay did the same a few years later [Gar73, Mat76]. Denisov and Chubukov produced cross sections for the individual ^{7}Li$(\gamma,p)^6$He reaction channels [Den74] and also produced a cross section for ^{7}Li(γ,d) [Den75].

Other charged reaction products were studied in this time period. Murakami produced cross sections for the ^{6}Li(γ,t) and ^{6}Li(γ,pd) reactions [Mur68, Mur70] and Kotikov and Makhnovskiĭ did likewise for ^{7}Li(γ,pt) [Kot73].

Differential cross sections at 90° for the inverse reaction ^{3}H$(^3$He$,\gamma)^6$Li were obtained independently by two groups. Blatt *et al.* studied the reaction from Ohio State University [Bla68, You70a, You70b] while Ventura, Chang, Meyerhof and Young studied it from Stanford [Ven71, Ven73].

A very interesting, unique and relevant result was produced by Ahrens *et al.* from Mainz. They used a bremsstrahlung spectrum of photons and examined the total absorption of photons in the target. Using a computed absorption cross section due to electromagnetic interactions they were able to find the absorption due to nuclear interactions. From this they computed the cross section for natural lithium [Ahr74, Ahr75], which can be seen in figure 3.14.

3.8 Experiments from 1977 to 1983

A number of different experiments were performed between 1977 and 1983 and some of them concerned reactions which produced neutrons. However, not many produced cross sections in the energy range that we are interested. Better cross sections were produced for some charged particle

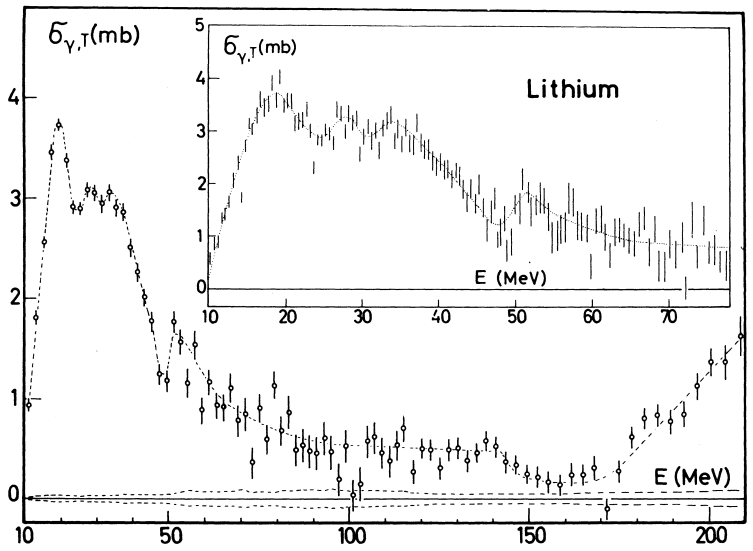

Figure 3.14: Total photonuclear cross section for natural lithium, from figure 2 of [Ahr75]

reactions. For both charged particle and neutron studies, angular dependence, excited states and reaction channels became more important. A BF_3 proportional counter, the standard technique used for many of the previous neutron experiments, requires neutrons to be moderated. This destroys information about their angular distribution and kinetic energy. New experiments strived to surpass this limitation.

Denisov and Chubukov examined the $^7\mathrm{Li}(\gamma, n)^6\mathrm{Li}^*$ reaction which left the ^{6}Li product in a 3.56 MeV final state. They studied the gamma rays produced by the decay of the excited state. Due to high background levels they were not able to produce a cross section for this reaction, but estimated the integrated cross section [Den78].

Ferdinande, Sherman, Lokan and Ross, working with the National Research Council of Canada linear accelerator, examined the reaction $^7\mathrm{Li}(\gamma, n)$ with detectors mounted at 90° to the beam axis. They obtained a differential cross section at this angle and attempted to break this cross section into the ground-state channel, $^7\mathrm{Li}(\gamma, n_0)^6\mathrm{Li}$, and an excited state channel, $^7\mathrm{Li}(\gamma, n_1)^6\mathrm{Li}^*$ [Fer77]. Their differential cross section at 90° is shown in figure 3.15, along with an estimated differential cross section from Bramblett *et al.* [Bra73]. This estimate was obtained by assuming a d-wave neutron promoted from a p-wave shell, giving an angular dependence of $1 + \frac{3}{2}\sin^2\theta$ [Fer77].

Another experiment that looked at the photodisintegration of ^{7}Li is that of Sené *et al.* They produced differential cross sections for the photoproton and photoneutron reactions. However, with photon energies between 60 and 120 MeV, their results are beyond the giant dipole region studied in this thesis [Sen83, Sen85]. Kusuhara studied the reactions $^6\mathrm{Li}(\gamma, p)^5\mathrm{He} \rightarrow {}^4\mathrm{He} + n$, $^6\mathrm{Li}(\gamma, n)^5\mathrm{Li} \rightarrow {}^4\mathrm{He} + p$ and $^6\mathrm{Li}(\gamma, np)^4\mathrm{He}$ using nuclear emulsion [Kus80].

A great number of charged particle reactions had their differential cross sections measured.

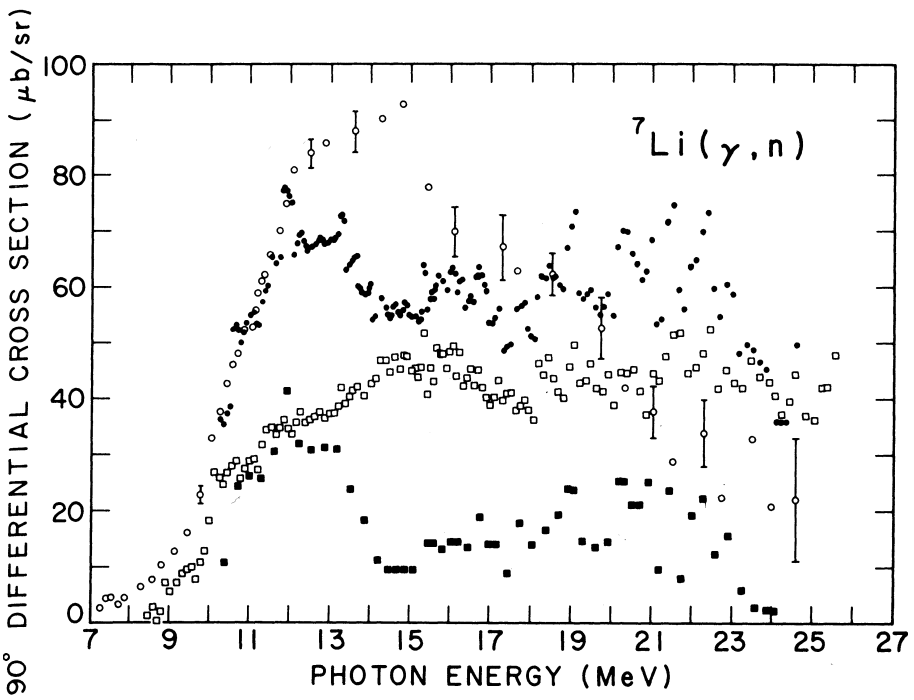

Figure 3.15: Differential cross section at 90° for the total reaction ^{7}Li(γ, n) (solid circles) with reaction channels ^{7}Li$(\gamma, n_0)^6$Li (open squares) and ^{7}Li$(\gamma, n_1)^6$Li* (solid squares) compared with the estimated differential cross section of Bramblett *et al.* (open circles), from figure 4 of [Fer77]

Volkov *et al.* measured the differential cross sections for several reactions involving tritons on both ^{6}Li and ^{7}Li [Vol78]. Junghans *et al.* found the differential cross sections and Legendre polynomial coefficients for (γ, p), (γ, d), (γ, t) and (γ, α) reactions on both isotopes [Jun77, Jun79]. Taneichi, Ueno and Shoda studied ^{6}Li(γ, d) [Tan77] while Denisov and Chubukov examined ^{7}Li(γ, t) [Den82].

There were three electrodisintegration reactions studied, two of which were performed at the University of Saskatchewan by Skopik, Murphy and Asai [Sko79a, Asa80]. The third was performed in Tokyo by Nakamura *et al.* [Nak78]. There was also an experiment from Moscow by Ishkhanov, Mokeev, Novikov and Piskarëv studying the inelastic scattering of gamma-rays from ^{7}Li [Ish80]. Rounding off this time period is the measurement of the inverse reaction ^{2}He$(\alpha, ^6$Li$)\gamma$ by Robertson *et al.* [Rob81].

3.9 Experiments from 1984 to 1989

The time period of 1984 to 1989 began and ended with experiments studying photoneutrons from the lithium isotopes. In this time period we see a continued interest in the electrodisintegration of lithium and in photodisintegration experiments with charged products. We also see a few experiments conducted with polarised photon beams. However, none of these experiments are concerned

with neutrons.

The Perth experiments, performed by Dytlewski, Siddiqui and Thies, produced a photoneutron cross section for both ^{6}Li [Dyt84] and ^{7}Li [Sid86]. They used BF_3 proportional tubes to study the reactions and therefore do not obtain any of the angular or reaction channel information found in the previously studied time period. The photoneutron cross sections for ^{6}Li and ^{7}Li are shown in figure 3.16. Although it is not shown in this figure, the authors compare their data to that of the

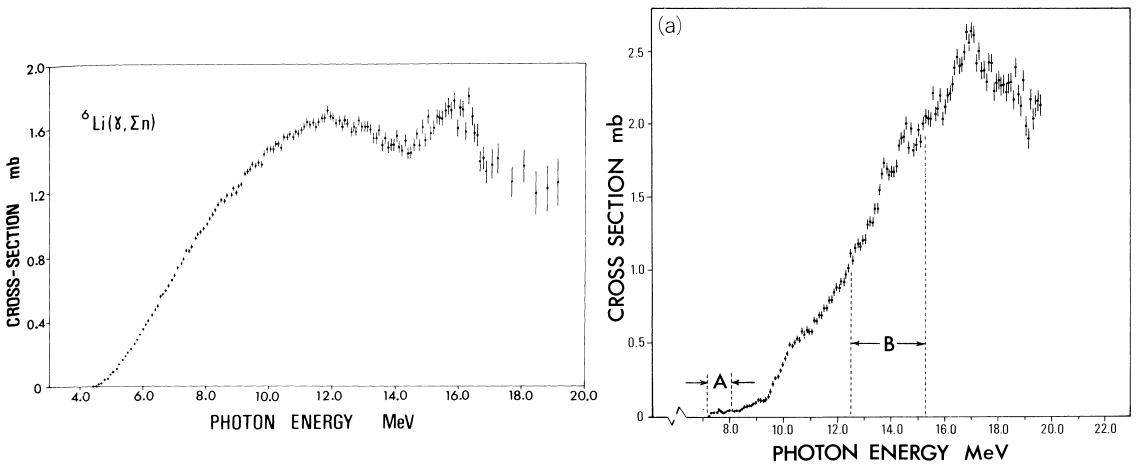

Figure 3.16: The ^{6}Li(γ, n) (left) and ^{7}Li(γ, n) (right) cross sections of Dytlewski, Siddiqui and Thies, from figure 2 of [Dyt84] and figure 2a of [Sid86]

Livermore group discussed in section 3.6. The agreement for ^{6}Li is excellent up to 14 MeV and reasonable up to 20 MeV [Dyt84]. The agreement of the ^{7}Li cross section with the Livermore data is not as good [Sid86]. While they conclude that they did not find any fine structure in the ^{6}Li cross section [Dyt84] they report that "[i]n the ^{7}Li$(\gamma, \sum n)$ cross section reported here, we see the onset of some very minor structure in the cross section, superimposed on an E1 giant resonance-like broad maximum" [Sid86].

Later, the group of Karataglidis, Zubanov, Harty and Thompson looked at the ^{7}Li(γ, n) reaction near threshold. They also used BF_3 proportional counters and concentrated on the energy region of 7.0 to 8.8 MeV [Kar89]. Their results can be seen in figure 3.17. Their results agree with neither the results of Siddiqui, Dytlewski and Thies [Sid86] or those of Bramblett *et al.* [Bra73]. Both of these previous results were primarily concerned with the giant dipole region at higher energies. However, the results of Karataglidis *et al.* agree well with the older results of Green and Donahue [Gre64] who concentrated their efforts in this lower energy region just above threshold.

Wade, Brussel, Koester and Smith looked at the quasideuteron reaction ^{6}Li(γ, np) reaction between 30 and 60 MeV. This work is important as it helps us better understand the onset of the quasideuteron reaction.

A number of charged particle reactions were studied. Kotikov and Makhnovskiĭ studied the

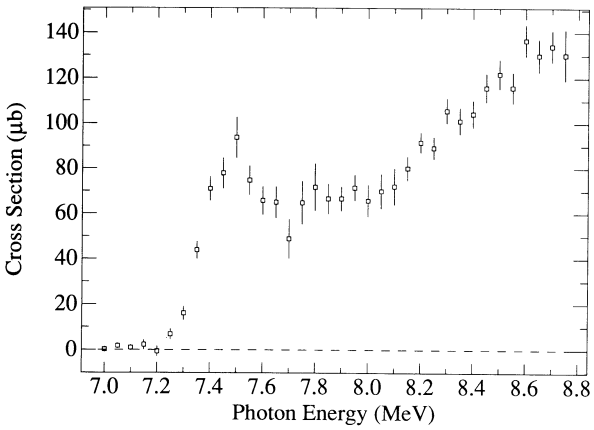

Figure 3.17: The cross section of the ^{7}Li(γ, n) reaction near threshold measured by Karataglidis *et al.*, from figure 2 of [Kar89]

more exotic ^{6}Li(γ, pdt) [Kot85] and ^{7}Li(γ, ptt) [Kot87] reactions by using nuclear emulsion.

Some new techniques were employed in the study of charged particle reactions. Carlos *et al.* studied ^{6}Li(γ, p) using tagged photons [Car88] with energies above the giant dipole resonance. Tagged photons are photons produced through bremsstrahlung and have a bremsstrahlung energy spectrum. However, the recoil electrons are analysed using a magnetic spectrometer, and by demanding a coincidence between a reaction and a measured electron, an experimenter is able to determine the energy of the photon that initiated the reaction [Car88]. In this way a tagged photon beam can be considered a monochromatic photon beam.

Another new technique employed is that of using a beam of polarised photons. Bremsstrahlung does not usually produced polarised photons. However, by using a diamond or other crystal as the radiator, photons with a degree of polarisation can be produced [Gan87]. One of the principle advantages of the HIGS facility is that the photon beam is nearly 100% polarised, where coherent bremsstrahlung is not. "The spectrum of coherent-bremsstrahlung γ rays has a characteristic interference maximum, against the background of an incoherent (Schiff) bremsstrahlung" [Gan87]. Using polarised gamma-rays an experimenter is able to compute a new parameter, the asymmetry. The asymmetry is defined as

$$A(\theta, E_\gamma) \equiv \frac{\frac{d\sigma_\parallel}{d\Omega}(\theta, E_\gamma) - \frac{d\sigma_\perp}{d\Omega}(\theta, E_\gamma)}{\frac{d\sigma_\parallel}{d\Omega}(\theta, E_\gamma) + \frac{d\sigma_\perp}{d\Omega}(\theta, E_\gamma)}$$

where $\frac{d\sigma_\parallel}{d\Omega}(\theta, E_\gamma)$ and $\frac{d\sigma_\perp}{d\Omega}(\theta, E_\gamma)$ are the differential cross sections corresponding to angles parallel and perpendicular the photon polarisation (azimuthal angle), θ is the emission angle with respect to the beam axis (polar angle) and E_γ is the photon energy [Bur89].

Several experiments involving polarised photons occurred at the Kharkov Institute of Physics and Technology. Ganenko *et al.* examined the ^{6}Li$(\vec{\gamma}, p)$ reaction at energies well above the giant dipole resonance and found its asymmetry [Gan87]. Burkova *et al.* found the asymmetry of the

^{6}Li($\vec{\gamma}, t^3$He) reaction [Bur89, Bur95], while Vladimirov *et al.* did the same for ^{7}Li($\vec{\gamma}, \alpha^3$He) [Vla89, Bur95].

A number of electrodisintegration experiments were performed. Volkov *et al.* studied the ^{7}Li(e, t) reaction and used the virtual photon spectrum to compute the ^{7}Li(γ, t) cross section [Vol86]. The first two experiments from Amsterdam were performed by Ent *et al.* [Ent86, Ent94] and Lanen *et al.* [Lan89a, Lan89b] to study the ^{6}Li$(e, e'd)$ and ^{6}Li$(e, e'p)$ reactions, respectively. More experiments of this type would come out of Amsterdam in the 1990's. An experiment studying the inelastic scattering of gamma-rays was performed by Piskarëv at Moscow State University [Pis87].

3.10 Experiments from 1990 to the Present

After 1990, the experiments dealing with the photodisintegration of lithium tended to deal with energies much higher than the dipole resonance. There were also a number of electrodisintegration reactions studied at higher energies and some experiments involving inverse reactions with an emphasis on big-bang nucleosynthesis.

The Amsterdam electrodisintegration experiments continued with Zubanov *et al.* studying ^{6}Li$(e, e't)$ [Zub90], Mitchell *et al.* studying ^{6}Li$(e, e'\alpha)$ [Mit91], and Connelly *et al.* studying ^{6}Li$(e, e'^3$He) [Con98]. From Saclay, Jodice *et al.* studied the ^{6}Li$(e, e'd)$ electrodisintegration reaction [Jod92].

Denyak, Evseev, Likhachev, Pashchuk and Khvastunov studied the ^{6}Li$(\gamma, ^3$He) and ^{7}Li$(\gamma, ^4$He) reactions using both electrons and photons. They unfolded the virtual photon spectrum of the electrodisintegration experiment and unfolded the bremsstrahlung spectrum of the photodisintegration experiment to make two cross section measurements for each reaction [Den93]. The agreement between the two methods is reasonable.

On the high energy end, Adamian *et al.* made a measurement of the asymmetry of the quasideuteron reaction ^{6}Li$(\vec{\gamma}, np)$ using polarised, coherent bremsstrahlung photons of energies between 300 and 900 MeV [Ada91]. On the lower energy end, Likhachev *et al.* found the differential cross section of ^{7}Li(γ, t) at energies near 6.6 and 8.8 MeV [Lik99].

A number of photodisintegration experiments with energies well above the giant dipole resonance were performed at MAX-lab in Lund, Sweden. These experiments used tagged photons to generate an effectively monochromatic photon beam. While the results of the experiments were sometimes a cross section, the missing energy spectrum was often obtained. For example, Nilsson *et al.* studied the ^{6}Li(γ, p) reaction and computed the missing energy spectrum, $E_m = E_\gamma - T_p - T_r$ where E_γ is the energy of the photon, T_p is the kinetic energy of the proton and T_r is the kinetic energy of the recoiling nucleus. The excitation energy, E_x, of the final products can be computed by taking into account the threshold energy of the reaction, the Q-value, which is negative by convention: $E_x = E_m + Q$ [Nil94]. They did likewise for the ^{6}Li(γ, d) reaction [Nil90]. Dias *et al.* also produced

missing energy spectra for the ^{6}Li(γ, p) reaction, as well as differential cross sections at 59 and 75 MeV [Dia95]. Ryckbosch *et al.* found the missing energy spectra for ^{6}Li(γ,*pt*), ^{6}Li(γ,*pd*) and ^{6}Li(γ,*dt*) and also reported a cross section for ^{6}Li(γ,*pt*) at energies near 60 MeV [Ryc94]. The last results from Lund concerning the photodisintegration was published by Dias *et al.*, who measured information about the differential cross sections of the ^{6}Li(γ, d) and ^{6}Li(γ, t) reactions in the energy range 59 to 75 MeV [Dia97].

Two groups studied the inverse reaction ^{2}H$(\alpha, \gamma)^6$Li with the intent of determining whether the ^{6}Li found in the universe was produced by cosmic ray spallation or by radiative capture in the early universe. Both the groups of Mohr *et al.* and Cecil, Yan and Galovich determined that only a small amount of the existing ^{6}Li could have been produced through big-bang nucleosynthesis [Moh94, Cec96].

3.11 Remarks on the History of Experiments

Now that we have seen a glimpse of the history of experiments concerning the photodisintegration of lithium, we can consider how the results of this thesis fit with previous literature reports. Most of the relevant photoneutron work was done with BF_3 proportional counters in the 1960's with only a few results in the 1980's. The cross sections produced are total neutron cross sections which cannot take into account the angular distribution of the neutrons or the individual reaction channels.

In section 1.3 we saw how new theoretical techniques and the advance of powerful computers has led theoretical physicists to produce new predictions of the photonuclear cross sections of the lithium isotopes. However, these theorists have looked at the same history as just outlined, and have found insufficient and often contradictory data to compare their results. For instance, there are few experiments producing cross sections for the individual photoneutron reaction channels, so there is no incentive for these researchers to produce predictions to match missing data.

This thesis aims to add new data in order to further stimulate theoretical research into the photodisintegration of the lithium isotopes. Our attention to individual photoneutron reaction channels is unprecedented for these isotopes. The angular distributions of these reaction channels have never before been measured. We have worked hard to make measurements of the absolute cross sections with uncertainties quantified so that they truly represent the experimental uncertainties.

Chapter 4

Experimental Apparatus and Instrumentation

4.1 Introduction

In this chapter we discuss the apparatus used to study the photodisintegration of lithium isotopes. We begin with the photon source, the High Intensity Gamma-Ray Source, in section 4.2. This photon source can produce monochromatic, polarised gamma-ray photons where historically photon sources have been able to only produce gamma-ray photons with continuous spectra and limited polarisation. In order to detect the neutrons produced by photodisintegration reactions we use the Blowfish Neutron Detector array, discussed in section 4.3. The 88 detectors that make up Blowfish allow us to study of the angular distributions of the cross sections. The principles of operation of these detectors will be discussed in section 4.4. The data acquisition system takes the raw output of these detectors, allowing all 88 signals to work in concert together and digitises important information. This system is discussed in section 4.5. In order to measure absolute cross sections we must know the photon flux, and instruments for doing this are discussed in section 4.6. To study the photodisintegration of the lithium isotopes we need quantities of the lithium isotopes. We call the volumes of lithium that we place in the beam the targets and we discuss them in section 4.7.

4.2 The Gamma-Ray Facility

The High Intensity Gamma-Ray Source (HIGS, or alternatively, HIγS) is a facility for producing a monochromatic, polarised gamma-ray beam. It is housed at the Duke Free Electron Laser Laboratory (DFELL) on the Duke University campus in Durham, North Carolina, USA. HIGS is managed by the Triangle Universities Nuclear Laboratory (TUNL) which is also located on the Duke University Campus.

DFELL is a third generation synchrotron which incorporates a free-electron laser; figure 4.1 presents a conceptual diagram of the light source. The synchrotron is a 'race track' style synchrotron consisting of two straight sections and two bends. One straight section contains the radio-frequency (RF) chamber and the electron beam is injected into the storage ring on this side. The electron

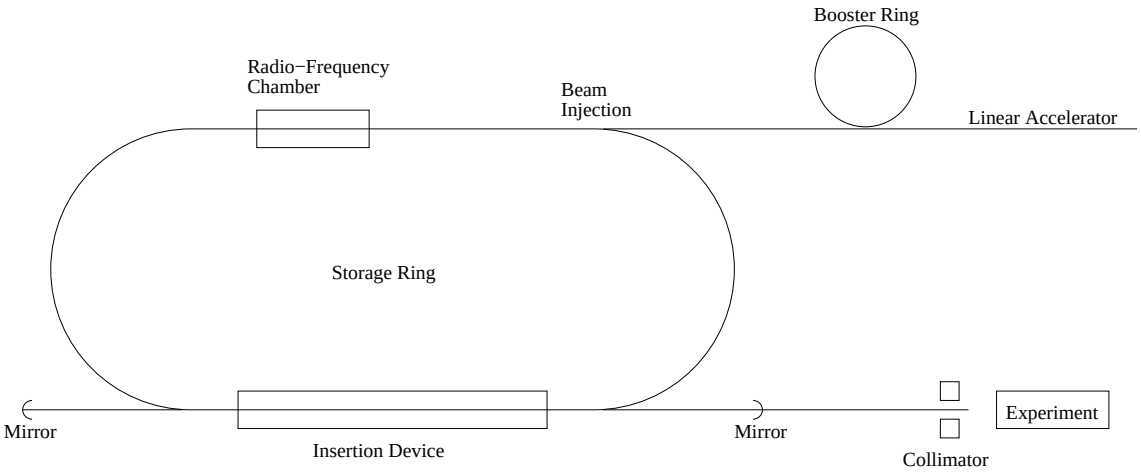

Figure 4.1: The Duke Free-Electron Laser Laboratory

beam is produced in a linear accelerator and is accelerated further in the booster ring before it is injected into the storage ring at full energy. The other straight section contains the insertion device that is the central component of the free-electron laser (FEL). Since the free-electron laser used at DFELL uses a buncher between its wiggler magnets, it is distinct from conventional free electron lasers and is called an optical klystron (OK) [Lit96].

The insertion device used for measurements with photon energies below 16 MeV was the OK-4, originally used at the Budker Institute of Nuclear Physics, Novosibirsk, Russia [Lit96]. The OK-4 consists of two 3.5 m wigglers with a buncher located between them [Lit96]. It produced photons that are linearly polarised in the horizontal plane.

The OK-4 is limited in that it can only produce linearly polarised photons, and the strong on-axis synchrotron radiation it produces causes significant mirror damage [Wu01, Lit01]. The OK-5 free-electron laser is designed to address these limitations. It uses two-to-four 4 m wiggler magnets with three bunchers between them. It can produce photons with arbitrary polarisation. Circularly polarised photons minimise mirror damage [Lit01].

We used the OK-5 for the measurements with photon energies above 16 MeV. The optical klystrons are placed inside an optical cavity 55.73 m long. The two ends of the optical cavity are capped with mirrors capable of reflecting photons in the visible and ultra violet ranges. When an electron bunch travels through the wiggler magnets, it moves laterally and emits photons, which is shown in the first part of figure 4.2. These photons travel in the forward direction and are reflected by the forward mirror. The electrons continue around the ring and the photons travel back though the insertion device to the other mirror. The photons are reflected again and they pass though the insertion device at the same time as the electron bunch. This causes the electrons to form micro-bunches which produce more photons with the same polarisation and phase as the original photons.

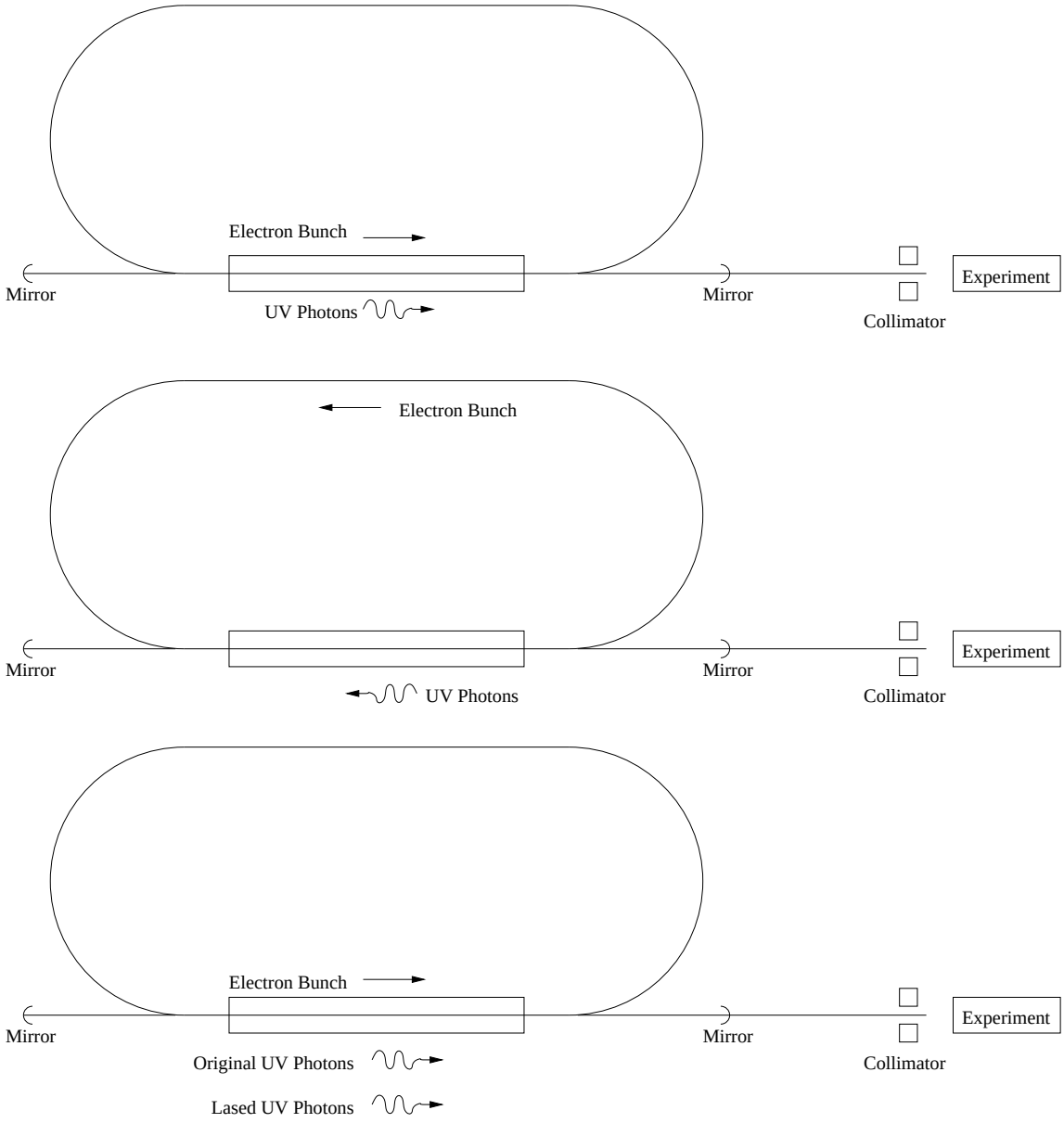

Figure 4.2: The production of visible and ultraviolet photons in the free-electron laser

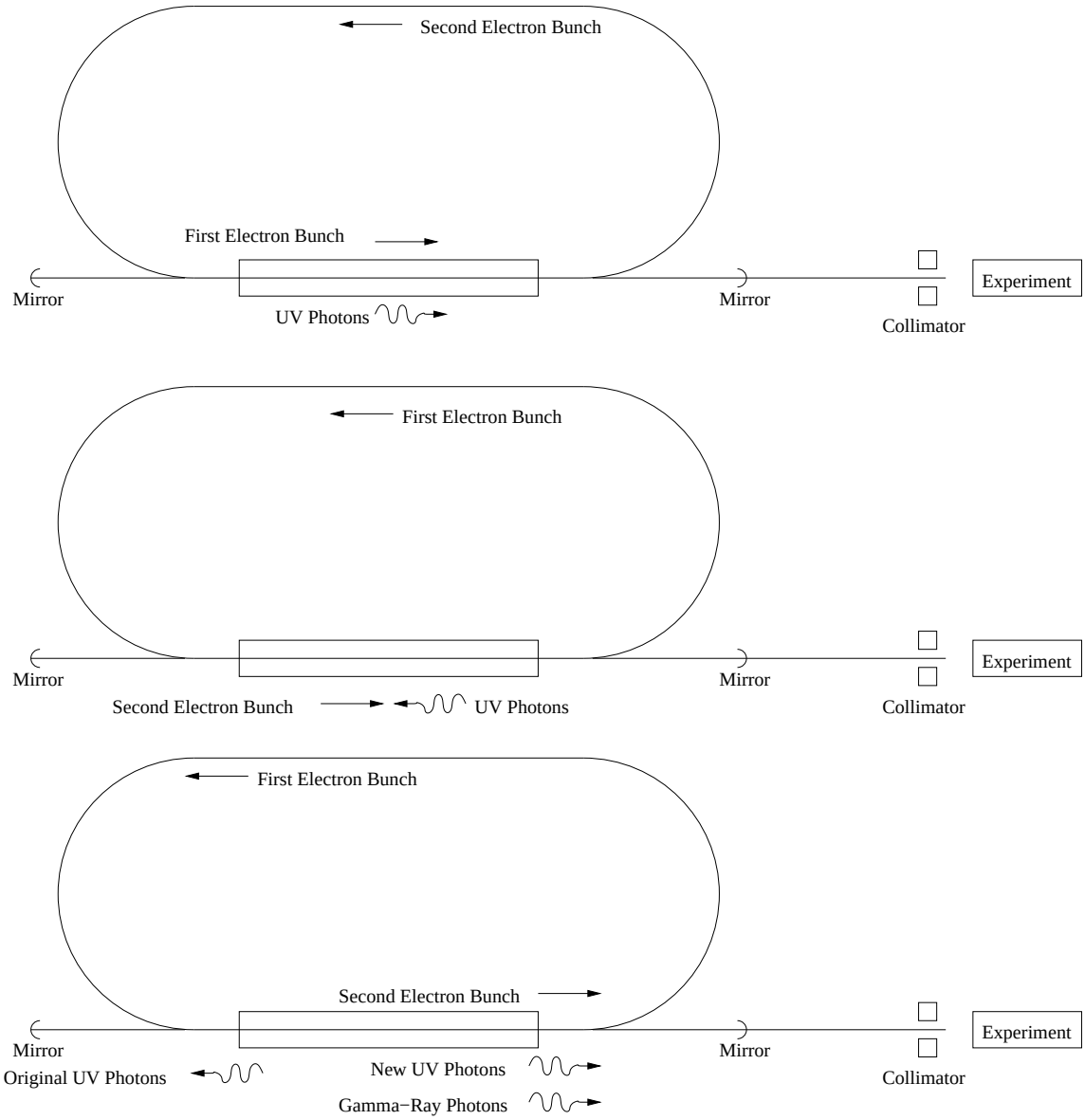

Figure 4.3: The production of gamma-ray photons in the free-electron laser

The HIGS facility uses the ultraviolet photons produced by the free-electron laser to produce gamma-ray photons. This is done by adding a second electron bunch into the storage ring. Figure 4.3 shows the effect of adding a second electron bunch into the storage ring. As the photons from the first bunch are travelling back though the insertion device, some collide with the second bunch. This process is known as Compton backscattering as the photons are scattered backward with energy [Lit97]

$$E_\gamma \simeq \frac{4\gamma^2 E_{uv}}{1 + (\gamma\theta)^2 + 4\gamma\frac{E_{uv}}{m_e c^2}} \tag{4.1}$$

where E_γ is the energy of the resulting gamma-ray photons, E_{uv} is the energy of the incident ultraviolet photons, m_e is the mass of the electron, $\gamma = E_e/m_e c^2$ where E_e is the electron's energy and θ is the angle between the electron beam direction and the direction of the produced gamma-ray photon. Compton backscattering produces gamma-ray photons with the same polarisation as the initial ultraviolet photons and the energy resolution is given by [Lit97]

$$\Delta E_\gamma / E_\gamma \simeq (\gamma\theta)^2. \tag{4.2}$$

Since the energy resolution is proportional to the square of θ, an experimenter can control the resolution by collimator selection and achieve an essentially monochromatic beam of photons.

4.3 The Blowfish Neutron Detector Array

The Blowfish Neutron Detector Array, or Blowfish for short, is housed at the HIGS facility. It consists of 88 neutron detectors arranged in a spherical shell with radius 40.6 cm covering about $\frac{1}{4}$ of 4π steradians. Figure 4.4 shows a photograph of Blowfish beside an image generated by a simulation of the array.

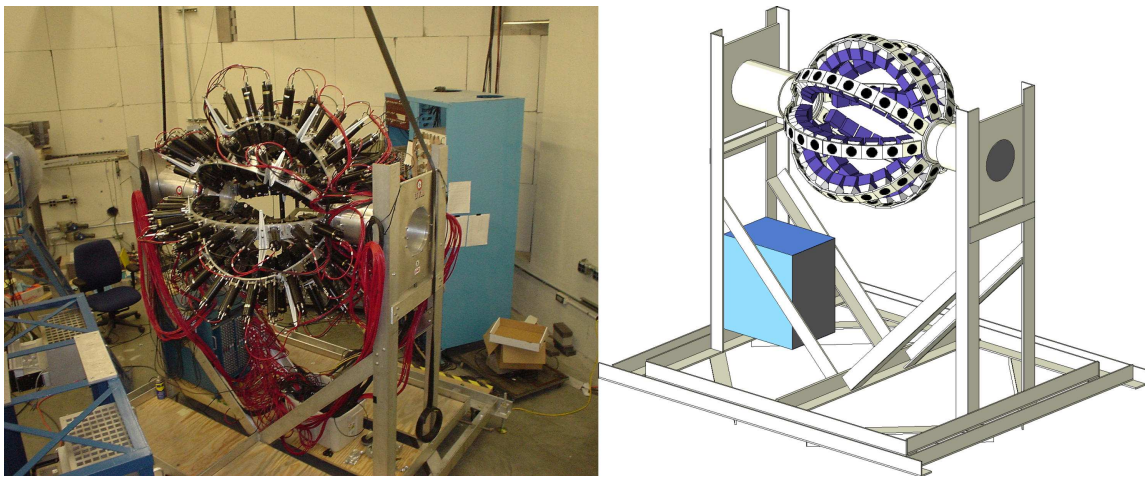

Figure 4.4: The Blowfish Neutron Detector Array

In a typical experiment, gamma-ray photons are produced though Compton backscattering, as

discussed in section 4.2, and are incident on a material at the centre of Blowfish. The material is called a target and some of the photons interact with the target while others pass through. Most of the interacting photons will simply interact with one of the electrons in the target, Compton scattering or producing an electron-positron pair. Some of the interacting photons will interact with a nucleus in the target. If the photon has enough energy, it can eject nucleons from the nucleus through nuclear photodisintegration. Depending on the energy of the photon and the structure of the nucleus, a single nucleon may be emitted or the entire nucleus may shatter. The emitted protons, due to their electric charge, will slow quickly in the target and surrounding atmosphere; they will not be detected. The neutrons will pass though the target and can then be detected by Blowfish.

4.3.1 Detector Arrangement

The neutron detectors are arranged so that their faces are 40.6 cm[1] from the centre of the array. As can be seen from figure 4.4, the detectors are supported by eight arcing aluminum 'arms' and there are eleven detectors in each of these arms. Figure 4.5 shows how the detectors are arranged in Blowfish. The left half of figure 4.5 shows the neutron detectors arranged in the arms of Blowfish.

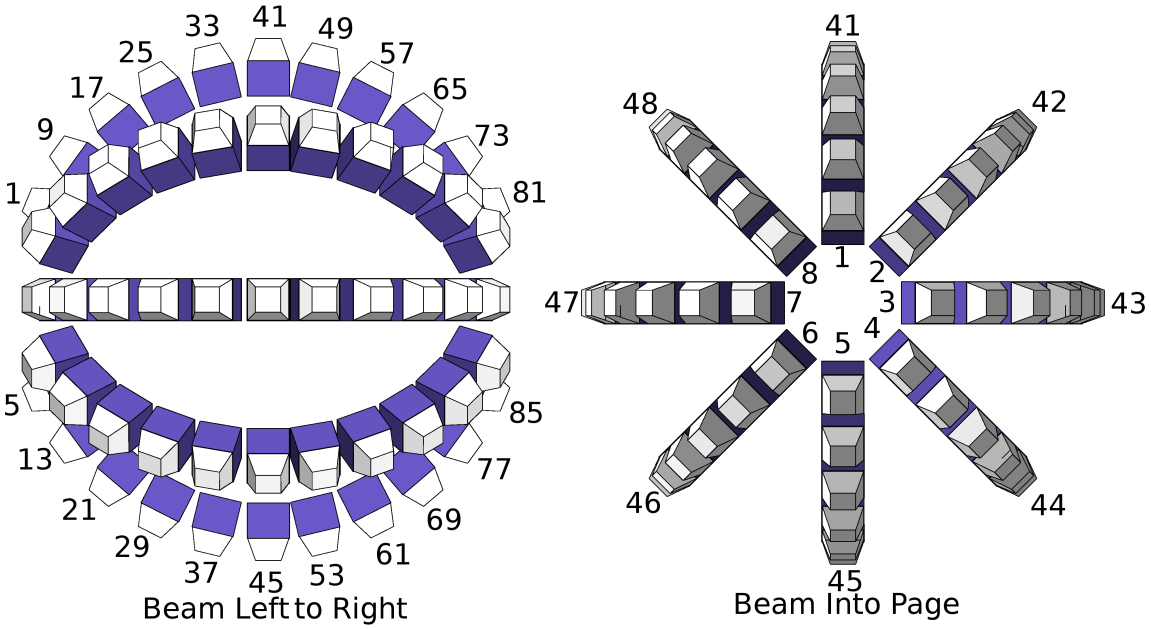

Figure 4.5: The arrangement of neutron detectors in Blowfish

Detectors 1 through 8 are at the end of the array known as the 'upstream' end, likening the beam direction to the direction of a stream. Likewise, detectors 81 through 88 are at the 'downstream'

[1]The Blowfish neutron detector array was originally designed in imperial units and the frame was designed for the detector faces to be 16 inches from the centre. Note 1 inch = 2.54 cm.

end of the array. One can remember the beam direction by remembering that the photons in the beam count up as they pass detectors.

The right half of figure 4.5 shows the array as it would appear to photons coming from the accelerator. Detectors 1 through 8 are arranged in a 'ring'. When looking at the array from the accelerator, the detector numbering increases clockwise with the ring. When analysing data collected with Blowfish, one often looks at the rings from the centre of the array, which means that the upstream rings will progress counterclockwise and the downstream rings will progress clockwise from this orientation. We number the rings 1 to 11, and arms 1 to 8, and can therefore map detectors into a ring and arm number by

$$\text{ring} = (\text{detector} - 1)/8 + 1 \text{ (Integer Division)} \tag{4.3}$$

$$\text{arm} = (\text{detector} - 1) \bmod 8 + 1. \tag{4.4}$$

We can also map arms and rings into spherical coordinates. Figure 4.6 shows the coordinate system as it will be used in this thesis. This coordinate system is essentially spherical coordinates but the definitions are somewhat unusual. The x, y and z-axes are defined as the natural coordinate

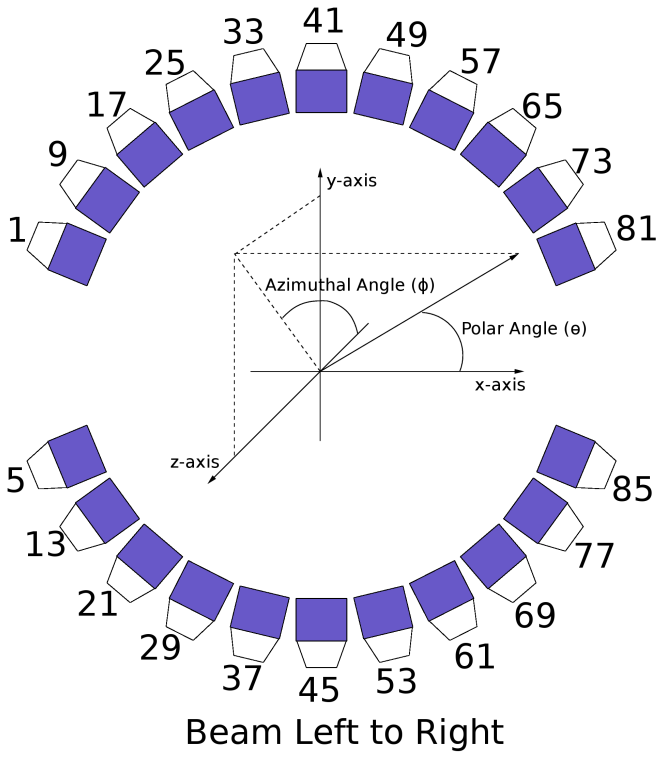

Figure 4.6: The coordinate system used in this thesis

system of a Geant4 simulation, as described in chapter 5: the x-axis is aligned along the beam direction, the y-axis is vertical and the z-axis is horizontal and perpendicular to the other axes. The polar angle, θ, is defined as the angle to the beam axis, or x-axis in this case. The azimuthal

angle, ϕ, is defined as the angle from the HIGS beam polarisation noting that the HIGS beam is polarised in the horizontal.[2] Since there are two possible ways to choose this angle, it is chosen so that the detectors on top are at $\phi = 90°$. One can now compute the polar and azimuthal angles for the centre of each of the detectors in Blowfish using

$$\theta = 157.5° - 13.5° \times (\text{ring} - 1) \tag{4.5}$$

$$\phi = 45° \times (\text{arm} + 1). \tag{4.6}$$

The equation for θ, equation (4.5), has two non-intuitive numerical values. The first comes from the fact that the centre of the detectors in ring 11 are 22.5° from the beam axis and, because the array is symmetric, the detectors in ring 1 must be $180.0° - 22.5° = 157.5°$ from the beam axis. The second comes from the fact that the rings are evenly spaced in angle. Also, the expression for ϕ in equation (4.6) only applies when arm 1 is on the top of the array. Blowfish does rotate and it is neither convenient nor desirable to assume that arm 1 will always be on top so we can modify equation 4.6 so that it reads

$$\phi = 45° \times [(\text{arm}) - (\text{arm on top}) + 2] \tag{4.7}$$

and is more general.

4.3.2 The Frame

The Blowfish frame is made from aluminum. Each arm is supported by an almost-circular aluminum arc. There are holes in the arc for the photomultiplier tubes to pass through and the detectors are held to the frame by clamping around the detector casings. As can be seen in figure 4.4, the arms are connected to round cylinders called the hub. The hub rotates, allowing all detectors to rotate about the beam axis. The hub is connected to the main frame and can be raised and lowered by the turning of bolts. The frame is on wheels so that the array can be easily moved but can be locked down during an experiment. The frame also allows for fine adjustment in the horizontal plane by bolts at its base.

4.4 Neutron Detector Principles and Operation

The process of neutron detection requires multiple steps. Each step uses special equipment and has its own unique characteristics. In this section we discuss the steps required to detect neutrons and some of the issues and techniques associated with each step.

[2]Note that we will use this definition of the azimuthal angle, ϕ, for discussing polarisation. For other discussions we may choose a different definition that is more convenient.

4.4.1 Scintillation

Although the neutron is comprised of charged quarks, its total charge is zero and it does not readily react electromagnetically. This means that detecting neutrons is fundamentally different than detecting protons, electrons or photons. Since we cannot rely on electromagnetism, we must look to another one of nature's forces in order to detect neutrons. The weak force and gravity are much too weak to be practical in neutron detection, leaving us with only the strong force. There are a few different processes involving the strong force that are usable for neutron detection. In this thesis we will use detectors based on neutron elastic scattering, but those relying on neutron capture reactions, such as BF_3 proportional counters, are also in wide use.

In order to make use of neutron elastic scattering, we need a large volume of a material for the incoming neutron to interact with. Hydrogen nuclei are a good choice since a neutron scattering elastically with a hydrogen nucleus can transfer up to all of its energy to the hydrogen nucleus because they have nearly the same mass. Since hydrogen is a gas at room temperature, we use a molecule rich in hydrogen as our material. Organic molecules are rich in hydrogen and are often used for this kind of application. Toluene (C_7H_8) is a common choice, but it dissolves acrylic and we desire to build our detector containers out of acrylic since the acrylic containers are more robust than glass containers. We use 1,2,4-trimethylbenzene (C_9H_{12}) which does not dissolve acrylic. When a neutron is incident on the organic material, it can scatter elastically from the hydrogen or carbon. Note that it can also interact inelastically with the carbon nucleus. The result is that a neutral particle has transfered energy to a charged particle: the hydrogen ion, carbon ion or inelastic scattering products. We can now use electromagnetic processes to detect these charged scattering products.

The electromagnetic process we use is fluorescence. The organic material is mixed with a fluorescing molecule known as a scintillating impurity or fluor and we call the combination of these materials an organic scintillator. When the charged ion collides with a fluor molecule, the fluor molecule becomes excited. The excited fluor molecule then decays, emitting light. However, in this simple scenario, the fluor will absorb light of the same frequency it emits and the scintillator will not be transparent to its own light. A more careful choice of the fluor will take care of this problem.

The discussion presented here follows the standard texts of Birks, Knoll and Leo [Bir64, Kno00, Leo94]. We can choose the fluor to be a molecule with a π-electron structure and make use of the vibrational energy states of the molecule, as well as the electron configuration states. Let S_{nv} be a singlet state of the fluor with electron configuration energy level n and vibrational energy level v. Figure 4.7 shows the singlet states for a molecule with π-electron structure. For molecules of interest, the spacing between the first configuration state, S_{00}, and the second configuration state, S_{10}, is 3 or 4 eV. The spacing between vibrational states is on the order of 0.15 eV. Initially the molecule is assumed to be in the lowest energy state, S_{00}. When an ion collides with a fluor molecule, the

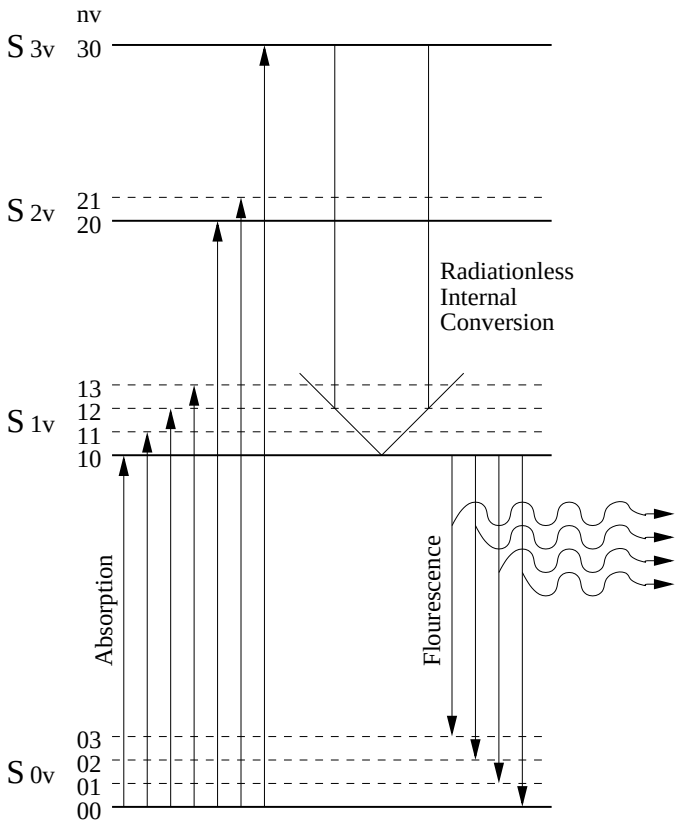

Figure 4.7: Energy level diagram for fluorescent molecule with π-electronic energy levels

fluor molecule can be promoted into a higher energy state. The higher electron configuration states quickly drop to an S_{1v} state though internal conversion between adjacent excited states. Internal conversion is a intramolecular radiationless transition [Bix68] and the energy is ultimately lost to heat. The vibrational energy is also quickly lost to thermal degradation and the molecule is then in the S_{10} state. The fluor molecule can then decay into an S_{0v} state, producing radiation. With the above mechanism, only the radiation produced by the $S_{10} \rightarrow S_{00}$ transition can be reabsorbed by a fluor molecule in the ground state. The radiation produced in a transition $S_{10} \rightarrow S_{0v}$ where $v \neq 0$ does not have enough energy to excite a fluor molecule in the ground state. Thus, using a fluor with a π-electron structure allows one to construct a transparent scintillator.

The scintillator employed in this thesis has the trade name BC-505 and is currently produced by Saint-Gobain Crystals [Sai05]. BC-505 is an organic scintillator that uses 1,2,4-trimethylbenzene as its principle organic compound and a proprietary cocktail of chemicals as the fluor. Its light emission spectrum is shown in figure 4.8.

We have converted the kinetic energy of a neutron into the light output of a scintillator. However, we have not yet related the neutron's energy to the light output of the scintillator. Note that a neutron of energy E_n can deposit an amount of energy from 0 to E_n in the scintillator through its

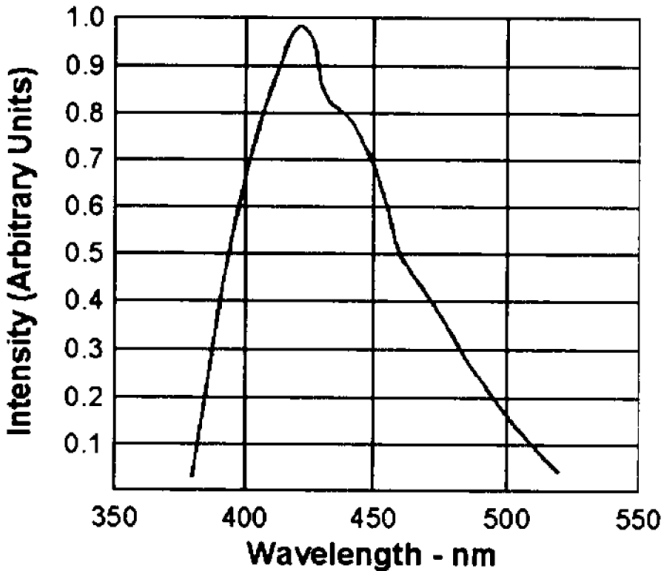

Figure 4.8: BC-505 emission spectrum from [Sai05]

collision with a nucleus in the scintillator. Neutrons depositing less than E_n can exit the scintillator and carry away energy. The spectrum of energy deposited in a detector is most easily computed by using a simulation, such as the Geant4 simulation used in this thesis.

4.4.2 Light-Output Response

The relationship between the light output caused by the recoil nucleus and the energy transferred to that nucleus is not linear. We have examined the light output response using a novel approach developed at the former Saskatchewan Accelerator Laboratory [ORi96] and adapted to BC-505 [Pyw06].

Only as a first approximation, the light output of the scintillator is directly proportional to the energy deposited in the scintillator,

$$L(E, x) = SE \tag{4.8}$$

where S is a constant [Bir64] and x is the particle type. We can write this in differential form by differentiating by the particle's position in mass thickness units[3]

$$\frac{dL}{dr}(E, x) = S\frac{dE}{dr}. \tag{4.9}$$

Notice that in general, $\frac{dE}{dr}$ is implicitly a function of particle type and energy.

For most particles, a high density of ionised and excited molecules causes a quenching effect and the light output is reduced. Birks [Bir51] has proposed a semi-empirical formula to compute

[3]Mass thickness units take the density of the material into effect. If y is the particle's position measured in cm and ρ is its density measured in g/cm^3 then its position in mass thickness units is $r = y\rho$ in units g/cm^2.

the light output

$$\frac{dL}{dr}(E,x) = \frac{S\frac{dE}{dr}}{1 + kB\frac{dE}{dr}}. \tag{4.10}$$

The constant B controls the density of ionised and excited molecules and the constant k is a quenching parameter. Although k and B have different physical interpretations, we need not determine them independently. Therefore, we treat kB as a single constant.

Chou [Cho52] extended Birks' parameterisation to include a third constant, C. Chou's semi-empirical parameterisation is

$$\frac{dL}{dr}(E,x) = \frac{S\frac{dE}{dr}}{1 + kB\frac{dE}{dr} + C\frac{dE}{dr}^2} \tag{4.11}$$

which has better low-energy behaviour than Birks' parameterisation. Using this parameterisation we can compute the response of our detectors to charged particles with different masses.

The details of the calculation have been published [ORi96, Pyw06], and the results for BC-505 [Pyw06] are given here. Using the parameterisation of Chou in equation 4.11 we obtained values of $kB = 0.0061 \pm 0.0003$ g cm^{-2}MeV^{-1} and $C = (1.0 \pm 0.1) \times 10^{-5}$ g^2/cm^{-4}MeV^{-2}.

Part of our approach is to define a unit to measure the light output response. We define 1.0 MeV$_{ee}$ to be the light output response of a 1.0 MeV electron coming to a full stop in the detector. We calculate that a proton coming to a stop would require 3.0 MeV of kinetic energy to produce the same light output. We therefore say that the light output response of a 3.0 MeV proton is 1.0 MeV$_{ee}$.

A plot of the light output as a function of the energy of various charged particles can be found in figure 4.9.

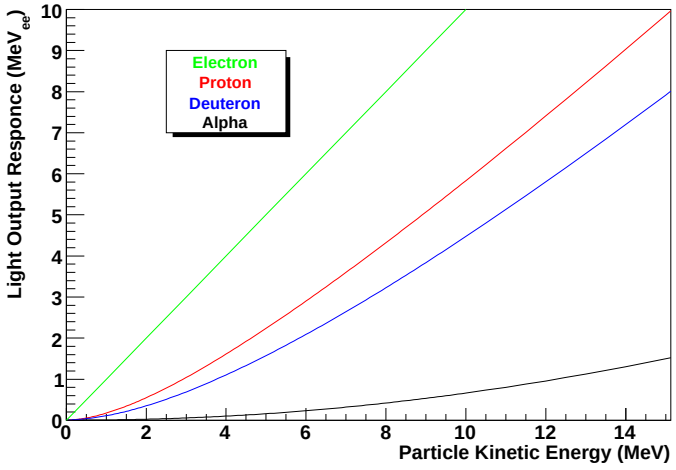

Figure 4.9: Light output response of BC-505 to various charged particles

4.4.3 Photomultiplier Tubes

Now that we can relate the light output of the scintillator to the energy deposited in it, we need to find a method of converting this light into a usable electric signal. This is done by using a photomultiplier tube (PMT).

A conceptual diagram of PMT operation is provided in figure 4.10. The photon created by

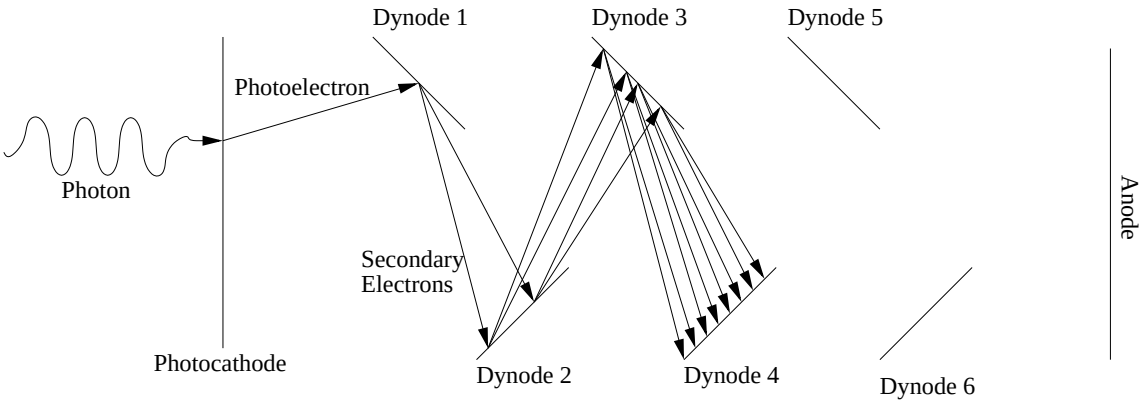

Figure 4.10: Conceptual diagram of photomultiplier tube operation

our scintillator is incident on the photocathode of the PMT. The photon strikes the photocathode and can create a photoelectron though the photoelectric effect with an efficiency on the order of 20% [Kno00, Leo94]. The photocathode is held at a lower potential than the first dynode and the electron is accelerated to the dynode. The dynode is constructed from a specially selected metal and will re-emit electrons when it it struck. A typical dynode may emit five electrons for each electron that strikes it [Kno00, Leo94], but the gain is dependent on the PMT voltage. Each dynode is held at a lower potential than the next one and the electrons continue to strike dynode after dynode in a chain reaction. This causes a multiplication in the number of electrons and therefore a small number of photons can be converted into a large number of electrons. This causes an electric current that is measurable by external electronics.

The photomultiplier tubes used in this work were Photonis XP2262/B and the base electronics, which create the voltage divider to power the dynodes, were Vorg Electronics PMTV-2-O1U. The Photonis XP2262 is a fast, 12 dynode PMT with a diameter[4] of 51 mm and the B variant is optimised for the best timing/linearity compromise [Pho98]. Also, the XP2262 has its maximum sensitivity at the same wavelengths of light as BC-505 emits, as seen in figure 4.8.

Figure 4.11 shows the signal generated by a XP2262/B to a gamma-ray event. Notice that the signal has a peak voltage ~ 1 V and width ~ 10 ns. The signal drops quickly and has a slower rise.

It is important to note that the gain of the PMT can vary greatly over time with small changes

[4]This tube is usually referred to as having a diameter of 2 inches. Recall 1 inch = 2.54 cm.

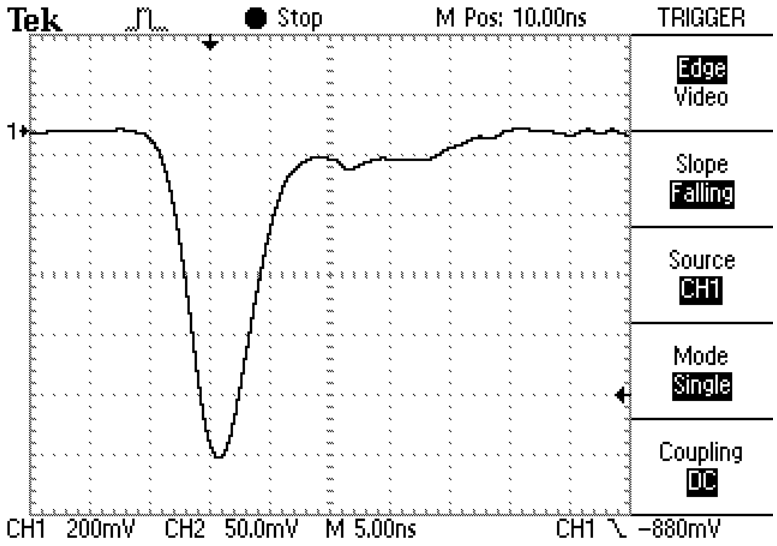

Figure 4.11: Signal from a photomultiplier tube viewed on an oscilloscope

in the supply voltage and temperature. Therefore, a gain monitoring system was constructed by a previous graduate student and is described in section 4.4.4.

4.4.4 Gain Monitoring System

An important component of the Blowfish neutron detector array is its gain monitoring system. The neutron detectors are calibrated using a radioactive source at the beginning and end of an experimental run. While the accelerator is in operation, it is not possible to use the source to measure the gain. Since the gain of the 88 PMTs can drift, the gain monitoring system tracks the gain over time.

The gain monitoring system uses a light emitting diode (LED) to inject a small amount of light into a neutron detector. The resulting spectrum is a Gaussian with a mean value that can be used to find the relative gain of the neutron detector over time. A monitor detector is used to measure the drift of the light output by the LEDs. This monitor detector is continuously calibrated using a radioactive source.

Each LED and corresponding monitor detector serve 22 neutron detectors. See the MSc thesis by B. Bewer for a complete discussion of the gain monitoring system [Bew05, Bew09].

4.4.5 Pulse-Shape Discrimination

In certain scintillators, different particles with different ionisation powers use different fluorescence mechanisms [Leo94]. In these scintillators, the light output pulses are longer when the ionising particle is a proton rather than an electron. We can use the differences in signal shapes to discrim-

inate between neutron and gamma-ray events since neutrons transfer their energy to protons while gamma-rays transfer their energy to electrons. This technique is known as pulse-shape discrimination (PSD).

Figure 4.12 shows two pulses from Blowfish neutron detector number 43 measured by a digital

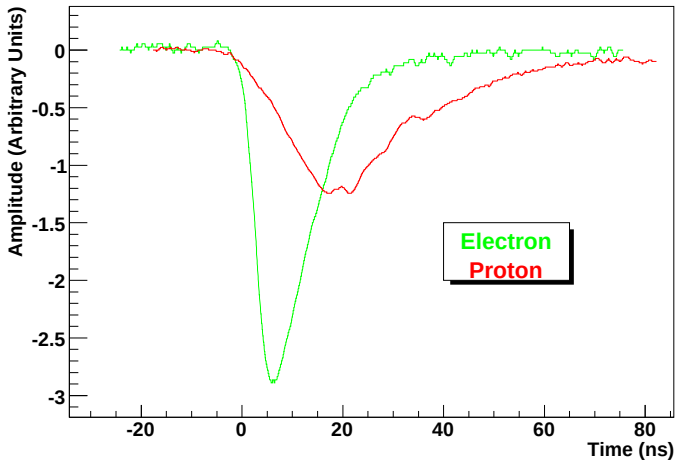

Figure 4.12: Normalised detector output pulses for two ionising particles as viewed on an oscilloscope

oscilloscope. The pulses have been normalised by area. Notice that the pulse due to a proton is much longer than that of the electron. If we integrate from 0 to 40 ns we will get a different result for both pulses. We have integrated the entire electron pulse, but only part of the proton pulse. By comparing the integral over the full pulse with the integral over part of the pulse, we can determine which particle was responsible for the pulse.

4.5 Data Acquisition System

There are many electronic modules between the neutron detectors and the computer that records the data. The subsystems of this electronic system are described in the next section. The descriptions provide the essential logic for understanding the system, sometimes sacrificing the subtleties of nanosecond timing and nuclear instrumentation. The technical trigger diagram can be found in appendix A.

4.5.1 Data Acquisition System Overview

Now that we have an understanding of how the neutron detectors function, let us examine how we handle the signals that they produce. First, we must separate the meaningful signals from electronic noise. This is done using an electronic module known as a discriminator. The discriminator emits

a logic pulse when the signal from the detector exceeds a threshold set by the experimenter. There is one discriminator channel for each detector.

Now we have a logic signal indicating the presence of an event in a specific detector and an analogue signal which contains information about the interaction. The analogue signal is sent to an integrating analogue-to-digital converter (ADC). Since the ADC integrates, and the electric current is the derivative of electric charge with respect to time, it is often called a charge-to-digital converter and given the acronym QDC. Each detector has two QDC channels that integrate over the electric pulse from the photomultiplier tube and each of these channels integrate over a different length of time. The channel that integrates over the longest time is called the long-gate QDC and it integrates over the entire electric signal; we can use that information to determine the light-output of the scintillator. The other channel integrates over a shorter time is called the short-gate QDC and does not integrate over the entire electric signal. The short-gate QDC can be used in conjunction with the long-gate QDC to determine what type of particle caused the signal through pulse-shape discrimination, as described in section 4.4.5.

Nothing more is done with the analogue information, but the digital information still has many uses. The digital information is responsible for counting, timing and data reduction at the time of the experiment.

Nuclear physics experiments are generally reducible to simply counting the number of times an event occurs. The digital information from each detector and every subsystem of Blowfish is fed into a device called a scaler. The scaler counts the number of times the digital signal occurs. Each digital signal is fed into two scalers. The first scaler counts always. The second scaler counts only when the data acquisition system is not busy and is able to accept new data. By comparing the two scalers we are able to determine the amount of time that the system is unresponsive, its dead time. Understanding the dead time is important when extracting absolute cross sections.

The digital data is also responsible for timing. We use a module called a time-to-digital converters (TDC) to determine a particle's time-of-flight. A TDC is essentially a stop watch. In our case, a TDC is started by the digital signal from either the accelerator or the target and stopped by a delayed signal from its corresponding detector. After calibrating the TDC we are able to obtain the particle's time-of-flight and, therefore, its kinetic energy if it is massive.

The digital data is also used in data reduction at the time of the experiment. This is closely related to its role in timing; events at different times are treated differently. Events that occur at times indicating that they could not be caused by the accelerator are declared to be from background radiation sources and are suppressed. It is more probable for a photon to scatter from the target than for a neutron to be produced. We, therefore, wish to suppress the events caused by photons. Since photons travel faster than neutrons, they arrive first and, since they travel at the speed of light, they all arrive at the same time. We are able to reduce the number of photon events by

rejecting most of the events that occur at this time.

For any signal from a detector we determine the amount of energy that the incident particle deposited in the detector, the particle's type and its kinetic energy. Taking into account the dead time of the system and the number of photons from the accelerator, we are able to determine the probability that a photoneutron reaction has occurred and, therefore, we can find the cross section of the reaction.

4.5.2 Data Acquisition Windows

The photon beam from the synchrotron is not continuous but comes in bunches. We can use the timing of each bunch to compute the time-of-flight for particles, reduce the effects of background radiation on the neutron detectors and reduce the number of gamma rays detected. We use a signal generated by the synchrotron, the bunch signal, to generate several data acquisition windows as seen conceptually in figure 4.13. Figure 4.13 is simplified to show the logic of window generation

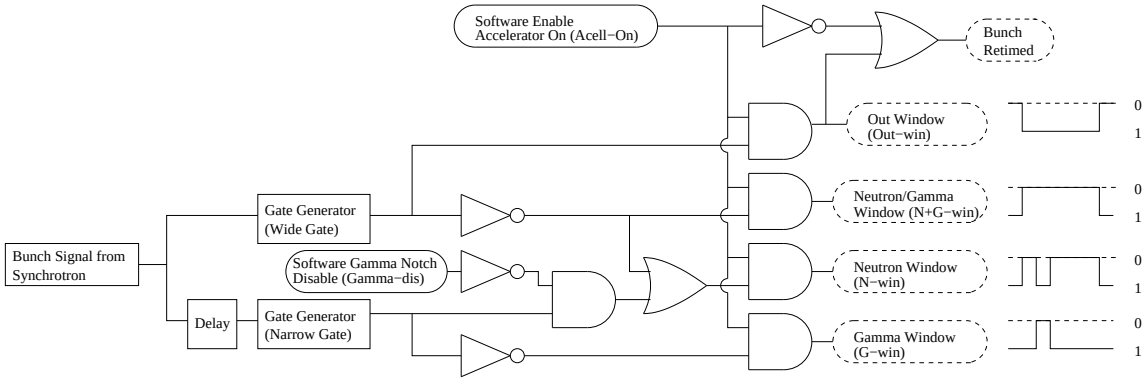

Figure 4.13: Conceptual diagram of acquisition window generation

and the delicate and subtle aspects of nanosecond-level timing have been removed for clarity.

Four windows are generated. The neutron/gamma window (N+G-win) will contain all neutron and gamma-ray events due to an interaction with the beam and the target. The out window (Out-win) will contain all events outside of the N+G-win. The gamma window (G-win) will contain all events due to gamma rays that Compton scatter from the target. Notice that since gamma-rays all travel at the speed of light, they will all traverse the distance from the target to the detectors in almost the same amount of time. Therefore, the G-win is very short. The neutron window is the window in which an event could be from a neutron but not a gamma-ray. The neutron window contains time before the gamma-window notch in order to allow for estimates of the background radiation in the room. Also notice that the gamma notch in the neutron window can be disabled in software. If it is disabled most of the time and occasionally enabled, an experimenter can reduce the number of gamma-rays detected without completely eliminating this important data. This technique is called prescaling.

Instrumentation in nuclear physics follows the nuclear instrumentation module (NIM) standard. In the NIM standard, the voltage level 0 V corresponds to the logic 0 while the voltage level −0.8 V corresponds to the logic 1 [Leo94]. Therefore, the windows of figure 4.13 have logic value 1 below logic value 0. Furthermore, the windows are used as vetos, which have the opposite sense.

4.5.3 The Neutron Trigger

The neutron trigger occurs when a particle is detected in one of Blowfish's neutron detectors.[5] The neutron trigger system is shown conceptually in figure 4.14 along with the pedestal trigger system which will be described in the next section. The 88 detectors are connected to discriminators. When

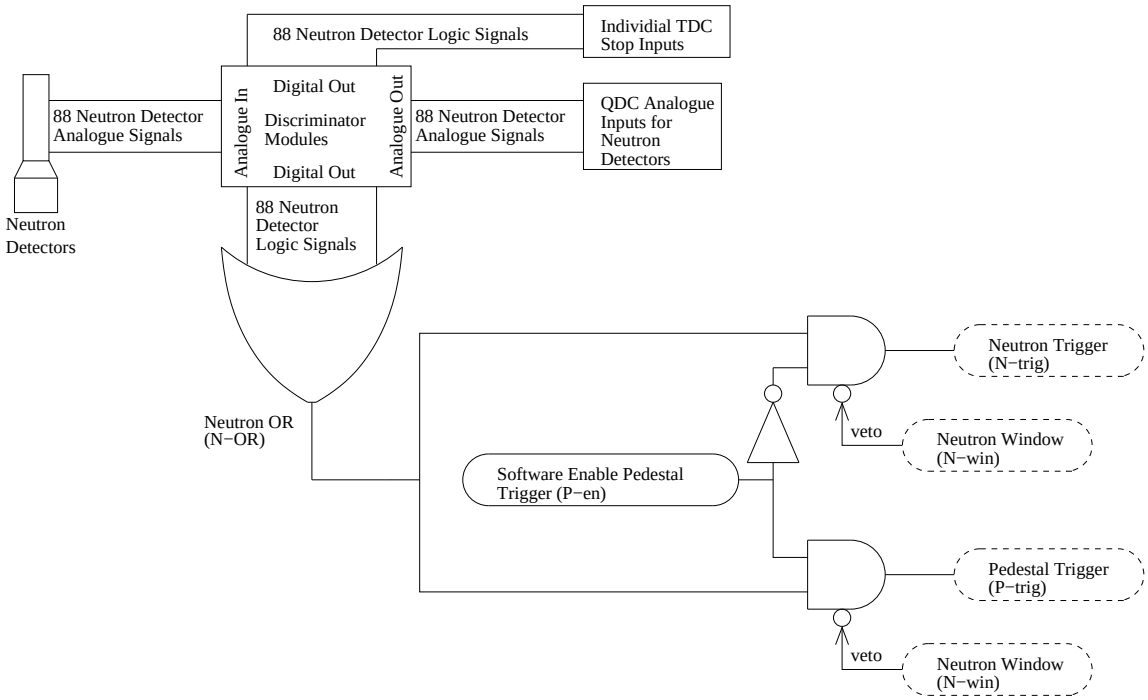

Figure 4.14: Conceptual diagram of neutron and pedestal trigger generation

a signal greater than the discriminator threshold occurs, the discriminator emits a logic pulse that stops the TDC for that detector and is combined with all the other detector signals though a logical OR to create the neutron OR (N-OR) signal. If the pedestal enable is not selected in software, then a neutron trigger (N-trig) is generated. Notice that an N-trig can only be generated during the neutron window.

[5]The neutron trigger occurs when any type of particle is detected, not just neutrons.

4.5.4 The Pedestal Trigger

The QDC modules used in this work require a small amount of charge to be continuously injected into their circuitry in order to perform linearly. This means that the zero of the QDC will have shifted proportional to the amount of time the QDC integrates. This offset is called the 'pedestal on which the data stands', or simply the pedestal, and must be subtracted from any measurements made with the QDC. We therefore measure the pedestal using the pedestal trigger which functions alongside the neutron trigger in order to make sure that the experimental conditions are the same during a pedestal measurement as a measurement due to a particle hitting a detector.

The pedestal trigger generation system is shown in figure 4.14 along with the neutron trigger. If the pedestal is enabled in software (P-en), then a pedestal trigger (P-trig) is generated when N-OR occurs. Otherwise, the N-OR generates an N-trig.

4.5.5 The Monitor Trigger

In order for the gain monitoring system to function, the monitor detectors are calibrated using a radioactive source [Bew05, Bew09]. The monitor detectors are connected to the same data acquisition system as the neutron detectors. The conceptual diagram is shown in figure 4.15. When a monitor detector detects a photon and the software enable for the monitor trigger is on,

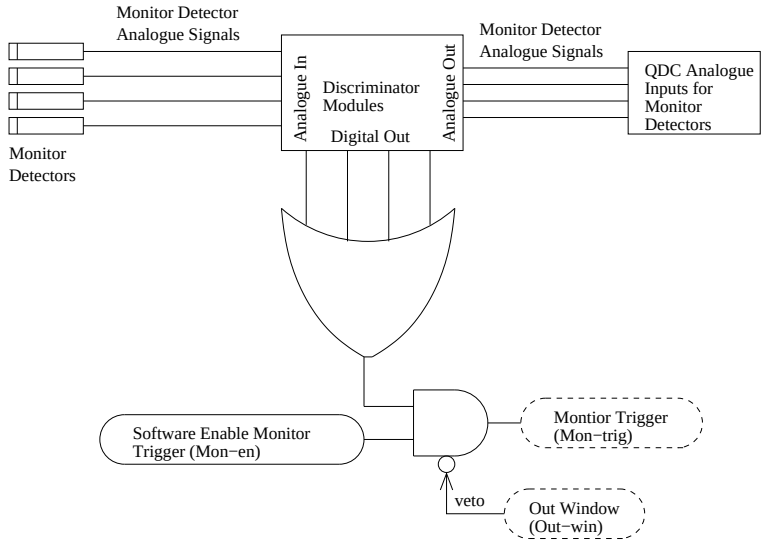

Figure 4.15: Conceptual diagram of monitor trigger generation

a monitor trigger (Mon-trig) will be generated. Notice that the veto is the Out-win, meaning that the monitor trigger can only be generated at times when the neutron trigger cannot.

4.5.6 The Flasher System Trigger

The flasher system trigger is the second trigger associated with the gain monitoring system. Through it, the calibrated monitor detectors are used to calibrate the neutron detectors. The system is shown conceptually in figure 4.16. A square pulse generator generates a short, positive

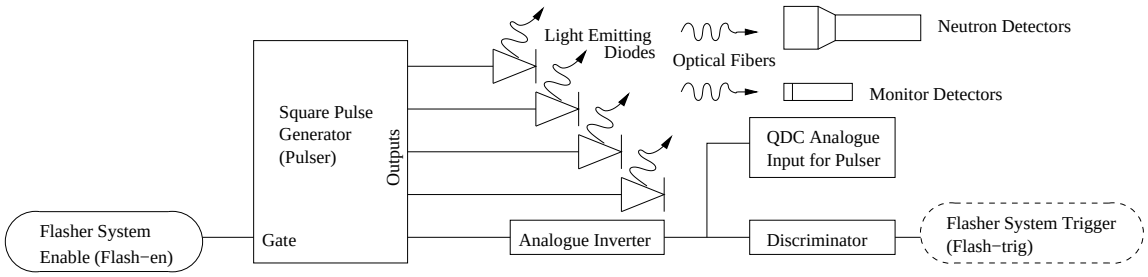

Figure 4.16: Conceptual diagram of flasher system trigger

voltage pulse that causes four light emitting diodes (LED) to emit light that is injected into the neutron detectors and monitor detectors through optical fibres. A fifth pulse is inverted so that it is negative going and generates the flasher system trigger (flash-trig).

4.5.7 Trigger Logic

The last few sections describe how the various triggers are created. Figure 4.17 shows how those triggers are combined and how they start the QDC and TDC modules. The neutron, pedestal,

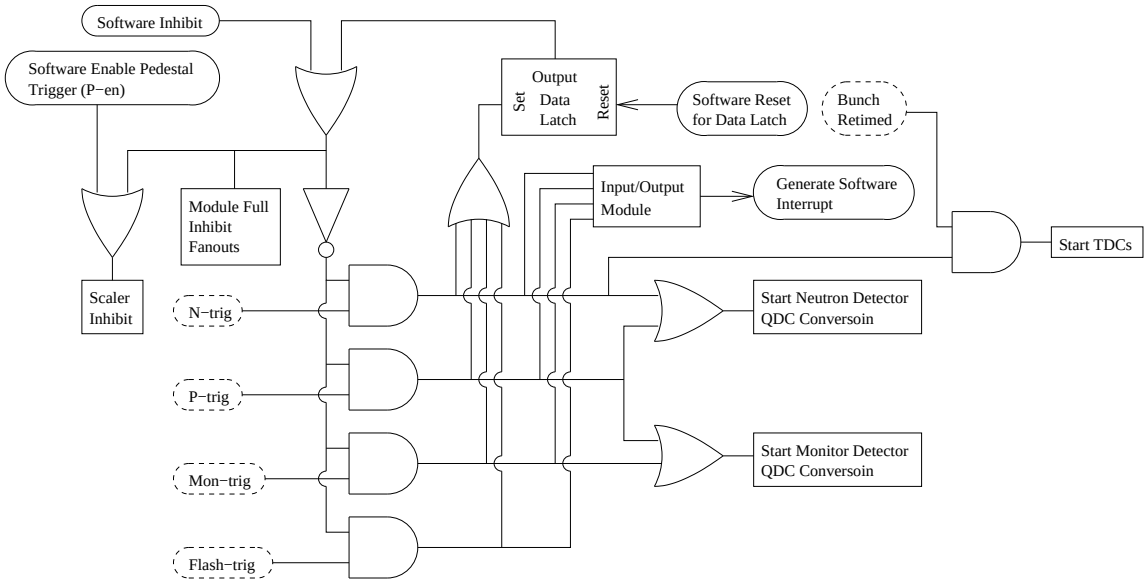

Figure 4.17: Conceptual and highly simplified diagram of trigger electronics

flasher and monitor triggers set a data latch which sets a hardware inhibit. An inhibit causes all modules connected to the 'module full inhibit fanout' to stop their output. This inhibit also

prevents additional triggers from occurring. The hardware inhibit is reset by the data acquisition system after it has finished reading out the QDC and TDC modules. Also, the software can set its own inhibit if it needs to halt the data acquisition system.

The neutron, pedestal, monitor and flasher triggers also cause a software interrupt in the data acquisition system. This signals the data acquisition system to read out the modules and then reset the electronics and wait for another event.

The neutron, monitor and flasher triggers all start the analogue-to-digital conversion for their respective QDC modules. The pedestal trigger starts all conversions since pedestals are needed for each QDC module. Note that the QDC modules attached to the neutron detectors are doubled-up, but this is not shown explicitly on the diagrams. Each signal from the neutron detectors is split into two as it is fed into the modules. One module uses a long integration time and the other uses a short integration time so that we may use pulse-shape discrimination to distinguish between neutron and gamma-ray events.

4.5.8 Scalers

Although they were not included in the previous conceptual electronics diagrams, scalers play a major role in the data acquisition system. A scaler is a device that counts up every time it receives a logic 1 and can be read and reset by the controlling computer. Logic signals such at the N-OR, triggers, discriminator logic outputs and clock ticks are fed into the scalers. Each signal is fed into two scalers. The first records all logic signals sent into it. The second records only those logic signals that occur when the data acquisition system is ready to accept new data. This gives a measurement of the time that system is unresponsive, the dead time of the system.

4.5.9 Computer Control

The QDCs, TDCs and scalers are read out by a computer. The software used is called Lucid [Cha04]. Lucid is a data acquisition system with some basic analysis abilities used to ensure data integrity at runtime and perform basic analysis tasks afterward.

The computer control system is shown in figure 4.18. The user controls the system through a

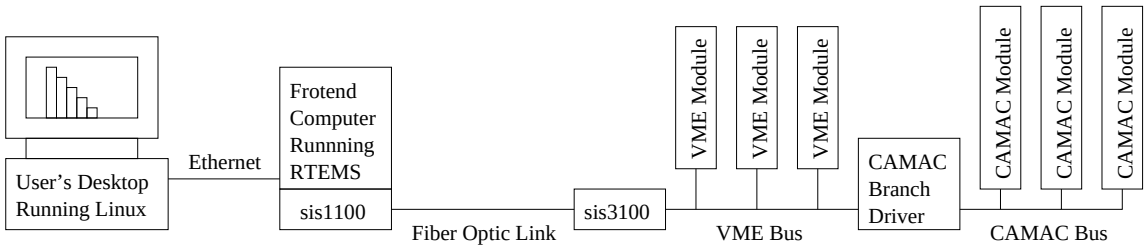

Figure 4.18: Computer control system

desktop computer. Runtime data integrity analysis can be performed on this desktop during an experiment. The desktop gets data and issues instructions to the frontend computer. The frontend computer runs a real-time operating system, the Real-Time Executive for Multiprocessor Systems (RTEMS). A real-time operating system is an operating system that can guarantee deadlines can be met within a specified time. The frontend computer communicates with the electronics modules that contain data, such as the TDCs, QDCs and scalers. It does this though the sis1100/3100 system. The sis1100 is an expansion card that fits into a PCI slot of the computer. The sis3100 is a VME module that attaches to the VME bus. The sis1100 and sis3100 are connected using a fibre-optic link. Through the sis1100/3100 the frontend computer can receive data from and write instructions to the VME modules. There are also older CAMAC modules in use and these are connected to the CAMAC bus. The VME and CAMAC buses are connected through the CAMAC branch driver. The CAMAC modules are much slower than the VME modules and their use is restricted to infrequent events.

4.6 Flux Monitoring

In order to compute absolute cross sections, and to compare separate data acquisition runs, we must know the number of photons that were produced by the accelerator. We used a combination of two systems to do this. The three-paddle system uses three scintillating paddles placed in the photon beam upstream of Blowfish. It is an existing system designed by HIGS to measure relative changes in the photon flux. The five-paddle system uses five scintillating paddles and an aluminum radiator placed downstream of Blowfish. It is a system designed by the University of Saskatchewan Experimental Subatomic Physics Group and can measure the absolute photon flux.

4.6.1 The Three-Paddle Flux Monitoring System

The three-paddle system uses three plastic scintillating paddles and a thin foil used as a converter. The converter is placed between the veto paddle and second paddle to convert some beam photons into charged particles through the processes of Compton scattering and pair production. These processes are depicted in the first two diagrams of figure 4.19. The second and third paddles then detect the charged particles but not the chargeless gamma rays. The veto paddle ensures that any signals produced by charged particles in the second and third paddles are from gamma-ray events in the converter and not radiation from other sources. If the veto paddle is triggered, it suppresses the output of the other two paddles and the event is not counted.

It is also possible for charged particles to be produced in the veto paddle without triggering it and in the second paddle while triggering it. These types of events are not shown in figure 4.19 but are important. Due to events of this type and the tendency of PMT gains to drift, the three-paddle

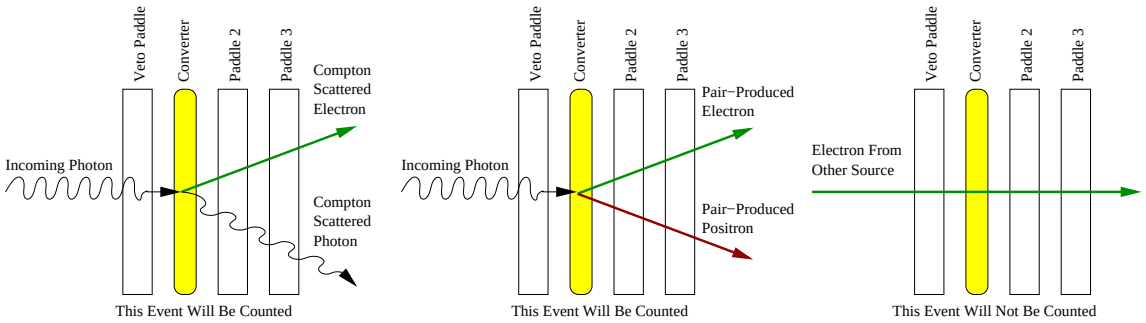

Figure 4.19: Operation of the three-paddle flux monitoring system

flux monitoring system is not suitable for measuring the absolute flux of the photon beam. Instead, it is useful as a rough guide and relative measure.

The three-paddle system was connected to our electronics through a scaler. No pulse height information for the various paddles was obtained as the system is configured to be a black box.

4.6.2 The Five-Paddle Flux Monitoring System

The five-paddle flux monitoring system [Pyw09b] uses the same principles of operation as the three-paddle system. The diagrams in figure 4.20 involving pair production and Compton scattering in the radiator and the vetoing of external charged particles are the same as the three-paddle system except with the addition of paddle 5. Using paddle 5, the system now requires a triple coincidence and will no longer trigger on events where the two previous paddles can be accidentally triggered by two separate background events. The gain monitor paddle is used to monitor the gains of the veto paddle and paddle 3.

We could not use the three-paddle system as an absolute flux monitor since we could not determine the gain of the PMTs. We can observe a coincidence between the gain paddle, the veto paddle and paddle 3, in order to measure the gains of the veto paddle and paddle 3. An electron produced in the gain monitoring paddle will deposit energy in the veto paddle and paddle 3 with a well understood distribution. By comparing this distribution with a calculation for the energy deposited, we can determine the gains of these paddles. Knowing the gains of these paddles will allow us to account for events where charged particles are produced in the veto paddle without triggering it and where charged particles are produced in paddle 3 while triggering it. Accounting for these events will allow us to use the five-paddle system to measure the absolute flux of the photon beam.

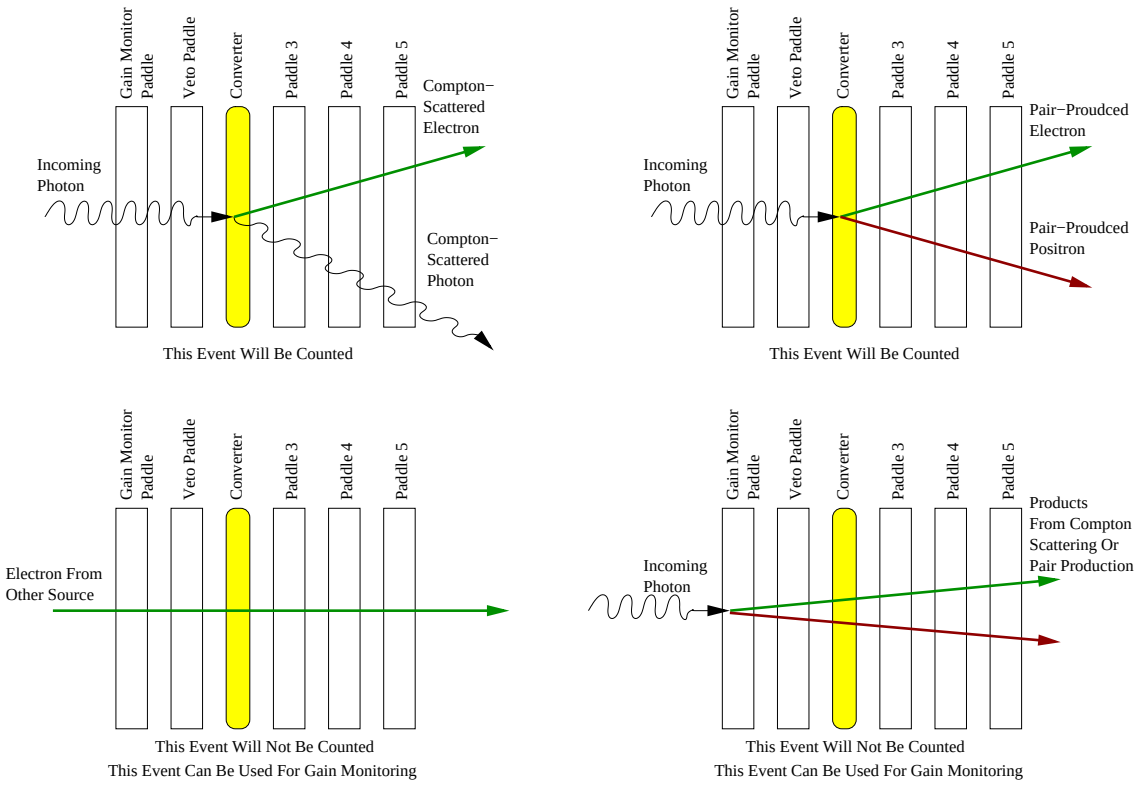

Figure 4.20: Operation of the five-paddle flux monitoring system

4.7 The Lithium Targets

A target is a piece of material either solid, liquid or gas, that is placed in a particle beam. In this case we have two targets of interest, ^{6}Li and ^{7}Li, and the particle beam is the HIGS gamma-ray beam. This section describes the geometry of the targets, which is very important in analysing the experimental data, and discusses how the targets were created.

The target container was designed by W.A. Wurtz and J. Vogt based on the previous design of Bergstrom, Igarashi and Vogt [Ber99]. The casting apparatus was designed by W.A. Wurtz. Both the target and casting apparatus were built at the Department of Physics and Engineering Physics machine shop. The casting of the target was performed by W.A. Wurtz and J. Vogt at the Canadian Light Source.

4.7.1 Geometry and Properties of the Lithium Targets

For the purpose of this experiment, three identical target containers were built, one of which is shown in figure 4.21. One target container remained empty and was used for background studies while the others were filled with lithium. Since we are studying both ^{6}Li and ^{7}Li, one target container was filled with isotopically enriched ^{6}Li, while an other was filled with natural lithium,

Figure 4.21: The lithium target container

which is 92.4% ^{7}Li. The ^{6}Li was obtained from a target used at the Saskatchewan Accelerator Laboratory (SAL) [Ber99]. Because these authors used the approximation that the ^{6}Li target was 100% pure in their analysis [Iga08], we will use the same approximation in our analysis. The natural lithium was purchased from Sigma-Aldrich. Natural lithium was used instead of enriched ^{7}Li due to the prohibitively high cost of enriched ^{7}Li.

The interior diameter of the target was chosen to be 4.1 cm based on previously used deuterium targets [Swa05]. This allows the 3.8 cm HIGS beam to pass though the target without interacting with the target walls. A length[6] of 12.7 cm was chosen to ensure that we would have enough ^{6}Li to fill the target. The new target has a total volume of 167 cm^3. The old SAL ^{6}Li target had a volume of approximately 200 cm^3 and the 100 g of purchased natural lithium had a volume of 187 cm^3.

Lithium reacts exothermically with oxygen, nitrogen and many metals, with water being a major concern. Therefore, only plastics and argon gas came into contact with the lithium during the construction of the targets. The target bodies themselves are made out of Teflon, which has a high melting point. It is crucial that the target bodies have a high melting point as the lithium must be melted and cast into the target bodies. In figure 4.21, the Teflon body is the white cylinder extending the length of the target. The top and bottom of the cylinder are thicker to better hold the end caps, while the middle is reduced in order to reduce the number of neutrons scattering from the target walls.

While we desired the walls of the Teflon cylinder to be thick in order to support the target, we wished for the ends to be very thin in order to allow gamma rays to pass though. We capped the ends with aluminum foil to prevent water from entering the target and forming LiOH. In order to keep the lithium and aluminum separate, as they do react, a PVC film was placed between them. The aluminum and PVC were held onto the target by aluminum rings referred to as end caps. The end caps were attached to the target by four screws which ran the length of the target, as can be seen in figure 4.21. The end caps were held in place by pressure.

The original design drawings for the targets can be found in appendix B.

4.7.2 Casting the Lithium Targets

In order to create the new targets, the SAL ^{6}Li target and the purchased natural lithium needed to be melted and cast into the new geometry. The SAL ^{6}Li target was a solid piece of lithium encased in a Teflon cylinder that was the inspiration for the target bodies used in this thesis. The natural lithium came in the form of a wire and was easier to handle.

Since lithium reacts exothermically with air, the casting procedure was done in an argon atmosphere in a sealed glove box at the Canadian Light Source on the University of Saskatchewan

[6]Note that the HIGS beam and targets are designed in inches where 1 inch = 2.54 cm. The target was designed for a HIGS beam with a diameter of $1\frac{1}{2}$ inches and the targets have diameters of $1\frac{5}{8}$ inches and lengths of 5 inches.

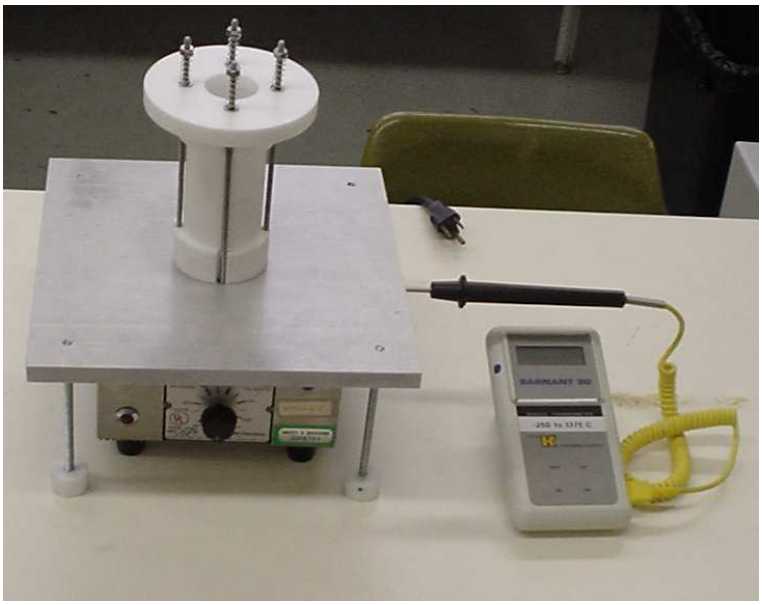

Figure 4.22: The basic lithium target casting apparatus

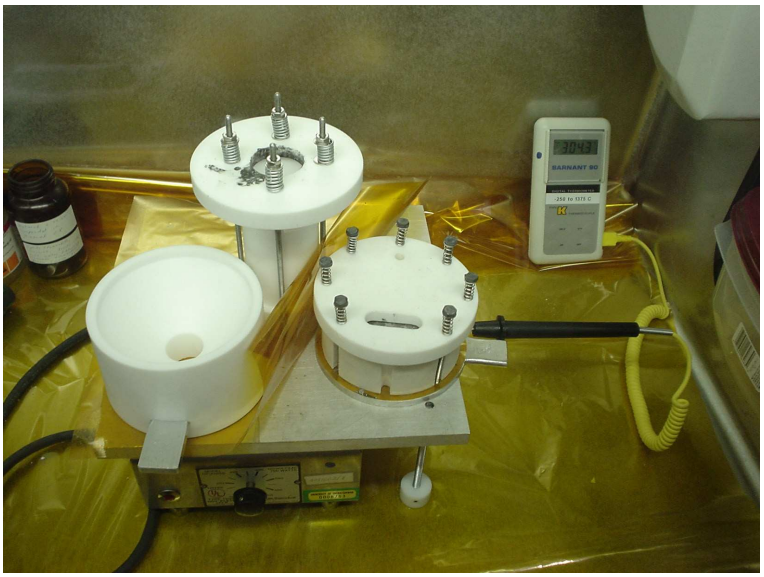

Figure 4.23: The full ^{6}Li target casting apparatus

campus. The apparatus was designed to function inside this glove box. An electric heater was used to melt the lithium. An aluminum plate was placed on this heater and the Teflon target container was mounted on this plate. In order to keep the lithium from touching the aluminum, a layer of Kapton film was placed on top of the plate. The basic apparatus without the Kapton film can be seen in figure 4.22. Notice also that the plate is supported by four legs and has a special hole for the probe of the digital thermometer.

For creating the natural lithium target, we were able to heat the aluminum plate and place the lithium wire inside of the Teflon cylinder. The wire melted and formed a column of molten lithium inside. Once the cylinder was full, the heater was turned off and the lithium was allowed to cool. When the cylinder had cooled sufficiently, it was removed from the apparatus, the end caps were put on and it was placed in a jar of mineral oil to prevent air from interacting with the lithium during shipping and long-term storage.

The ^{6}Li target casting was somewhat more complicated. Since the SAL ^{6}Li target was not a wire but a solid mass it needed to be melted outside of the Teflon cylinder. Figure 4.23 shows the complete ^{6}Li target casting apparatus inside of the glove box. Notice the addition of a solid Teflon funnel on the left of the aluminum plate and the SAL target on the right of the plate. The SAL target consisted of a geometry similar to our design but shorter and with a larger diameter. The ends of this target were removed and it was placed on a special aluminum plate that would allow for it to be lifted. A special cap that would make it easy to pour was placed on top. The heater supplied the heat to melt the SAL target and it was then poured though the Teflon funnel and into the new target cylinder. As with the natural lithium target, the new ^{6}Li target was allowed to cool and placed in a jar of mineral oil.

The end result of the casting process was two lithium targets. The targets were then shipped to HIGS for the experiment. A more detailed discussion of the target casting procedure and apparatus can be found in the internal report [Wur07a].

Chapter 5

Simulation of the Experiment

5.1 Introduction

If all the components in the experiment were ideal, there would be no need to implement a simulation. However, there are many factors that affect the resolution of our experiment, such as detector resolution and the physical size of the photon beam, target and detectors. These factors are convolved with the quantities we are studying. If we understood the effect of these factors on our data perfectly and had extremely good statistics in our data, we could simply perform a deconvolution and extract the quantity of interest. However, this deconvolution is very difficult to impossible. Instead we use a simulation to perform an effective deconvolution.

The Geant4 Simulation Toolkit [Gea03, Gea06] is a set of software libraries that provide the tools we need to perform such a simulation. Geant4 allows a user to specify the geometry of an experiment and tracks particles as they pass through the different media using Monte-Carlo simulation techniques. Using this information, it then computes the amount of energy the particles deposit in each piece of the geometry. The name Geant is derived from the words 'geometry' and 'tracking', as these are the two main functions it performs.

To better understand what Geant4 does and how it works, let us consider an example. Let us assume that our geometry consists of a target in a photon beam and a detector outside the beam. A user can implement this geometry, or at least an approximation of it, in Geant4 by defining geometric elements constructed from materials. For instance, one can define a target made out of lithium and set the fraction of the isotopes ^{6}Li and ^{7}Li. Once the user has defined the geometry, the simulation is ready for the initial particle. This initial particle can by nearly any particle imaginable including photons, protons, neutrons, pions, ions and more exotic particles. It must be given a starting position and initial energy and momentum. In this example, let us take the particle to be a photon and its initial position to be upstream of the target. Let it have sufficient energy to produce an electron-positron pair and let its momentum point toward the target. Once the user has set the properties of the initial particle, the simulation takes over. It calculates the probability that the photon will interact with an air molecule between its initial position and the target. Let us assume, as is most likely, that the photon travels unhindered through the air and is incident on

the target. Then the simulation will compute the probability that the photon will interact with the target and, if it does, where it interacts and which interaction it undergoes. For the sake of the example, let us say that the photon produces an electron-positron pair. The simulation must now track both the positron and the electron. Let us say that the positron exits the target, misses the detector and annihilates with an atmospheric electron. The simulation then must deal with the annihilation photons which, let us assume, leave the simulated world without further interacting. Let the electron, on the other hand, leave the target and pass through the detector on its way out of the world. When it passes though the detector, Geant4 will record a number of details including the amount of energy the electron deposits in the detector. Once all of the particles have left the world, the simulation tallies the results. Geant4 calculates the energy deposited by each particle in the detector and other information such as the time and location of the interaction. It is now up to the experimenter to interpret this information. In the next section, we discuss how the geometry is defined, and the detector response is found, for the simulation used in this thesis.

5.2 Implementing the Geant4 Simulation

While Geant4 provides the toolkit that we will use to build our simulation, we must write the actual implementation. The simulation used in this thesis is based on the BlowfishX template. The BlowfishX template was written by W. A. Wurtz specifically for this thesis but has already been used by other researchers [Bla07]. This simulation is designed to simulate Blowfish and its associated electronics as accurately as possible. It outputs data in the Lucid format, just as the real Blowfish does. Therefore, the same analysis software can be used to analyse the simulated data as the real data. This allows for better debugging of the analysis software.

The basic geometry of the simulation is shown in figure 5.1, with a photon Compton scattering from the target. The entire array is not needed and we concentrate on the materials closest to the target and detectors. The target was implemented as accurately as possible and the four steel mounting rods were added. The target mount brackets are approximations of the real mounting brackets and are made from very simple geometric forms.

There were two basic types of simulations performed. The first involves emitting photons from upstream of the array to see the effect of electromagnetic processes on our data. The second involves emitting neutrons from within the target itself in order to isolate the effect of a single reaction channel. In both cases, the beam is simulated as being circular with a constant photon density and diameter 2.54 cm. The energy spread of photons in the beam was given as $\Delta E_\gamma / E_\gamma \cong (\gamma\theta)^2$ in equation (4.2). The energies of the individual photons in the beam were simulated by using the resolutions calculated in [Wu07] using equation (4.2). When we are emitting neutrons directly, we must consider the attenuation of the photon beam in the target. This attenuation was found to be

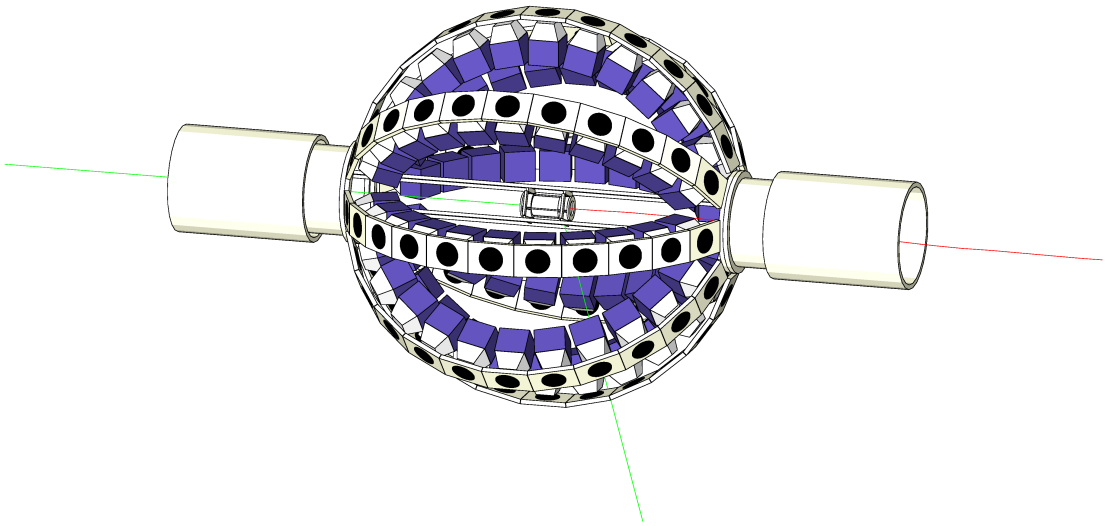

Figure 5.1: The geometry of the Geant4 simulation used in this thesis with a photon (green) Compton scattering and producing a free electron (red)

as high as 9.8% with photons of energy 8 MeV.

The TDC is simulated by determining when a particle interacting with a detector produces enough light output to trigger the discriminator. Since the real timing signal is not ideal, we take the resolution into affect by adding to the TDC output a Gaussian random variable with mean zero and standard deviation

$$\sigma_t = (0.61 \text{ ns}) \exp\left(\frac{-L}{270 \text{ keV}_{ee}}\right) + 0.15 \text{ ns} \tag{5.1}$$

where L is the light output. This factor was determined by fitting the simulated TDC response of Compton scattered gamma-rays to the data.

We must also take into account TDC walk. TDC walk is caused by variations in the time it takes a pulse to rise above the discriminator threshold due to its variable amplitude [Leo94, Kno00]. We use constant fraction (CF) discriminators to minimise the effect of TDC walk on our data. However, by examining the centre of the gamma-ray peak in the TDC spectrum for different pulse amplitudes, we find that there is a non-negligible dependence of the TDC on the QDC. We add the factor (in dimensionless units of TDC channels)

$$7.1 \exp\left(-\frac{\text{QDC Channel}}{328}\right) \tag{5.2}$$

to the simulated TDC values in order to better simulate the TDC.

The long gate QDC is simulated by taking the energy deposited, as computed by Geant4, and using the results of section 4.4.2 to find the light-output response of the scintillator. The light-output resolution is simulated by the prescription used in [Pyw06]. The ideal light output, L_i, is

used to find the actual light output,

$$L_a = L_i + G(\sigma_n) + G(\sigma_\ell) \times \sqrt{\frac{L_i}{1\text{MeV}_{ee}}}, \tag{5.3}$$

where $G(\sigma)$ is a Gaussian random number with mean zero and standard deviation σ. Two effects are considered: First, electronic noise is simulated by the light-output term with $\sigma_n = 5$ keV$_{ee}$. Second, the statistics of light output are simulated by the term with a square root and $\sigma_\ell = 77$ keV$_{ee}$.

The short gate QDC is also simulated. For an electron interacting with the scintillator, the short gate QDC is taken to be 88.2% of the long gate QDC. For a proton depositing less than 300 keV$_{ee}$ in the scintillator, the short gate is taken to be 77.2% of the long gate QDC. The short gate QDC for a proton depositing more than 300 keV$_{ee}$ is calculated by

$$\text{Short Gate QDC} = 0.826 \times (\text{Long Gate QDC}) - 13.0 \text{ keV}_{ee}. \tag{5.4}$$

These factors were calculated by examining the PSD plot of an actual detector. Lines were drawn on the PSD scatter plot by hand to estimate the above parameters.

In this section we have described how the instrumentation of the Blowfish Neutron Detector Array was implemented in our Geant4 simulation. In the next sections we describe how the physics of photodisintegration was implemented.

5.3 Implementing the Kinematics of Photodisintegration in the Simulation

Energy distributions of the emitted neutrons must be calculated for the various possible reaction channels discussed in section 1.5. We wish to emit neutrons from within the target with energy and momentum as would happen in a photodisintegration event. Geant4 will then use its built-in physical processes to simulate the journey of the neutron and secondary particles through the experimental geometry. However, we must first consider the kinematics of such photodisintegration reactions. In the following sections we use the conservation of energy and momentum to compute the energies of the emitted neutrons. We examine two-body, relativistic photodisintegration in section 5.3.1, two-body relativistic radioactive decay in section 5.3.2, three-body, semi-relativistic photodisintegration in section 5.3.3 and three-body, semi-relativistic decay in section 5.3.4.

5.3.1 Kinematics of Relativistic Two-Body Photodisintegration

Given a two-body photodisintegration reaction we would like to derive a relationship between the energy of the emitted neutron and the angle at which it was emitted. Due to the constraints of conservation of energy and momentum, the energy of the neutron should depend only on this angle, the total energy available and the masses of the final products. We begin with a photon with

laboratory frame energy $E_{L\gamma}$ and a ^{6}Li or ^{7}Li target nucleus which is stationary in the laboratory frame and has a rest mass of m_A. Through photodisintegration this nucleus breaks into a neutron with mass m_n and a ^{5}Li or ^{6}Li daughter nucleus which may-or-may-not be in an exited state.

Of these possible final states, only ^{6}Li(g.s.) is stable. All other states will decay and will have a decay width, Γ, which is related to their mean lifetime, τ, by $\tau\Gamma = \hbar$ [Sak94]. This can be modelled by the mass of the daughter nuclei having a Breit-Wigner like distribution,

$$\rho_{BW}(m_d) = \frac{1}{(2\pi)} \frac{\Gamma}{(m_d - \langle m_d \rangle)^2 - \Gamma^2/4} \tag{5.5}$$

centred on the daughter's mean mass and having a width Γ [Sak94]. The distribution is not exactly Breit-Wigner as cuts must be made to make the reaction kinematically allowable. Figure 5.2 shows a Breit-Wigner distribution compared to a Gaussian distribution with the same full width at half maximum. Also shown is the cut Breit-Wigner distribution for the mass of the ^{5}Li daughter nucleus

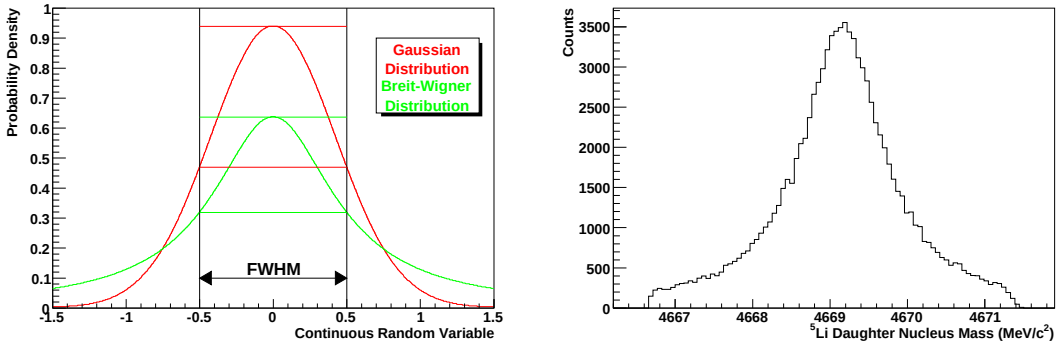

Figure 5.2: A Breit-Wigner distribution compared with a Gaussian distribution (left) and a Breit-Wigner distribution with cuts ensuring that the reaction is kinematically possible (right)

for the reaction $^6\text{Li} + \gamma \rightarrow n + {}^5\text{Li(g.s.)} \rightarrow n + p + {}^4\text{He}$ with 8 MeV gamma rays. The high energy cut ensures that the daughter ^{5}Li nucleus and neutron have non-negative kinetic energy while the low energy cut ensures that the ^{4}He nucleus and proton have non-negative kinetic energy.

We begin this calculation by finding the Lorentz transformation between the laboratory (L) and centre-of-momentum (CM) reference frames. The laboratory frame is the frame where the Li target nucleus is stationary giving four momenta of

$$p_{L\gamma} = (E_{L\gamma}, E_{L\gamma}, 0, 0) \tag{5.6}$$

and

$$p_{LA} = (m_A, 0, 0, 0) \tag{5.7}$$

for the photon and target nucleus respectively.[1] By performing a Lorentz transformation along the

[1]We use a unit system where the speed of light, c, is 1. We can easily add in all the factors of c at the end of the calculation. We use the subscript L for the laboratory frame quantities and no subscript for the CM frame quantities. If p and q are four vectors we use the convention that $p \cdot q = p^0q^0 - p^1q^1 - p^2q^2 - p^3q^3$.

beam direction we can find the four momenta of particles in the CM frame

$$\begin{pmatrix} p^0 \\ p^1 \\ p^2 \\ p^3 \end{pmatrix} = \begin{pmatrix} \gamma & -\beta\gamma & 0 & 0 \\ -\beta\gamma & \gamma & 0 & 0 \\ 0 & 0 & 1 & 0 \\ 0 & 0 & 0 & 1 \end{pmatrix} \begin{pmatrix} p_L^0 \\ p_L^1 \\ p_L^2 \\ p_L^3 \end{pmatrix} \tag{5.8}$$

where β is the CM frame's velocity in the laboratory frame and $\gamma = \left(1-\beta^2\right)^{-1/2}$. We can find β by equating the momenta of the photon and target nucleus in the CM frame. This gives

$$\beta = \frac{E_{L\gamma}}{E_{L\gamma} + m_A} \tag{5.9}$$

which can be used to find expressions for the four momenta in the CM frame for the photon

$$p_\gamma = \left(\gamma\left(1-\beta\right)E_{L\gamma}, \gamma\left(1-\beta\right)E_{L\gamma}, 0, 0\right) \tag{5.10}$$

and for the target nucleus

$$p_A = \left(\gamma m_A, -\beta\gamma m_A, 0, 0\right). \tag{5.11}$$

We define the total energy of the system in the CM frame to be the sum of the energy of the photon and the target nucleus, $E_{tot} = E_\gamma + E_A$. Figure 5.3 shows the initial and final configurations in the CM frame.

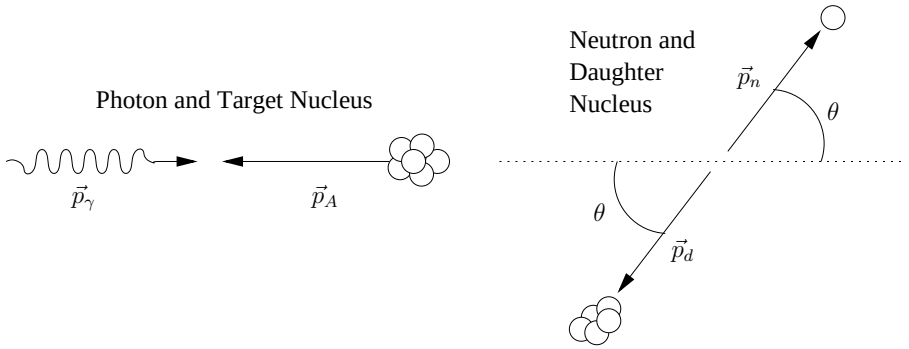

Figure 5.3: Photodisintegration of a nucleus in the centre-of-momentum reference frame

The neutron and daughter nucleus must have the same total momentum, $|\vec{p}_n|$, in this frame and are emitted in opposite directions. If θ is the angle between the neutron's direction and the beam direction, the four-vectors for the neutron and daughter nucleus can be written as

$$p_n = \left(\sqrt{|\vec{p}_n^2| + m_n^2}, |\vec{p}_n|\cos\theta, |\vec{p}_n|\sin\theta, 0\right) \tag{5.12}$$

and

$$p_d = \left(\sqrt{|\vec{p}_n^2| + m_d^2}, -|\vec{p}_n|\cos\theta, -|\vec{p}_n|\sin\theta, 0\right) \tag{5.13}$$

respectively. We have chosen the rotation of our reference frame so that the reaction occurs in the x-y plane. Using the conservation of energy, we find the momentum of the neutron

$$|\vec{p}_n| = \frac{1}{2}\sqrt{\frac{\left(m_d^2 - m_n^2\right)^2}{E_{tot}^2} + E_{tot}^2 - 2\left(m_d^2 + m_n^2\right)}. \tag{5.14}$$

It is interesting to note that the neutron's absolute value of the momentum in the CM frame is completely determined by the available energy and rest masses of the final products and has no dependence on θ. We can now find the momenta and energies of the neutron and daughter nucleus in the laboratory frame by performing an inverse Lorentz transform, which can be found by inverting the Lorentz transform in equation (5.8).

To take into account the azimuthal angle, we can rotate the momenta of the neutron and daughter nucleus about the beam axis. Note that this angle will be the same in the CM frame as the laboratory frame and is not affected by the Lorentz transformation.

We have been able to determine the energy and momentum of the neutron and the daughter nucleus in the laboratory frame.

5.3.2 Kinematics of the Relativistic Two-Body Decay

In the case where an unstable daughter is produced in a photodisintegration reaction, such as in the reactions $^6\mathrm{Li} + \gamma \rightarrow p + {}^5\mathrm{He}$ and $^7\mathrm{Li} + \gamma \rightarrow d + {}^5\mathrm{He}$, the daughter nucleus will decay. Using the kinematics presented in the previous section and replacing the neutron mass with the proton or deuteron mass we can compute the four momentum of the daughter nucleus, p_{Ld}. Using this four momentum and the fact that the decay in the centre-of-momentum frame is isotropic, we can simulate this decay reaction.

We will do our calculations in the centre-of-momentum frame of the daughter nucleus, which is also its rest frame. Defining $\vec{\beta}$ to be the daughter's velocity in the laboratory frame we can use

$$\vec{\beta} = \frac{\vec{p}_{Ld}}{E_{Ld}} \tag{5.15}$$

to find the transformation from the laboratory frame to the daughter's rest frame. In this case we use the general Lorentz transformation[2] [Jac99]

$$\begin{pmatrix} p^0 \\ p^1 \\ p^2 \\ p^3 \end{pmatrix} = \begin{pmatrix} \gamma & -\beta\gamma_1 & -\beta\gamma_2 & -\beta\gamma_3 \\ -\beta\gamma_1 & 1+(\gamma-1)\frac{\beta_1^2}{\beta^2} & (\gamma-1)\frac{\beta_1\beta_2}{\beta^2} & (\gamma-1)\frac{\beta_1\beta_3}{\beta^2} \\ -\beta\gamma_2 & (\gamma-1)\frac{\beta_1\beta_2}{\beta^2} & 1+(\gamma-1)\frac{\beta_2^2}{\beta^2} & (\gamma-1)\frac{\beta_2\beta_3}{\beta^2} \\ -\beta\gamma_3 & (\gamma-1)\frac{\beta_1\beta_3}{\beta^2} & (\gamma-1)\frac{\beta_2\beta_3}{\beta^2} & 1+(\gamma-1)\frac{\beta_3^2}{\beta^2} \end{pmatrix} \begin{pmatrix} p_L^0 \\ p_L^1 \\ p_L^2 \\ p_L^3 \end{pmatrix}. \tag{5.16}$$

The matrix in equation (5.16) can easily be inverted by taking $\vec{\beta} \rightarrow -\vec{\beta}$.

In the daughter's rest frame the decay will be isotropic and is shown in figure 5.4. The analysis

[2]It was found to be easier to use the general Lorentz transformation equation than to use the one-dimensional transformation, equation (5.8), and coordinate system rotations.

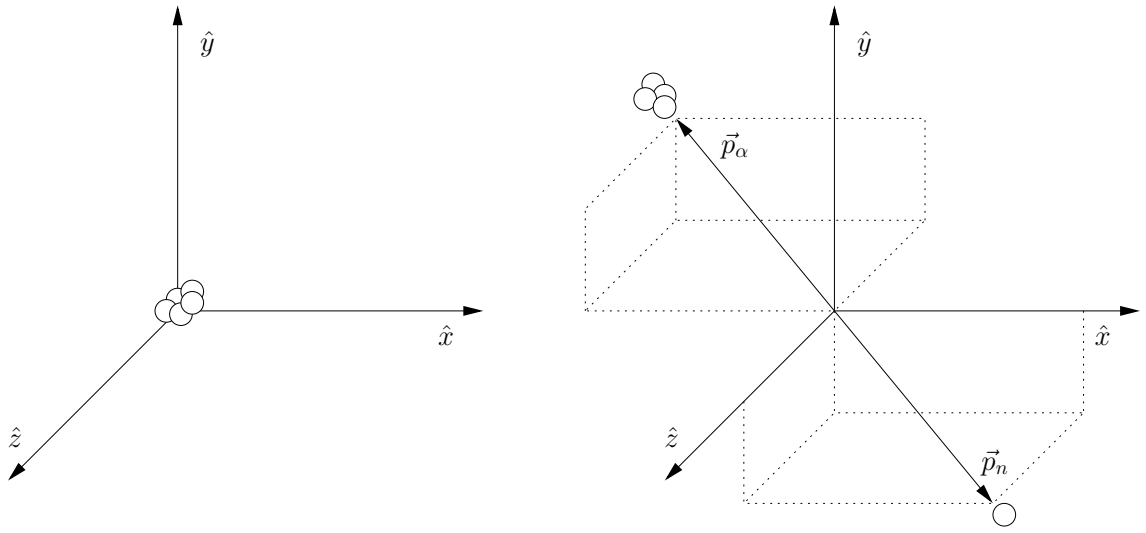

Figure 5.4: Decay of a nucleus in its rest frame

for this decay in the CM frame is exactly the same as our study of the relativistic two-body photodisintegration reaction with the total initial energy being the rest mass energy of the daughter nucleus, $E_{tot} = m_d$. The momentum of the neutron is then

$$|\vec{p}_n| = \frac{1}{2}\sqrt{\frac{\left(m_\alpha^2 - m_n^2\right)^2}{m_d^2} + m_d^2 - 2\left(m_\alpha^2 + m_n^2\right)} \tag{5.17}$$

where m_α is the mass of the second decay product, often an alpha particle. The isotopic nature of the decay is simulated by generating random angles ϕ and θ by sampling ϕ and $\cos\theta$ from uniform distributions with appropriate ranges.

We can now find the CM frame four momenta of the neutron

$$p_n = \left(\sqrt{|\vec{p}_n^2| + m_n^2}, |\vec{p}_n|\cos\theta, |\vec{p}_n|\sin\theta\cos\phi, |\vec{p}_n|\sin\theta\sin\phi\right) \tag{5.18}$$

and second decay product

$$p_\alpha = \left(\sqrt{|\vec{p}_n^2| + m_\alpha^2}, -|\vec{p}_n|\cos\theta, -|\vec{p}_n|\sin\theta\cos\phi, -|\vec{p}_n|\sin\theta\sin\phi\right). \tag{5.19}$$

These four momenta can be transformed into the laboratory frame by using the inverse of equation (5.16).

Using the combination of the two-body photodisintegration calculation of section 5.3.1 and the decay reaction discusses in this section, we can simulate the production of neutrons by the daughter nucleus.

5.3.3 Kinematics of Semi-Relativistic Three-Body Photodisintegration

In section 5.3.1 we examined the kinematics of the two-body photodisintegration reaction and found that the energy of the neutron depends only on the angle at which it is emitted. However, reactions

such as $\gamma + {}^6\mathrm{Li} \rightarrow n + p + {}^4\mathrm{He}$ have three particles in the final state. In this section, we will discuss the three-body photodisintegration reaction and find that it is somewhat more complicated. The energy of the neutron now depends not only on its angle, but the angles at which the other particles are emitted. To perform this calculation we will use a semi-relativistic approximation.

As in the case of the two-body photodisintegration, we have a photon with energy E_γ and a target nucleus with energy E_A in the centre-of-momentum (CM) frame. The total energy available to this reaction is then $E_{tot} = E_\gamma + E_A$.

Before we write our equations for the momenta of the final products, let us choose a rotation of the reference frame to simplify our work. Let us take the reference frame where the neutron has momentum only in the x-y plane and the CM momenta can be written as

$$\vec{p}_n = (|\vec{p}_n| \cos\theta_n, |\vec{p}_n| \sin\theta_n, 0) \tag{5.20}$$

$$\vec{p}_p = (|\vec{p}_p| \cos\theta_p, |\vec{p}_p| \sin\theta_p \cos\phi_p, |\vec{p}_p| \sin\theta_p \sin\phi_p) \tag{5.21}$$

$$\vec{p}_\alpha = (|\vec{p}_\alpha| \cos\theta_\alpha, |\vec{p}_\alpha| \sin\theta_\alpha \cos\phi_\alpha, |\vec{p}_\alpha| \sin\theta_\alpha \sin\phi_\alpha)\,. \tag{5.22}$$

We note that there are eight[3] unknowns in the above, $|\vec{p}_n|$, $|\vec{p}_p|$, $|\vec{p}_\alpha|$, θ_n, θ_p, θ_α, ϕ_p and ϕ_α. With three equations for the conservation of momentum and one for the conservation of energy, four of these eight quantities will be constrained. The remaining four will be independent variables and all four will have an effect on the energy of the neutron. This can be contrasted with the two-body decay where there is only one quantity, θ_n, that has an effect on the neutron energy. We will chose θ_n, θ_p, ϕ_p and ϕ_α to be the independent variables and $|\vec{p}_n|$, $|\vec{p}_p|$, $|\vec{p}_\alpha|$ and θ_α to be the dependent variables. Through careful elimination, we can find an equation for $|\vec{p}_n|$ which is related to only the independent variables and known quantities.

Begin by writing the equations for the conservation of momentum

$$\hat{x}: 0 = |\vec{p}_n| \cos\theta_n + |\vec{p}_p| \cos\theta_p + |\vec{p}_\alpha| \cos\theta_\alpha \tag{5.23}$$

$$\hat{y}: 0 = |\vec{p}_n| \sin\theta_n + |\vec{p}_p| \sin\theta_p \cos\phi_p + |\vec{p}_\alpha| \sin\theta_\alpha \cos\phi_\alpha \tag{5.24}$$

$$\hat{z}: 0 = |\vec{p}_p| \sin\theta_p \sin\phi_p + |\vec{p}_\alpha| \sin\theta_\alpha \sin\phi_\alpha \tag{5.25}$$

and use the $\hat{z}$-momentum equation to isolate the dependent variable $\sin\theta_\alpha$

$$\sin\theta_\alpha = \frac{-|\vec{p}_p| \sin\theta_p \sin\phi_p}{|\vec{p}_\alpha| \sin\phi_\alpha} \tag{5.26}$$

which we can use to eliminate θ_α from the equation for $\hat{y}$-momentum. We can use our expression for $\sin\theta_\alpha$ to write the equation for $\hat{y}$-momentum in a very simple way

$$|\vec{p}_p| = \frac{|\vec{p}_n| \sin\theta_n \sin\phi_\alpha}{\sin\theta_p \sin(\phi_p - \phi_\alpha)} = A\,|\vec{p}_n| \tag{5.27}$$

[3]Recall that there is no ϕ_n by our choice of coordinate system.

where

$$A \equiv \frac{\sin\theta_n \sin\phi_\alpha}{\sin\theta_p \sin\left(\phi_p - \phi_\alpha\right)} \tag{5.28}$$

depends only on independent variables. Since A depends only on independent variables, this equation links the two dependent variables $|\vec{p}_p|$ and $|\vec{p}_n|$. In order to deal with the equation for $\hat{x}$-momentum, we must first eliminate $|\vec{p}_p|$ from our expression for $\sin\theta_\alpha$, giving

$$\sin\theta_\alpha = \frac{-|\vec{p}_n|}{|\vec{p}_\alpha|}\frac{\sin\theta_n \sin\phi_p}{\sin\left(\phi_p - \phi_\alpha\right)} = \frac{-|\vec{p}_n|}{|\vec{p}_\alpha|}B \tag{5.29}$$

where

$$B \equiv \frac{\sin\theta_n \sin\phi_p}{\sin\left(\phi_p - \phi_\alpha\right)} \tag{5.30}$$

and find the expression

$$\cos\theta_\alpha = \pm\sqrt{1 - \frac{|\vec{p}_n|^2}{|\vec{p}_\alpha|^2}B^2}. \tag{5.31}$$

Using our expression for $\cos\theta_\alpha$ and $|\vec{p}_p| = A\,|\vec{p}_n|$, the equation for $\hat{x}$-momentum becomes

$$0 = \pm\,|\vec{p}_\alpha|\sqrt{1 - \frac{|\vec{p}_n|^2}{|\vec{p}_\alpha|^2}B^2} + A\,|\vec{p}_n|\cos\theta_p + |\vec{p}_n|\cos\theta_n \tag{5.32}$$

which can be expressed as

$$|\vec{p}_\alpha|^2 = |\vec{p}_n|^2\left(B^2 + \left(A\cos\theta_p + \cos\theta_n\right)^2\right) = D^2\,|\vec{p}_n|^2 \tag{5.33}$$

where

$$D \equiv \sqrt{B^2 + \left(A\cos\theta_p + \cos\theta_n\right)^2}. \tag{5.34}$$

We can now link the two dependent variables $|\vec{p}_\alpha|$ and $|\vec{p}_n|$ using D, which depends only on independent variables.

Now that we have the expressions $|\vec{p}_p| = A\,|\vec{p}_n|$ and $|\vec{p}_\alpha| = D\,|\vec{p}_n|$, we can use the conservation of energy to compute $|\vec{p}_n|$. The conservation of energy can be written as

$$\begin{aligned} E_{tot} &= E_n + E_p + E_\alpha \\ &= \sqrt{|\vec{p}_n|^2 + m_n^2} + \sqrt{|\vec{p}_p|^2 + m_p^2} + \sqrt{|\vec{p}_\alpha|^2 + m_\alpha^2} \\ &= \sqrt{|\vec{p}_n|^2 + m_n^2} + \sqrt{A^2\,|\vec{p}_n|^2 + m_p^2} + \sqrt{D^2\,|\vec{p}_n|^2 + m_\alpha^2}. \end{aligned} \tag{5.35}$$

Unfortunately, this is very difficult to solve analytically, so we use the expansion

$$E_n = \sqrt{|\vec{p}_n|^2 + m_n^2} = m_n + \frac{|\vec{p}_n|^2}{2m_n} + \frac{|\vec{p}_n|^4}{8m_n^3} + \frac{3\,|\vec{p}_n|^8}{48m_n^7} + \ldots \tag{5.36}$$

and take only the terms we need. If we consider a neutron with mass $m_n \sim 1$ GeV/c^2 and momentum $|\vec{p}_n| \sim 250$ MeV/c. Taking the first significant figure of each term the energy is

$$E_n \sim 1000\text{ MeV} + 30\text{ MeV} - 0.5\text{ MeV} + 0.001\text{ MeV} + \ldots \tag{5.37}$$

which means that the neutron has non-relativistic, kinetic energy ~ 30 MeV and the first relativistic correction is ~ 0.5 MeV. It will be more than sufficient to truncate this series at the first relativistic correction. This truncation is the reason that we describe this calculation as being semi-relativistic.

The conservation of energy can then be written

$$0 = (m_n + m_p + m_\alpha - E_{tot}) + \frac{1}{2}\left(\frac{1}{m_n} + \frac{A^2}{m_p} + \frac{D^2}{m_\alpha}\right)|\vec{p}_n|^2 - \frac{1}{8}\left(\frac{1}{m_n^3} + \frac{A^4}{m_p^3} + \frac{D^4}{m_\alpha^3}\right)|\vec{p}_n|^4 \quad (5.38)$$

which is a quadratic in $|\vec{p}_n|^2$ and can be solved using the normal quadratic equation. We can then find our other dependent variables using the previously derived equations

$$|\vec{p}_p| = A\,|\vec{p}_n| \text{ and } |\vec{p}_\alpha| = D\,|\vec{p}_n| \quad (5.39)$$

and the $\hat{z}$-momentum

$$\theta_\alpha = \arccos\left(-\frac{|\vec{p}_p|\cos\theta_p + |\vec{p}_n|\cos\theta_n}{|\vec{p}_\alpha|}\right). \quad (5.40)$$

By a careful analysis we have determined our four dependent quantities $|\vec{p}_n|$, $|\vec{p}_p|$, $|\vec{p}_\alpha|$ and θ_α in terms of our independent quantities θ_n, θ_p, ϕ_p and ϕ_α. Using these eight quantities together we can find the three components of the momentum for each particle using equations (5.20) to (5.22). Once we have the momentum, the energy can be found using the standard $E_n^2 = |\vec{p}_n|^2 + m_n^2$ formula. We can use the same Lorentz transform as we used in the case of two-body photodisintegration to transform these quantities into the laboratory reference frame.

Note that while momentum will be conserved exactly, the energy will not be exactly conserved due to our truncating the series. This approximation is very good for the energies we are considering in this thesis.

Using the calculations of this section we can find the energy of the emitted neutron in a three-body photodisintegration reaction given the direction of that neutron, the direction of the proton and the azimuthal angle of the α-particle.

5.3.4 Kinematics of the Semi-Relativistic Three-Body Decay

The decay of some intermediate states may proceed directly through a three-body process and not through two subsequent two-body processes. An example of such a decay is $^6\text{He}(1.80) \rightarrow 2n + {}^4\text{He}$ which can occur in the photodisintegration of ^{7}Li. If one computes the Q values for the two and three-body decays of ^{6}He(1.80), one sees that the two-body decay does not occur. This is discussed further in section 10.2, and we concentrate on the kinematic equations here.

Fortunately, we can use the mathematics of sections 5.3.2 and 5.3.3 to simplify our discussion of the three-body decay. The general Lorentz transformation of equation (5.16) is the same as we need here as we have only a single body in the initial system. This equation can be used to transform Lorentz vectors between the laboratory and CM frames.

We can use many equations from the discussion of the three-body photodisintegration reaction of section 5.3.3 to help us describe the three-body decay. In the CM frame we need only to set $E_{tot} = m_d$, where m_d is the mass of the nucleus undergoing the decay. It is important to note that, unlike the two-body decay, the CM frame momenta of the final products does depend on the angles at which they are emitted. We assume that there is no correlation between the direction of any two decay products. The momentum of one particle can be found using equation (5.38) and the momenta of the other two can be found using equation (5.39). The remaining angle can be found using equation (5.40).

By adapting the equations of the two-body decay and three-body photodisintegration of sections 5.3.2 and 5.3.3 to the current problem, we are able to compute the kinematic equations for a three-body decay.

5.4 Implementing Angular Distributions in the Simulation

In section 5.3.1 we discussed two-body photodisintegration and the kinematics of the final products. We found that, given the photon energy and the masses of the target nucleus and the final products, the energies of the final products are determined only by the angle at which they are emitted relative to the photon beam, θ. We have not yet considered the angular distribution of the emitted particles. In this section we use a method for emitting particles with specified angular distributions based on the work of Sawatzky [Swa05], which was also used in the thesis of Blackston [Bla07]. We will present a more mathematically rigorous description of a somewhat modified method.

In section 2.2 we derived a parameterisation of the differential cross section in terms of associated Legendre functions. The parameterisation is given by equation (2.27) and the associated Legendre functions are listed in equation (2.29). We wish to be able to emit particles with angular distributions given by a single term of the parameterisation in order to compare with experimental data and estimate the fitting coefficients a_k and e_k. By simulating particle angular distributions with only one non-zero a_k and e_k, and setting all others to zero, we can compare with the measured data to extract the angular dependence of the cross section. For our calculations we will only consider terms with $k \leq 4$.

We wish to build probability density functions for ϕ and $\cos\theta$. For the term with no angular dependence, this is accomplished by sampling ϕ from a uniform distribution with range 0 to 2π and by sampling $\cos\theta$ from a uniform distribution with range -1 to 1. This is equivalent to writing probability density functions

$$\rho_0^0(\cos\theta) = \frac{1}{2} \text{ and } \rho_\phi^0(\phi) = \frac{1}{2\pi}. \tag{5.41}$$

Unfortunately, the rest of the terms are more complicated since none of them are positive over their entire domains. The polarisation independent terms, corresponding to the a_k coefficients, can

be dealt with by sampling $\cos\theta$ with a probability density function of

$$\rho_k^0(\cos\theta) = \frac{1}{2}\left(1 + P_k^0(\cos\theta)\right) \tag{5.42}$$

with a $\cos\theta$ range from -1 to 1 and sampling ϕ from the uniform distribution. After we have run the simulation, we can account for the constant factor to obtain the angular dependence we need. To generate random numbers with these distributions, we compute the cumulative distribution function

$$C_k^0(\cos\theta) = \int_{-1}^{\cos\theta} \rho_k^0(\cos\theta')d\cos\theta', \tag{5.43}$$

and sample $C_k^0(\cos\theta)$ from a uniform random distribution with range from 0 to 1 and invert it to find the properly distributed value of $\cos\theta$. The cumulative distribution functions are

$$\begin{aligned}
C_1^0(\cos\theta) &= \frac{1}{4}\left(\cos^2\theta + 2\cos\theta + 1\right) \\
C_2^0(\cos\theta) &= \frac{1}{4}\left(\cos^3\theta + \cos\theta + 2\right) \\
C_3^0(\cos\theta) &= \frac{1}{16}\left(5\cos^4\theta - 6\cos^2\theta + 8\cos\theta + 9\right) \\
C_4^0(\cos\theta) &= \frac{1}{16}\left(7\cos^5\theta - 10\cos^3\theta + 11\cos\theta + 8\right).
\end{aligned} \tag{5.44}$$

There are two cases where we can explicitly invert the cumulative distribution functions. We can sample values with the correct distributions by generating values for u from a uniform distribution with range 0 to 1:

$$\begin{aligned}
k = 1 : \cos\theta_s &= 2\sqrt{u} - 1 \\
k = 2 : \cos\theta_s &= \sqrt[3]{2u - 1 + 2\sqrt{u^2 - u + \frac{7}{27}}} - \sqrt[3]{1 - 2u + 2\sqrt{u^2 - u + \frac{7}{27}}}.
\end{aligned} \tag{5.45}$$

For all other cases we must invert the cumulative distribution functions numerically; for this work we use Newton's method.

The terms with dependence on linear polarisation, corresponding to the e_k coefficients, are yet more complicated. At first glance it would appear that the distributions for $\cos\theta$ and ϕ are independent. Unfortunately, this is not true, and we build two-dimensional probability density functions

$$\begin{aligned}
\rho_2^2(\cos\theta, \phi) &= \frac{1}{12\pi}\left(3 + P_2^2(\cos\theta)\cos 2\phi\right) \\
\rho_3^2(\cos\theta, \phi) &= \frac{1}{24\pi}\left(6 + P_3^2(\cos\theta)\cos 2\phi\right) \\
\rho_4^2(\cos\theta, \phi) &= \frac{1}{40\pi}\left(10 + P_4^2(\cos\theta)\cos 2\phi\right)
\end{aligned} \tag{5.46}$$

where the constant factors are chosen to ensure the density functions are never negative. All the angular distributions are represented graphically in figure 5.5.

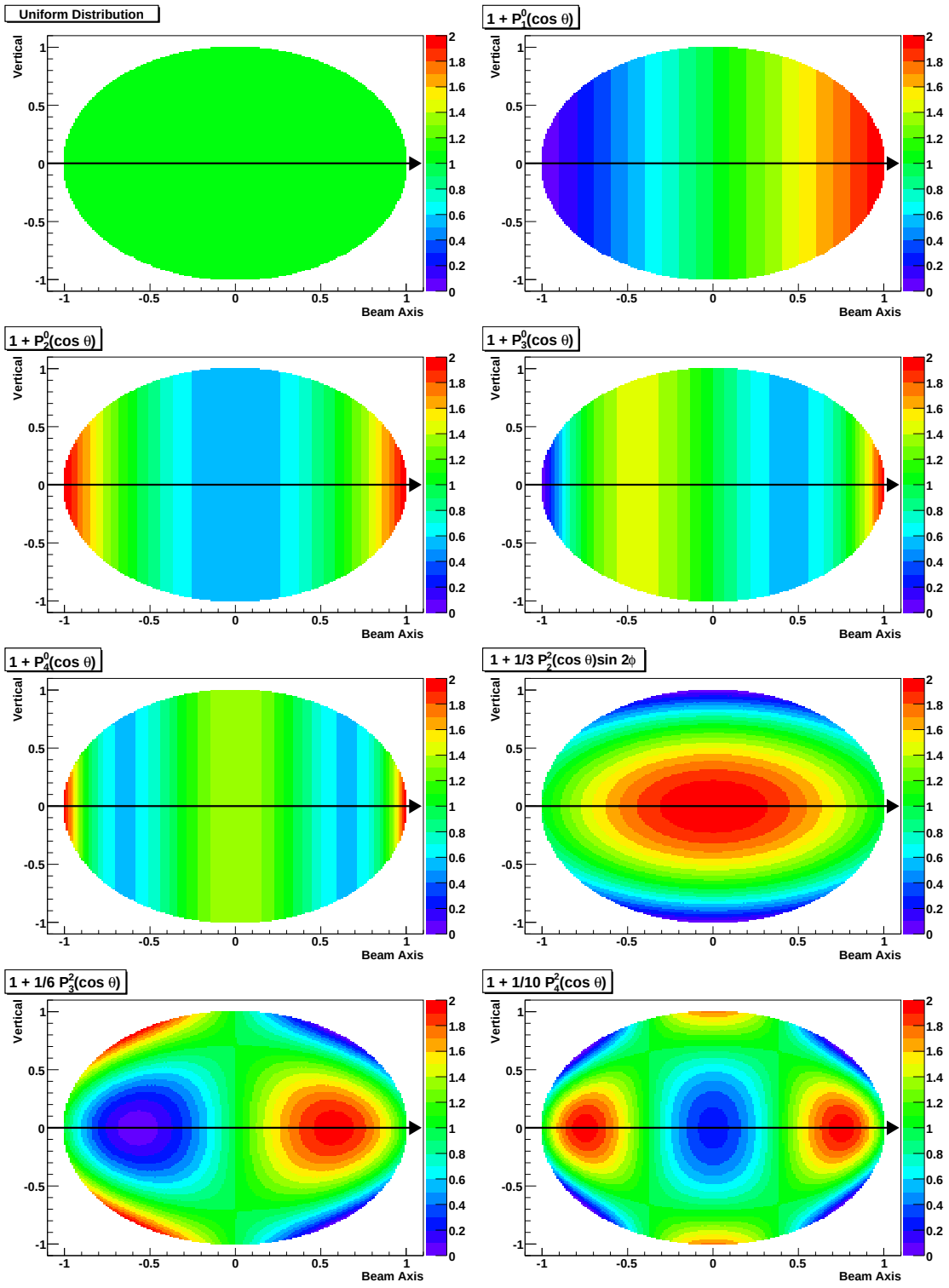

Figure 5.5: Visual representation of the neutron angular distributions for each of the eight associated Legendre polynomials. Red means more neutrons and blue means fewer neutrons. These are the distributions seen by an observer in the centre-of-momentum frame looking at the experiment from the side. Recall that the linearly polarised photons are polarised in the horizontal plane. Normalisation is performed on each plot to maximise the colour range.

Since we cannot separate $\cos\theta$ and ϕ as we did for the polarisation independent terms, we must consider them together. First we find the cumulative distribution function for $\cos\theta$ integrated over all ϕ,

$$C^2_{k,\cos\theta}(\cos\theta) = \int_{-1}^{\cos\theta}\int_0^{2\pi} \rho^2_k(\cos\theta', \phi) d\phi d\cos\theta' = \frac{1+\cos\theta}{2} \tag{5.47}$$

which means that $\cos\theta$ is uniformly distributed with range -1 to 1. We sample this distribution and obtain a sampled value, $\cos\theta_s$. We can then use this value to find the cumulative distribution function for ϕ,

$$C^2_{k,\phi}(\phi) = 2\int_0^{\phi} \rho^2_k(\cos\theta_s, \phi') d\phi', \tag{5.48}$$

where the factor of 2 comes from the need for normalisation. We can then write the cumulative distribution functions

$$\begin{aligned} C^2_{2,\phi}(\phi) &= \frac{\phi}{2\pi} + \frac{P^2_2(\cos\theta_s)\sin 2\phi}{12\pi} \\ C^2_{3,\phi}(\phi) &= \frac{\phi}{2\pi} + \frac{P^2_3(\cos\theta_s)\sin 2\phi}{24\pi} \\ C^2_{4,\phi}(\phi) &= \frac{\phi}{2\pi} + \frac{P^2_4(\cos\theta_s)\sin 2\phi}{40\pi} \end{aligned} \tag{5.49}$$

which can be numerically inverted using Newton's method to find the sampled value of ϕ. Using the above distributions and methods, we can generate particles in our simulation with selected angular distributions that can be compared with the measured data in order to extract the coefficients a_k and e_k.

The simulated relative neutron yields for the eight distributions are shown in figure 5.6 for a reaction where neutrons are emitted directly from the target nucleus, and in figure 5.7 for a reaction where the neutrons are emitted in the decay of a produced daughter nucleus. We see in figure 5.6 that the eight distributions for the direct knockout reaction produce prominent features in the relative neutron yield plots. However, in figure 5.7 we see that these features are washed out for the neutrons produced by the isotropic decay of the daughter nucleus. Any plot of a distribution with $k > 2$ is indistinguishable from the $k = 0$ plot where the daughter nuclei are emitted isotropically. Also note the much lower total yields, and hence poorer statistics, for the neutrons produced in the decay rather than those produced directly, due to the lower kinetic energies of the decay produced neutrons.

Since we simulate particles emitted with each of the eight separate probability density functions, we must be able to recombine them, given values for a_k and e_k, to reconstruct the cross section. We now write our associated Legendre function expansion of the cross section in terms of our

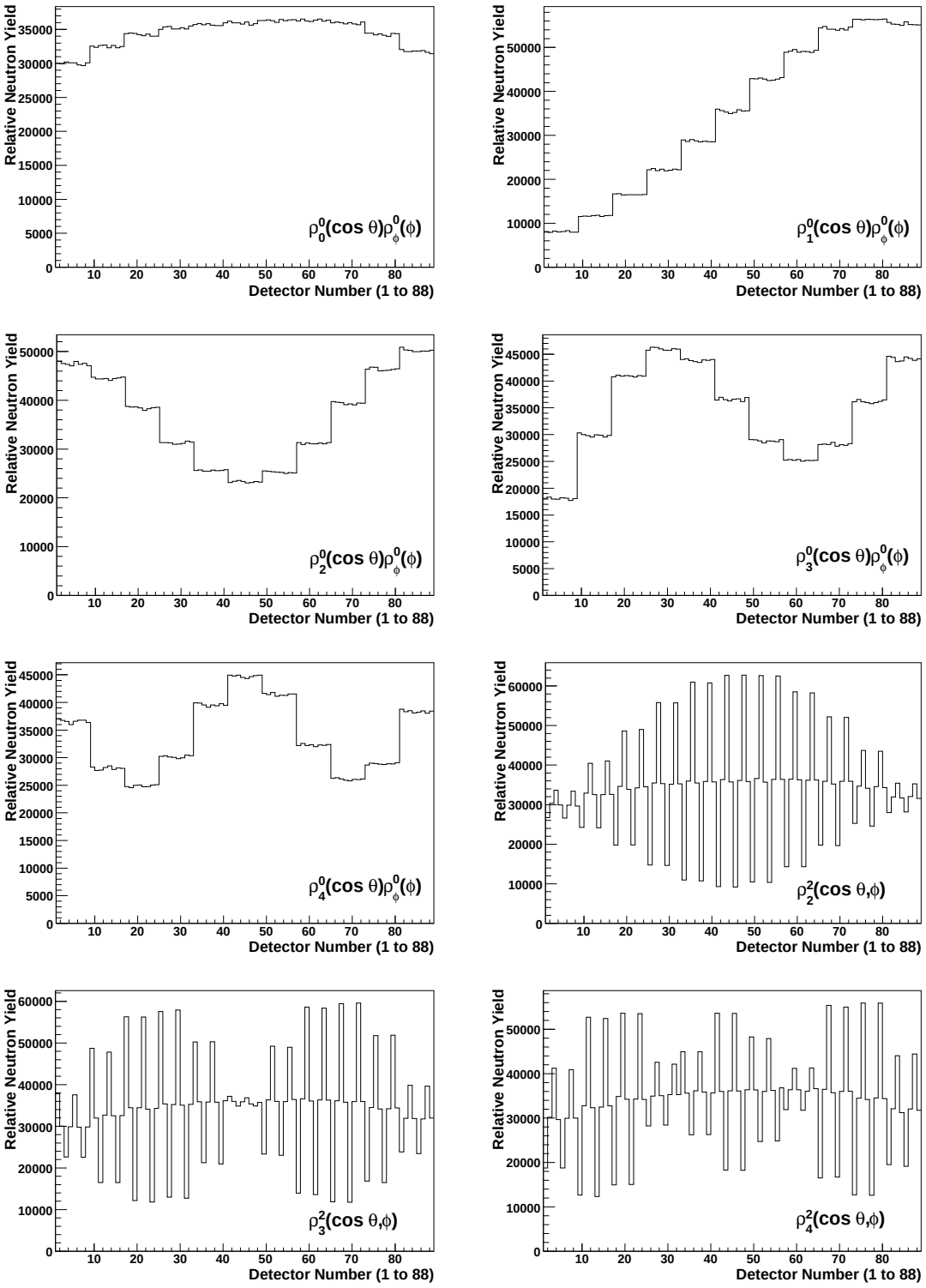

Figure 5.6: Relative neutron yields as a function of detector number from the simulation of the eight angular distributions. The yields are for the single neutron knockout reaction $^7\mathrm{Li} + \gamma \rightarrow n + {}^6\mathrm{Li}$(g.s.). The neutrons were emitted by the simulation with the angular distributions marked on the plots, which include offsets to ensure positive neutron yields at all angles. The photon beam had an energy of 13 MeV and 50 million photodisintegration events were simulated. A 500 keV$_{ee}$ light-output cut has been placed on the data.

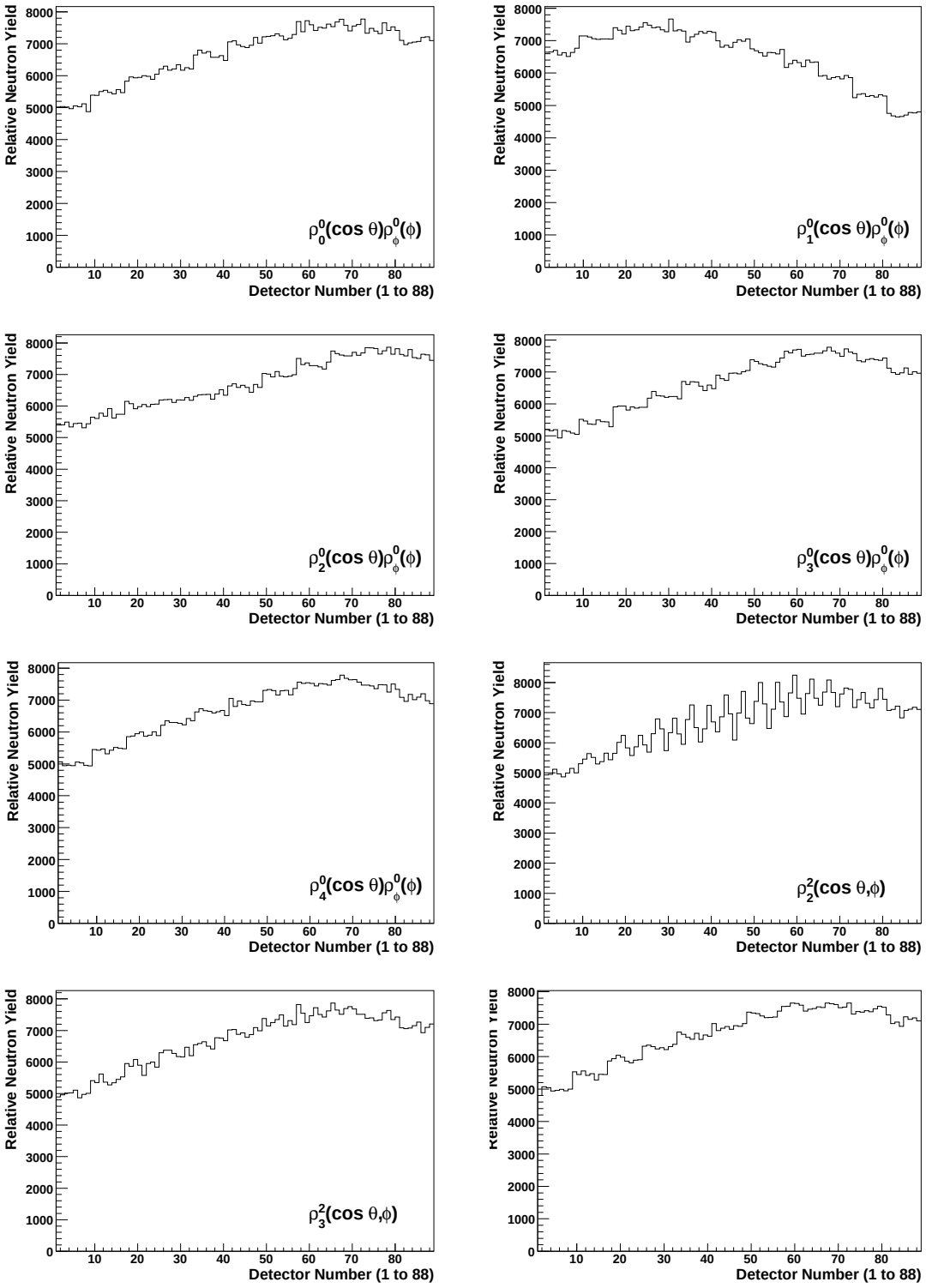

Figure 5.7: Relative neutron yields as a function of detector number from the simulation of the eight angular distributions. The yields are for the reaction $^7\mathrm{Li} + \gamma \rightarrow d + {}^5\mathrm{He}(1.27) \rightarrow d + n + {}^4\mathrm{He}(\mathrm{g.s.})$ where the neutrons are produced in the decay of the daughter nucleus. The deuterons were emitted by the simulation with the angular distributions marked on the plots. The photon beam had an energy of 13 MeV and 50 million photodisintegration events were simulated. A 500 keV_{ee} light-output cut has been placed on the data.

probability density functions

$$\begin{aligned}\frac{d\sigma}{d\Omega}(\theta,\phi) &= \frac{\sigma}{4\pi}\left[1+\sum_{k=1}^{4}a_k P_k^0(\cos\theta)+\sum_{k=2}^{4}e_k P_k^2(\cos\theta)\cos 2\phi\right] \\ &= \frac{\sigma}{4\pi}\left[4\pi\left(1-\sum_{k=1}^{4}a_k-3e_2-6e_3-10e_4\right)\rho_0^0(\cos\theta)\rho_\phi^0(\phi)\right. \\ &\quad \left.+4\pi\sum_{k=1}^{4}a_k\rho_k^0(\cos\theta)\rho_\phi^0(\phi)+12\pi e_2\rho_2^2(\cos\theta,\phi)+24\pi e_3\rho_3^2(\cos\theta,\phi)+40\pi e_4\rho_4^2(\cos\theta,\phi)\right].\end{aligned} \tag{5.50}$$

This equation will be very useful when we compare the simulations with the measured data later in the analysis.

If, instead of trying to isolate the a_k and e_k coefficients by setting all but one to zero, we wish to simulate the angular distribution of the particles given values for a_k and e_k, we can construct another probability density function. Since the cross section is positive by definition, we can easily construct the probability density function

$$\rho(\cos\theta,\phi)=\frac{1}{4\pi}\left[1+\sum_{k=1}^{4}a_k P_k^0(\cos\theta)+\sum_{k=2}^{4}e_k P_k^2(\cos\theta)\cos 2\phi\right] \tag{5.51}$$

for the angular distribution of the emitted particles. In order to sample values for $\cos\theta$ from this distribution we must construct the cumulative distribution function integrated over all ϕ

$$\begin{aligned}C_{\cos\theta}(\cos\theta) &= \int_{-1}^{\cos\theta}\int_0^{2\pi}\rho(\cos\theta',\phi)d\phi d\cos\theta' \\ &= \frac{1}{16}\left[(8-4a_1+a_3)+(8-4a_2+3a_4)\cos\theta+(4a_1-6a_3)\cos^2\theta\right. \\ &\quad \left.+(4a_2-10a_4)\cos^3\theta+5a_3\cos^4\theta+7a_4\cos^5\theta\right]\end{aligned} \tag{5.52}$$

which can be numerically inverted to obtain the sampled value, $\cos\theta_s$. From this we can compute the cumulative distribution function needed to find a sample value of ϕ,

$$\begin{aligned}C_\phi(\phi) &= \frac{\int_0^\phi\rho(\cos\theta_s,\phi')d\phi'}{\int_0^{2\pi}\rho(\cos\theta_s,\phi')d\phi'} \\ &= \frac{\phi}{2\pi}+\frac{\sum_{k=2}^{4}e_k P_k^2(\cos\theta_s)}{4\pi\left[1+\sum_{k=1}^{4}a_k P_k^0(\cos\theta_s)\right]}\sin 2\phi \\ &= \frac{\phi}{2\pi}+\frac{\Sigma(\theta_s)}{4\pi}\sin 2\phi\end{aligned} \tag{5.53}$$

where $\Sigma(\theta_s)$ is the cross section asymmetry. Equations (5.52) and (5.53) can be used together to emit particles with an angular distribution given by a_k and e_k associated Legendre function coefficients.

Using the probability density functions described in this section, and the cumulative distribution functions derived from them, we can add useful angular distributions to the reactions we simulate. Two different kinds of angular distributions have been discussed: the case where we must find a_k and e_k by simulating individual terms of the cross section, and the case where we are given a_k and e_k and we wish to emit particles with the given distribution.

5.5 Validation of the Simulation

The analysis performed in this thesis relies heavily on the simulation in order to correct for the effects of the geometry on the neutron angular distributions due to the neutrons scattering from the target, light guides and other detectors before they reach the detector in question. The simulation is also used to correct for the efficiencies of the neutron detectors, which will likely be no more than 30 % efficient. This section discusses the steps taken to ensure that the neutron detectors are accurately modelled in our Geant4 simulation.

The efficiency of a neutron detector is interwoven with its light-output response discussed in section 4.4.2. In order to eliminate electronic noise, we also eliminate good signals due to low light-output events. We set a threshold, a minimum light-output, and the value of the threshold has a large effect on the efficiency of the detector.

The first measurement of the light output and efficiencies of the neutron detectors in Blowfish was performed at TRIUMF by Sawatzky *et al.* [Kor99, Swa99, Pyw06]. The neutrons used in this measurement were produced from the $p+\pi^- \rightarrow n+\gamma$ reaction. Light output spectra were obtained with neutron kinetic energies from 6 to 12 MeV. The efficiency of the detectors was measured using stopped pions which produce monochromatic, tagged neutrons with energy 8.9 MeV. The light output spectrum due to these tagged neutrons is shown in figure 5.8. The original analysis showed

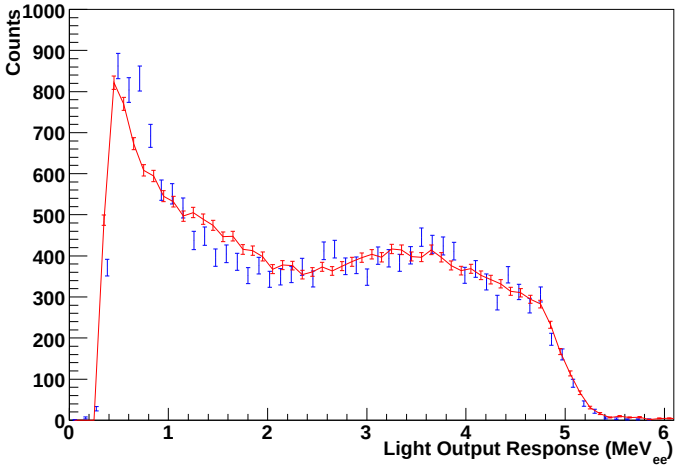

Figure 5.8: Light output spectrum for 8.9 MeV neutrons. Blue points are the measured data for the tagged neutrons at TRIUMF. Red points with line are from a Geant4 simulation of the experimental setup. Figure created using the data from figure 2 of reference [Pyw06].

a 9% difference between the simulation and experiment. The measured efficiency was found to be 0.213 ± 0.001 (stat) ± 0.006 (syst). During the reanalysis of the data by Pywell, a new Geant4 simulation was constructed [Pyw06]. This simulation showed that the detector gains used in the

previous analysis were incorrect. If the threshold is moved from 500 keV$_{ee}$ to 546 keV$_{ee}$, then the simulation reports an efficiency of 0.219 ± 0.001, which is within error of the measured value.

Data was desired at lower neutron energies. Ives measured the light output of the detectors using neutrons produced by a ^{252}Cf radioactive source within an ionisation chamber [Ive03, Pyw06]. This source undergoes spontaneous fission, producing neutrons with known energy distributions. These measurements were very successful in determining the light output spectra for neutron energies between 0.4 and 1.3 MeV but they were not overly successful in determining the absolute efficiency of the detectors due to instrumentation issues. The simulation performed by Ives is consistent with the measured data but the systematic errors on the measured data are too large to make a stronger conclusion.

In order to rectify this situation, we attempted a second measurement. In December of 2005 we made some measurements using the same ^{252}Cf radioactive source. While we built upon the work of Ives and avoided the instrumentation issues he encountered, a new issue arose. The QDC gain anomaly, which is described later in section 6.5 and discussed in great detail in reference [Pyw09a], introduces an apparent distortion into the measurement of light-output spectra. This distortion made the measured detector efficiencies difficult to quantify. We can conclude from the 2005 measurements that the simulation reproduces the measured efficiency with better than 10% uncertainty. A stronger statement is not possible.

It is important to note that the QDC gain anomaly does not appear to affect the measurement of Ives, which was performed using the FastBus QDCs. The subsequent measurement was performed using the VME QDCs, as do all measurements that conclusively demonstrate the QDC gain anomaly.

It is unfortunate that there is no decisive measurement showing that the simulation accurately reproduces the actual detector efficiency at all energies. However, based on the successful TRIUMF measurement and the fair agreement of the two ^{252}Cf measurements, we can conclude that the efficiency is reproduced well enough for the current experiment. Any systematic errors in the efficiency will be taken into account along with the QDC gain anomaly to be discussed later.

5.6 A Note on Physics Lists

The concept of a physics list is very important for a Greant4 simulation. The electromagnetic interactions are considered to be well modelled by Geant4 and, except for some extraordinary cases, the default models are sufficient. However, the hadronic interactions are more involved [Apo08].

Traditionally we have used the LHEP_PRECO_HP physics list to model the Blowfish neutron detector array and all validations of the simulation have been performed with this physics list. This physics list uses parametrised models for the high and low energy interactions which were inherited

from Geant3 [Apo08]. The important flag is 'HP', which indicates that high precision neutron libraries are used. The physics list LHEP is also available without the high precision neutron libraries, but it is unsuitable for simulations of Blowfish.

Unfortunately, the high precision neutron libraries are only defined up to neutron kinetic energy of 20 MeV. Our data taken with photon energies of 30 and 35 MeV produce neutrons with more energy than this. Beyond 20 MeV, Geant4 will default to the LHEP physics list if LHEP_PRECO_HP is being used, which causes an unacceptable deviation from the measured spectra. Instead, we use the QGSP_BERT_HP physics list, which is popular with high energy physics projects [Apo08]. This model will be sufficient for the work performed in this thesis. However, for work requiring more precision with neutrons of kinetic energies greater than 20 MeV, it may be necessary to extend the high-precision neutron physics beyond 20 MeV for the reactions needed to model Blowfish.

In order to aid the above discussion, two plots have been included. Figure 5.9 shows the light output of a simulated detector using the LHEP, LHEP_PRECO_HP and QGSP_BERT_HP physics lists and a photon beam of 15 MeV. Notice that the LHEP_PRECO_HP and QGSP_BERT_HP

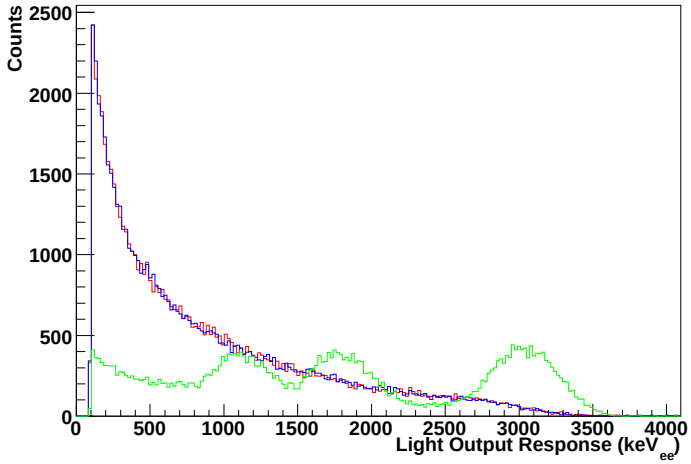

Figure 5.9: Simulated light-output spectra for a photon beam of energy 15 MeV and a natural lithium target. The LHEP_PRECO_HP physics list generated spectrum is red, the QGSP_BERT_HP spectrum is blue and the LHEP spectrum is green.

physics lists produce the same results as they are both using the high-precision neutron libraries and these results agree with the measured spectra. The LHEP physics list produces results that do not agree with measurements.

Figure 5.10 shows the output of the LHEP_PRECO_HP and QGSP_BERT_HP physics lists and a photon beam of 35 MeV. Notice that the LHEP_PRECO_HP physics list breaks down for neutrons with kinetic energy greater than 20 MeV and the resulting light-output spectrum is distorted. The QGSP_BERT_HP physics list does not break down and agrees well with the measured spectra.

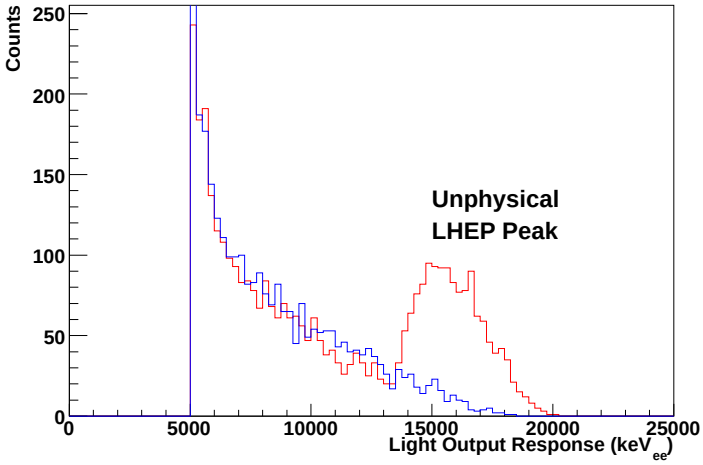

Figure 5.10: Simulated light-output spectra for a photon beam of energy 35 MeV and a ^{6}Li target. The LHEP_PRECO_HP physics list generated spectrum is red and the QGSP_BERT_HP physics list generated spectrum is blue.

Chapter 6

Data Acquisition, Calibration and Reduction

6.1 Data Acquisition

The photodisintegration measurements described in this thesis were performed at HIGS using the Blowfish Neutron Detector Array. The measurements were performed in two separate experiments.

6.1.1 Data Acquisition With Photon Energies Below 16 MeV

The first experiment, with energies below 16 MeV, was performed from the 30th of June to the 3rd of July, 2008. Data were taken at photon energies of 8, 9, 10, 11, 12, 13, 15 and 15.6 MeV for ^{6}Li and 10, 11, 12, 13 and 15 MeV for ^{7}Li. No data were taken at the photon energy of 14 MeV due to lack of time and no ^{7}Li data were taken at 15.6 MeV due to issues with recovering a stable photon beam after a target change. The photon energy of 15.6 MeV was used instead of 16 MeV since it was difficult to achieve photon energies higher than 15 MeV with the accelerator configuration used and a reduction in beam energy was chosen to increase stability. Two array orientations were used for all measurements except ^{6}Li at 10 MeV and ^{7}Li at 10 and 11 MeV. Only one array orientation was used at these energies because of time constraints. The OK-4 planar wiggler and 450 nm mirror set were used to produce linearly polarised photons.

This experiment was the first data taken with Blowfish and a photon beam since February of 2005. This experiment was deemed critical for testing Blowfish after the long upgrade of the HIGS facility. As such, there were a number of issues with the data acquisition system. The system would periodically lose communication between the RTEMS frontend and the VME crate. This would later be traced to the sis1100 VME module, which we replaced with another module from Saskatoon. The gain monitoring system suffered from a timing problem that we were unable to diagnose. As a result, we performed periodic measurements of the detector gains with a radioactive source. The five-paddle flux-monitoring system did not function correctly, although the three-paddle system was used to measure relative flux changes. It was these problems that necessitated a complete rebuild of the trigger electronics for the above 16 MeV experiment. This rebuild was performed by Dr. Pywell.

6.1.2 Data Acquisition With Photon Energies Above 16 MeV

The second experiment, with energies above 16 MeV, was performed from the 1st to the 3rd of October, 2008. Data were taken at photon energies of 20, 25, 30 and 35 MeV for both ^{6}Li and ^{7}Li. Two array orientations were used for the data at 20, 25 and 35 MeV while only one was used at 30 MeV. The OK-5 helical wiggler and 245 nm mirror set were used to produce circularly polarised photons. Linearly polarised photons were not possible at these energies due to the damage that the OK-4 would cause to the FEL mirrors [Wu07]. The reactions were not studied beyond 35 MeV since these were the most energetic photons HIGS could produce at the time of the experiment.

The rebuild of the electronics proved successful. The replacement sis1100 VME module worked without issue. The five-paddle system was able to accurately measure the beam flux. The gain monitoring system worked well, but with one caveat. The pulse generator would periodically lock up and need to be reset. This was not a problem during the day, but the pulse generator would have to be turned off at night. It took some time for the gain monitoring system LEDs and pulse generator to warm up in the morning, and care must be taken when interpreting the gain monitoring system data for the first runs in the morning, including the morning source run.

6.2 Data Calibration

Once the data has been acquired, it must be calibrated in order to make it meaningful. In chapter 4 we described the principles of operation of the data-acquisition system. We now build on that discussion and describe how we compute physically meaningful parameters from the output of the data acquisition system.

6.2.1 QDC Calibration

When calibrated, the QDC gives us the amount of light output by the scintillator. The first step in calibrating the QDC is to find its zero value. In order to maintain linearity, the QDC injects a small amount of charge during data acquisition. This shifts the zero value to a non-zero channel and is known as the pedestal. A pedestal spectrum can be seen in figure 6.1. This pedestal must be subtracted from any QDC measurement in order to ensure a proper zero value.

In section 4.4.2, we determined how to compute the light output of a scintillator for different particles given the energy they deposit. This information is especially useful when calibrating the QDC as it can be used to relate the light output of an electron to that of a neutron.

To calibrate the QDC we measure the spectrum due to gamma rays of known energy. Such a spectrum can be seen in figure 6.2. The edge is due to the maximum amount of energy a single photon can deposit though a single Compton scattering event. This feature is called the Compton

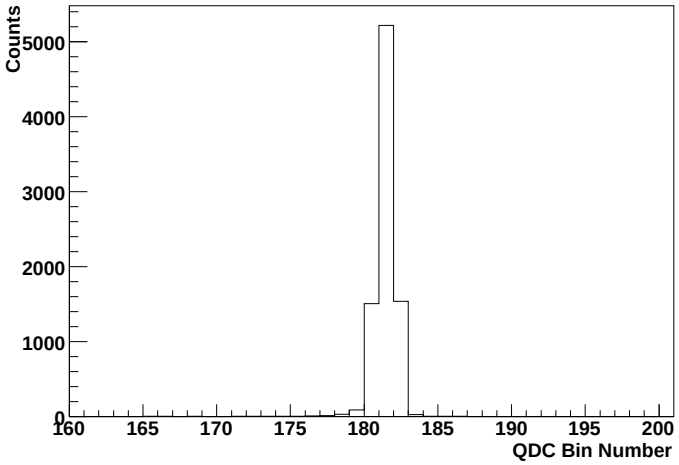

Figure 6.1: Typical pedestal spectrum for a long gate QDC which represents the effective zero value

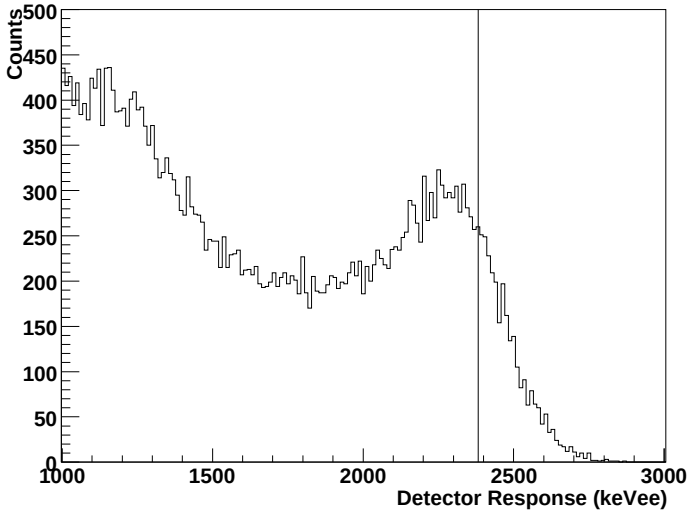

Figure 6.2: Spectrum for a ^{232}Th source as reported by a Blowfish neutron detector with a vertical line at the Compton edge

edge and its energy is given by

$$E_c = \frac{2E_\gamma^2}{m_e c^2 + 2E_\gamma} \tag{6.1}$$

where E_γ is the energy of the photon and m_e is the mass of the electron. Note that photons can undergo multiple scattering causing events with energy deposited greater than the Compton edge.

The Compton edge is determined by finding the inflection point in the spectrum. Using the simulation we can determine a relationship between the inflection point and the actual Compton edge. For instance, the 2.615 MeV gamma rays emitted by ^{232}Th source have a correction factor of 0.9628 ± 0.0002. Due to multiple scattering, this correction factor is dependent on the geometry of a neutron detector.

Once we have found the location of the Compton edge in the QDC spectrum, we know the gain of the neutron detector. We can use the gain monitoring system, described in section 4.4.4, to track this gain over the course of a day.

6.2.2 TDC Calibration

The TDC functions as a stopwatch and gives the amount of time between the start and stop signals. The start signal comes from the accelerator and the stop signal comes from the individual detectors. A raw TDC spectrum can be seen in the top plot of figure 6.3. This spectrum consists primarily of gamma rays from the scattered photon beam and the room background but also contains some neutrons from photodisintegration.

The resolution of the TDC is controlled by the experimenter. For the work of this thesis we set the TDC's full scale range register to 0x5e, giving a resolution of 95.8 ± 0.7 ps/bin. This value was found by using different lengths of cables to create delays between the stop and start signals. The delays were measured using an oscilloscope.

Both the start and stop signals for the TDCs must travel through a number of cables and delays and this causes a constant offset in the TDC spectra. The constant offset can be found by examining the location of the gamma-ray peak in the spectra. Since gamma rays travel at a constant speed, they arrive at the neutron detectors at the same time, causing the sharp peak visible in figure 6.3. We use the time-of-flight of the gamma rays to find the zero of the TDC and convert the TDC spectrum into a time-of-flight spectrum as can be seen on the bottom of figure 6.3.

The detectors are at a fixed distance from the centre of the array. Using this fixed difference and the time-of-flight we can compute the neutron's velocity, v_n. We can then compute the neutron's kinetic energy using

$$K_n = (\gamma - 1)\, m_n c^2 \tag{6.2}$$

where $\gamma = (1 - v_n^2/c^2)^{-1/2}$ and m_n is the neutron's mass.

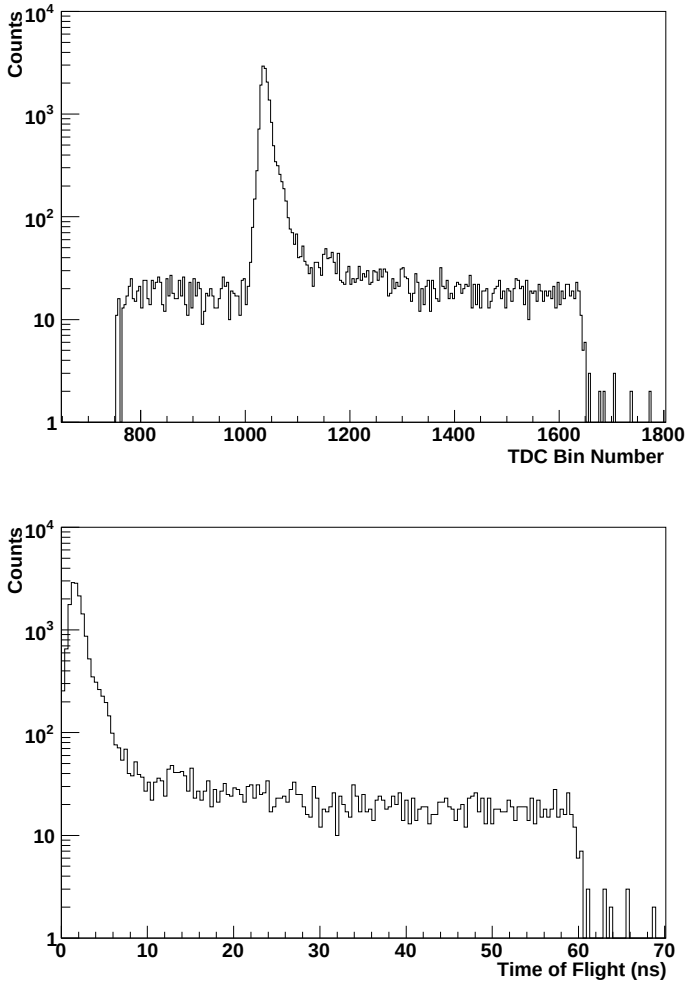

Figure 6.3: Raw TDC spectrum (top) and calibrated time-of-flight spectrum (bottom). Note that the vertical scale is logarithmic.

6.2.3 Pulse-Shape Discrimination Calibration

In section 4.4.5 we discussed how pulse-shape discrimination (PSD) can be used to distinguish between neutron and gamma-ray events. The top of figure 6.4 shows a comparison between the long and short gate QDCs. Note the separation of the two features, one of which is due to gamma-

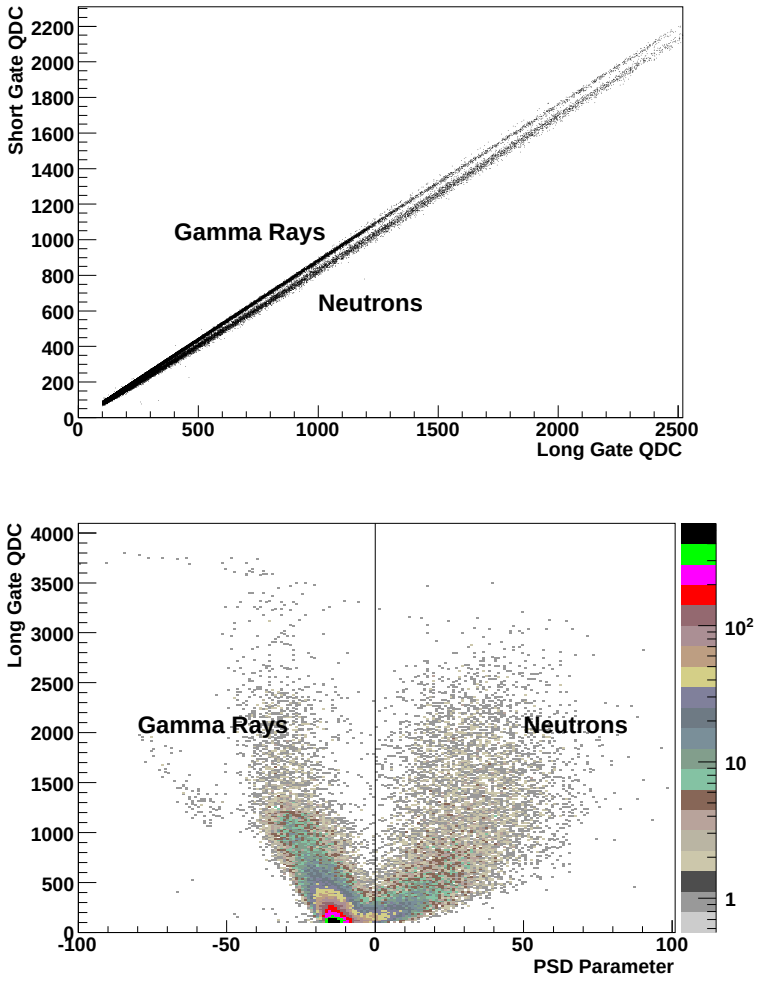

Figure 6.4: Long and short gate QDC scatter plot (top) and a rotated PSD scatter plot (bottom)

ray events and the other which is due to neutron events. In order to make working with the PSD spectrum easier we define the PSD parameter

$$\text{PSD Parameter} = (\text{Long QDC} - \text{Short QDC}) - (\text{PSD Rotation})(\text{Long QDC}) + \text{PSD Offset}. \tag{6.3}$$

We choose the PSD rotation and offset so that all gamma-ray events have a PSD parameter less than zero and most neutron events have a PSD parameter greater than zero. Plotting the PSD parameter and long gate QDC gives us the plot on the bottom of figure 6.4. Note that the neutron

events with low light output get mixed with the gamma-ray events with low light output.

6.3 Data Reduction

Now that we have calibrated the data, we must compensate for the limitations of the hardware and also remove background events. This is done by implementing a series of cuts on the calibrated data discussed in the previous section. A cut is a limit or boundary placed on a quantity, such as the light output, time-of-flight or PSD parameter. Events that have values outside any cut are rejected and only those that pass all cuts are accepted.

6.3.1 Light-Output Cut

Very small light output events are indistinguishable from electronic noise. To ensure that the data acquisition is not swamped, we eliminate these events in hardware by setting a threshold on the discriminators. Since the discriminators are not ideal components, the threshold has a finite width. We use software to eliminate all events below a slightly higher threshold. This software threshold allows us to make a very sharp cut. It is also important to note that since the discriminator makes cuts based on pulse height and the QDC integrates over the signal, the hardware threshold for neutrons will be different than that for gamma rays.

Changing the threshold will change the efficiency of the neutron detector. A higher threshold means less neutron events are counted given the same number of incident neutrons. In fact, some low-energy neutrons will be eliminated altogether if the threshold is too high. The efficiency is accounted for by applying the same software threshold to the simulated data as the measured data.

6.3.2 Time-of-Flight Cut

The time-of-flight can be used to find the kinetic energy of an emitted neutron. It can also be used to eliminate most, but not all, gamma-ray events. Since the neutrons in this experiment travel at a fraction of the speed of light, events with a time-of-flight that is too small must be due to gamma-rays.

Very low-energy neutrons will not be detected by our detectors since they cannot transform sufficient kinetic energy into scintillator light output. By eliminating events with a time-of-flight calculated to be beyond this low-energy cutoff, we can eliminate many of the random, background events. Unfortunately, not all gamma-ray events can be eliminated using a time-of-flight cut since there will be random background events that fall within the acceptance window. We must use PSD to eliminate these events.

6.3.3 Pulse-Shape Discrimination Cut

To eliminate the remaining gamma rays, we must use PSD. The PSD parameter has been setup so that all gamma-ray events have a negative PSD value. If we eliminate all events with negative PSD, we will be left with only neutrons. Figure 6.5 shows the results of such a PSD cut on a time-of-flight spectrum. Note that a time-of-flight cut has already been applied to remove the prompt gamma

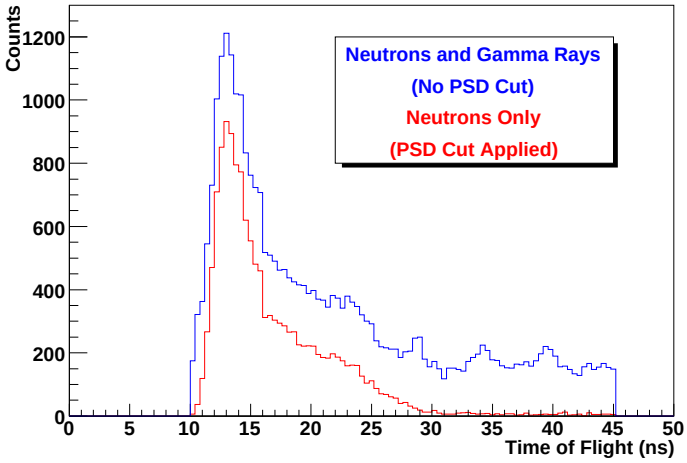

Figure 6.5: Time-of-flight spectrum before and after a PSD cut eliminating all gamma-ray events

rays from Compton scattering.

We must consider the neutrons that are eliminated by the PSD cut. For events with high light output, the PSD cut is nearly perfect. However, for events with low light output, there are many neutron events that will have negative PSD value. These events will be eliminated as they are indistinguishable from gamma-ray events. We must therefore consider the efficiency of the PSD cut. This is done by adding PSD to the Geant4 simulation and applying the same PSD cut to both the simulated data and experimental data.

The efficiency of the PSD cut will also depend on the light output cut. If a low light-output cut is required, then there will be much more dependency on the efficiency of the PSD cut. If a high light-output cut is allowed, then the PSD cut will be nearly perfect.

6.3.4 Multiplicity Cut

The timing of the long and short gate QDCs are common to all channels. It is the particle that arrives first that will start QDC integration. If two particles are detected during the same event, the PSD value of the particle that arrives second will be invalid as the short gate QDC will integrate over too little of the pulse. We do not consider such events since we cannot separate the neutrons

from gamma rays using PSD. This will eliminate some events but we correct for this elimination by also making the same cut on any data generated by the simulation.

6.3.5 The Most Downstream Ring

The Compton scattering cross section is heavily peaked in the forward direction. Therefore the detectors in the most downstream ring, detectors 81 to 88, are exposed to far more Compton scattered photons than any other detectors in Blowfish. Even though the events due to Compton scattered photons are pre-scaled in hardware, the detectors do emit a signal. Since these events are so frequent, the detectors do not necessarily have sufficient time to recover between events. Figure 6.6 shows PSD scatter plots for a detector in the most downstream ring under two different conditions. When the empty target is used, fewer photons are scattered into the detector and we

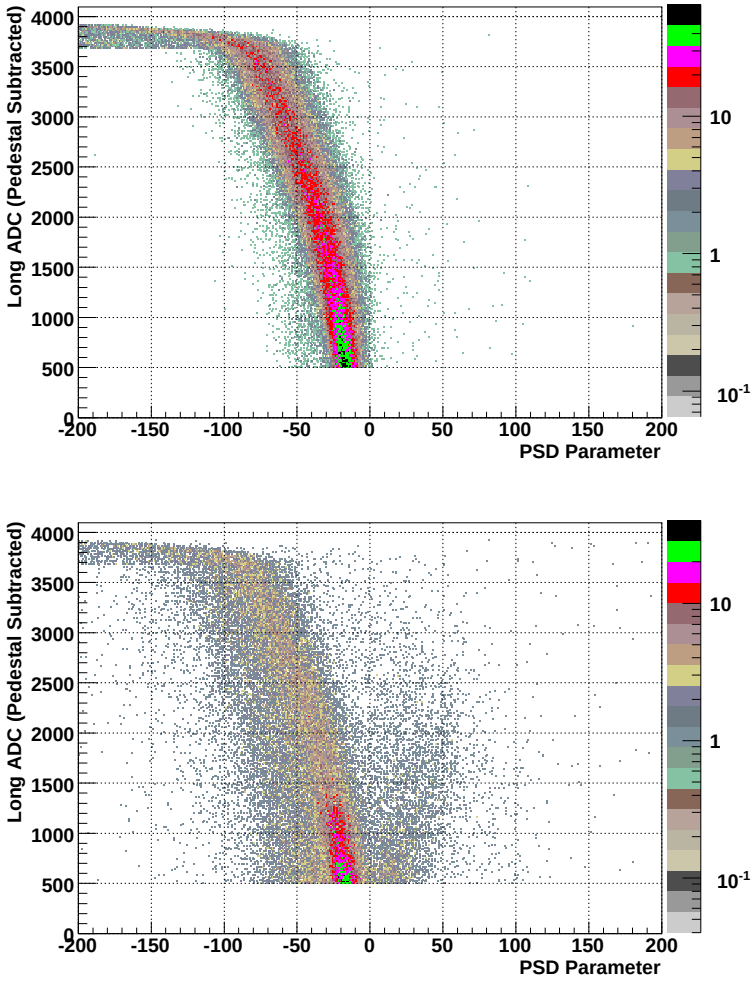

Figure 6.6: PSD scatter plots for detector 82 with the empty target (top) and ^{6}Li target (bottom) and a 13 MeV photon beam

see a clean PSD scatter plot where an extreme majority of particles are due to photon interactions. When the ^{6}Li target is placed inside Blowfish we get the bottom PSD plot. There certainly are some neutrons visible in this plot, but the separation between the neutrons and gamma-ray arms has blurred. It is questionable as to whether or not separation of gamma-ray events and neutron events is valid at any light-output level for the most downstream detectors. As a result, we do not use the eight most downstream detectors in the final analysis. This does not mean that their information is useless as it has proven useful in the preliminary stages of analysis. However, it was decided for these detectors that it is not possible to make a sufficiently accurate computation of the systematic uncertainties for the neutron yields.

6.4 Software

As with any project with large datasets, a number of software applications are required in order to perform the tasks of data acquisition, calibration, reduction and analysis.

In section 4.5.9 we discussed Lucid, the software used to acquire the data. Lucid is excellent for data acquisition because of its simplicity, speed and fault-tolerant nature.

However, we desire to use the ROOT data analysis framework [Bru97] in order to perform the actual analysis, so we must convert our datafiles from the Lucid format to the ROOT format. ROOT has many desirable libraries and abilities that greatly assist our analysis. I wrote RLucid in order to perform this conversion in a principled way [Wur07b]. RLucid links to both the Lucid libraries and the ROOT libraries to facilitate a direct conversion.

Once the data has been converted to the ROOT format, it can be handled by the Blowfish-ROOT Analysis Package [Wur08b]. This package provides software for viewing and calibrating the data as well as the ability to apply some basic cuts. It can be used to find meaningful PSD values, calibrate the TDC starting with the raw spectrum and ending with time-of-flight and neutron kinetic energy spectra, and calibrate the QDC using the gain monitoring system. Figure 6.7 shows the graphical user interface for computing PSD values.

While the Blowfish-ROOT Analysis Package does have some ability to make cuts, more specialised cuts and optimised software were needed. These tasks were performed by writing scripts using the ROOT framework.

Through these software packages, some preexisting, some created for analysing Blowfish-specific data and some created specifically for analysing the data of this thesis, we are able to effectively perform tasks on the data and extract the quantities of interest.

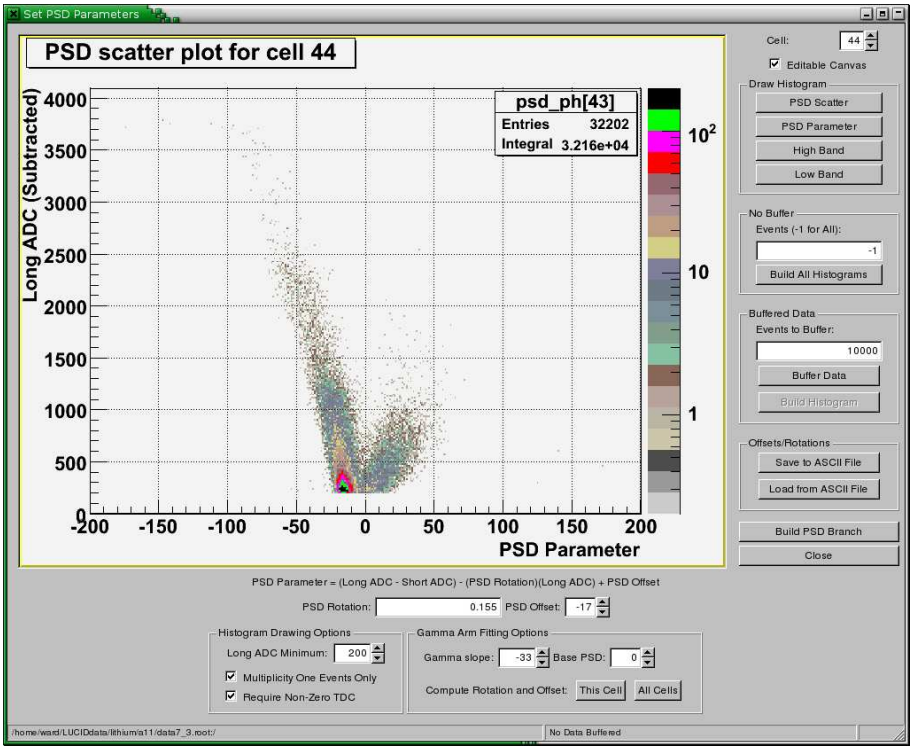

Figure 6.7: Graphical user interface used to find meaningful PSD values. The data are for the natural lithium target with an 11 MeV photon beam and the gamma-ray peak suppressed in hardware.

6.5 The QDC Gain Anomaly

An anomaly in finding the QDC gains was first noted by M. Blackston [Bla07]. He found that the light-output spectra for the neutrons generated from the simulation did not agree with that of the experimental data.

At first one may think that the light output curves reported in section 4.4.2 and the paper [Pyw06] are suspect, but we have the greatest confidence in these values for a number of reasons. First, the values were obtained at two different laboratories, using two different electronics setups, looking at two different energy intervals and using two different neutron sources. Second, the light output curves were compared with those measured by previous researchers [Czi64, Mad78] and our parameterisation fits their data better than their own parameterisations. It is interesting to note that we were unaware of this previous data[1] until our light-output paper was submitted for publication and a referee alerted us to its existence and asked that they be included. It is for these reasons that we have confidence in our light-output curves.

Blackston suggests that the cause for his anomaly was that "the simulation integrated all the energy deposited in a detector and converted it to a value for the light output, whereas the ex-

[1]The trade name of the scintillator used was NE-224, which is identical to BC-505.

periment integrated the charge in a pulse over the long gate that did not completely extend over the entire pulse" [Bla07]. He goes on to say that "for γ-rays, whose shorter decay times allowed almost the entire pulse to be integrated over the long gate, the conditions for the simulation and experiment were very similar and good agreement was found for the detector gains". This is a very interesting supposition that deserves examination in greater detail. However, we can go a step further and find an anomaly in the experimental data without considering the simulation.

Further examination of the data provides more evidence of the anomaly and is discussed in great detail in the internal report [Pyw09a]. Signals from a neutron detector were examined after they passed through a long cable and a short cable in two separate measurements. If the end of the pulse was being clipped, we would expect more signal to be lost when using the long cable due to dispersion. However, the opposite is observed and more signal is lost when using the short cable indicating that we are not clipping the end of the pulse. If we are clipping part of the pulse, it must be the beginning.

We compare the gains found using the 0.968 MeV and 2.614 MeV gamma rays from a ^{232}Th source to those found using the 4.438 MeV gamma rays from an AmBe source and the 1.461 MeV from the decay of ^{40}K in the room background spectra. The gains for detector 10 are plotted in figure 6.8 for these four sources. Notice that for the different sources the gains are not the same

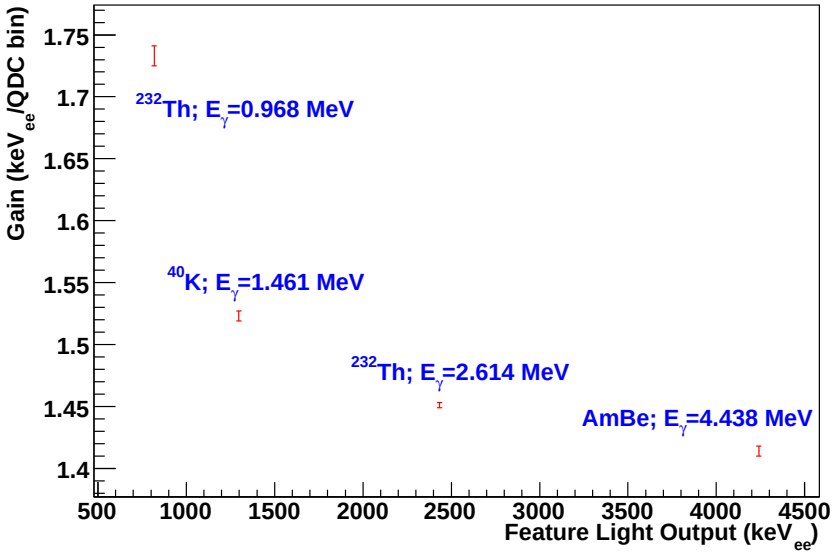

Figure 6.8: The detector gains found from four Compton edges for detector 10 at a PMT voltage of -1706 V [Pyw09a]

even though they should be, a clear indication of the anomaly. Figure 6.9 shows the position of the feature used to calculate these gains as a function of the QDC bin number. Notice that the points lie in a straight line with an offset. The source of this offset is not well understood [Pyw09a]

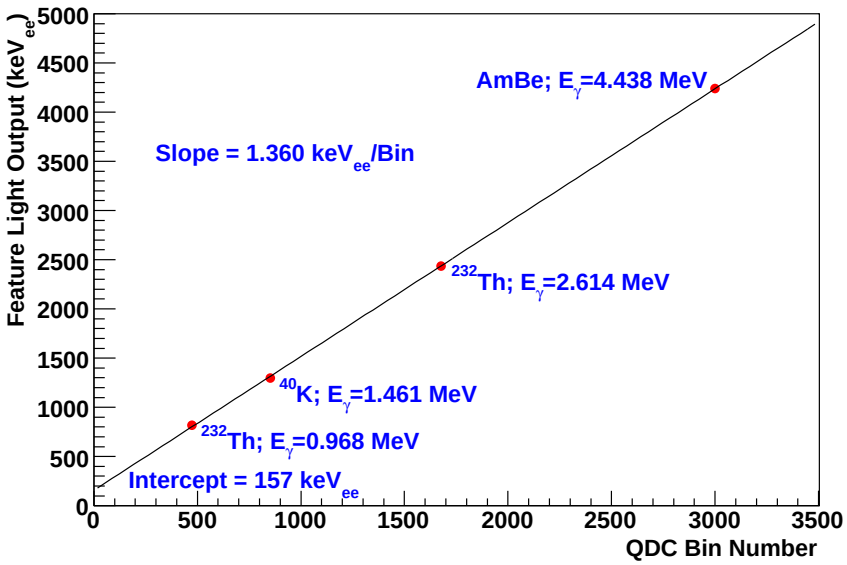

Figure 6.9: The Compton edges as a function of their bin numbers for detector 10 at a PMT voltage of -1706 V [Pyw09a]. Error bars are smaller than markers.

but we can take comfort in the fact that the anomaly appears to be linear in nature, at least for gamma-rays. In order to correct for the anomaly, we extrapolate these results from gamma-rays to neutrons.

We take the method of Blackston and multiply the gains by a constant factor in order to match the experimental light-output spectra with the simulation. We scale the measured spectrum to compensate for the gain anomaly and then make cuts and perform analysis on the scaled spectrum. Ideally we would also subtract the offset, but we lack sufficient information to make a meaningful subtraction and instead assume a larger uncertainty in cuts placed on the light-output spectra.

To compensate for the anomaly, an approximate multiplication factor was chosen and applied to all detectors for individual runs at a single photon energy. Then the measured light output curve was fit to the simulated curve to make small adjustments for individual detectors. In this way, we work around the QDC gain anomaly for the purposes of this thesis.

Chapter 7

Overview of the Data Analysis

The next chapters are all concerned with the analysis of the data. This chapter gives an overview of the techniques used in the analysis. Chapter 8 describes the analysis of the gamma-ray spectra and how they can be used for diagnostics and calculations of absolute cross sections. Chapters 9 and 10 deal with the analysis of the data taken with photon energies less than 16 MeV for ^{6}Li and ^{7}Li respectively, while chapters 11 and 12 present the analysis for photon energies above 16 MeV for ^{6}Li and ^{7}Li respectively. The results of these chapters will all be summarised and discussed in chapter 13.

7.1 Introduction

It is common practice in science and mathematics to reduce a problem to one that has already been solved. That is the approach that will be taken in this analysis. Already two theses concerning deuterium measurements with Blowfish have been completed [Swa05, Bla07]. These researchers measured the angular dependence of the photodisintegration cross section of deuterium. The difficulty in applying their methods to our current analysis is that deuterium has only one reaction channel, while the lithium isotopes have several. By separating the reaction channels in our lithium measurements, we can reduce our analysis to the analysis of individual reaction channels and use the same techniques that were used on deuterium.

We will say a reaction channel is isolatable if it can be isolated from all other reaction channels by making a simple cut on the time-of-flight or light-output spectra. This case is the most like the deuterium measurements and will be discussed in section 7.2.1. If the reaction channels cannot be isolated by a simple cut, we say they are non-isolatable. We must fit simulated spectra to the experimental data in order to separate the reaction channels, and we discuss this method in section 7.2.2. The goals of these sections will be to determine the relative number of neutrons detected by each detector, the relative neutron yield.

Once we have separated the reaction channels by either method, we can apply the existing deuterium analysis methods and determine the angular dependence of the cross section and we discuss this in section 7.3.

Neither of the previous two theses report an absolute cross section so we will need to develop methods of doing so. In section 7.4 we describe three methods that can be used to obtain absolute cross sections. Two of these methods involve comparisons with known cross sections and do not explicitly require knowledge of the photon flux. The third method simply uses the photon flux monitor to measure the flux.

Section 7.5 describes some of the systematic uncertainties encountered and how they are handled in the analysis.

7.2 Separating Reaction Channels

We make use of two methods for separating the reaction channels depending on the situation presented to us. If it is possible to isolate one channel with a simple cut, we use the methods of section 7.2.1. Otherwise, we say the reaction channel is non-isolatable and use the methods of section 7.2.2.

7.2.1 Isolatable Reaction Channels

Our goal is to extract the relative neutron yield for a single reaction channel by placing a simple cut on the data. We will use a light-output cut even though, in principle, a time-of-flight cut would also work. We make this choice because the light-output cut is almost completely insensitive to the experimental geometry, while a time-of-flight cut is extremely sensitive to the geometry. Therefore, the light-output cut will be much less sensitive to systematic uncertainties even though it may increase statistical uncertainties.

We use the PSD cut to eliminate all gamma-ray events so that we can assume that the resulting spectrum is free from background. This technique allows us to neglect the background subtraction which was done by Sawatzky [Swa05].

After applying the light-output and PSD cuts, we are left with neutrons from a single reaction channel. Assuming that all of the neutron detectors in Blowfish have the same efficiency, the number of neutrons detected by each detector will be the relative neutron yield.[1] We may now proceed to extract the angular dependence of the cross section, as discussed in section 7.3.

7.2.2 Non-Isolatable Reaction Channels

Unfortunately, we will not always be able to isolate a single reaction channel with a simple cut. In some cases it may be possible to isolate the reaction channel that produces the most energetic neutrons but not the others. In other cases, it will not be possible to isolate any reaction channels.

[1] Of course, the detectors will all have slightly different efficiencies and this will be accounted for when we discuss systematic uncertainties in section 7.5.

We must separate the reaction channels by fitting simulated spectra to the experimental spectra. The spectra we choose to use for the fitting are the time-of-flight spectra. The light-output spectra lack the detailed features of the time-of-flight spectra, so they are not used. The neutron kinetic energy spectra, which are computed from the time-of-flight spectra, are useful for displaying the results of a fit because they are more intuitive than the time-of-flight spectra. However, the kinetic energy spectra are not as useful for fitting as they depend on the squares of the flight distance, d, and the time-of-flight, t, because the non-relativistic equation for kinetic energy is

$$K = \frac{m_n d^2}{2t^2}. \tag{7.1}$$

Small uncertainties in the flight distance and TDC alignment are amplified and the fits obtained are inferior to the fits obtained using the time-of-flight spectra.

Figure 7.1 shows an example time-of-flight spectrum for data collected with the natural lithium target which we will attempt to separate into reaction channels. The three reaction channel histograms are computed from the Geant4 simulation, while the experimental data and ^{6}Li histograms are from the analysis of the measured data. Let the histograms of the three simulated reaction

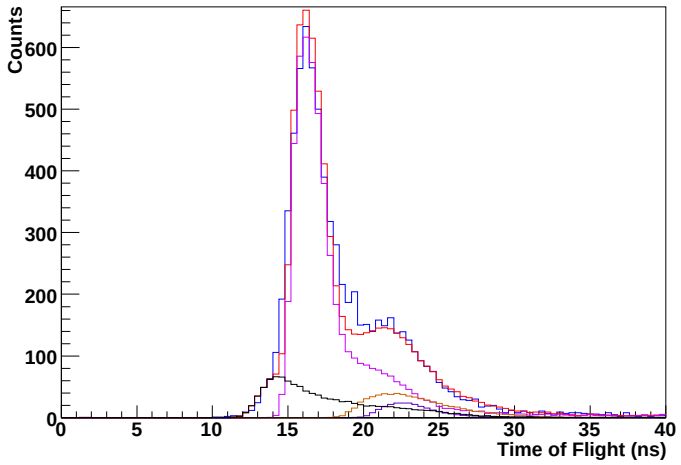

Figure 7.1: Fitting three reaction channels (two purple, one orange) to the experimental data (blue) obtained from detector 44 using the natural lithium target and a 12 MeV photon beam. The black line is the ^{6}Li contribution and the red line is the sum of the fitted reaction channels.

channels be described by the functions $H_1(t)$, $H_2(t)$ and $H_3(t)$, while the measured data and ^{6}Li contributions are described by $H_{exp}(t)$ and $H_{^6\mathrm{Li}}(t)$ respectively. We then define our fitting function

$$f(t; t_{off}, c_1, c_2, c_3) \equiv c_6 H_{^6\mathrm{Li}}(t) + c_1 H_1(t + t_{off}) + c_2 H_2(t + t_{off}) + c_3 H_3(t + t_{off}) \tag{7.2}$$

where t_{off} is a small offset parameter which was found to give better fits since it compensated for slight misalignments between the simulated and measured time-of-flight spectra.[2] The coefficient

[2]This misalignment is possibly due to the QDC gain anomaly discussed in section 6.5 as the anomaly causes

for the ^{6}Li contribution term is given by

$$c_6 \equiv 0.0759 \times \frac{\text{Natural Lithium Target Flux}}{^6\text{Li Target Flux}} \tag{7.3}$$

where the constant multiple is the fraction of ^{6}Li in natural lithium [DeL03]. We can then fit equation (7.2) to $H_{exp}(t)$ to obtain the coefficients c_1, c_2 and c_3 which gives us the relative contribution of each reaction channel. The experimental data can then be divided amongst the various reaction channels. The analysis on the ^{6}Li data proceeds in the same way except there is no need to take into account a contribution from another isotope.

It will not always be possible, even in principle, to separate all the reaction channels. It is clear that we need at least two reaction channels to describe the data in figure 7.1. However, could we describe it with only two? It is not clear from this histogram that the third reaction channel is even necessary. Instead we may have to treat them as a combination of two channels that cannot be separated. Even if we cannot separate individual reaction channels, we can still use a representative sample of reaction channels to create a simulation which reproduces the measured spectra. Such a simulation is useful when extracting absolute cross sections from our data.

In this section we have discussed a method that, with varying success, separates a time-of-flight spectrum into various reaction channels. This method is not as ideal as the isolatable method and will suffer from greater systematic uncertainties. However, it will allow us to say a great deal about the individual reaction channels under consideration.

7.3 Angular Dependence of the Cross Sections

Once we have computed the relative neutron yields for the different reaction channels we can obtain the angular dependence of their cross sections. We do this by comparing simulations of the processes in question to the experimental data. Instead of comparing spectra, as we did when discussing non-isolatable reaction channels, we compare relative neutron yields.

We discussed how the angular distributions were included in the the simulation in section 5.4. We related the cross section to these angular distributions in equation (5.50), which has been slightly simplified here,

$$\begin{aligned} \frac{d\sigma}{d\Omega}(\theta,\phi) &= \sigma\left[\left(1-\sum_{k=1}^{4} a_k - 3e_2 - 6e_3 - 10e_4\right)\rho_0^0(\cos\theta)\rho_\phi^0(\phi)\right. \\ &\quad \left. + \sum_{k=1}^{4} a_k\rho_k^0(\cos\theta)\rho_\phi^0(\phi) + 3e_2\rho_2^2(\cos\theta,\phi) + 6e_3\rho_3^2(\cos\theta,\phi) + 10e_4\rho_4^2(\cos\theta,\phi)\right]. \end{aligned} \tag{7.4}$$

gamma-ray photons, which are used to align the TDC spectra, to have different modeled responses than neutrons. Another possible explanation is that the simplistic algorithm for determining a hit time needs to be reconsidered. Since the addition of t_{off} (which can have values from zero to a few nano-seconds) proved to be a simple and highly effective solution to the misalignment issue, a detailed analysis of the TDC alignments was not performed.

We can run the simulation with each of the eight angular distributions and match the output to the experimental data in order to extract a_k to e_k. At this point we will not concern ourselves with the absolute cross section, σ, but only the angular distributions. Methods for determining σ will be discussed in section 7.4.

If we had an ideal, point target and ideal detectors with infinitesimal solid angles and zero mass, we would not need to use a simulation but could fit equation (7.4) to the data directly. However, the geometry of the apparatus will influence the detector output. Neutrons can scatter within the target, scatter from the light guide into the scintillator and scatter from one detector into the next. We use the simulation described in chapter 5 to account for all these effects.

The ideal number of particles passing through each detector is given by

$$\frac{dN_{scat}}{d\Omega}(\theta,\phi) = \Phi N \ell \frac{d\sigma}{d\Omega}(\theta,\phi) \tag{7.5}$$

where Φ is the photon flux, N is the atomic density and ℓ is the length of the target. We can think of the geometry as applying a convolution to the emitted neutron distributions, $G[\rho]$. The number of neutrons passing through the infinitesimal detector after corrections for geometry is

$$G\left[\frac{dN_{scat}}{d\Omega}(\theta,\phi)\right] = \Phi N \ell G\left[\frac{d\sigma}{d\Omega}(\theta,\phi)\right]. \tag{7.6}$$

Our detectors are not infinitesimal so we must integrate over their solid angles, Ω_d. They are also not 100 % efficient so we must apply their efficiencies, ϵ, which we assume are all the same.[3] The number of neutrons detected by detector d is given by

$$\begin{aligned}
N_d &= \epsilon \int_{\Omega_d} G\left[\frac{dN_{scat}}{d\Omega}(\theta,\phi)\right] d\Omega \\
&= \epsilon \Phi N \ell \int_{\Omega_d} G\left[\frac{d\sigma}{d\Omega}(\theta,\phi)\right] d\Omega \\
&= \epsilon \Phi N \ell \sigma \left[\left(1 - \sum_{k=1}^{4} a_k - 3e_2 - 6e_3 - 10e_4\right) \int_{\Omega_d} G\left[\rho_0^0(\cos\theta)\rho_\phi^0(\phi)\right] d\Omega \right. \\
&\quad + \sum_{k=1}^{4} a_k \int_{\Omega_d} G\left[\rho_k^0(\cos\theta)\rho_\phi^0(\phi)\right] d\Omega + 3e_2 \int_{\Omega_d} G\left[\rho_2^2(\cos\theta,\phi)\right] d\Omega \\
&\quad \left. + 6e_3 \int_{\Omega_d} G\left[\rho_3^2(\cos\theta,\phi)\right] d\Omega + 10e_4 \int_{\Omega_d} G\left[\rho_4^2(\cos\theta,\phi)\right] d\Omega \right].
\end{aligned} \tag{7.7}$$

Let N_{dk}^p be the number of neutrons detected by the simulated detector d for the probability distribution function with appropriate indices k and p. If N_{sim} is the number of simulated photodisintegration events, which we keep the same between all comparable simulations, and ϵ^s is the efficiency of the simulated detectors, then

$$N_{dk}^p = \epsilon^s N_{sim} \int_{\Omega_d} G\left[\rho_k^p(\cos\theta,\phi)\right] d\Omega. \tag{7.8}$$

[3] We assume this until we estimate systematic uncertainties in section 7.5.

We can define A to be an overall constant and write

$$\begin{aligned} N_d &= A\left[\left(1-\sum_{k=1}^{4}a_k-3e_2-6e_3-10e_4\right)N_{d0}^0\right. \\ &\quad \left.+\sum_{k=1}^{4}a_kN_{dk}^0+3e_2N_{d2}^2+6e_3N_{d3}^2+10e_4N_{d4}^2\right]. \end{aligned} \tag{7.9}$$

By performing eight simulations with the eight distributions for the same number of photodisintegration events and finding the neutron yields for each detector, we can fit the right hand side of equation (7.9) to the measured neutron yields in order to find the coefficients A, a_k and e_k.

Notice that $A = \epsilon\Phi N\ell\sigma/\epsilon^s N_{sim}$. Imagine that we fit equation (7.9) to the data and obtain values for A, a_k and e_k for two separated reaction channels, r_1 and r_2. Let us denote the two values of A as A_{r_1} and A_{r_2}, and the cross sections as σ_{r_1} and σ_{r_2}. Note that Φ, N, ℓ and N_{sim} are the same for both reaction channels so, assuming that the simulated detectors have the same efficiencies as the actual detectors, we can write

$$\frac{\sigma_{r_1}}{\sigma_{r_2}} = \frac{A_{r_1}}{A_{r_2}} \tag{7.10}$$

which tells us that we can find relative cross sections for different reaction channels using the A values found in our fitting function, equation (7.9).

7.4 Absolute Cross Sections

This section presents three methods for obtaining the absolute photoneutron cross sections of the lithium isotopes, given knowledge of the angular dependence of the differential cross section. Each of these methods has advantages and disadvantages. Sometimes missing data, due either to equipment failure or time constraints, makes one of these methods impossible for a given isotope at a given photon energy. Using all three methods, we can obtain values for the absolute photoneutron cross sections under examination. This section describes the methods but does not discuss their use in practice; that is discussed in later analysis chapters.

7.4.1 Compton Scattering Comparison Method

We describe a technique for measuring the absolute cross section without explicitly measuring the photon beam flux. Instead we perform a comparison with the Compton scattering cross section which is well understood and can be measured using our neutron detectors when we do not reject gamma-ray events in hardware. In such a measurement, we accept events resulting from neutrons from photodisintegration and gamma-rays from the Compton scattering of the photon beam.

While the detectors used in our measurements are optimised for neutron detection and are not ideal for detecting gamma-ray photons, they are still able to detect gamma-rays. These gamma-rays

can be from photons scattered from the target by the process of Compton scattering or background from the environment. A sizeable majority of the photons detected will be from the scattered beam and these photons carry with them information about the flux of the photon beam.

Let $\frac{d\sigma_\gamma}{d\Omega}$ be the cross section for the processes that scatter photons into the target. The number of detected gamma-ray photons is given by

$$N_{d,\gamma} = \epsilon_\gamma \Phi N \ell \int_{\Omega_d} G_\gamma \left[\frac{d\sigma_\gamma}{d\Omega}(\theta,\phi) \right] d\Omega. \tag{7.11}$$

For neutron events we can write $\frac{d\sigma_n}{d\Omega} = \sigma_n \rho(\cos\theta,\phi)$ where $\rho(\cos\theta,\phi)$ is the neutron emission angle probability density function. For a single reaction channel this is given by equation (5.51). For multiple reaction channels, it is the sum of the individual angle probability density functions weighted with the relative cross sections for each reaction channel. The number of detected neutrons is then

$$N_{d,n} = \epsilon_n \Phi N \ell \sigma_n \int_{\Omega_d} G\left[\rho(\cos\theta,\phi)\right] d\Omega. \tag{7.12}$$

Notice that we use different efficiencies for photons and neutrons, ϵ_γ and ϵ_n. We divide equation (7.12) by (7.11) and solve for the absolute neutron cross section,

$$\sigma_n = \frac{\epsilon_\gamma}{\epsilon_n} \frac{N_{d,n}}{N_{d,\gamma}} \frac{\int_{\Omega_d} G_\gamma \left[\frac{d\sigma_\gamma}{d\Omega}(\theta,\phi) \right] d\Omega}{\int_{\Omega_d} G\left[\rho(\cos\theta,\phi)\right] d\Omega} \tag{7.13}$$

noting that the flux of the beam and the target density and length have cancelled. We have eliminated systematic uncertainties due to uncertainty in the length of the target and in measuring the photon flux. We use the Geant4 simulation discussed in chapter 5 to evaluate the geometry-affected parts, $\int_{\Omega_d} G_\gamma \left[\frac{d\sigma_\gamma}{d\Omega}(\theta,\phi) \right] d\Omega$ and $\int_{\Omega_d} G\left[\rho(\cos\theta,\phi)\right] d\Omega$.

The simulation to evaluate $\int_{\Omega_d} G_\gamma \left[\frac{d\sigma_\gamma}{d\Omega}(\theta,\phi) \right] d\Omega$ is straight forward. We emit photons in a beam that simulates the HIGS beam and these photons are incident on a target with atomic density N^s and length ℓ^s. The flux of the simulated photon beam is Φ^s and has units of photons per simulation; it is the number of photons emitted. The differential cross section for the interactions of photons with matter at the energies of interest are well known. If we assume that the simulation geometry closely matches the experimental geometry, we can write the gamma-ray yields for the simulated detectors as

$$N^s_{d,\gamma} = \epsilon^s_\gamma \Phi^s N^s \ell^s \int_{\Omega_d} G_\gamma \left[\frac{d\sigma_\gamma}{d\Omega}(\theta,\phi) \right] d\Omega. \tag{7.14}$$

The evaluation of $\int_{\Omega_d} G\left[\rho(\cos\theta,\phi)\right] d\Omega$ proceeds using a slightly different method. We emit the neutrons directly using the angular distributions and relative cross sections found using the methods of section 7.3. Once we have determined the parameters a_k and e_k and the relative cross sections for the reaction channels of interest, we can simulate the full spectrum of emitted neutrons using the techniques described in section 5.4. The number of neutrons detected by a simulated neutron detector is then

$$N^s_{d,n} = \epsilon^s_n N_{sim} \int_{\Omega_d} G\left[\rho(\cos\theta,\phi)\right] d\Omega \tag{7.15}$$

where N_{sim} is the number of simulated photodisintegration events and we have assumed again that Geant4 is able to accurately simulate the neutrons as they pass through the geometry of the simulation. It is important to note at this point that we have not assumed the efficiencies of the simulated neutron detectors are equal to those of the actual detectors.

We can now divide equation (7.14) by equation (7.15) to obtain

$$\frac{\int_{\Omega_d} G_\gamma \left[\frac{d\sigma_\gamma}{d\Omega}(\theta,\phi)\right] d\Omega}{\int_{\Omega_d} G\left[\rho(\cos\theta,\phi)\right] d\Omega} = \frac{\epsilon_n^s}{\epsilon_\gamma^s}\frac{N_{d,\gamma}^s}{N_{d,n}^s}\frac{N_{sim}}{\Phi^s N^s \ell^s} \tag{7.16}$$

which, assuming the simulation accurately reproduces the effects of geometry on the particle distributions, we can combine with equation (7.13) to find

$$\sigma_n = \frac{N_{sim}}{\Phi^s N^s \ell^s}\frac{\epsilon_\gamma}{\epsilon_n}\frac{\epsilon_n^s}{\epsilon_\gamma^s}\frac{N_{d,n}}{N_{d,\gamma}}\frac{N_{d,\gamma}^s}{N_{d,n}^s} \tag{7.17}$$

If we assume that the ratio of the efficiencies for the simulation is equal to the actual ratio of efficiencies,

$$\frac{\epsilon_\gamma^s}{\epsilon_n^s} = \frac{\epsilon_\gamma}{\epsilon_n}, \tag{7.18}$$

then we can find the total, absolute cross section for the considered reaction channels

$$\sigma_n = \frac{N_{sim}}{\Phi^s N^s \ell^s}\frac{N_{d,n}}{N_{d,n}^s}\frac{N_{d,\gamma}^s}{N_{d,\gamma}}. \tag{7.19}$$

Notice that Φ^s and N_{sim} are simply the number of photons emitted in the gamma-ray simulation and the number of neutrons emitted in the photodisintegration simulation. The simulated length of the target is exactly $\ell^s = 12.7$ cm and its atomic density in the simulation is $N = 0.07693$ mol/cm^3 for both isotopes. Using Avogadro's number, 6.022×10^{23} mol^{-1}, we can evaluate these constants to obtain

$$\sigma_n = (170\bar{0}\text{ mb})\frac{N_{sim}}{\Phi^s}\frac{N_{d,n}}{N_{d,n}^s}\frac{N_{d,\gamma}^s}{N_{d,\gamma}} \tag{7.20}$$

where mb, or milibarn, is the unit of cross section (1 mb = 10^{-27} cm^2). What is significant about this method for finding the cross section is that no independent instrument is needed to find the photon flux, such as the three-paddle or five-paddle monitor systems. This implies that a dead-time correction is not required, although a rate-dependent correction may be. Also, any systematic uncertainties resulting from uncertainty in the actual target length or density have been removed.

Equation (7.20) will give a result for each of the neutron detectors. A final result can be obtained by performing a weighted average of each detector. Even with low statistics in each neutron detector, the overall statistics for the entire array are good. With 88 neutron detectors we have almost two orders of magnitude better statistics when the array is considered as a whole. This method is expected to work best for low Z materials, such as lithium, since the Compton scattering cross section has a linear dependence on Z due to the assumption that the photons are interacting with quasi-free electrons.

7.4.2 Isotope Neutron Yield Comparison Method

For measurements with photon energies near the ^{7}Li photoneutron threshold, the ^{7}Li cross section is small but the ^{6}Li cross section is appreciable. At these photon energies, the photodisintegration of ^{6}Li produces neutrons with appreciably more energy than that of the photodisintegration of ^{7}Li. We can use knowledge of the ^{6}Li photoneutron cross section to compute the ^{7}Li photoneutron cross section due to the 7.58% concentration of ^{6}Li in the natural lithium target.

This method is based on making two cuts; in practice we use cuts on the light-output spectra. The first cut isolates the ^{6}Li contribution due it its more energetic neutrons. This cut is used to find the photon flux in terms of neutron yields. A second cut is then made which includes contributions from both ^{7}Li and ^{6}Li. We can eliminate the need for flux monitoring using the first cut and we can solve for the photoneutron cross section of ^{7}Li in terms of the photoneutron cross section of ^{6}Li.

For the first cut, used to isolate the ^{6}Li reaction, we write the measured neutron yield as per equation (7.12),

$$N_d' = \epsilon' \Phi N_6 \ell \sigma_6 \int_{\Omega_d} G\left[\rho_6(\cos\theta, \phi)\right] d\Omega, \tag{7.21}$$

and the simulated neutron yield as per equation (7.15),

$$N_{d,6}'^s = \epsilon'^s N_{sim} \int_{\Omega_d} G\left[\rho_6(\cos\theta, \phi)\right] d\Omega, \tag{7.22}$$

where σ_6 and $\rho_6(\cos\theta, \phi)$ are the absolute cross section and the angular distribution of the photoneutrons from ^{6}Li and $N_6 = 0.0759N$ is the atomic density of ^{6}Li in the target. We are able to isolate the experimental constants,

$$\Phi N \ell = \frac{1}{0.0759} \frac{\epsilon'^s}{\epsilon'} \frac{N_{sim}}{\sigma_6} \frac{N_d'}{N_{d,6}'^s} \tag{7.23}$$

so that we may eliminate them later. Here it is important to note that the efficiency of a neutron detector is a function of energy. However, we can also consider the efficiency to be a single constant if the neutron kinetic energy spectrum is known, as is the case in this calculation; we can say that ϵ' is the efficiency of the neutron detector for the photoneutron kinetic energy distribution of ^{6}Li for this cut.

For the second cut we must take into account both the ^{6}Li and ^{7}Li contributions. The number of particles passing through solid angle $d\Omega$ is

$$\frac{dN_{scat}}{d\Omega}(\theta, \phi) = \Phi N_6 \ell \frac{d\sigma_6}{d\Omega}(\theta, \phi) + \Phi N_7 \ell \frac{d\sigma_7}{d\Omega}(\theta, \phi) \tag{7.24}$$

where $N_6 = 0.0759N$ and $N_7 = 0.9241N$, and $\frac{d\sigma_6}{d\Omega}(\theta, \phi)$ and $\frac{d\sigma_7}{d\Omega}(\theta, \phi)$ are the differential cross sections for the photoneutrons from ^{6}Li and ^{7}Li respectively. We compute the neutron yields for this cut to be

$$N_d = (0.0759)\epsilon_6 \Phi N \ell \sigma_6 \int_{\Omega_d} G\left[\rho_6(\cos\theta, \phi)\right] d\Omega + (0.9241)\epsilon_7 \Phi N \ell \sigma_7 \int_{\Omega_d} G\left[\rho_7(\cos\theta, \phi)\right] d\Omega. \tag{7.25}$$

The effects of the geometry on the angular distributions can once again be handled by the simulation with

$$N_{d,6}^{s} = \epsilon_{6}^{s} N_{sim} \int_{\Omega_d} G\left[\rho_6(\cos\theta, \phi)\right] d\Omega \tag{7.26}$$

and

$$N_{d,7}^{s} = \epsilon_{7}^{s} N_{sim} \int_{\Omega_d} G\left[\rho_7(\cos\theta, \phi)\right] d\Omega \tag{7.27}$$

where we perform two simulations that take into account only the photoneutrons from their respective isotopes. Note that the simulation for ^{6}Li is the same as the one used in the first cut but with the second cut employed, giving different yields and efficiency. We can substitute equations (7.23), (7.26) and (7.27) into equation (7.25) to eliminate the flux and dependence on geometry and find

$$N_d = \left(\frac{N_d'}{N_{d,6}'^{s}}\right)\left[\left(\frac{\epsilon'^{s}}{\epsilon'}\frac{\epsilon_6}{\epsilon_6^{s}}\right) N_{d,6}^{s} + \left(\frac{0.9241}{0.0759}\right)\left(\frac{\epsilon'^{s}}{\epsilon'}\frac{\epsilon_7}{\epsilon_7^{s}}\right)\frac{\sigma_7}{\sigma_6} N_{d,7}^{s}\right]. \tag{7.28}$$

We now assume that the simulation is able to accurately model the detector efficiencies and take

$$\frac{\epsilon'^{s}}{\epsilon'}\frac{\epsilon_6}{\epsilon_6^{s}} = \frac{\epsilon'^{s}}{\epsilon'}\frac{\epsilon_7}{\epsilon_7^{s}} = 1. \tag{7.29}$$

We solve for the absolute photoneutron cross section of ^{7}Li and obtain

$$\sigma_7 = \sigma_6 \left(\frac{0.0759}{0.9241}\right)\left(\frac{1}{N_{d,7}^{s}}\right)\left[\frac{N_d}{N_d'} N_{d,6}'^{s} - N_{d,6}^{s}\right]. \tag{7.30}$$

Using this technique, we are able to calculate the ratio of absolute photoneutron cross sections for the two isotopes without directly making use of a photon flux monitor.

7.4.3 Photon Flux Monitor Method

Given an accurate measurement of the photon flux, we can compute the cross section directly. The three-paddle flux monitoring system was not designed to provide an accurate measurement of the absolute flux but acts only as a relative flux monitor between experimental runs at the same photon energy. The five-paddle flux monitoring system, on the other hand, was designed to provide an absolute flux measurement and its design, testing and application to this purpose are described in detail in reference [Pyw09b].

The cross section is related to the neutron yields for a detector by

$$\sigma_n = \frac{N_{d,n}}{\epsilon_n \Phi N \ell \int_{\Omega_d} G\left[\rho(\cos\theta, \phi)\right] d\Omega} \tag{7.31}$$

where we have rearranged equation (7.12). We still must incorporate a simulation to account for the effect of the experimental geometry on the angular distribution of the neutrons. Given N_{sim} emitted neutrons and $N_{d,n}^{s}$ neutrons detected by the simulation, we can rearrange equation (7.15) and write

$$\epsilon_n \int_{\Omega_d} G\left[\rho(\cos\theta, \phi)\right] d\Omega = \frac{N_{d,n}^{s}}{N_{sim}} \tag{7.32}$$

where we have assumed the the efficiency of the actual detector is equal to the efficiency of the simulated detector. This allows us to calculate the absolute cross section by

$$\sigma_n = \frac{N_{sim}}{\Phi N \ell} \frac{N_{d,n}}{N^s_{d,n}} \tag{7.33}$$

which requires explicit knowledge of the beam flux, Φ, the target atomic density, N, and the target length, ℓ. Uncertainties in Φ and ℓ will introduce systematic uncertainties into the calculation.

7.5 Systematic Uncertainties

7.5.1 Introduction

Even more important than the final value of a quantity is an estimate of the uncertainty in that value. Photonuclear physics has been plagued by measurements which do not agree with each other within their stated uncertainties. It is therefore critical that we estimate reasonable uncertainties for our measurements.

The first source of uncertainty is from statistics. If we have a neutron yield, N, in a detector then the statistical uncertainty in the yield is given by Poisson statistics as $\sqrt{N}$. The relative uncertainty is $\frac{\sqrt{N}}{N} = \frac{1}{\sqrt{N}}$ which becomes smaller as N becomes larger. Therefore the relative statistical uncertainty can be reduced simply by taking more data. In this thesis, we have tried to use our limited experimental time wisely in order to have small statistical uncertainties, while ensuring that we collected data at as many different energies and array configurations as possible.

The systematic uncertainties, on the other hand, are not as simple. We extract our neutron yields using several spectra recorded by our instruments: light output, time-of-flight and PSD parameter. Placing cuts on each of these spectra results in uncertainties in the measured neutron yields. There are also geometric aspects such as target, detector and beam alignments. These effect the neutron yields of the detectors. The photon flux monitors have associated uncertainties that affect the ^{6}Li subtraction from the ^{7}Li data and absolute flux measurements. The algorithm for separating non-isolatable reaction channels described in section 7.2.2 will introduce uncertainties into the neutron yields for individual reaction channels.

Each source of uncertainty is discussed below.

7.5.2 Light-Output Cut

The light-output spectra contain very important sources of experimental uncertainty when computing cross sections. It is intimately connected with the efficiency of the detector as described in section 5.5. A light-output spectrum is also influenced by the QDC gain anomaly described in section 6.5. Small uncertainties in the light-output cut can have large effects on the efficiency.

We estimate the uncertainty in neutron yields due to the light-output spectra by using a 3% uncertainty in the light-output cut as in the analysis of Blackston [Bla07]. It is felt that this value is reasonable in light of the QDC gain anomaly.

7.5.3 Pulse-Shape Discrimination Cut

PSD is not perfect. Above a certain light output it gives excellent discrimination between gamma rays and neutrons. Below this light output the neutrons and gamma rays get mixed together and are impossible to separate. In this region we use the simulation to estimate the efficiency of the PSD cut. We will estimate the uncertainty due to PSD by applying an uncertainty of the PSD cut of ± 2 channels independently to both the measured PSD spectrum and the PSD spectrum from the simulation.

The value of ± 2 channels stems from the observation that most neutrons that have negative PSD value are only slightly negative. By increasing the psd cut to a positive value, the neutron yield goes down because we are loosing additional neutrons. By decreasing the psd cut to a negative value, the neutron yield goes up as we are including more neutrons, but we are also mistakenly including gamma-rays as neutrons.

7.5.4 Time-of-Flight Cut

The leading and trailing edges of the window were straightforward to determine. Little uncertainty is expected due to the time-of-flight cut.

7.5.5 Photon Flux

The photon flux is used in order to account for the ^{6}Li contribution to the ^{7}Li data and to measure absolute cross sections. The uncertainty in the flux for the three-paddle system is taken to be 8%. This number was found by comparing the neutron yields of the detectors in the centre ring, at azimuthal angle 45°, divided by the output of the three-paddle system at two array orientations for several different energies. We will use an uncertainty of 2% for the five-paddle system, after gamma-ray attenuation and rate-dependent effects are taken into account [Pyw09b].

7.5.6 Target, Detector and Beam Alignment

Every effort was made to ensure that the target was placed in the centre of the array, that the beam passed through the centre of the target and that the detectors were aligned at a constant distance from the centre of the array. A tolerance of 3 mm is used for each of these alignments. The uncertainty in the neutron yields is estimated using the Geant4 simulations. First the reaction channels are simulated using the measured neutron angular distribution. The neutron yields are

extracted from this simulation. Second the target, beam or detector alignment in the simulation is changed and the analysis is redone to find the effect on the neutron yields.

7.5.7 Non-Isolatable Reaction Channels

The time-of-flight spectra are used to separate the non-isolatable reaction channels as discussed in section 7.2.2. The performance of the algorithm can be reduced by small distortions in the spectra and the neutron yields are subject to large uncertainties. In some cases, the separation algorithm itself can introduce more uncertainty into the neutron yields than any other source. However, it is difficult to quantify these uncertainties as they vary dramatically from case-to-case. In order to attempt to quantify the uncertainties introduced by the fitting algorithm we use the following semi ad-hoc method. We do not claim that this method is optimal but, in practice, it appears to function well. We encourage the exploration of alternative methods based on more rigorous statistical arguments.

The following method was used in the thesis of Sawatzky, [Swa05] page 107. When the simulated neutron yields are fit to the experimental data in order to find the coefficients for the associated Legendre function expansion, the reduced χ^2 value, χ^2_r, can be very high. We therefore take the uncertainty in a coefficient due to the process of isolating the reaction channels to be the coefficient's uncertainty from all other sources times $\sqrt{\chi^2_r - 1}$. We find the total uncertainty by multiplying the calculated uncertainty by $\sqrt{\chi^2_r}$ when employing the methods for non-isolatable reaction channels.

We justify this semi-ad hoc method as follows. Take N_d to be the neutron yield for detector d computed using the method of separating non-isolatable reaction channels and let its uncertainty be u_d. The neutron yield computed from fitting the associated Legendre functions to the data is given by F_d. The reduced χ^2 is then computed by

$$\chi^2_r = \frac{1}{D} \sum_{d=1}^{88} \frac{(N_d - F_d)^2}{u_d^2} \tag{7.34}$$

where D is the number of degrees of freedom. The number of degrees of freedom is calculated by taking the number of data points used in the fit and subtracting the number of fitting coefficients. The reduced χ^2 is thus a measure of how well the fitting function reproduces our data and how well we have quantified our uncertainties. Ideally, we desire $\chi^2_r = 1$.

The method of separation of non-isolatable reaction channels introduces uncertainties into our neutron yields that we cannot quantify with the limited information available. Therefore, the uncertainties, u_d, will be too small and χ^2_r will be large. When we extract quantities A, a_k and e_k from out fit, their associated uncertainties will be too small. Multiplying these uncertainties by $\sqrt{\chi^2_r}$ will make them larger. Let σ_a be the uncertainty in A, a_k or e_k computed by the fit. We can

write

$$\begin{aligned} \text{Final uncertainty in } A,\, a_k \text{ and } e_k &= \sigma_a \times \sqrt{\chi_r^2} \\ &= \sqrt{\frac{1}{D}\sum_{d=1}^{88}\left(\frac{\sigma_a}{u_d}\right)^2 (N_d - F_d)^2}. \end{aligned} \tag{7.35}$$

In a qualitative way, the underestimation of σ_a will cancel with the underestimation of u_d and give more reasonable values of the uncertainties.

An alternate method for handling the uncertainty introduced by the fitting algorithm was suggested during the defence of this thesis [Iga10]. Instead of directly adjusting the uncertainties of quantities calculated by the fit, we adjust the uncertainties of the neutron yields before performing the fit.

One such scheme is to multiply the uncertainties in the neutron yields for all detectors, u_d for $1 \leq d \leq 88$, by a constant, c. This transforms the uncertainty in detector d as $u_d \rightarrow cu_d$, and the reduced χ^2 is transformed as $\chi_r^2 \rightarrow \chi_r^2/c^2$ by equation 7.34. The actual values of A, a_k and e_k are not altered. The constant c can be chosen to make χ_r^2 any desired value; presumably $\chi_r^2 = 1$ is desired so we set $c = \sqrt{\chi_r^2}$. In other words, we multiply the uncertainties in the neutron yields by $\sqrt{\chi_r^2}$.

Note that for weighted regression analysis, the two methods produce the same result. In weighted regression analysis [Bev69],

$$\sigma_a^2 \sim \sum_{d=1}^{88} u_d^2. \tag{7.36}$$

Transforming $u_d \rightarrow cu_d = u_d \times \sqrt{\chi_r^2}$ transforms the uncertainty A, a_k or e_k as $\sigma_a \rightarrow \sigma_a \times \sqrt{\chi_r^2}$. As a check we reanalysed some of our fits using this alternate technique. The answers were the same up to round-off error.

7.6 Discussion of Non-Isolatable Reaction Channels

In this thesis we endeavour to develop a new algorithm for handling non-isolatable reaction channels. Such a technique has not been tried with the lithium isotopes. When studying lighter nuclei, the limited number of reaction channels make such techniques unnecessary. Given the great body of research on the photodisintegration of nuclei heavier than lithium, it is likely that such techniques have been attempted, although we are unaware of any such studies. We do not claim that our technique is either original or optimal. It should be seen as a reasonable attempt to divide complex spectra into individual reaction channels.

In section 7.2.1 we discussed isolatable reaction channels and the technique we use for obtaining the neutron yields for each detector. We do the same for non-isolatable reaction channels in section 7.2.2. The methods used for determining the neutron yields for each detector are different for

the isolatable and non-isolatable cases. We discuss how to obtain the angular distributions for both isolatable and non-isolatable reaction channels in section 7.3. An important point is that we handle both isolatable and non-isolatable reaction channels in the same way when finding angular distributions.

Another way that the methods differ is in finding uncertainties. For isolatable reaction channels the principle source of uncertainty comes from the light output cut; this is equivalent to uncertainty in the detection efficiency. For non-isolatable reaction channels the principle source of uncertainty comes from the separation algorithm described in 7.2.2. Since we perform fits on the time-of-flight spectra on a detector-by-detector basis, we get variations in the neutron yields for each detector. These variations tend to be larger than the uncertainties from the light-output cut, statistical uncertainties, or uncertainties from any other source. See figure 7.2 for a comparison of fits used to obtain the associated Legendre function coefficients for an isolatable and non-isolatable reaction channel using the methods of section 7.3.

From figure 7.2 we see that the fit for the isolatable case passes through nearly all of the error bars. We obtain a reduced χ^2 value of 0.34, indicating that we may have overestimated the uncertainties in our neutron yields. We do not artificially decrease our uncertainties as we feel that the calculation of the uncertainties in the neutron yields is principled and reasonable.

The measured neutron yields for the non-isolatable reaction channel look chaotic. We remind the reader that there are effects due to polarisation and these effects can be difficult to visualise on a plot where the x-axis is the detector number. The neutron yield plot is actually more orderly than it may appear at first. Still, we see that the red histogram does not pass through many of the error bars on our neutron yields and we obtain a reduced χ^2 value of 24.0. These neutron yields were computed using the methods for non-isolatable reaction channels of section 7.2.2. The uncertainties represent the statistical uncertainty and systematic uncertainties from all sources other than the separation algorithm. It is clear that we must re-evaluate these uncertainties.

In section 7.5.7 we discussed an algorithm for computing uncertainties due to the separation algorithm. We multiply the uncertainty in the associated Legendre function coefficients by $\sqrt{\chi^2_r}$. This is equivalent to increasing the error bars in figure 7.2 by a factor $\sqrt{\chi^2_r} = 4.9$. In other words, the algorithm used to determine the neutron yields introduces almost 5 times as much uncertainty as any other source. The result is increased uncertainty in the associated Legendre function coefficients.

Once we have obtained the associated Legendre function coefficients we can show that our methods actually work. Using these coefficients as inputs to the cumulative distribution functions of equations (5.52) and (5.53), we can produce spectra using all relevant reaction channels in order to compare with the measured spectra. Such a comparison is performed in figure 7.3. Note that the high energy (low time-of-flight) feature is due to the isolatable reaction channel while the low

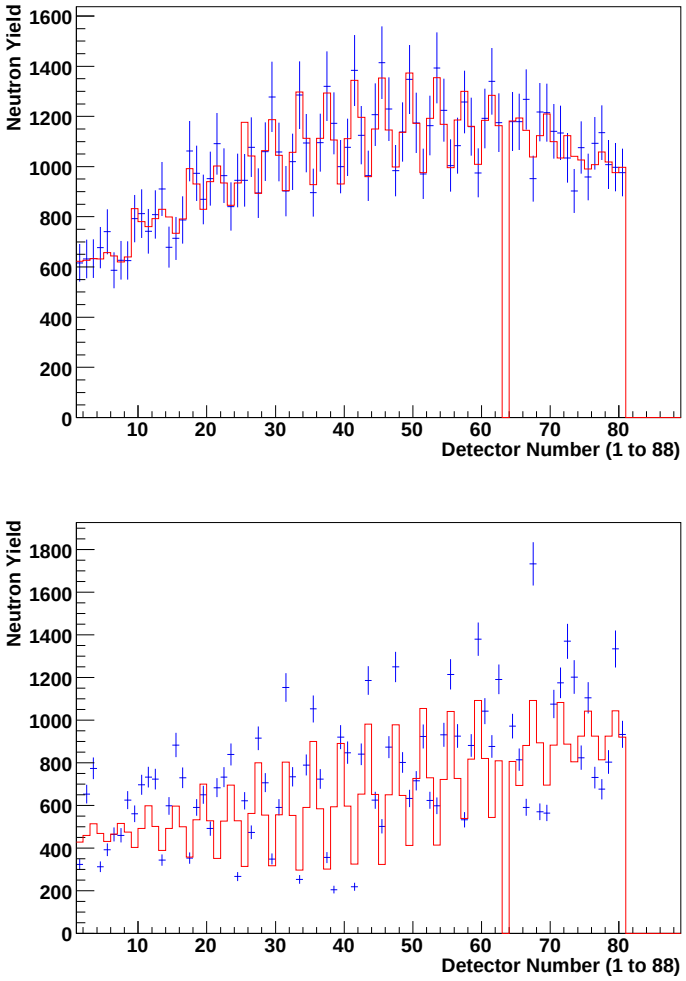

Figure 7.2: Neutron yields for the isolatable reaction channel ^{7}Li+$\gamma \rightarrow n+^6$Li(g.s.) (top) and for the non-isolatable reaction channel $^7\mathrm{Li} + \gamma \rightarrow n + ^6$Li(2.19) (bottom) at a photon energy of 13 MeV. The blue data points are the measured neutron yields obtained with the methods of section 7.2.1 for the isolatable case and section 7.2.2 for the non-isolatable case. The red histogram is the associated Legendre function coefficient fit performed using the methods of section 7.3. Note that we neglect the most downstream ring as discussed in section 6.3.5 and we neglect detector number 63 because of technical problems with that detector. Uncertainties are statistical and systematic uncertainties added in quadrature.

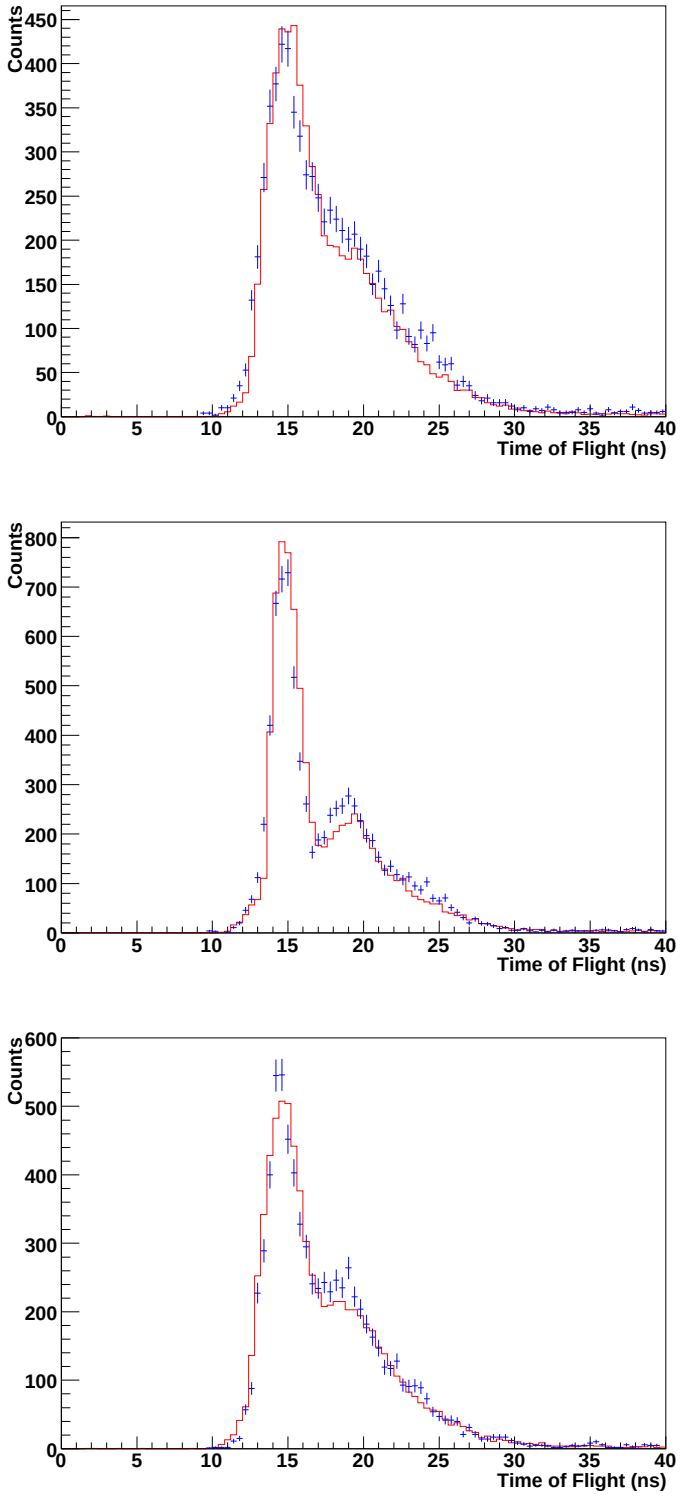

Figure 7.3: Comparison between the measured spectra (blue data points) and the simulated spectra (red histogram) which uses the associated Legendre function coefficients found for the isolatable and non-isolatable reaction channels. The error bars are statistical only. The top figure is for an upstream detector, the middle figure is a detector in the centre of the array and the bottom figure is a downstream detector. The areas under the curves are normalised over the entire array, not detector-by-detector.

energy (high time-of-flight) feature is due to multiple, non-isolatable reaction channels. Recall that the uncertainties in the measured spectra are statistical only and that there is uncertainty in the measured associated Legendre function coefficients, which is not taken into account with the simulation histogram. Overall, the comparison is reasonable and we can say that our methods are working as designed.

An alternate method for finding the associated Legendre function coefficients for non-isolable reaction channels was suggested during the defence of the thesis [Iga10]. The method used in this thesis requires two fits: one to obtain the neutron yields by fitting to time-of-flight spectra as discussed in section 7.2.2 and shown in figure 7.1, and one to obtain the associated Legendre function coefficients by fitting to the neutron yields as discussed in section 7.3 and shown in figure 7.2. The new suggestion is to perform only one fit. That is, we would fit the time-of-flight spectra for every detector simultaneously with the time-of-flight spectra generated from simulations using individual associated Legendre functions to determine the associated Legendre function coefficients directly. In other words, we would not compute the neutron yields first but would directly compute the coefficients. In this method, isolatable and non-isolatable reaction channels would be treated fundamentally differently. Further investigation is desired, but this is beyond the scope of this thesis.

Chapter 8

Analysis of the Gamma-Ray Spectra

8.1 Introduction

While it is ultimately neutrons we wish to study, an examination of the gamma-ray spectra observed during a photodisintegration measurement can provide important information about the experimental setup and instrumentation. Using the fact that gamma-rays all travel at the same speed, we can align the TDC as described in section 6.2.2. We are able to use comparisons with the cross section of Compton scattering to obtain measurements of photoneutron cross sections as described in section 7.4.1. The gamma-ray spectra can also tell us information about the operation of the accelerator.

Figure 8.1 shows a typical TDC spectrum as reported by a TDC channel, with no modification except for some binning to make it more presentable. The region from bin 750 to bin 1650 represents

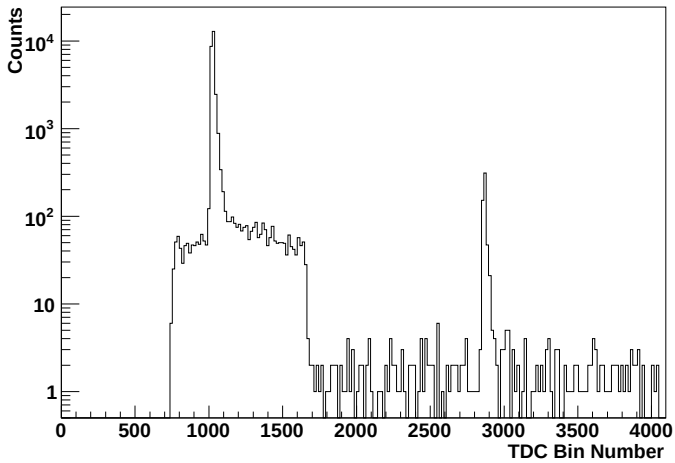

Figure 8.1: Raw TDC spectrum for a detector in the centre ring with a photon beam energy of 13 MeV and the natural lithium target. Note that the vertical scale is logarithmic.

the data acquisition window, the N+G-win in the data acquisition window diagram, figure 4.13. Within this window there is a peak due to the gamma-rays that are Compton scattered into the detector from the target. This peak rests on a constant plateau due to background radiation within

the experimental hall. A small neutron contribution is visible to the right of the gamma-ray peak as a small rise in the plateau. It is possible to get events beyond the acquisition window due to multiple detectors producing signals. With these events, a second detector starts the TDC which makes it possible for the first to accept events outside of the data acquisition window. Beyond bin 1650 there are sporadic background events and at bin 2900 we see a second gamma-ray peak due to the next bunch of photons produced by the accelerator 180 ns after the first.

Figure 8.1 is for a detector in the centre ring, which makes it relatively insensitive to some of the oddities experienced by both the extreme upstream and downstream detectors. In the next sections we examine these oddities, determine their causes and discuss any effects they may have on our data. We then discuss the use of the gamma-ray spectra as a flux monitor to determine photonuclear cross sections.

8.2 The Upstream Double Peak

In the most upstream detectors, an extra peak can be seen in the gamma-ray spectrum that comes before the expected gamma-ray peak and has a similar magnitude. An example of such a double peaked spectrum can be seen in figure 8.2. The peak on the right is due to gamma rays scattering

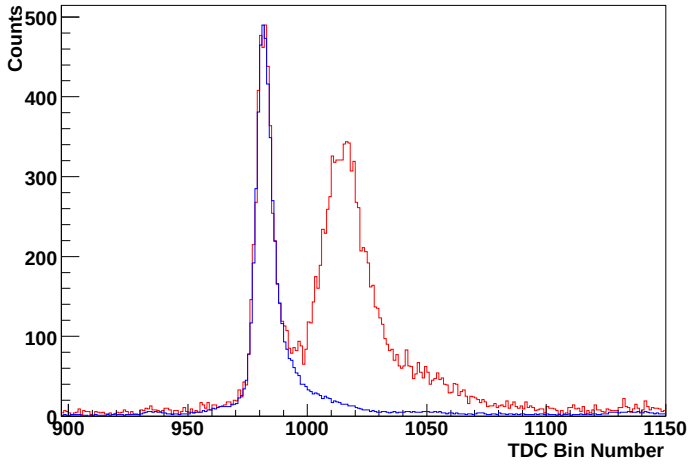

Figure 8.2: Raw TDC spectra for a detector in the most upstream ring with a photon beam energy of 13 MeV. The red spectrum was obtained with the natural lithium target and the blue spectrum was obtained with the empty target. The two spectra were normalised using the three-paddle flux monitoring system.

from the target. The peak on the left must be from a different source.

This extra peak can be explained by gamma-rays from the photon beam Compton scattering off air molecules. Figure 8.2 shows that the peak is certainly not from the target as it appears in the empty target spectrum and has the wrong timing. It can also be observed in simulations with no

target and no other obstructions in the beam. The only matter that can scatter the photon beam in these simulations is the air.

All detectors detect gamma-rays that are scattered from the air. Detectors closest to the photon beam, such as the most upstream and downstream rings, are most affected. Detectors furthest from the photon beam, such as the centre ring, detect very few photons scattered from the air. These effects will be discussed further in section 8.5 when we discuss the spectra measured using the empty target.

8.3 The Extra Bunch Peaks

In figure 8.3, we see a TDC spectrum for a detector in one of the downstream rings. Since the

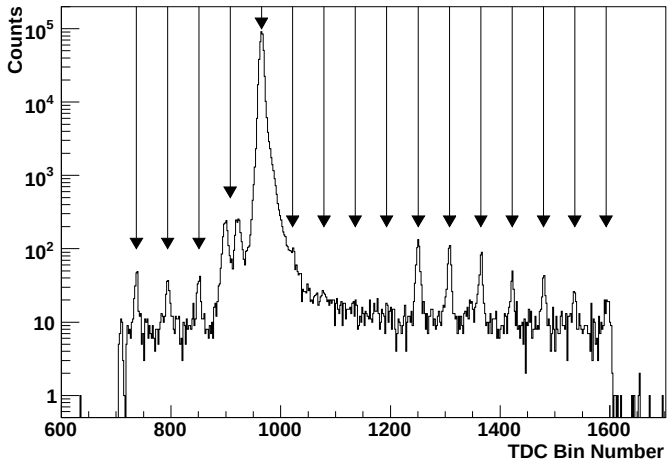

Figure 8.3: Raw TDC spectrum for a detector in the most downstream ring with a photon beam energy of 13 MeV and the natural lithium target showing the peaks due to extra electron bunches in the storage ring (note that the vertical scale is logarithmic). The arrows show the peaks separated by 5.602 ns (see text for details).

Compton scattering cross section is peaked forward, these detectors see a great many Compton scattered photons. In this figure, extra peaks can be seen protruding before and after the main gamma-ray peak in a periodic fashion. The two peaks to the immediate left of the main gamma-ray peak appear as one peak in other rings but split into two peaks in the most downstream ring. It is also interesting to note that there are no peaks immediately following the main gamma-ray peak.

The periodic peaks can be explained by considering that the RF cavity frequency for the storage ring is 178.5 MHz [Lit96]. We can then suppose that it is possible for electrons, knocked out of the main bunch by a Compton backscattering interaction, to find their way into other stable positions and build bunches both before and after the main bunch. These bunches would produce photons separated by 5.602 ns, which is the separation between the peaks in figure 8.3.

Since these peaks are three orders of magnitude less intense than the main peak, we can neglect any photodisintegration events that photons from the extra bunches may cause. However, they can pollute the neutron spectra and interfere with flux monitoring. They may become more important if they are larger under other operating conditions, especially for experiments requiring extreme accuracy.

8.4 The Beam Stop Back-Flash Peak

Figure 8.4 shows a time-of-flight spectrum for detector 75 with a photon beam energy of 20 MeV and no target in the array. Notice that this spectrum has an anomalous peak with a time-of-flight

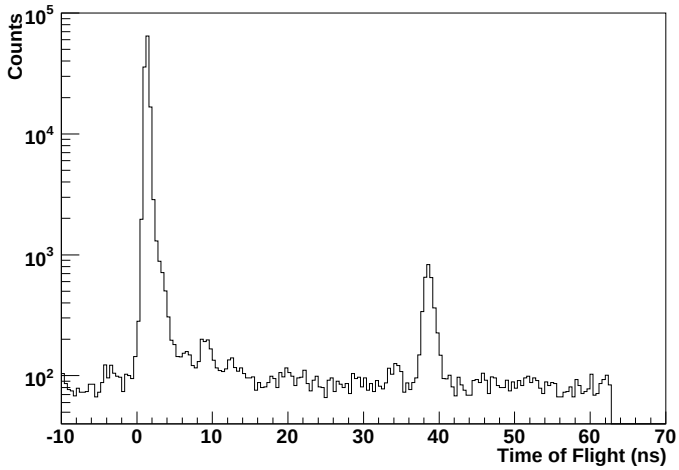

Figure 8.4: A time-of-flight spectrum for detector 75 with a beam energy of 20 MeV and no target. Prominent features include the main gamma-flash at 1.5 ns and a smaller peak near 40 ns. Vertical scale is logarithmic.

around 40 ns. This peak is due to gamma rays scattering backwards from the beam stop at the end of the gamma-vault and can be reproduced in the Geant4 simulation. It was first identified in the 20 MeV data but is certainly present in the data with photon energies below 16 MeV.

Figure 8.5 shows the number of detected gamma-rays in each of the downstream detectors after a time-of-flight cut has been applied around the 40 ns peak, isolating it. Notice that there is a constant background, making most detectors green and only some downstream detectors on top of the array are red. The upstream detectors are all green. This indicates that only the downstream detectors on top of the array have the 40 ns peak, which can be confirmed by looking at their individual time-of-flight spectra. This pattern can be explained by the steel support structures under the photon flux monitor attenuating all photons headed toward the lower detectors in the array. It is also observed in the simulation.

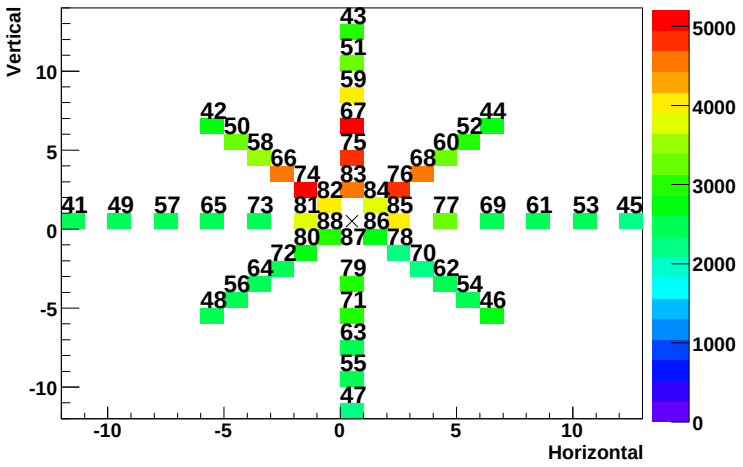

Figure 8.5: Experimental hits on the downstream detectors of Blowfish with no target and a beam energy of 20 MeV. Time-of-flight cuts eliminate all events except the 40 ns peak and uncorrelated background events that happen to fall into the window. The detectors are labelled by their detector numbers and the number of hits are given by the colour index.

8.5 Spectra for the Empty-Target Data

An empty target was built with a Teflon tube and end caps the same as those of the ^{6}Li and natural lithium targets. Data were collected with the empty target in order to better understand background effects.

The first thing we note about the data collected with the empty target is the lack of neutrons. For example, if we apply a PSD cut to the data, we see that there are fewer than 10 neutrons detected per detector for twenty minutes of data collection with a 13 MeV photon beam. This is orders of magnitude less than neutrons from photodisintegration events in the target. We can concluded that a subtraction for background neutrons is not required in measurements with photon energies less than 16 MeV. At photon energies above 16 MeV we will have to reconsider and do this in section 11.2.

Second, we wish to examine the gamma-ray spectra. Since there is no solid target used in these measurements, the detected spectra will be sensitive to other parts of the experimental geometry. We constructed a simulation that uses an empty target in order to compare with the measured data. This simulation emits gamma-rays 2.0 m upstream of the target centre. Figure 8.6 shows these photons travelling from their source point toward the target. Since the dead time for these measurements is quite low, we must take into account the no-beam background in our spectra. Figure 8.7 shows example gamma-ray yields for the detectors in Blowfish, comparing the simulation with the measured data. The simulation and measured spectra were normalised using the five

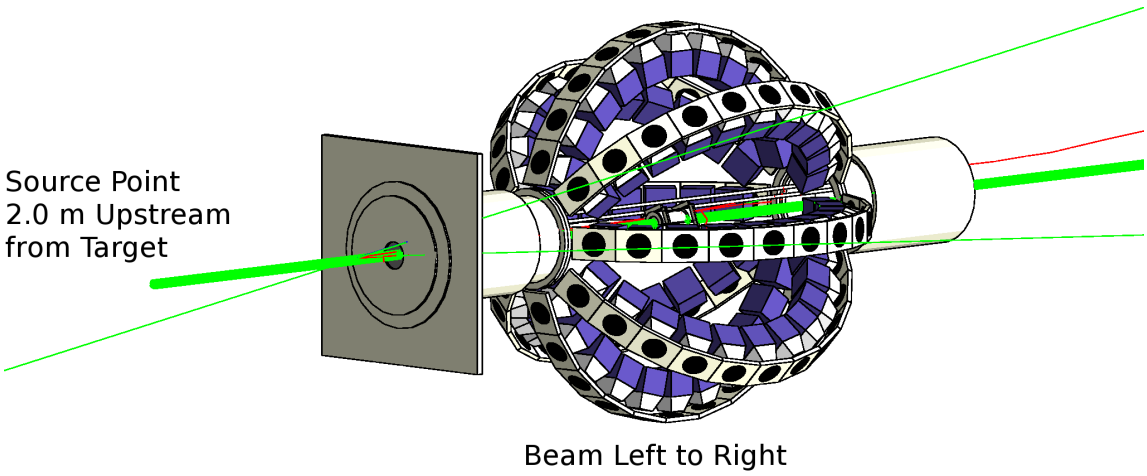

Figure 8.6: Photons of energy 13 MeV (green lines) emitted 2.0 m upstream of the target centre and travelling through the Geant4 geometry. Notice the scattered photons (green) and electron (red) produced by the photon beam before the start of the array.

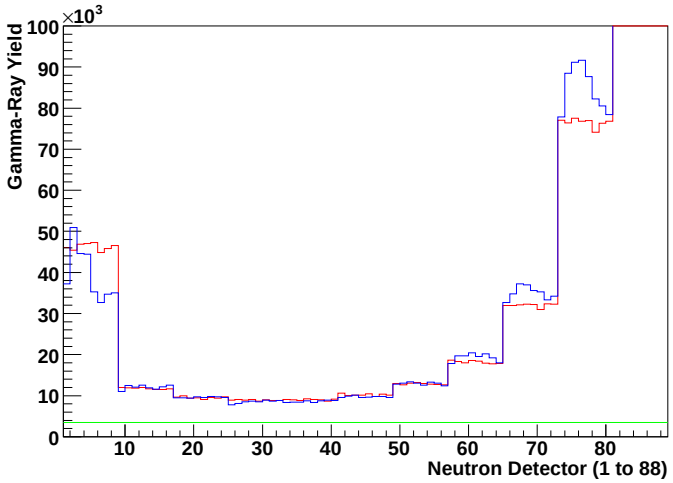

Figure 8.7: Gamma-ray yields for the detectors in Blowfish using a 13 MeV photon beam and the empty target. The blue histogram is the measured data, the green histogram is the no-beam background (which we assume is flat as this is a very good approximation), and the red line is the simulated yield added with the no-beam background.

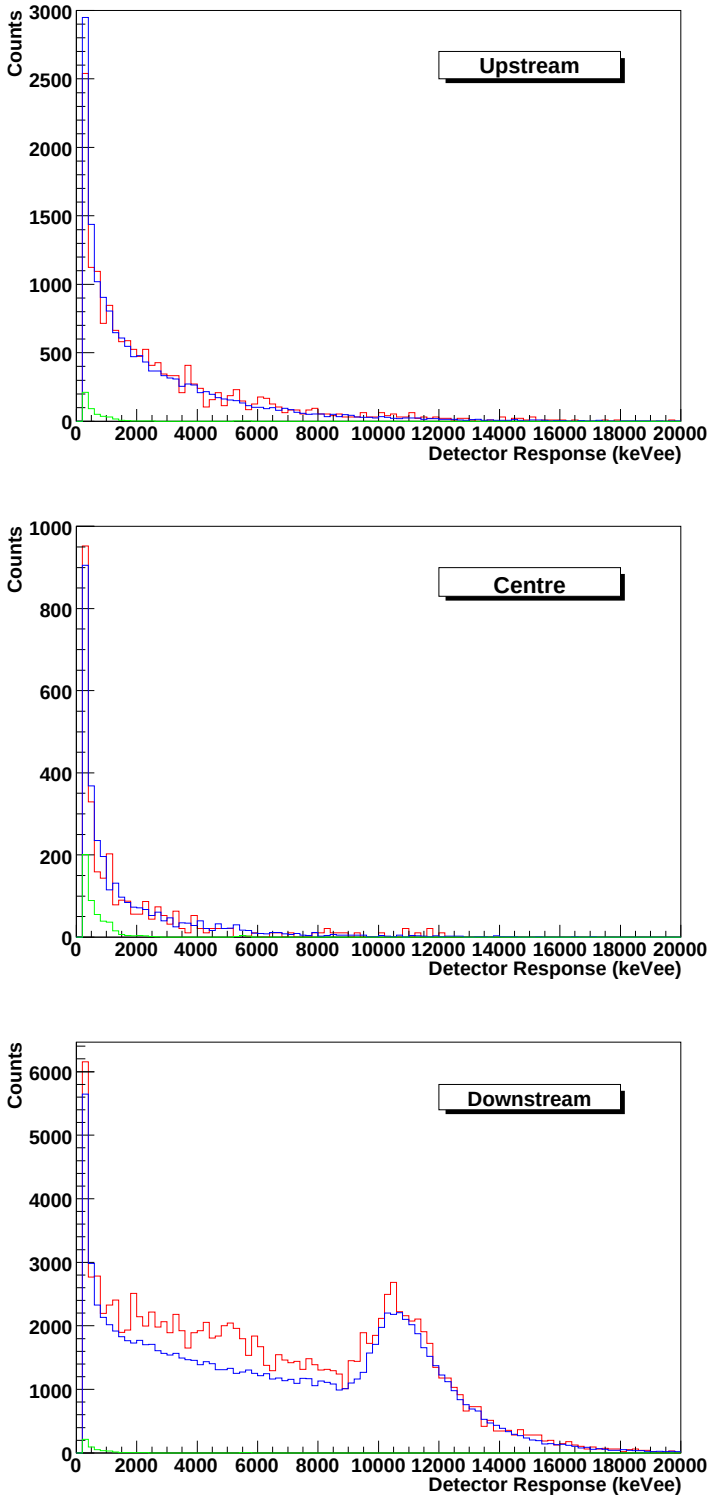

Figure 8.8: Light-output spectra obtained with the empty target and a 30 MeV photon beam for detectors in the most upstream ring (top), centre ring (middle) and most downstream ring (bottom). The blue line is the measured spectrum, the green line is the no-beam background and the red line is the simulation data added with the no-beam background.

centre-most rings of Blowfish detectors and agree qualitatively. The variation in gamma-ray yields for the most upstream and downstream detectors show that there are some systematic uncertainties present. It is possible that the gamma-ray beam does not pass through the axial centre of the array, as discussed in section 7.5.6. Also, there is a large amount of uncertainty in the geometry upstream of Blowfish. When data was being taken, there was another array placed upstream of Blowfish that was used for a different experiment. While this array did not directly interfere with the photon beam, it would have collimated photons that were scattered from the air.

It is also useful to look at the simulated and measured light-output spectra. Figure 8.8 compares these spectra for detectors in three different rings of Blowfish.

When the no-beam background is taken into account, the simulated and measured data qualitatively agree very well, with some disagreement concerning the downstream detectors. This disagreement is due to systematic uncertainties in the experimental geometry which are very difficult to quantify. We see the disagreement in the downstream detectors since these are the most sensitive to scattered gamma rays. Since the gamma-ray background is considered a small but non-negligible effect, the small uncertainties in its spectra need not be investigated further.

In the next section we will apply what we learned with the empty target data to the ^{6}Li and natural lithium target data. Those measurements will be used to determine absolute cross sections.

8.6 Using the Gamma-Ray Spectra for Absolute Cross Section Extraction

It is our desire to compute absolute cross sections for the reactions observed in our measurements. In section 7.4.1 we described a method to do this based on the spectra of photons that Compton scatter from our targets. While not optimised for the purpose, the detectors in Blowfish can also detect gamma-rays. By carefully analysing the gamma-ray spectra of our detectors and comparing them to the simulation, we can essentially measure the photon flux of the beam. As an additional bonus, some systematic uncertainties, such as the target length and density, cancel in our calculations.

We must first consider the consequences of Compton scattering from air molecules on our data. A calculation of the effective target thickness of the air compared to the thickness of our lithium targets will be helpful in establishing the importance of this effect. A useful set of units for measuring target thickness is the mass thickness units, also called surface density units. To convert a target thickness from units of length to mass thickness units, simply multiply by the density. In this way it is easy to compare targets with different densities. For instance, our natural lithium target of length 12.7 cm has a density of 0.534 g/cm^3, giving a mass thickness of 6.78 g/cm^2. If we assume that the photon beam passes through 3.0 m of air and the air has a density of about 1.2 kg/m^3, then we get a mass thickness of about 0.36 g/cm^2. While we cannot neglect Compton

scattering from the air, any of the uncertainties mentioned in section 8.5 will have small effects on our final results. By including Compton scattering from air in the simulation, we should be able to effectively take this contribution into account.

Table 8.1 shows the maximum energy deposited in the Blowfish detectors by a photon that Compton scatters from the lithium target. There will be a large smearing effect due to the finite

Table 8.1: Maximum energy deposited in a detector by a photon of original energy 13 MeV which Compton scatters from the lithium target

Ring	Polar Angle, θ (deg)	Energy of Scattered Gamma-Ray (MeV)	Maximum Energy Deposited (MeV)
1	157.5	0.26	0.13
2	144.0	0.28	0.14
3	130.5	0.30	0.16
4	117.0	0.34	0.20
5	103.5	0.40	0.25
6	90.0	0.49	0.32
7	76.5	0.63	0.45
8	63.0	0.87	0.68
9	49.5	1.31	1.10
10	36.0	2.22	1.99
11	22.5	4.43	4.19

geometry of the target and detector, and also because of detector resolution. This table shows that the detectors in the upstream rings, 1 through 7, will not have gamma-rays depositing more than 500 keV$_{ee}$. The rings 8, 9 and 10 make good candidates for measuring the gamma-ray yields. The most downstream ring, ring 11, is neglected as discussed in section 6.3.5. Note that the energy deposited is, possibly surprisingly, not very sensitive to the photon beam's energy. For the detectors in ring 8, the maximum energy deposited only varies from 0.64 MeV to 0.71 MeV for photon beam energies of 8 MeV and 35 MeV respectively.

If we make a cut of 500 keV$_{ee}$ and use only rings 8, 9 and 10 we can eliminate much of the background. We can also use a cut above the Compton edge in order to eliminate more air-scattered photons. We use maximum light-output cuts of 1200 keV$_{ee}$ for ring 8, 2000 keV$_{ee}$ for ring 9 and 3500 keV$_{ee}$ for ring 10. The remaining air-scattered photons are negligible. The contribution from the no-beam background is negligible. Figure 8.9 shows the light-output spectra for a detector in each of the rings 8, 9 and 10.

If we exclude so many of our detectors, we may wish to reexamine equation (7.20), which is

reproduced here,

$$\sigma_n = (170\bar{0} \text{ mb}) \frac{N_{sim}}{\Phi^s} \frac{N_{d,n}}{N^s_{d,n}} \frac{N^s_{d,\gamma}}{N_{d,\gamma}}. \tag{8.1}$$

While we only use three rings to find the ratio of gamma-ray yields, we can use many more to find the ratio of neutron yields. We do not want to throw away useful neutron data so we modify equation (7.20)/(8.1) to read

$$\sigma_n = (170\bar{0} \text{ mb}) \frac{N_{sim}}{\Phi^s} \left\langle \frac{N_{d,n}}{N^s_{d,n}} \right\rangle \left\langle \frac{N^s_{d,\gamma}}{N_{d,\gamma}} \right\rangle \tag{8.2}$$

where $\left\langle N^s_{d,\gamma}/N_{d,\gamma} \right\rangle$ is the weighted average of gamma-ray yield ratios taken over rings 8, 9 and 10 and $\left\langle N_{d,n}/N^s_{d,n} \right\rangle$ is the weighted average of neutron yield ratios taken over all detectors with valid data. Figure 8.10 shows the ratios $N^s_{d,\gamma}/N_{d,\gamma}$ and $N_{d,n}/N^s_{d,n}$ for data taken with the ^{6}Li target and the 13 MeV photon beam. Notice that the statistical uncertainty in $N_{d,n}/N^s_{d,n}$ for a single detector is somewhat large, but when we perform a weighted average over all detectors the overall statistical uncertainty will become small. The ratio $N^s_{d,\gamma}/N_{d,\gamma}$ has small statistical uncertainty but the scattering of the points indicates that the systematic uncertainties will be significant.

In section 7.5 we discussed the systematic uncertainties that affect the neutron yields. Many of these uncertainties will also affect our calculations of the gamma-ray yields. We will have to take into account uncertainty in the light-output cut and the alignment of the target, detectors and photon beam. We will not have to consider uncertainty due to a PSD cut as we are able to remove the neutrons based on timing. We also will not have to consider uncertainty due to the time-of-flight cut as the timing peaks for the scattered gamma-rays are sharp and we are able to neglect the no-beam background.

We must also consider the need for a rate-dependent correction similar to the one required for the five-paddle monitor. For the five-paddle monitor, it is possible to have two gamma-rays strike the radiator, but this will produce only a single count. We can make a simple argument showing that such a correction is not necessary for the Compton scattering comparison method. Consider the gamma-ray spectrum for a data acquisition run, for example the run using the natural lithium target with a photon beam of 30 MeV. The detectors in ring 10 had a real-time, uninhibited rate of no more than 4 kHz. In other words, no more than 4000 gamma-rays were detected each second by one of these detectors. On the other hand, the accelerator is producing gamma-ray pulses with a frequency of 5.5 MHz. Since the count rate for the gamma-rays is three orders of magnitude less than the rate at which gamma-ray bunches come from the accelerator, events in which two gamma-rays are detected in the same detector at the same time are very rare. We therefore do not have to consider a rate dependent correction.

Using the technique described in this section and section 7.4.1, we are able to measure the absolute photoneutron cross sections of the reaction channels under study without external flux monitoring. It is sufficient to use the detectors in the Blowfish neutron detector array to detect

Compton scattered photons. This technique also has the benefit that some systematic uncertainties, such as the target length, cancel. Target length and density variations cause uncertainty when using an independent flux monitor.

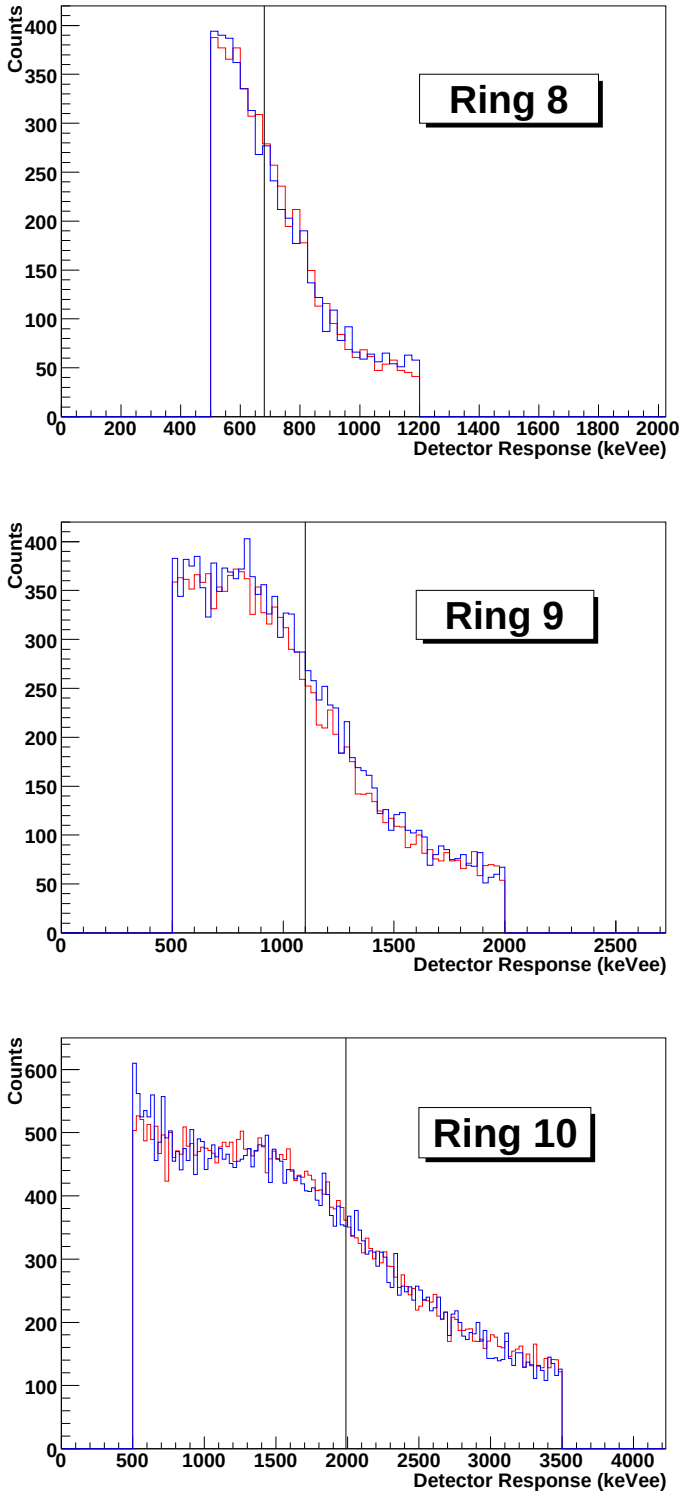

Figure 8.9: Light-output spectra due to gamma-rays for detectors in rings 8 (top), 9 (middle) and 10 (bottom) using the ^{6}Li target and a 13 MeV photon beam. The simulation is the red line and the measured data is the blue line. Vertical lines indicate the position of the ideal Compton edge; notice the large smearing effect due to finite geometry. Each spectrum is cut below the Compton edge at 500 keV$_{ee}$ and cut above at 1200 keV$_{ee}$ for ring 8, 2000 keV$_{ee}$ for ring 9 and 3500 keV$_{ee}$ for ring 10.

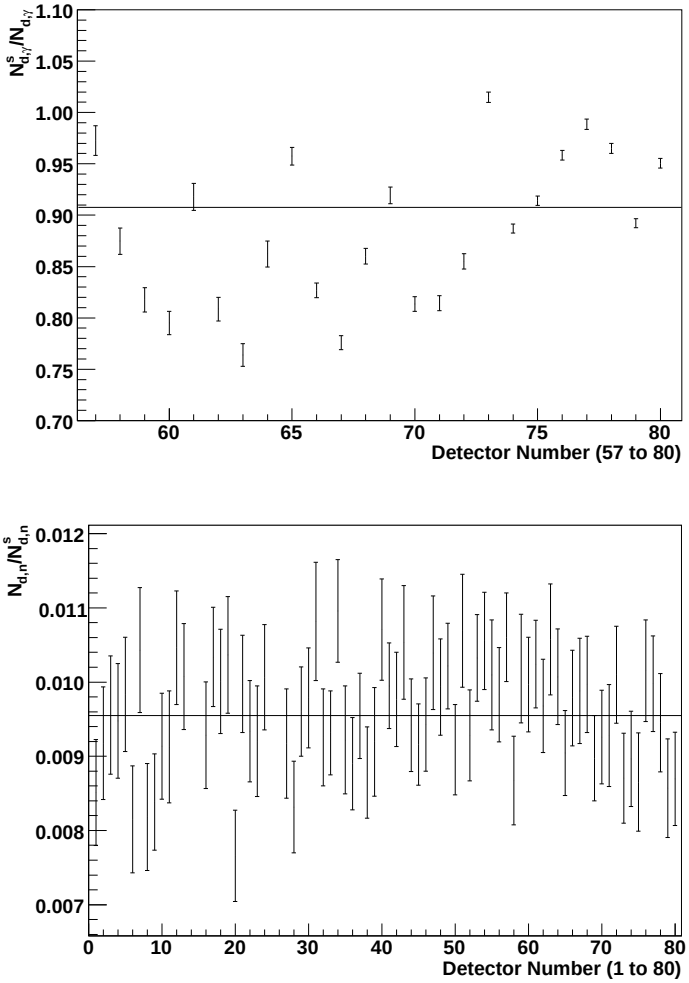

Figure 8.10: The ratios $N^s_{d,\gamma}/N_{d,\gamma}$ (top) and $N_{d,n}/N^s_{d,n}$ (bottom) for data taken with the ^{6}Li target and the 13 MeV photon beam. Uncertainties are statistical only. The horizontal lines represent the weighted averages of the ratios. The statistical uncertainties for the gamma-rays in the top plot are much less than the neutrons in the bottom plot. Given the scatter in the top plot, there are systematic uncertainties that must be accounted for in the analysis of the gamma-ray spectra.

Chapter 9

Data Analysis for ^{6}Li With Photon Energies Below 16 MeV

9.1 Introduction

Photoneutrons have been observed with the Blowfish Neutron Detector Array for eight energies below 16 MeV. Before beginning a quantitative analysis, we can make some qualitative statements about the distribution of the neutrons. There is certainly structure in the kinetic energy spectrum of the detected neutrons. The kinetic energy plots in figure 9.1 have two prominent features. The

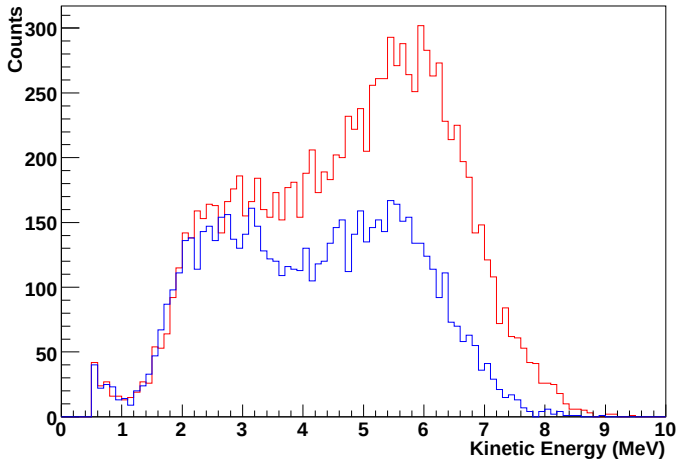

Figure 9.1: Experimental neutron kinetic energy spectrum reported by two neutron detectors at a polar angle $\theta = 90°$ with one detector at an angle-to-polarisation of $\phi = 0°$ (red) while the other is at $\phi = 90°$ (blue) with a photon beam of 13 MeV and ^{6}Li target.

high energy features are due mainly to neutrons emitted from the single-neutron knockout reaction, $^{6}\mathrm{Li} + \gamma \rightarrow n + {}^{5}\mathrm{Li}$, while the lower energy features are due mainly to neutrons that occur from the decay of ^{5}He from the single-proton knockout reaction, $^{6}\mathrm{Li} + \gamma \rightarrow p + {}^{5}\mathrm{He}$. The sharp edge at approximately 2 MeV is due to the cut on light output eliminating all low-energy neutrons from the analysis.

Figure 9.2 shows histograms representing the locations of the upstream detectors in Blowfish after appropriate cuts have been applied. Recall that the HIGS beam is polarised in the horizontal

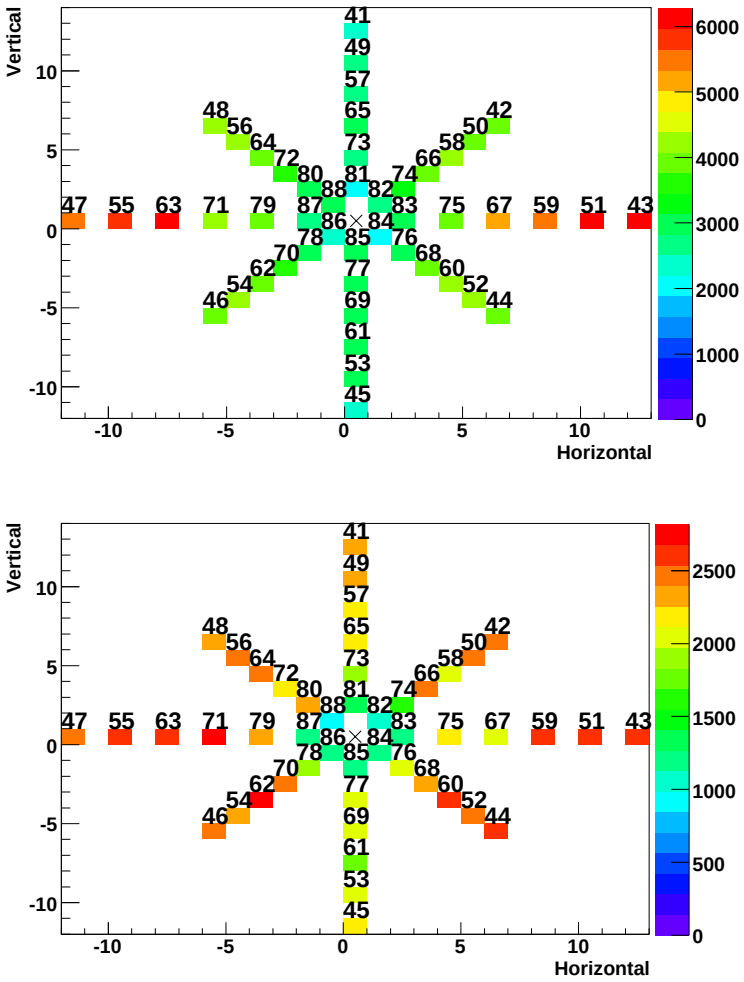

Figure 9.2: Experimental hits on the downstream detectors of Blowfish for the high-energy neutrons (top) and low-energy neutrons (bottom) emitted from ^{6}Li. The photon beam has an energy of 13 MeV and is travelling into the page. The detectors are labelled by their detector numbers and the number of hits are given by the colour index.

plane and note the strong dependence of the high-energy neutrons on the beam polarisation. We see only a weak dependence on polarisation in low-energy neutrons. It is also possible that any perceived dependence is due to the high-energy feature leaking into the low-energy feature. We expect little dependence on polarisation for the low energy neutrons since the decay of ^{5}He should be isotropic in its rest frame. To turn this qualitative discussion into a quantitative analysis, we must model the reaction channels that produce these two features.

The structure of the A=5 nuclei are not understood as well as we would like. However, we can use the most up-to-date information and attempt to reproduce the kinetic energy spectra detected

by Blowfish. Table 9.1 shows the five reaction channels that we will model. Four of these channels

Table 9.1: Reaction channels to consider in the analysis of the ^{6}Li data below 16 MeV.

Label	Reaction	Threshold (MeV)
6np	$^6\mathrm{Li} + \gamma \rightarrow n + p + {}^4\mathrm{He}$(g.s.)	3.7
6p0	$^6\mathrm{Li} + \gamma \rightarrow p + {}^5\mathrm{He}$(g.s.) $\rightarrow n + p + {}^4\mathrm{He}$(g.s.)	4.6
6n0	$^6\mathrm{Li} + \gamma \rightarrow n + {}^5\mathrm{Li}$(g.s.)	5.7
6p1	$^6\mathrm{Li} + \gamma \rightarrow p + {}^5\mathrm{He}(1.27)$ $\rightarrow n + p + {}^4\mathrm{He}$(g.s.)	5.9
6n1	$^6\mathrm{Li} + \gamma \rightarrow n + {}^5\mathrm{Li}(1.49)$	7.0

involve two-body decays with an intermediate A=5 nucleus which are discussed further in section 9.2, while the fifth involves three bodies in the final state and is discussed in section 9.3.

9.2 Discussion of the Two-Body Reaction Channels

Two-body reaction channels dominate the photodisintegration of ^{6}Li below 16 MeV. There are four two-body reaction channels listed in table 9.1: 6n0, 6n1, 6p0 and 6p1.

The reaction channels 6n0 and 6n1 are the easiest to understand. These involve knocking out a single neutron, leaving a ^{5}Li nucleus in either its ground or first excited state. The mechanism for decay of this nucleus is not important to our analysis. We model these reactions in the simulation by using two-body, relativistic photodisintegration, as discussed in section 5.3.1. The first excited state is taken to be at an energy of 1.49 MeV and the decay widths of the ground state and first excited state are taken to be 1.23 MeV and 6.60 MeV respectively (no uncertainty estimates given in reference) [Til02]. The mean mass of the ^{5}Li nucleus is taken to be 4669.15 ± 0.05 MeV/c^2 [Aud03].

The reaction channels 6p0 and 6p1 are more complex. These reactions involve the knocking out of a proton and leaving a ^{5}He nucleus in either its ground or first excited state. This nucleus can then decay into ^{4}He and a neutron, meaning we must use the two-body, relativistic decay discussed in section 5.3.2 to model these reaction channels. Note that if the nucleus undergoes a decay into final products that do not include a neutron, such as a deuteron and triton, we will not observe the reaction. We will use the value of 1.27 MeV for the energy of the first excited state [Til02]. For the decay widths, we will not use the total widths but the partial widths of the neutron decay channels: 0.578 MeV for the ground state and 3.18 MeV for the first excited state (no uncertainty estimate given in reference) [Til02]. The mean mass of the ^{5}He nucleus is taken to be 4668.85 ± 0.05 MeV/c^2 [Aud03]. Unfortunately the neutrons from the 6p0 reaction have very

low energies. While they can be observed in the data, their light output tends to be at the same level as the hardware thresholds, meaning very little about them can be quantified.

We will see in the next section that the two-body reactions dominate at the energies of interest.

9.3 Discussion of the Three-Body Reaction Channel

We now discuss the three-body reaction channel. Obviously this reaction occurs at higher energies through the quasideuteron effect. However, the question of its existence and nature at lower energies is not as clear.

Proctor and Voelker studied the photodisintegration of ^{6}Li using a bremsstrahlung spectrum with maximum energy 17.3 MeV [Pro60]. They used a proton detector placed at a polar angle of 90° and a neutron detector placed on the other side of the target. They make the following conclusion.

> "The lack of any effect in the $\mathrm{Li}^6(\gamma, np)\mathrm{He}^4$ experiment indicates that a correlated (γ, np) reaction of the type predicted by [the deuteron-alpha particle model of Carome] produces at most 2% of the total observed neutron yield. However, this experiment by itself does not eliminate the possibility of a weakly correlated or uncorrelated (γ, np) process which would produce a considerably higher fraction of the neutron yield." [Pro60]

The results of Proctor and Voelker suggest that we can eliminate the strongly correlated three-body reaction. The results of Wade *et al.* [Wad84] also strongly suggest that there are negligible quasideuteron interactions below 16 MeV. However, this conclusion requires an extrapolation of their work as they studied the energy range between 25 and 65 MeV.

There appears to be no reason to consider a strongly correlated three-body reaction below 16 MeV. However, a weakly correlated or uncorrelated reaction must be investigated and we will refer to this reaction with the label 6np.

Kusuhara makes the strong claim that "[i]t is concluded that only the $^6\mathrm{Li}(\gamma, p)^5\mathrm{He}(n)^4\mathrm{He}$ and $^6\mathrm{Li}(\gamma, n)^5\mathrm{Li}(p)^4\mathrm{He}$ reactions occur in the energy range lower than the $(\gamma, ^3\mathrm{H})$ threshold, and the energetically possible $^6\mathrm{Li}(\gamma, np)^4\mathrm{He}$ reactions of various types do not exist in practice" [Kus80]. However, Kusuhara's analysis may not be valid. Kusuhara assumes the existence of a 8.37 MeV excited state of ^{6}Li, which we no longer believe exists; the closest states are 5.65 and 17.98 MeV [Til02]. Furthermore Kusuhara does not take into account the decay widths of the A=5 reaction products and makes conclusions based on proton energy distributions that are not valid. An application of the relativistic kinematics treated in sections 5.3.1 and 5.3.2 show that protons can be produced with energies in excess of Kusuhara's stated maxima for the $^6\mathrm{Li} + \gamma \rightarrow p + {}^5\mathrm{He}$ reaction channels. We will have to make a detailed investigation into our data to determine whether or not this reaction is important to our analysis.

We simulate the 6np reaction using the three-body kinematics discussed in section 5.3.3. We choose, in the centre-of-momentum frame, random and uncorrelated directions for the proton and

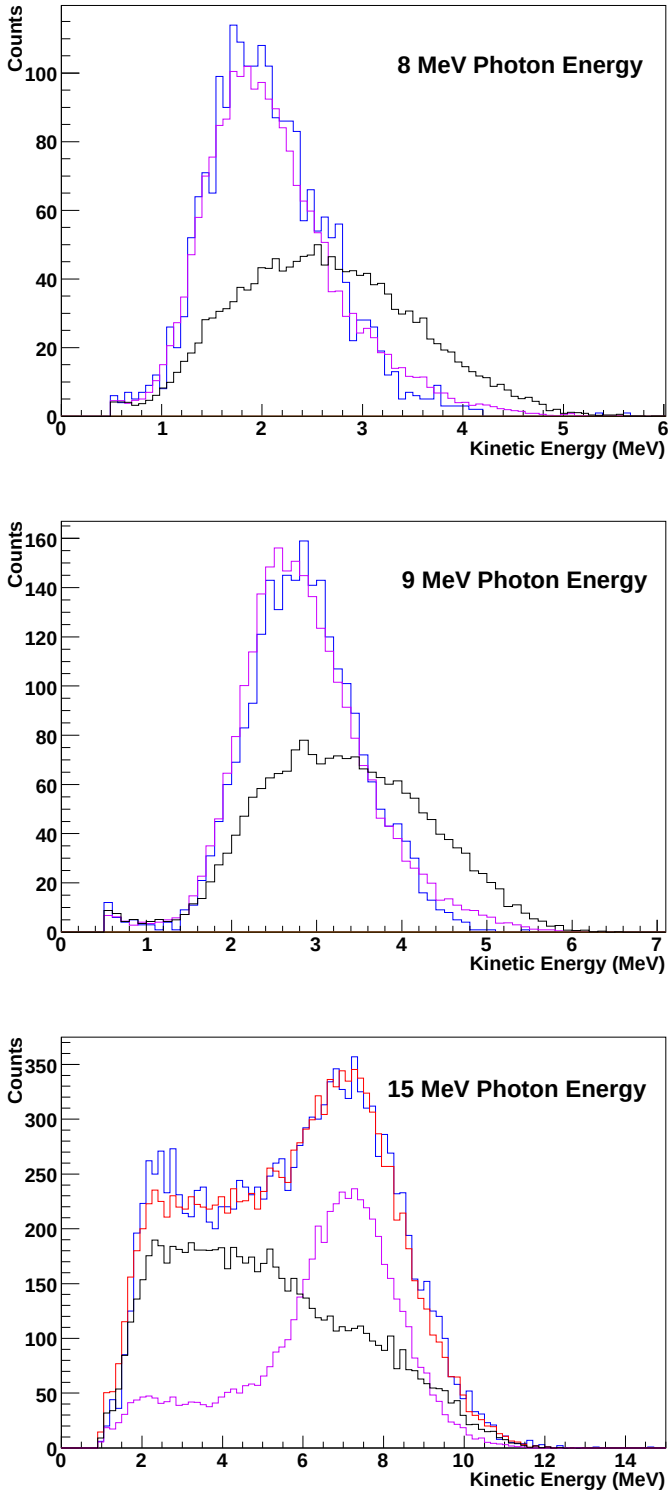

Figure 9.3: Comparison of the experimental neutron kinetic energy spectra detected by a Blowfish neutron detector (blue) with the simulated spectra for the 6n0 reaction channel (purple) and the 6np reaction channel (black). The red histogram on the 15 MeV plot is the sum of the 6n0 and 6np reaction channels.

neutron. This simulation can be used to produce neutron kinetic energy spectra that we can compare to our experimental data.

Figure 9.3 shows three neutron kinetic energy spectra detected by three detectors at three different photon energies. These particular spectra have been selected as they demonstrate features of the 6np reaction channel kinetic energy spectrum. The first two plots are very similar. For both 8 and 9 MeV, we see that the spectra can be explained completely by the 6n0 reaction channel. The 6np reaction channel simulation produces neutrons with kinetic energies greater than the experimental kinetic energies. From these plots we can say that the cross section for the 6np reaction is much smaller than the 6n0 reaction channel.

However, as the energy of the neutrons increase, the energy resolution of the detectors decrease since the kinetic energy is computed from time-of-flight. For the 15 MeV histogram we cannot say that the 6np reaction channel can be neglected based on its kinetic energy spectra. In fact, the 15 MeV plot in figure 9.3 suggests that we can use the 6np reaction channel and 6n0 reaction channel to explain this particular histogram, without the 6n1 or 6p1 reaction channels. This shows the danger of making conclusions looking at a single detector. When all detectors are examined, it is seen that better fits are obtained if the 6p1 and 6n1 reactions are used, rather than the 6np reaction. For comparison see figure 9.8 which shows the same plot with 6np replaced with 6n1 and 6p1. We cannot eliminate the 6np reaction for beam energies of 15 MeV as easily as we did at 8 and 9 MeV.

We will make the assumption, based on the lack of a 6np reaction at lower energies and its lack of necessity at higher energies, that the 6np reaction does not occur and we will model our spectra using the 6n1 and 6p1 reaction channels. It should be noted that the 6np reaction is, in a way, an approximation of these two reaction channels. Because of the high decay widths of the first excited states of the A=5 nucleons, the 6n1 and 6p1 reactions have very broad neutron kinetic energy spectra. Since they immediately break apart, they are similar to a three-body reaction.

It should also be noted that none of this discussion completely eliminates a weakly correlated three-body reaction. If such a reaction were found to exist, it would require a reexamination of this analysis.

9.4 Analysis for the Photon Energy of 9 MeV

The first thing we would like to determine is whether or not we can isolate the 6n0 reaction channel. We cannot isolate it with complete confidence as there may be small contributions from the 6p0, 6n1 and 6p1 reaction channels. However, the 6n0 reaction channel will dominate and these reaction channels will not be distinguishable.

In figure 9.4, we plot the simulated light-output spectra for the 6n0 and 6p0 reaction channels.

If we assume that the cross sections are approximately equal, as would be suggested by the charge

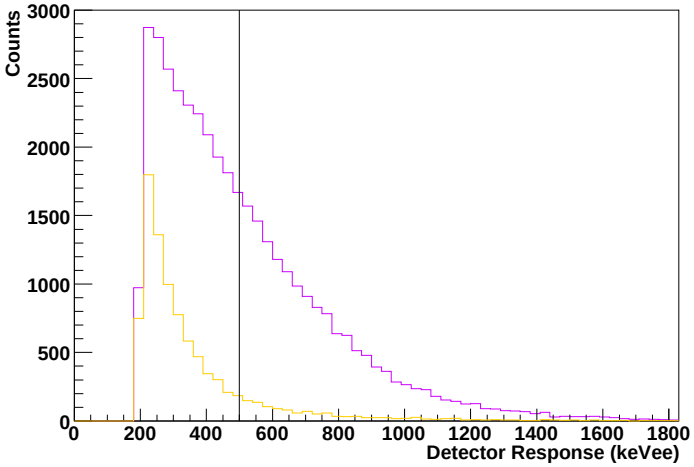

Figure 9.4: The light-output spectra from the simulation of the 6n0 (purple) and 6p0 (yellow) reaction channels for a detector in the centre ring

independence of the nuclear force, we can estimate the approximate contribution of neutrons from the 6p0 reaction. For a light-output cut of 500 keV_{ee} we estimate that 7.4% of the neutrons detected will be from the 6p0 reaction channel. The PSD cut is nearly 100% efficient with this light-output cut.

Because of the large decay widths of ^{5}He(1.27) and ^{5}Li(1.49), the neutron kinetic energy spectra we generate through our models are essentially the same for the 6n1 and 6p1 reaction channels at these photon energies. We cannot completely eliminate these reaction channels but we can argue that their effects will be small. It is obvious from looking at the time-of-flight spectra in figure 9.5 that most of the neutrons must be from the 6n0 reaction. We will make the assumption that the 6p1 and 6n1 reaction channels do not contribute a substantial number of neutrons, with the understanding that this assumption may introduce some additional uncertainty into our measurements. We can then say that the 6n0 reaction channel is isolatable at this photon energy and use the method described in section 7.2.1.

Table 9.2 reports the results of fitting the simulated spectra to the measured spectra. We report the raw results of the fits to four decimal places, with separate systematic and statistical uncertainties. The fit uncertainties will typically be dominated by the systematic uncertainties. When we refine our raw fit results and perform further analysis on them, we will add the systematic and statistical uncertainties in quadrature and report only a single uncertainty. In this way we can show how the uncertainties are dominated by the systematic uncertainties and have a single, simple, intuitive and convenient measurement of uncertainty in the later analysis.

The quantity A is not useful as it can only tell us about the relative contribution between two

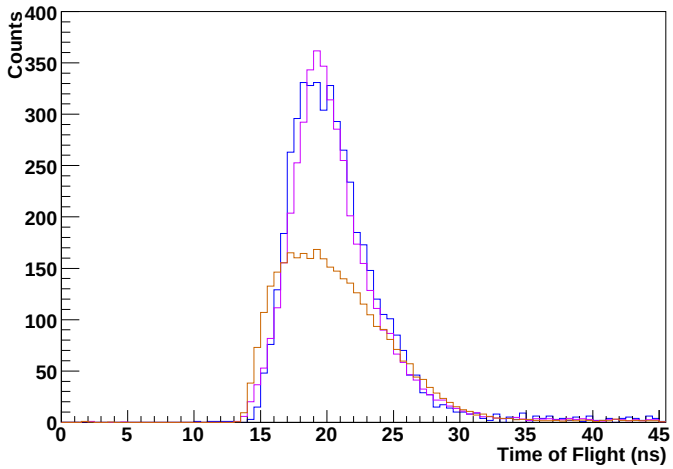

Figure 9.5: The time-of-flight spectra from the simulation of the 6n0 (purple) and 6p1 (yellow) reaction channels for a detector in the centre ring compared with the measured spectrum (blue). A lower, 250 keV_{ee}, light-output cut was applied to better show the qualitative shapes of the spectra.

Table 9.2: Associated Legendre function coefficient fitting results for ^{6}Li at a photon energy of 9 MeV. The orientation signifies which detector in the most upstream ring was on top of the array.

Channel	Orientation	Coefficient	Fit Result	Reduced χ^2
6n0	1	A	0.0970 ± 0.0003 (stat) ± 0.0008 (syst)	1.06
		a_1	0.0569 ± 0.0058 (stat) ± 0.0152 (syst)	
		a_2	-0.1735 ± 0.0092 (stat) ± 0.0246 (syst)	
		a_3	0.0450 ± 0.0119 (stat) ± 0.0322 (syst)	
		e_2	0.1077 ± 0.0022 (stat) ± 0.0058 (syst)	
		e_3	-0.0081 ± 0.0011 (stat) ± 0.0031 (syst)	
6n0	3	A	0.1590 ± 0.0004 (stat) ± 0.0013 (syst)	1.10
		a_1	0.0771 ± 0.0045 (stat) ± 0.0152 (syst)	
		a_2	-0.1690 ± 0.0073 (stat) ± 0.0248 (syst)	
		a_3	0.0263 ± 0.0094 (stat) ± 0.0324 (syst)	
		e_2	0.0828 ± 0.0017 (stat) ± 0.0060 (syst)	
		e_3	-0.0006 ± 0.0009 (stat) ± 0.0031 (syst)	

reaction channels and we have only one reaction channel to discuss. We can perform a weighted average on the coefficients for the associated Legendre function expansion, and find $a_1 = 0.067 \pm 0.011$, $a_2 = -0.171 \pm 0.018$, $a_3 = 0.036 \pm 0.024$, $e_2 = 0.0953 \pm 0.0044$ and $e_3 = -0.0043 \pm 0.0023$. These values will be discussed further in chapter 13.

9.5 Analysis for the Photon Energy of 8 MeV

We can use some of our results from the analysis of the data taken with a 9 MeV photon beam to aid us with the 8 MeV photon beam data. Since we concluded that the 6n1 and 6p1 reaction channels are negligible for 9 MeV, we may also assume that they are negligible for 8 MeV. It would be extremely unusual for the cross sections of 6n1 and 6p1 to be higher at a photon energy of 8 MeV than 9 MeV.

Like the 9 MeV data, we will treat the 6n0 reaction channel as being isolatable. For the 8 MeV data we use a light-output cut of 500 keV_{ee} to ensure maximum effectiveness of the PSD cut. We estimate from the simulation and approximate equality of the cross sections, that 13% of the neutrons may actually be from 6p0 and not 6n0. A higher light-output cut could reduce this fraction, but our statistics are already lower than we would like. We will treat the 6n0 reaction channel with an 8 MeV photon beam as being isolatable.

There is a small anomaly in the time-of-flight spectrum that requires our attention. If we set our simulation's smearing of the time-of-flight to zero, and plot it with the measured time-of-flight, as is done in figure 9.6, we see that the simulated spectrum is wider than the measured spectrum. A possible explanation is that we are using a decay width for ^{5}Li that is too high. It is also possible

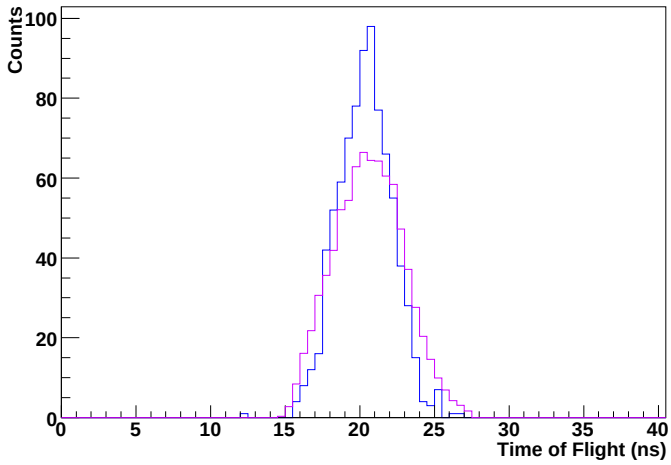

Figure 9.6: The time-of-flight spectra from the simulation of the 6n0 (purple) and the measured spectrum (blue) for a detector in the centre ring.

that we are over estimating the spread of beam energy or position. This anomaly should have only

a minimal effect on our results since we are treating the 6n0 reaction at this photon energy as being isolatable and do not fit to the time-of-flight spectra.

The results of fitting the simulated spectra to the measured spectra in order to determine the associated Legendre function coefficients are shown in table 9.3. The format for this table is the

Table 9.3: Associated Legendre function coefficient fitting results for ^{6}Li at a photon energy of 8 MeV. The orientation signifies which detector in the most upstream ring was on top of the array.

Channel	Orientation	Coefficient	Fit Result	Reduced χ^2
6n0	1	A	0.1252 ± 0.0005 (stat) ± 0.0014 (syst)	0.47
		a_1	0.0654 ± 0.0084 (stat) ± 0.0219 (syst)	
		a_2	-0.2023 ± 0.0130 (stat) ± 0.0336 (syst)	
		a_3	0.0831 ± 0.0173 (stat) ± 0.0462 (syst)	
		e_2	0.1362 ± 0.0030 (stat) ± 0.0078 (syst)	
		e_3	-0.0058 ± 0.0013 (stat) ± 0.0042 (syst)	
6n0	3	A	0.0652 ± 0.0004 (stat) ± 0.0007 (syst)	0.88
		a_1	0.0757 ± 0.0117 (stat) ± 0.0217 (syst)	
		a_2	-0.1954 ± 0.0183 (stat) ± 0.0336 (syst)	
		a_3	0.0816 ± 0.0237 (stat) ± 0.0457 (syst)	
		e_2	0.1152 ± 0.0043 (stat) ± 0.0080 (syst)	
		e_3	-0.0015 ± 0.0022 (stat) ± 0.0043 (syst)	

same as that of the 9 MeV data.

As was done for the data taken with a photon energy of 9 MeV, the weighted average of the associated Legendre Polynomial coefficients are $a_1 = 0.070 \pm 0.017$, $a_2 = -0.199 \pm 0.026$, $a_3 = 0.082 \pm 0.036$, $e_2 = 0.1266 \pm 0.0061$ and $e_3 = -0.0039 \pm 0.0033$. These values will be discussed further in chapter 13 in context of the values at other energies.

9.6 Analysis for the Photon Energies of 10, 11, 12 and 13 MeV

For photon energies above 9 MeV, we can no longer isolate any reaction channels in our ^{6}Li data, and all further discussion in this chapter will concern non-isolatable reaction channels that will be separated using the methods of section 7.2.2. We can no longer neglect the 6n1 and 6p1 reaction channels but their neutron kinetic energy spectra are very similar so we cannot separate the two. We will fit the 6n0 and a sum of the 6n1 and 6p1 reaction channels to the measured time-of-flight.

This is somewhat justified by the charge independence of the nuclear force. However, angular information may be lost and we must understand that this is an approximation forced upon us by the reality of the data.

We make a light-output cut of 250 keV$_{ee}$ for the 10 MeV data and 350 keV$_{ee}$ for the 11 MeV data. These cuts will introduce some systematic uncertainties since the PSD cut is not 100 % efficient in this region, so we rely on the simulation to estimate its efficiency. Making a higher cut would reduce this problem but it would also make it nearly impossible to find the 6n1 and 6p1 reaction channels in the measured data. We rely on the lower energy neutrons produced by these reactions in order to separate them from 6n0. This can be seen in figure 9.7, which shows the neutron kinetic energy spectrum measured by a detector.

We make a light-output cut of 500 keV$_{ee}$ for the 12 and 13 MeV data. This light output cut allows us to effectively distinguish between neutrons and gamma-ray photons based on PSD. An example detected neutron kinetic energy spectrum is shown in figure 9.7 for 12 MeV and figure 9.8 for 13 MeV.

We expect the contribution from 6p0 to be about 16% the contribution from 6n0 for the 10 MeV photon beam, about 9.3% for the 11 MeV photon beam, 5.6% for the 12 MeV photon beam and 5.3% for the 13 MeV photon beam. This contribution will mainly affect results regarding the 6n1 and 6p1 reaction channels.

Table 9.4: Associated Legendre function coefficient fitting results for ^{6}Li at a photon energy of 10 MeV. The orientation signifies which detector in the most upstream ring was on top of the array.

Channel	Orientation	Coefficient	Fit Result	Reduced χ^2
6n0	1	A	0.0911 ± 0.0002 (stat) ± 0.0009 (syst)	2.65
		a_1	0.1946 ± 0.0040 (stat) ± 0.0180 (syst)	
		a_2	-0.4445 ± 0.0059 (stat) ± 0.0256 (syst)	
		e_2	0.1438 ± 0.0016 (stat) ± 0.0077 (syst)	
		e_3	0.0019 ± 0.0008 (stat) ± 0.0038 (syst)	
6n1	1	A	0.0459 ± 0.0002 (stat) ± 0.0004 (syst)	23.44
		a_1	-0.1942 ± 0.0064 (stat) ± 0.0223 (syst)	
6p1	1	A	0.0460 ± 0.0002 (stat) ± 0.0004 (syst)	22.20
		a_1	0.6530 ± 0.0219 (stat) ± 0.0735 (syst)	

Tables 9.4, 9.5, 9.6 and 9.7 report the results of fitting the simulated spectra to the measured spectra. Notice that, due to the methods required to extract neutron yields from non-isolatable reaction channels, that the reduced chi-square values are very high. These high χ^2 values come

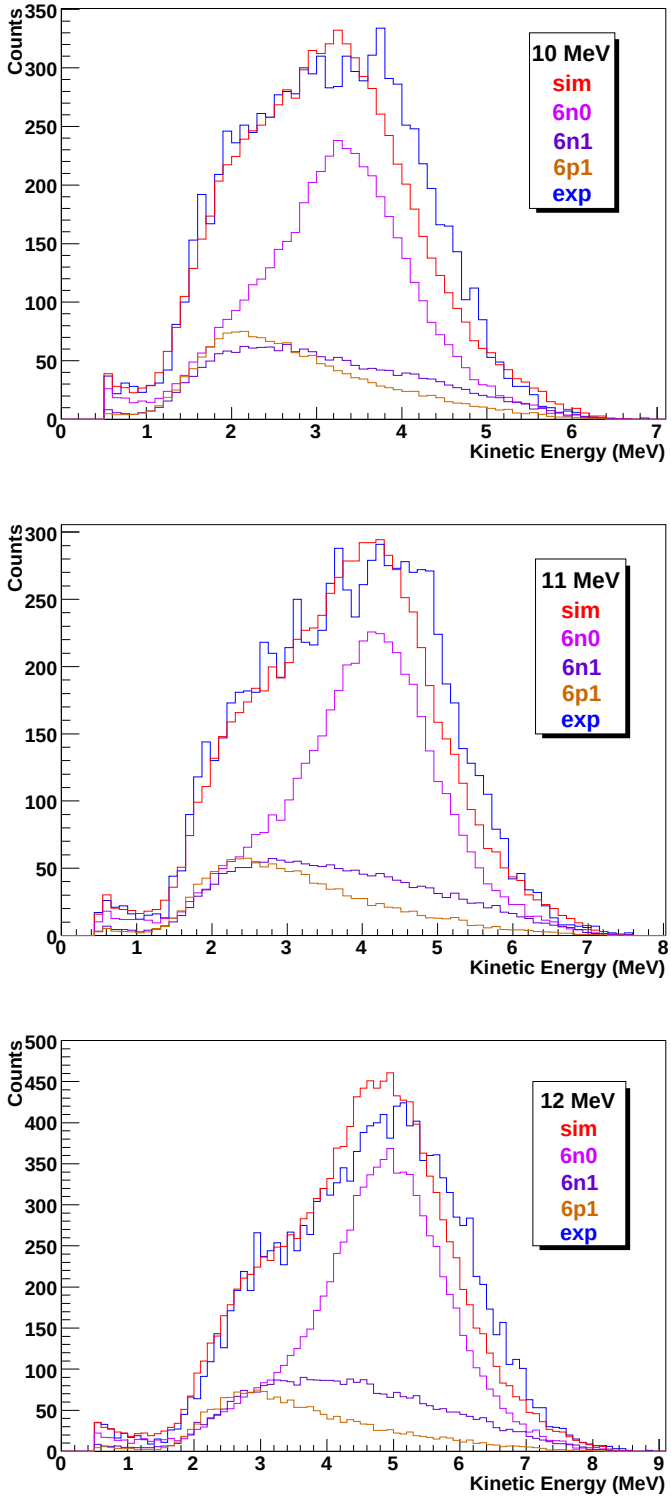

Figure 9.7: The neutron kinetic energy spectra for a beam energy of 10 MeV (top), 11 MeV (centre) and 12 MeV (bottom) for a detector in the centre ring. Shown are the simulation of the 6n0, 6n1 and 6p1 reaction channels and the measured spectrum (blue). The red histogram is the sum of the simulation histograms.

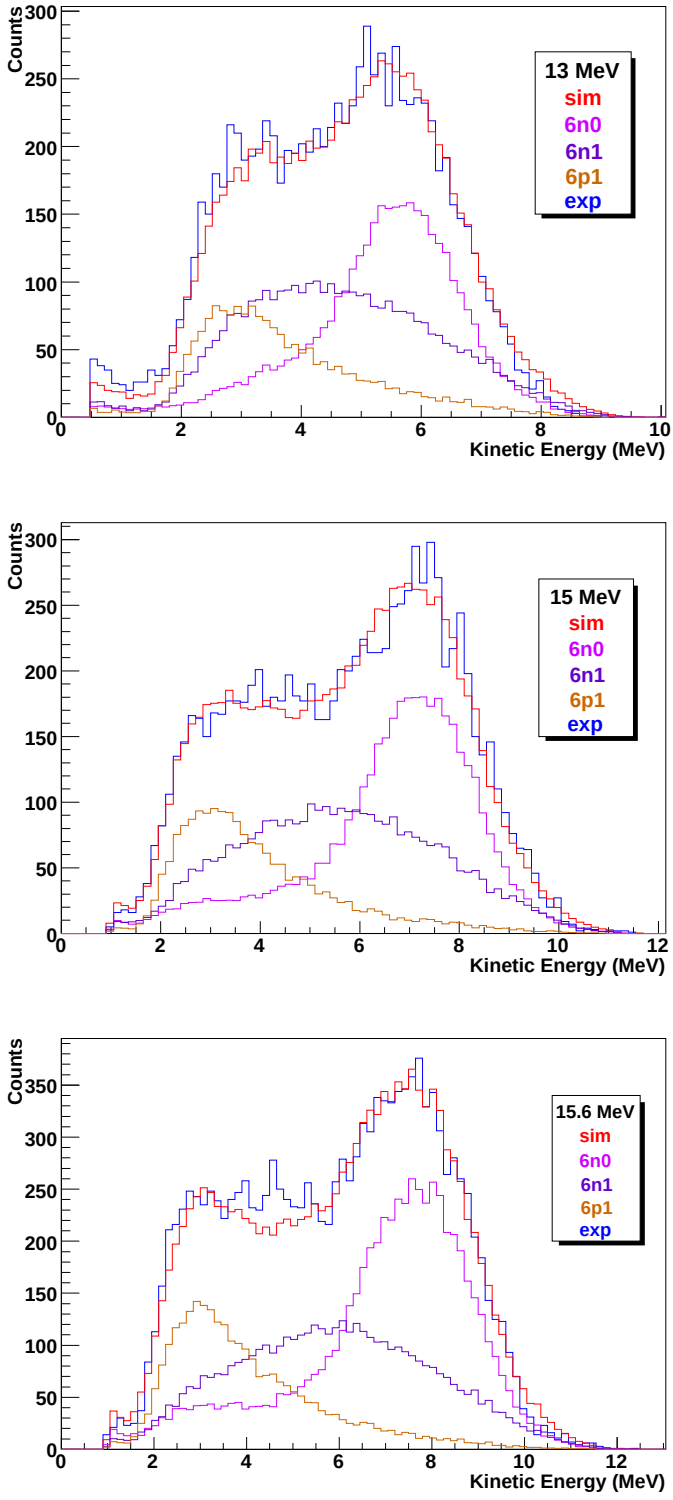

Figure 9.8: The neutron kinetic energy spectra for a beam energy of 13 MeV (top), 15 MeV (centre) and 15.6 MeV (bottom) for a detector in the centre ring. Shown are the simulation of the 6n0, 6n1 and 6p1 reaction channels and the measured spectrum (blue). The red histogram is the sum of the simulation histograms.

Table 9.5: Associated Legendre function coefficient fitting results for ^{6}Li at a photon energy of 11 MeV. The orientation signifies which detector in the most upstream ring was on top of the array.

Channel	Orientation	Coefficient	Fit Result	Reduced χ^2
6n0	1	A	0.0781 ± 0.0002 (stat) ± 0.0006 (syst)	6.31
		a_1	0.2464 ± 0.0044 (stat) ± 0.0124 (syst)	
		a_2	-0.4051 ± 0.0065 (stat) ± 0.0180 (syst)	
		e_2	0.2154 ± 0.0018 (stat) ± 0.0051 (syst)	
		e_3	0.0060 ± 0.0009 (stat) ± 0.0024 (syst)	
6n0	3	A	0.0798 ± 0.0002 (stat) ± 0.0006 (syst)	13.44
		a_1	0.1688 ± 0.0043 (stat) ± 0.0129 (syst)	
		a_2	-0.3504 ± 0.0064 (stat) ± 0.0189 (syst)	
		e_2	0.2708 ± 0.0016 (stat) ± 0.0044 (syst)	
		e_3	-0.0074 ± 0.0009 (stat) ± 0.0023 (syst)	
6n1	1	A	0.0701 ± 0.0002 (stat) ± 0.0005 (syst)	7.79
		a_1	-0.1044 ± 0.0055 (stat) ± 0.0132 (syst)	
6n1	3	A	0.0667 ± 0.0002 (stat) ± 0.0005 (syst)	35.63
		a_1	-0.2175 ± 0.0055 (stat) ± 0.0161 (syst)	
6p1	1	A	0.0701 ± 0.0002 (stat) ± 0.0005 (syst)	6.44
		a_1	0.2922 ± 0.0183 (stat) ± 0.0408 (syst)	
6p1	3	A	0.0667 ± 0.0002 (stat) ± 0.0005 (syst)	29.27
		a_1	0.5758 ± 0.0185 (stat) ± 0.0507 (syst)	

Table 9.6: Associated Legendre function coefficient fitting results for ^{6}Li at a photon energy of 12 MeV. The orientation signifies which detector in the most upstream ring was on top of the array.

Channel	Orientation	Coefficient	Fit Result	Reduced χ^2
6n0	1	A	0.1564 ± 0.0003 (stat) ± 0.0010 (syst)	18.52
		a_1	0.3753 ± 0.0032 (stat) ± 0.0114 (syst)	
		a_2	-0.4122 ± 0.0049 (stat) ± 0.0160 (syst)	
		e_2	0.2235 ± 0.0013 (stat) ± 0.0041 (syst)	
		e_3	-0.0061 ± 0.0007 (stat) ± 0.0019 (syst)	
6n0	3	A	0.0762 ± 0.0002 (stat) ± 0.0005 (syst)	16.40
		a_1	0.4221 ± 0.0046 (stat) ± 0.0113 (syst)	
		a_2	-0.2916 ± 0.0069 (stat) ± 0.0151 (syst)	
		e_2	0.2019 ± 0.0018 (stat) ± 0.0044 (syst)	
		e_3	-0.0132 ± 0.0009 (stat) ± 0.0021 (syst)	
6n1	1	A	0.1286 ± 0.0003 (stat) ± 0.0008 (syst)	8.84
		a_1	-0.2073 ± 0.0043 (stat) ± 0.0117 (syst)	
6n1	3	A	0.0667 ± 0.0002 (stat) ± 0.0004 (syst)	5.67
		a_1	-0.1711 ± 0.0060 (stat) ± 0.0115 (syst)	
6p1	1	A	0.1292 ± 0.0004 (stat) ± 0.0009 (syst)	6.05
		a_1	0.4997 ± 0.0143 (stat) ± 0.0350 (syst)	
6p1	3	A	0.0668 ± 0.0003 (stat) ± 0.0005 (syst)	3.76
		a_1	0.4654 ± 0.0198 (stat) ± 0.0346 (syst)	

Table 9.7: Associated Legendre function coefficient fitting results for ^{6}Li at a photon energy of 13 MeV. The orientation signifies which detector in the most upstream ring was on top of the array.

Channel	Orientation	Coefficient	Fit Result	Reduced χ^2
6n0	1	A	0.1077 ± 0.0002 (stat) ± 0.0007 (syst)	12.11
		a_1	0.3070 ± 0.0039 (stat) ± 0.0118 (syst)	
		a_2	-0.2703 ± 0.0058 (stat) ± 0.0164 (syst)	
		e_2	0.2180 ± 0.0015 (stat) ± 0.0042 (syst)	
		e_3	-0.0123 ± 0.0008 (stat) ± 0.0021 (syst)	
6n0	3	A	0.1709 ± 0.0003 (stat) ± 0.0011 (syst)	15.48
		a_1	0.2197 ± 0.0032 (stat) ± 0.0124 (syst)	
		a_2	-0.3674 ± 0.0047 (stat) ± 0.0175 (syst)	
		e_2	0.2353 ± 0.0012 (stat) ± 0.0040 (syst)	
		e_3	0.0187 ± 0.0006 (stat) ± 0.0021 (syst)	
6n1	1	A	0.0922 ± 0.0003 (stat) ± 0.0006 (syst)	5.89
		a_1	-0.1197 ± 0.0047 (stat) ± 0.0118 (syst)	
6n1	3	A	0.1460 ± 0.0003 (stat) ± 0.0009 (syst)	6.05
		a_1	-0.1125 ± 0.0038 (stat) ± 0.0117 (syst)	
6p1	1	A	0.0923 ± 0.0003 (stat) ± 0.0007 (syst)	4.09
		a_1	0.2818 ± 0.0154 (stat) ± 0.0279 (syst)	
6p1	3	A	0.1462 ± 0.0004 (stat) ± 0.0011 (syst)	4.14
		a_1	0.2726 ± 0.0122 (stat) ± 0.0326 (syst)	

Table 9.8: Final associated Legendre function coefficient values for ^{6}Li at photon energies of 10 to 13 MeV for the reaction channel 6n0.

Energy	Coeff.	Value	Energy	Coeff.	Value
10 MeV	a_1	0.195 ± 0.030	11 MeV	a_1	0.223 ± 0.028
	a_2	-0.445 ± 0.043		a_2	-0.389 ± 0.040
	e_2	0.144 ± 0.013		e_2	0.237 ± 0.011
	e_3	0.0019 ± 0.0063		e_3	0.0015 ± 0.0052
12 MeV	a_1	0.399 ± 0.035	13 MeV	a_1	0.270 ± 0.033
	a_2	-0.348 ± 0.049		a_2	-0.311 ± 0.046
	e_2	0.213 ± 0.013		e_2	0.226 ± 0.011
	e_3	-0.0094 ± 0.0063		e_3	0.0017 ± 0.0058

from uncertainties in the neutron yields from the separation of non-isolatable reaction channels which we are unable to quantify. Table 9.8 lists the associated Legendre polynomial coefficients for the 6n0 reaction channel after taking into account the results of the two array orientations and the large chi-square values as discussed in section 7.5.

We do not report a value for a_3 as we found that computing this value made the fit unreliable. It is heavily influenced by the uncertainties introduced by the method of separating non-isolatable reaction channels. However, the value for e_3 does not appear to be so affected, as it depends mainly on polarisation, so we have left it in the calculations. The value for e_3 appears to be indistinguishable from zero at these energies.

The a_1 values reported for reaction channels 6n1 and 6p1 are not considered to be physical since the two reaction channels could not be separated and it was their sum that was used for the fitting algorithm. The values reported in tables 9.9 were computed so that we could better reproduce the observed neutron spectra in the Geant4 simulation.

Table 9.9: Coefficients a_1 for reaction channels 6n1 and 6p1 for photon energies of 10 to 13 MeV. Note that these values should not be taken to have physical meaning but are useful as input to the simulation.

Energy (MeV)	a_1 for 6n1	a_1 for 6p1
10	-0.19 ± 0.11	0.65 ± 0.36
11	-0.120 ± 0.037	0.33 ± 0.11
12	-0.186 ± 0.024	0.479 ± 0.059
13	-0.116 ± 0.022	0.278 ± 0.048

Table 9.10 reports the ratio of the cross sections of the separated reaction channels over the cross section of all observable reaction channels. These values were computed from the A values of the associated Legendre function fits using equation (7.10). It is important to note that in table 9.10, no corrections are made for the 6p0 reaction channel. There is a small correction needed in the cross section of 6n1 + 6p1 that will be made when we find absolute cross sections in chapter 13.

Table 9.10: Calculated cross section ratios computed from the A values of the associated Legendre function fits. No corrections are made at this point for the 6p0 reaction channel.

Energy (MeV)	σ[6n0]/σ[6n0 + 6n1 + 6p1]	σ[6n1 + 6p1]/σ[6n0 + 6n1 + 6p1]
10	0.498 ± 0.012	0.502 ± 0.019
11	0.362 ± 0.007	0.639 ± 0.011
12	0.370 ± 0.008	0.630 ± 0.008
13	0.369 ± 0.007	0.631 ± 0.007

9.7 Analysis for the Photon Energies of 15 and 15.6 MeV

With photon energies of 15 and 15.6 MeV, the 6n1 and 6p1 reaction channels have neutron kinetic energy spectra that are distinct enough to allow us to separate these channels and fit three, individual reaction channels to our data: 6n0, 6n1 and 6p1. We use a light-output cut of 500 keV_{ee}, which ensures good neutron/gamma-ray discrimination using PSD. Example detected neutron kinetic energy spectra can be seen in figure 9.8.

We expect the contribution from 6p0 to be about 10% the contribution from 6n0 for the 15 MeV photon beam, and about 8.3% for the 15.6 MeV photon beam. These neutrons all have low energies and will generally only affect the 6p1 reaction channel. We could further reduce their contribution by increasing the light-output cut, but this would make it more difficult to separate the 6p1 and 6n1 reaction channels.

Tables 9.11 and 9.12 show the raw output of the fitting routines. The data for 6n0 are averaged between the two array orientations and are reported in table 9.13.

The final associated Legendre function coefficient values reported in table 9.13 for the 6n0 reaction channel are consistent with those found at the lower energies, and will be discussed in context with the other values in chapter 13.

However, the a_1 values found for the 6n1 and 6p1 reaction channels are anomalous, and are reported in table 9.14. The a_1 values for 6n1 are all negative, while those for 6p1 are undoubtedly positive. This is not expected based on the charge independence of the nuclear potential. If the

Table 9.11: Associated Legendre function coefficient fitting results for ^{6}Li at a photon energy of 15 MeV. The orientation signifies which detector in the most upstream ring was on top of the array.

Channel	Orientation	Coefficient	Fit Result	Reduced χ^2
6n0	1	A	0.1091 ± 0.0002 (stat) ± 0.0005 (syst)	26.49
		a_1	0.3235 ± 0.0043 (stat) ± 0.0087 (syst)	
		a_2	-0.3707 ± 0.0068 (stat) ± 0.0129 (syst)	
		e_2	0.2028 ± 0.0016 (stat) ± 0.0029 (syst)	
		e_3	0.0098 ± 0.0009 (stat) ± 0.0017 (syst)	
6n0	3	A	0.1868 ± 0.0003 (stat) ± 0.0008 (syst)	25.33
		a_1	0.2607 ± 0.0034 (stat) ± 0.0096 (syst)	
		a_2	-0.2564 ± 0.0052 (stat) ± 0.0130 (syst)	
		e_2	0.1851 ± 0.0013 (stat) ± 0.0031 (syst)	
		e_3	-0.0043 ± 0.0007 (stat) ± 0.0017 (syst)	
6n1	1	A	0.0990 ± 0.0002 (stat) ± 0.0004 (syst)	49.91
		a_1	-0.1761 ± 0.0048 (stat) ± 0.0091 (syst)	
6n1	3	A	0.1546 ± 0.0003 (stat) ± 0.0007 (syst)	85.15
		a_1	0.1199 ± 0.0037 (stat) ± 0.0088 (syst)	
6p1	1	A	0.1597 ± 0.0004 (stat) ± 0.0007 (syst)	16.06
		a_1	0.3552 ± 0.0147 (stat) ± 0.0292 (syst)	
6p1	3	A	0.2146 ± 0.0005 (stat) ± 0.0013 (syst)	15.12
		a_1	0.5077 ± 0.0114 (stat) ± 0.0300 (syst)	

Table 9.12: Associated Legendre function coefficient fitting results for ^{6}Li at a photon energy of 15.6 MeV. The orientation signifies which detector in the most upstream ring was on top of the array.

Channel	Orientation	Coefficient	Fit Result	Reduced χ^2
6n0	1	A	0.1482 ± 0.0003 (stat) ± 0.0008 (syst)	21.98
		a_1	0.3119 ± 0.0041 (stat) ± 0.0109 (syst)	
		a_2	-0.2612 ± 0.0061 (stat) ± 0.0151 (syst)	
		e_2	0.2035 ± 0.0016 (stat) ± 0.0039 (syst)	
		e_3	-0.0036 ± 0.0009 (stat) ± 0.0023 (syst)	
6n0	3	A	0.3320 ± 0.0004 (stat) ± 0.0017 (syst)	13.53
		a_1	0.2392 ± 0.0026 (stat) ± 0.0105 (syst)	
		a_2	-0.1751 ± 0.0041 (stat) ± 0.0150 (syst)	
		e_2	0.1850 ± 0.0010 (stat) ± 0.0034 (syst)	
		e_3	0.0192 ± 0.0006 (stat) ± 0.0020 (syst)	
6n1	1	A	0.1234 ± 0.0003 (stat) ± 0.0006 (syst)	91.41
		a_1	-0.3019 ± 0.0041 (stat) ± 0.0109 (syst)	
6n1	3	A	0.2513 ± 0.0004 (stat) ± 0.0013 (syst)	95.30
		a_1	-0.0885 ± 0.0028 (stat) ± 0.0097 (syst)	
6p1	1	A	0.1920 ± 0.0005 (stat) ± 0.0012 (syst)	15.33
		a_1	0.1928 ± 0.0112 (stat) ± 0.0300 (syst)	
6p1	3	A	0.3527 ± 0.0007 (stat) ± 0.0023 (syst)	10.31
		a_1	0.3438 ± 0.0088 (stat) ± 0.0330 (syst)	

Table 9.13: Final associated Legendre function coefficient values for ^{6}Li at photon energies of 15 and 15.6 MeV for the reaction channel 6n0.

Energy	Coeff.	Value	Energy	Coeff.	Value
15 MeV	a_1	0.293 ± 0.036	15.6 MeV	a_1	0.264 ± 0.032
	a_2	-0.310 ± 0.051		a_2	-0.206 ± 0.046
	e_2	0.194 ± 0.012		e_2	0.191 ± 0.011
	e_3	0.0023 ± 0.0068		e_3	0.0122 ± 0.0064

nuclear potential is independent of the electric charge, we would expect the cross sections for these mirror reactions to be nearly equal. It is most likely that the method used to separate the two non-isolatable reaction channels is not able to completely separate the 6n1 reaction channel from the 6p1 reaction channel. Instead, there is still some mixing occurring and we should not take these a_1 values to be physical. The values reported in table 9.14 were computed so that we could better reproduce the observed neutron spectra in the Geant4 simulation.

Table 9.14: Coefficients a_1 for reaction channels 6n1 and 6p1 for photon energies of 15 and 15.6 MeV. Note that these values should not be taken to have physical meaning but are useful as input to the simulation.

Energy (MeV)	a_1 for 6n1	a_1 for 6p1
15	-0.056 ± 0.056	0.435 ± 0.090
15.6	-0.182 ± 0.074	0.278 ± 0.083

Table 9.15 reports the ratio of the cross sections of the separated reaction channels over the cross section of all observable reaction channels computed from the A values of the associated Legendre function fits. The differences in the results for 6n1 and 6p1 are likely due to the inability of the method of separating non-isolatable reaction channels to properly separate these two reaction channels based on their very broad time-of-flight spectra. No attempt has been made at this point to account for the contribution of neutrons from the reaction channel 6p0. These neutrons will mainly affect the computed neutron yield of the 6p1 reaction channel. A check of the empty-target data can confirm that there are negligible numbers of neutrons coming from sources other than the lithium target at theses energies.

Table 9.15: Calculated cross section ratios computed from the A values of the associated Legendre function fits. No corrections are made at this point for the 6p0 reaction channel.

Energy (MeV)	$\frac{\sigma[\text{6n0}]}{\sigma[\text{6n0 + 6n1 + 6p1}]}$	$\frac{\sigma[\text{6n1}]}{\sigma[\text{6n0 + 6n1 + 6p1}]}$	$\frac{\sigma[\text{6p1}]}{\sigma[\text{6n0 + 6n1 + 6p1}]}$
15	0.314 ± 0.007	0.272 ± 0.008	0.412 ± 0.008
15.6	0.341 ± 0.007	0.267 ± 0.011	0.391 ± 0.009

9.8 Analysis Performed on Data Generated by the Simulation

In order to verify that our analysis techniques for the separation of non-isolatable reaction channels are working as they should, we attempted to extract the Legendre polynomial coefficients from simulations of the photodisintegration of ^{6}Li at photon energies of 13 and 15 MeV. The simulations use the coefficients of tables 9.8, 9.9, 9.10, 9.13, 9.14 and 9.15 as inputs. They output the data in the same way that the real Blowfish Neutron Detector Array would, and we are able to extract spectra for the time-of-flight and light output in the same way as the measured data. We then ran the simulated spectra through the same analysis software as the real spectra. The computed Legendre polynomial coefficients are reported in tables 9.16 and 9.17. Notice that there is no systematic uncertainty since we are performing the analysis of data computed with the simulation.

Table 9.16: Associated Legendre function coefficient fitting results for ^{6}Li data from a Geant4 simulation at a photon energy of 13 MeV.

Channel	Coefficient	Fit Result	Reduced χ^2
6n0	A	0.3633 ± 0.0004 (stat)	40.13
	a_1	0.2788 ± 0.0017 (stat)	
	a_2	-0.3816 ± 0.0025 (stat)	
	e_2	0.2697 ± 0.0008 (stat)	
	e_3	0.0012 ± 0.0004 (stat)	
6n1	A	0.3155 ± 0.0004 (stat)	34.69
	a_1	-0.1238 ± 0.0023 (stat)	
6p1	A	0.3152 ± 0.0005 (stat)	18.45
	a_1	0.2944 ± 0.0074 (stat)	

We can perform an analysis on these values to obtain results which we can compare to the inputs. This comparison is done in tables 9.18 and 9.19. The normalised difference is calculated by taking the absolute value of the difference between the simulation input and the analysis result and dividing it by the uncertainty.

We can draw a few conclusions from tables 9.18 and 9.19. The method of separating non-isolatable reaction channels is working since we are getting results close to the input values. However, we may be underestimating our uncertainties. We use a semi-ad hoc method of finding the final uncertainty by multiplying the uncertainty returned by the fitting routine with the reduced χ^2 value. This is done in order to compensate for uncertainties in the neutron yields introduced by

Table 9.17: Associated Legendre function coefficient fitting results for ^{6}Li data from a Geant4 simulation at a photon energy of 15 MeV.

Channel	Coefficient	Fit Result	Reduced χ^2
6n0	A	0.3243 ± 0.0004 (stat)	64.78
	a_1	0.3402 ± 0.0019 (stat)	
	a_2	-0.3475 ± 0.0028 (stat)	
	e_2	0.2264 ± 0.0009 (stat)	
	e_3	0.0094 ± 0.0005 (stat)	
6n1	A	0.2489 ± 0.0003 (stat)	237.19
	a_1	-0.1229 ± 0.0025 (stat)	
6p1	A	0.4078 ± 0.0006 (stat)	38.32
	a_1	0.4464 ± 0.0060 (stat)	

Table 9.18: Comparison of simulation inputs to analysis results for ^{6}Li with a photon energy of 13 MeV. Note that σ[all] = σ[6n0 + 6n1 + 6p1].

Channel	Coefficient	Simulation Input	Analysis Result	Normalised Difference
6n0	σ[6n0]/σ[all]	0.369	0.365 ± 0.003	1.3
	a_1	0.270	0.279 ± 0.011	0.8
	a_2	-0.311	-0.382 ± 0.016	4.4
	e_2	0.226	0.270 ± 0.005	8.8
	e_3	0.0017	0.0012 ± 0.0025	0.2
6n1	$\frac{1}{2}\sigma$[6n1 + 6p1]/σ[all]	0.315	0.317 ± 0.002	1.0
	a_1	-0.116	-0.124 ± 0.014	0.6
6p1	$\frac{1}{2}\sigma$[6n1 + 6p1]/σ[all]	0.316	0.317 ± 0.002	0.5
	a_1	0.278	0.294 ± 0.032	0.5

Table 9.19: Comparison of simulation inputs to analysis results for ^{6}Li with a photon energy of 15 MeV. Note that σ[all] = σ[6n0 + 6n1 + 6p1].

Channel	Coefficient	Simulation Input	Analysis Result	Normalised Difference
6n0	σ[6n0]/σ[all]	0.314	0.331 ± 0.004	4.3
	a_1	0.293	0.340 ± 0.015	3.1
	a_2	-0.310	-0.348 ± 0.023	1.7
	e_2	0.194	0.226 ± 0.007	4.6
	e_3	0.0023	0.0094 ± 0.0040	1.8
6n1	σ[6n1]/σ[all]	0.273	0.254 ± 0.005	3.8
	a_1	-0.056	-0.123 ± 0.039	1.7
6p1	σ[6p1]/σ[all]	0.413	0.416 ± 0.005	0.6
	a_1	0.435	0.446 ± 0.037	0.3

the method of separating non-isolatable reaction channels.

9.9 Absolute Cross Section Determination

We apply the Compton scattering comparison method of section 7.4.1 to determine the absolute cross sections of the reactions we have examined in this chapter. We emit $N_{sim} = 5 \times 10^7$ neutrons and $\Phi^s = 5 \times 10^8$ photons in their respective simulations. The average neutron and gamma-ray yield ratios are calculated as discussed in section 8.6 and are reported in table 9.20. The cross sections are reported in table 9.21. The σ[6n0] cross section is reported for beam energies of 8 and 9 MeV, since this was the only reaction channel observable. The σ[6n0 + 6n1 + 6p1] cross section is reported for beam energies of 10, 11, 12, 13, 15 and 15.6 MeV since these three reaction channels were observable. These will be further discussed in chapter 13 and divided into their individual reaction channels when possible.

Table 9.20: Ratios of simulated and measured yields used to determine the absolute cross section of ^{6}Li photodisintegration through the Compton scattering comparison method for the data with photon energies below 16 MeV. The first uncertainty is statistical and the second is systematic.

Beam Energy	Orientation	$\left\langle N^s_{d,\gamma}/N_{d,\gamma} \right\rangle$	$\left\langle N_{d,n}/N^s_{d,n} \right\rangle$
8 MeV	1	$1.372 \pm 0.002 \pm 0.034$	$(2.46 \pm 0.08 \pm 0.25) \times 10^{-3}$
9 MeV	3	$1.342 \pm 0.002 \pm 0.033$	$(3.06 \pm 0.05 \pm 0.19) \times 10^{-3}$
10 MeV	1	$1.754 \pm 0.003 \pm 0.043$	$(3.48 \pm 0.05 \pm 0.14) \times 10^{-3}$
11 MeV	3	$1.764 \pm 0.003 \pm 0.043$	$(4.33 \pm 0.05 \pm 0.14) \times 10^{-3}$
12 MeV	3	$0.935 \pm 0.001 \pm 0.023$	$(9.10 \pm 0.08 \pm 0.24) \times 10^{-3}$
13 MeV	1	$1.901 \pm 0.003 \pm 0.047$	$(4.58 \pm 0.05 \pm 0.12) \times 10^{-3}$
13 MeV	3	$0.908 \pm 0.001 \pm 0.022$	$(9.55 \pm 0.08 \pm 0.23) \times 10^{-3}$
15 MeV	1	$1.880 \pm 0.004 \pm 0.046$	$(5.02 \pm 0.06 \pm 0.15) \times 10^{-3}$
15 MeV	3	$1.036 \pm 0.002 \pm 0.025$	$(9.16 \pm 0.08 \pm 0.25) \times 10^{-3}$
15.6 MeV	1	$1.089 \pm 0.002 \pm 0.027$	$(8.53 \pm 0.08 \pm 0.22) \times 10^{-3}$

Table 9.21: Absolute cross sections for the observable photonuclear reaction channels of ^{6}Li. For 8 and 9 MeV all = 6n0 and for 10 to 15.6 MeV all = 6n0 + 6n1 + 6p1.

Beam Energy (MeV)	σ[all] (mb)
8	0.573 ± 0.063
9	0.698 ± 0.048
10	1.038 ± 0.051
11	1.298 ± 0.055
12	1.446 ± 0.054
13	1.477 ± 0.038
15	1.609 ± 0.044
15.6	1.579 ± 0.058

Chapter 10

Data Analysis for ^{7}Li With Photon Energies Below 16 MeV

10.1 Introduction

Photoneutrons have been observed with the Blowfish Neutron Detector Array for five energies below 16 MeV. Again, we take a qualitative examination of the data before beginning a quantitative one. As was the case for the ^{6}Li data, we see definite structure in the neutron kinetic energy spectra. The kinetic energy plots in figure 10.1 have two prominent features, as did the ^{6}Li data. The

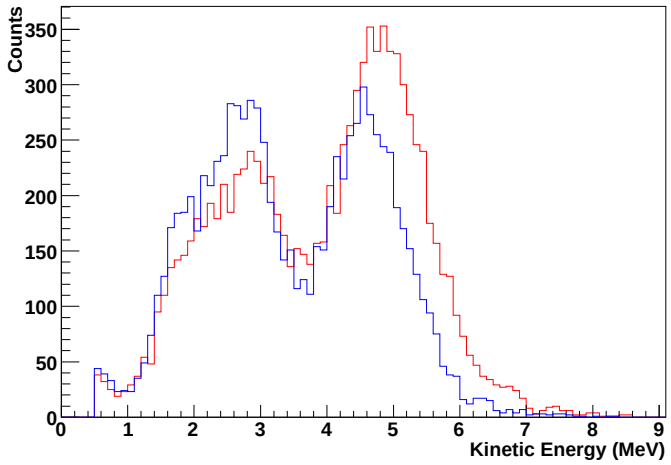

Figure 10.1: Experimental neutron kinetic energy spectrum reported by two neutron detectors at a polar angle $\theta = 90°$ with one detector at an angle-to-polarisation of $\phi = 0°$ (red) while the other is at $\phi = 90°$ (blue) with a photon beam of 13 MeV and ^{7}Li target.

high energy features are due to neutrons emitted from the single-neutron knockout reaction to the stable, ground state of ^{6}Li, $^7\text{Li} + \gamma \rightarrow n + {}^6\text{Li(g.s.)}$. The low energy feature is made up of the rest of the reaction channels, which include single-neutron knockout reactions to excited states of ^{6}Li, single deuteron knockout reactions, and possibly three-body decays.

We examine the angular distribution of the neutrons in figure 10.2. The high-energy feature

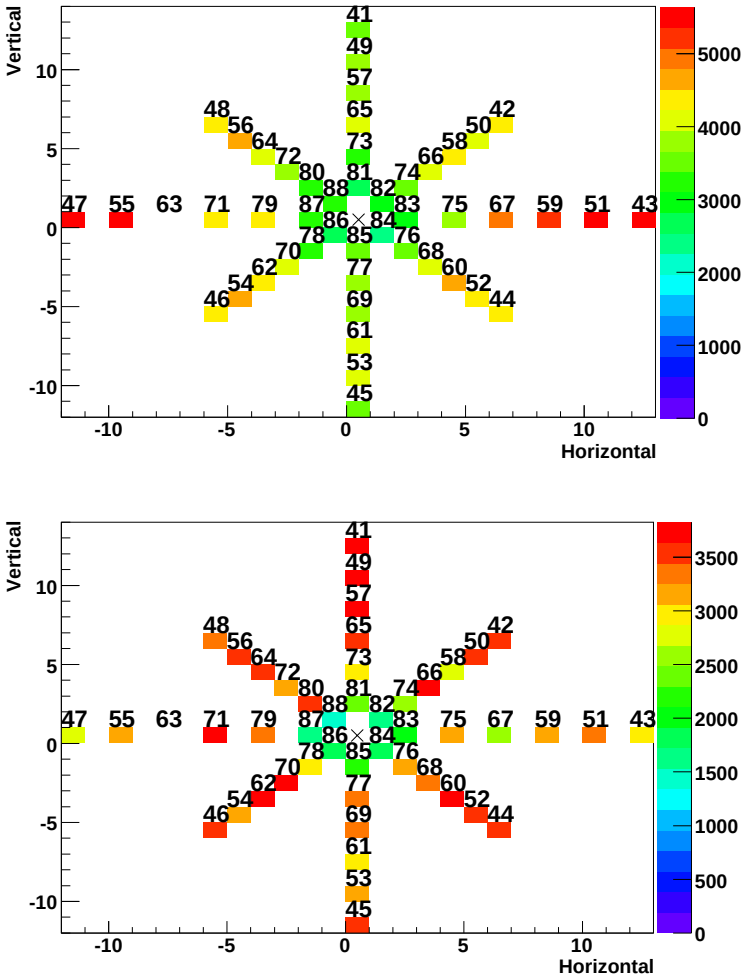

Figure 10.2: Experimental hits on the downstream detectors of Blowfish for the high-energy neutrons (top) and low-energy neutrons (bottom) emitted from ^{7}Li. The photon beam has an energy of 13 MeV and is travelling into the page. The detectors are labelled by their detector numbers and the number of hits are given by the colour index.

certainly has a dependence on polarisation. The very simple cuts placed on the data do not present as clear a picture of the low-energy neutrons. There may be some dependence on polarisation and it is even possible that the dependence is opposite to the high energy neutrons. Figure 10.1 also seems to show the high-energy and low-energy neutrons having opposite dependence on polarisation.

There are many more reaction channels involved with the photodisintegration of ^{7}Li than ^{6}Li, as can be seen from table 10.1. We can simplify things by sorting these reaction channels into groups.

Table 10.1: Reaction channels to consider in the analysis of the ^{7}Li data below 16 MeV.

Label	Reaction		Threshold (MeV)
7n0	$^7\mathrm{Li} + \gamma \rightarrow n + {}^6\mathrm{Li}$(g.s.)		7.3
7nd	$^7\mathrm{Li} + \gamma \rightarrow n + d + {}^4\mathrm{He}$(g.s.)		8.7
7n1	$^7\mathrm{Li} + \gamma \rightarrow n + {}^6\mathrm{Li}$(2.19)		9.5
7d0	$^7\mathrm{Li} + \gamma \rightarrow d + {}^5\mathrm{He}$(g.s.)	$\rightarrow n + d + {}^4\mathrm{He}$(g.s.)	9.6
7n2	$^7\mathrm{Li} + \gamma \rightarrow n + {}^6\mathrm{Li}$(3.56)		10.9
7d1	$^7\mathrm{Li} + \gamma \rightarrow d + {}^5\mathrm{He}$(1.27)	$\rightarrow n + d + {}^4\mathrm{He}$(g.s.)	10.9
7n3	$^7\mathrm{Li} + \gamma \rightarrow n + {}^6\mathrm{Li}$(4.31)		11.6
7p1	$^7\mathrm{Li} + \gamma \rightarrow p + {}^6\mathrm{He}$(1.78)	$\rightarrow p + 2n + {}^4\mathrm{He}$(g.s.)	11.8
7np0	$^7\mathrm{Li} + \gamma \rightarrow n + p + {}^5\mathrm{He}$(g.s.)	$\rightarrow 2n + p + {}^4\mathrm{He}$(g.s.)	11.8
7n4	$^7\mathrm{Li} + \gamma \rightarrow n + {}^6\mathrm{Li}$(5.37)		12.7
7n5	$^7\mathrm{Li} + \gamma \rightarrow n + {}^6\mathrm{Li}$(5.65)		12.9
7nn0	$^7\mathrm{Li} + \gamma \rightarrow 2n + {}^5\mathrm{Li}$(g.s.)	$\rightarrow 2n + p + {}^4\mathrm{He}$(g.s.)	12.9
7np1	$^7\mathrm{Li} + \gamma \rightarrow n + p + {}^5\mathrm{He}$(1.27)	$\rightarrow 2n + p + {}^4\mathrm{He}$(g.s.)	13.1
7nn1	$^7\mathrm{Li} + \gamma \rightarrow 2n + {}^5\mathrm{Li}$(1.49)	$\rightarrow 2n + p + {}^4\mathrm{He}$(g.s.)	14.4

There are six single-neutron knockout reactions at accessible energies: 7n0, 7n1, 7n2, 7n3, 7n4 and 7n5. There are two single-deuteron knockout reactions: 7d0 and 7d1. There is no 7p0 reaction channel as the ground state of ^{6}He undergoes beta decay and produces no neutrons. However, there is a 7p1 reaction channel as the excited states of ^{6}He are not particle stable. The reaction channels enumerated so far are all two-body decays and are discussed in section 10.2. There are a number of three-body reaction channels: 7nd, 7np0, 7nn0, 7np1 and 7nn1. These are discussed in section 10.3. We neglect the 4-body decay $^7\mathrm{Li} + \gamma \rightarrow 2n + p + {}^4\mathrm{He}$. While not technically a reaction channel, there will also be a contribution from the ^{6}Li content of the target. This is discussed in section 10.4.

10.2 Discussion of the Two-Body Reaction Channels

Even though ^{7}Li has only one more neutron than ^{6}Li, the two-body reaction channels are quite different. With ^{6}Li, the single neutron and proton knockout reactions lead to highly unstable intermediate states that decay quickly to the alpha particle. With ^{7}Li, the single neutron and proton knockout reactions lead to states of ^{6}Li and ^{6}He, which both have particle stable states.

It is possible to isolate the 7n0 reaction channel as it produces neutrons with higher energies than any other reaction channel. Unfortunately, the remaining reaction channels cannot be isolated. The first two excited states of ^{6}Li have narrow decay widths causing the 7n1 and 7n2 neutron kinetic energy spectra to be narrow. The higher excited states have greater decay widths causing the 7n3, 7n4 and 7n5 reaction channels to have broad neutron kinetic energy spectra. According to the review of Tilley *et al.* [Til02] only one of the excited states of ^{6}Li that we are considering can produce neutrons in its decay. This is the state ^{6}Li(5.36), corresponding to the 7n4 reaction channel. All other states decay into a deuteron and alpha particle or into the ground state ^{6}Li(g.s.) through the emission of a photon. It is not known, however, what the branching ratio of the ^{6}Li(5.36) decay is and we assume, for the purposes of this thesis, that only one neutron is produced by the 7n4 reaction channel. We model these reactions the same way as the single neutron knockout reactions of ^{6}Li, using the relativistic two-body photodisintegration kinematics discussed in section 5.3.1.

The knockout of a deuteron from ^{6}Li cannot proceed through the electric dipole process. This is not the case for ^{7}Li and we have two single deuteron knockout reactions, 7d0 and 7d1. These are similar to the ^{6}Li single proton knockout reactions 6p0 and 6p1 and we model them using the same relativistic two-body decay reaction discussed in section 5.3.2.

The 7p1 interaction is interesting for a number of reasons. First, there is no 7p0 reaction listed in table 10.1 as ^{6}He(g.s.) is particle stable and decays through beta decay. In contrast, the ^{6}He(1.80) branching ratio is $\Gamma_\gamma/\Gamma_\alpha \leq 2 \times 10^{-6}$ [Til02], so the first excited state will decay into two neutrons and an alpha particle. It is not yet clear how we should model this decay: as a direct three-body decay or two two-body decays. We can compute the Q values of each reaction to aid us. Including the excitation energy of $E_x = (1.797 \pm 0.025)$ MeV [Til02], the Q value of the two-body decay is

$$\begin{aligned} Q_2 &= m(^6\mathrm{He})c^2 + E_x - m(^5\mathrm{He})c^2 - m_n c^2 \\ &= (5606.561 \pm 0.001)\ \mathrm{MeV} + (1.797 \pm 0.025)\ \mathrm{MeV} - (4668.854 \pm 0.047)\ \mathrm{MeV} - 939.566\ \mathrm{MeV} \\ &= (-0.062 \pm 0.053)\mathrm{MeV} \end{aligned} \tag{10.1}$$

while the Q value of the three-body decay is

$$\begin{aligned} Q_3 &= m(^6\mathrm{He})c^2 + E_x - m(^4\mathrm{He})c^2 - 2 \times m_n c^2 \\ &= (5606.561 \pm 0.001)\ \mathrm{MeV} + (1.797 \pm 0.025)\ \mathrm{MeV} - 3728.402\ \mathrm{MeV} - 2 \times 939.566\ \mathrm{MeV} \\ &= (0.824 \pm 0.025)\mathrm{MeV} \end{aligned} \tag{10.2}$$

where we have taken the masses from [Aud03]. Since Q_2 is negative within the uncertainty bounds, it is an endothermic reaction and does not occur. We therefore conclude that the decay is a three-body decay and describe it using the kinematics of the semi-relativistic three-body decay described in section 5.3.4.

10.3 Discussion of the Three-Body Reaction Channels

There are not many measurements concerning the three-body reaction channels.

The emission of a neutron-proton pair is of minimal concern for these measurements since the threshold of the 7np0 reaction channel is high, 11.8 MeV. Several authors have studied the quasideuteron reaction at higher energies [Bar54, Bar58, Odi56, San70, Wat56, Whi58] but no measurements have been made in the energy range of interest. Given the results of Wade *et al.* [Wad84] on ^{6}Li, it seems reasonable to neglect the quasideuteron interaction.

The only other measurement of a three-body reaction channel is that of Kotikov and Makhnovskiĭ [Kot73], who studied the ^{7}Li+$\gamma \rightarrow p$+2^{3}H reaction channel, which has a threshold far above 16 MeV and does not produce neutrons. There is little experimental guidance to help us treat three-body reactions on ^{7}Li.

While we are unable to completely eliminate the three-body reaction channels from our discussion, we can reduce the effect of their possible existence on our data. When we make a light-output cut to isolate the 7n0 reaction channel, we can make the cut high enough to ensure that none of the neutrons are from a three-body reaction. For the other reaction channels we find that the data is well explained without the need of a three-body reaction. We therefore neglect the three-body reaction channels.

10.4 Discussion of the ^{6}Li Contribution

A natural lithium target[1] was found to be much more economical than an enriched ^{7}Li target. Natural lithium contains an amount of ^{6}Li and we must subtract this contribution from our data. The accepted concentration of ^{7}Li in naturally occurring lithium is 92.41 $\pm$ 0.04 % [DeL03]. There is very little variation in the mole fraction between ^{6}Li and ^{7}Li in natural lithium. The lowest recorded fraction of ^{7}Li in a sample is 92.27 % while the highest recorded fraction in a sample is 92.78 % [DeL03]. We can therefore feel confident in assuming that our target is 92.41 $\pm$ 0.04 % ^{7}Li and 7.59 $\pm$ 0.04 % ^{6}Li.

Since we have made measurements with the enriched ^{6}Li target for each measurement made with the natural lithium target we can perform a simple subtraction of the ^{6}Li contribution. The

[1] The terms natural lithium target and ^{7}Li target will be used interchangeably except when discussing the ^{6}Li content of the target.

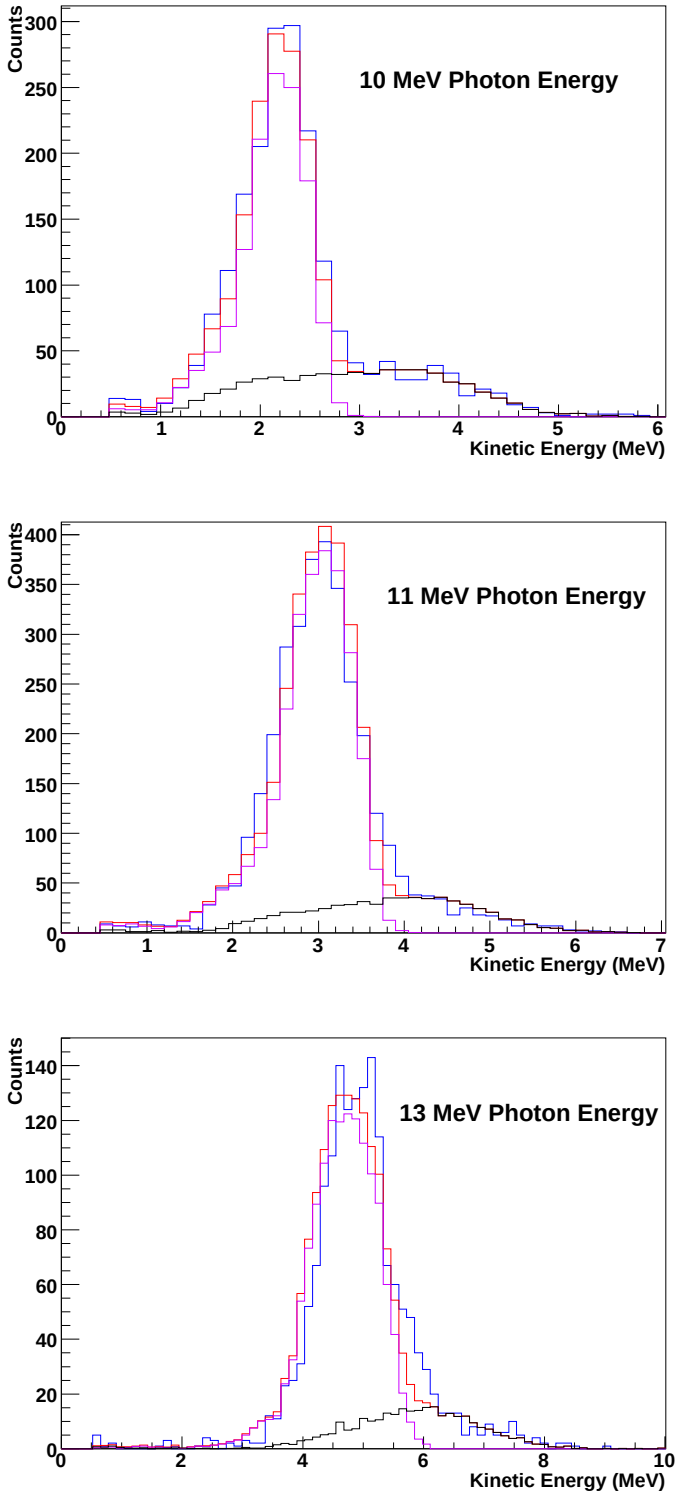

Figure 10.3: Neutron kinetic energy distributions for detector 48 at 10, 11 and 13 MeV with the experimental natural lithium target data (blue), ^{6}Li contribution (black), simulated 7n0 reaction channel (purple) and sum of the ^{6}Li contribution plus the 7n0 simulation (red). Minimum light-output cuts were made to ensure that the only ^{7}Li reaction channel contributing neutrons was 7n0: 200 keV$_{ee}$ for 10 MeV, 400 keV$_{ee}$ for 11 MeV and 1200 keV$_{ee}$ for 13 MeV.

^{6}Li contribution is computed by taking the neutron kinetic energy spectrum measured with the ^{6}Li target and scaling it. First, we scale by the relative number of photons incident on the targets. This is calculated by dividing the total number of counts from a flux monitor for the natural lithium measurement by the same quantity for the ^{6}Li measurement. Second, we scale by the ^{6}Li molar fraction of the target, 0.0759.

The plots in figure 10.3 show neutron kinetic energy spectra at three energies for a single detector. Notice how the ^{6}Li contribution has neutrons with higher energies than the ^{7}Li contribution due to the higher threshold of the ^{7}Li photoneutron reaction. This allows us to see that the scaling is effective and describes the neutrons with high energies very well. By computing the ^{6}Li contribution to our measurements in this way, we are easily able to make the required subtraction.

10.5 Analysis for the Photon Energies of 10 and 11 MeV

The 7n0 reaction channel at photon beam energies of 10 and 11 MeV is isolatable. It can be completely isolated by a 500 keV$_{ee}$ light-output cut which maximises PSD effectiveness. Figure 10.3, which is used to discuss the ^{6}Li contribution to our data, shows neutron kinetic energy distributions for the 7n0 reaction channel at these energies.

Note that the 500 keV$_{ee}$ cut is rather high for the 10 MeV data and it suffers from poor statistics. The dominant systematic uncertainty in this case is the light-output cut. This is the dominant systematic uncertainty since a small change in the light-output cut has a large change in the neutron yield due to the low light-output of the neutron events.

Tables 10.2 and 10.3 report the results of fitting the simulated spectra to the measured spectra. Good stability was found using a_k and e_k values up to and including $k = 4$. This can be contrasted against the case of ^{6}Li where the interfering and non-isolatable reaction channels would not allow fits of this precision. The reduced χ^2 for both of these fits is quite small. However, we feel that we are accurately estimating our uncertainties and will not adjust any values to artificially bring the reduced χ^2 closer to one.

No reduced χ^2 value, statistical or systematic uncertainty is reported for the ^{6}Li contribution to the natural lithium neutron spectra in tables 10.2 and 10.3. This is because we are normalising the neutron yields from the simulation, the distributions we found in chapter 9, to those of the measured spectra in order to determine A. We are not performing a χ^2 fit. We take the uncertainty in A for the ^{6}Li contribution to be the uncertainty in the flux monitor since this is by far the dominant source of uncertainty. Since there is uncertainty in both the photon flux for the run with the ^{6}Li target and the natural lithium target, we must add these uncertainties in quadrature to obtain a total uncertainty of 11% in the ^{6}Li contribution. By modifying equation (7.10) using the number

Table 10.2: Associated Legendre function coefficient fitting results for ^{7}Li at a photon energy of 10 MeV. The orientation signifies which detector in the most upstream ring was on top of the array.

Channel	Orientation	Coefficient	Fit Result	Reduced χ^2
7n0	1	A	0.0594 ± 0.0004 (stat) ± 0.0011 (syst)	0.54
		a_1	-0.3297 ± 0.0120 (stat) ± 0.0358 (syst)	
		a_2	0.0836 ± 0.0176 (stat) ± 0.0518 (syst)	
		a_3	0.1907 ± 0.0215 (stat) ± 0.0633 (syst)	
		a_4	-0.0005 ± 0.0287 (stat) ± 0.0863 (syst)	
		e_2	-0.0815 ± 0.0038 (stat) ± 0.0115 (syst)	
		e_3	-0.0114 ± 0.0020 (stat) ± 0.0063 (syst)	
		e_4	0.0037 ± 0.0014 (stat) ± 0.0041 (syst)	
^{6}Li	1	A	0.0174 ± 0.0019	

Table 10.3: Associated Legendre function coefficient fitting results for ^{7}Li at a photon energy of 11 MeV. The orientation signifies which detector in the most upstream ring was on top of the array.

Channel	Orientation	Coefficient	Fit Result	Reduced χ^2
7n0	3	A	0.1102 ± 0.0003 (stat) ± 0.0008 (syst)	0.73
		a_1	-0.0428 ± 0.0055 (stat) ± 0.0158 (syst)	
		a_2	0.0129 ± 0.0089 (stat) ± 0.0251 (syst)	
		a_3	0.0678 ± 0.0111 (stat) ± 0.0317 (syst)	
		a_4	-0.0137 ± 0.0134 (stat) ± 0.0391 (syst)	
		e_2	-0.0714 ± 0.0018 (stat) ± 0.0051 (syst)	
		e_3	-0.0019 ± 0.0010 (stat) ± 0.0028 (syst)	
		e_4	-0.0027 ± 0.0006 (stat) ± 0.0019 (syst)	
^{6}Li	3	A	0.0277 ± 0.0030	

densities of ^{6}Li and ^{7}Li in the natural lithium target, we can compute the relative cross section

$$\frac{\sigma_7}{\sigma_6} = \frac{0.0759}{0.9241}\frac{A_7}{A_6} \tag{10.3}$$

where 0.0759 is the fraction of ^{6}Li in the target and 0.9241 is the fraction of ^{7}Li in the target. We can therefore use the A values reported in tables 10.2 and 10.3 to find the relative photoneutron cross section of ^{7}Li to that of ^{6}Li. We can also use the isotope neutron yield comparison method, described in section 7.4.2, to compute the same quantity and the results are displayed in table 10.4. Note that these two methods have rather different dominant sources of uncertainties. The

Table 10.4: Calculation of σ[7n0]/σ[6n0 + 6n1 + 6p1] using the A values computed from the fits and the isotope neutron yield comparison method

Photon Energy	10 MeV	11 MeV
From A Values	0.280 ± 0.002 (stat) ± 0.031 (syst)	0.327 ± 0.001 (stat) ± 0.036 (syst)
Isotope Method	0.303 ± 0.006 (stat) ± 0.052 (syst)	0.273 ± 0.004 (stat) ± 0.048 (syst)
Weighted Average	0.286 ± 0.027	0.308 ± 0.029

dominant source of systematic uncertainties in the A value method is the three-paddle photon flux monitor. The dominant source of systematic uncertainty in the isotope neutron yield comparison method is due to the cut on the ADC that isolates the ^{6}Li contribution. Since these two methods have essentially independent sources of systematic uncertainties, we can add their uncertainties in quadrature when we compute the weighted average.

For the isotope neutron yield comparison method on the 10 MeV data, we use a 900 keV$_{ee}$ cut to isolate the ^{6}Li contribution, then a 500 keV$_{ee}$ cut as the second cut. Similarly we use a 1400 keV$_{ee}$ cut to isolate the ^{6}Li contribution for the 11 MeV data and we use the standard 500 keV$_{ee}$ cut as

Table 10.5: Final associated Legendre function coefficient values for ^{7}Li at photon energies of 10 and 11 MeV for the reaction channel 7n0.

Energy	Coeff.	Value	Energy	Coeff.	Value
10 MeV	a_1	-0.330 ± 0.038	11 MeV	a_1	-0.043 ± 0.017
	a_2	0.084 ± 0.055		a_2	0.013 ± 0.027
	a_3	0.191 ± 0.067		a_3	0.068 ± 0.034
	a_4	-0.001 ± 0.091		a_4	-0.014 ± 0.041
	e_2	-0.082 ± 0.012		e_2	-0.0714 ± 0.0054
	e_3	-0.0114 ± 0.0066		e_3	-0.0019 ± 0.0030
	e_4	0.0037 ± 0.0043		e_4	-0.0027 ± 0.0020

the second cut.

The final Legendre function coefficient values are computed by adding in quadrature the systematic and statistical uncertainties of tables 10.2 and 10.3. The results are reported in table 10.5.

10.6 Analysis for the Photon Energies of 12, 13 and 15 MeV

For the data taken with a photon beam energy of 12 MeV, we can isolate the 7n0 reaction channel with a 900 keV_{ee} light-output cut, while we use a 1400 keV_{ee} light-output cut for the 13 MeV data, and a 2200 keV_{ee} light-output cut for the 15 MeV data. An example of light-output spectra is given in figure 10.4 with the cut marked by a vertical line. These cuts allows for a nearly perfect

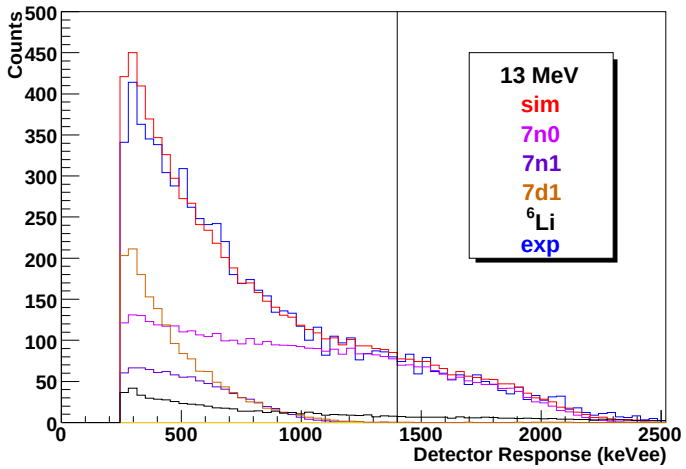

Figure 10.4: The light-output spectra for various simulated reaction channels and the measured spectrum. The data was taken with a 13 MeV photon beam and the vertical line is at the value of the cut used to isolate the 7n0 reaction channel, 1400 keV_{ee}. Notice that only the 7n0 reaction channel exists above this cut. The red histogram is the sum of the simulation histograms.

elimination of gamma-rays using PSD and eliminate the neutrons from all other possible reaction channels. The dominant source of uncertainty is the uncertainty associated with the light-output cut.

The other reaction channels are not isolatable. Reaction channels we must consider for the 12 MeV data include 7n1, 7d0 and 7d1, which have simulated neutron kinetic energy spectra shown in figure 10.5. The 7d0 reaction channel produces too few neutrons with sufficient kinetic energy to be a major contribution. Both the 7n1 and 7d1 reaction channels contribute neutrons and we cannot eliminate either one. The broader shape of 7d1 fits the data very well and we will use this single reaction channel in the fit to represent both 7d1 and 7n1. We will denote this reaction channel as $7d1^{+}$, where the '+' signifies that other reaction channels are making a contribution and we need

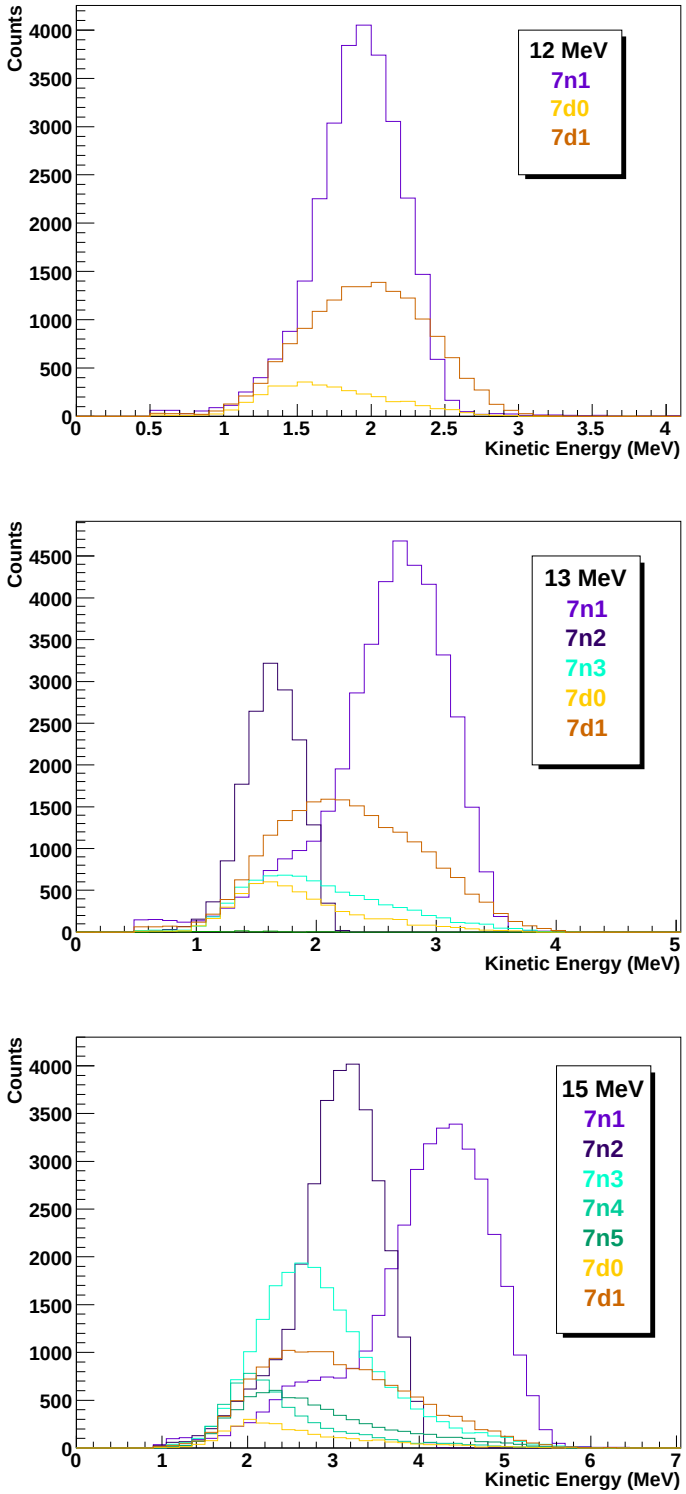

Figure 10.5: Two-body reaction channels with simulated neutron kinetic energies for a detector in the centre ring with a photon beam of 12 MeV (top), 13 MeV (centre) and 15 MeV (bottom). Each histogram is the result of 50 million simulated photodisintegration events for that reaction channel.

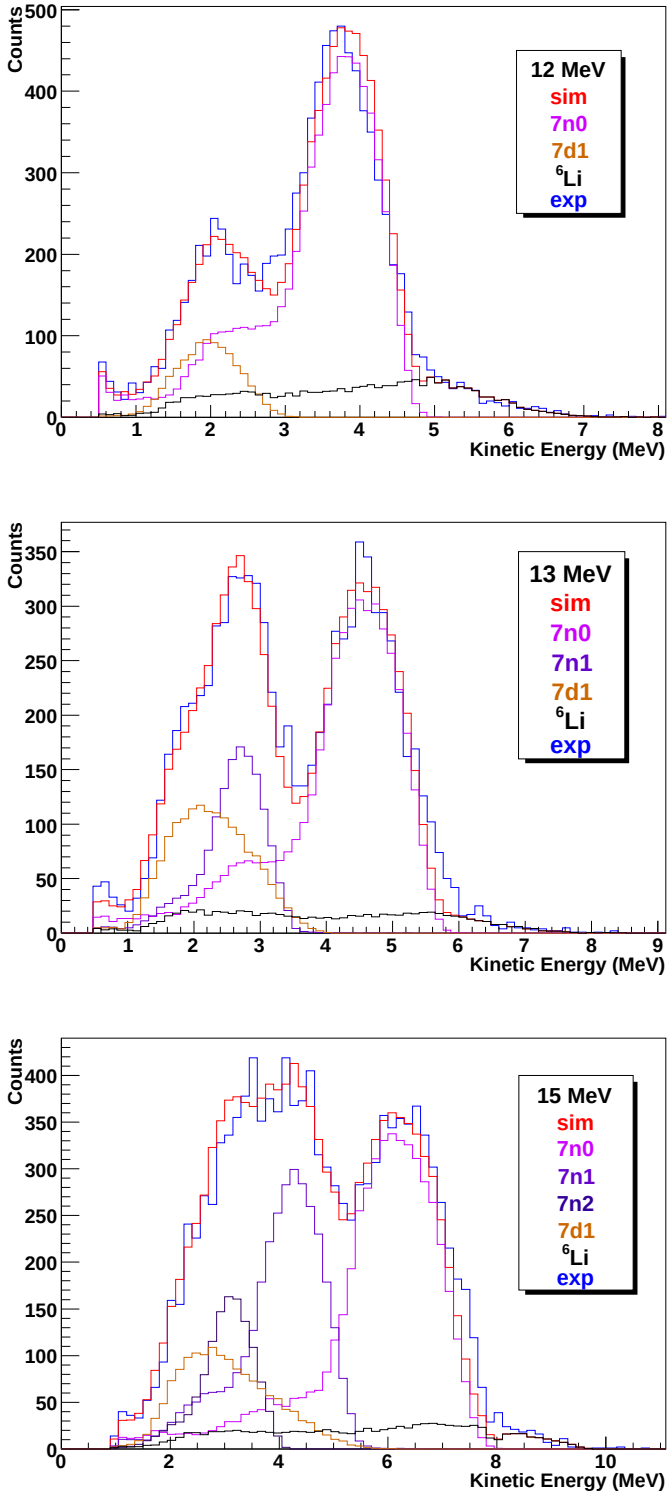

Figure 10.6: The neutron kinetic energy spectra for a beam energy of 12 MeV (top), 13 MeV (centre) and 15 MeV (bottom) for a detector in the centre ring. Shown are the simulations of various reaction channels, the ^{6}Li contribution (black) and the measured spectrum (blue). The red histogram is the sum of the simulation histograms.

Table 10.6: Associated Legendre function coefficient fitting results for ^{7}Li at a photon energy of 12 MeV. The orientation signifies which detector in the most upstream ring was on top of the array. The reaction channel 7d1 was used to fit to data but in reality the data contains contributions from 7n1 as well.

Channel	Orientation	Coefficient	Fit Result	Reduced χ^2
7n0	1	A	0.1182 ± 0.0004 (stat) ± 0.0012 (syst)	0.52
		a_1	-0.0204 ± 0.0051 (stat) ± 0.0152 (syst)	
		a_2	-0.0944 ± 0.0100 (stat) ± 0.0304 (syst)	
		a_3	0.0276 ± 0.0125 (stat) ± 0.0393 (syst)	
		a_4	-0.0388 ± 0.0163 (stat) ± 0.0521 (syst)	
		e_2	0.0204 ± 0.0022 (stat) ± 0.0072 (syst)	
		e_3	-0.0021 ± 0.0011 (stat) ± 0.0021 (syst)	
		e_4	-0.0005 ± 0.0008 (stat) ± 0.0021 (syst)	
7n0	3	A	0.1066 ± 0.0003 (stat) ± 0.0010 (syst)	0.50
		a_1	-0.0133 ± 0.0066 (stat) ± 0.0194 (syst)	
		a_2	-0.0670 ± 0.0107 (stat) ± 0.0313 (syst)	
		a_3	0.0552 ± 0.0110 (stat) ± 0.0340 (syst)	
		a_4	-0.0247 ± 0.0153 (stat) ± 0.0478 (syst)	
		e_2	0.0055 ± 0.0022 (stat) ± 0.0063 (syst)	
		e_3	-0.0002 ± 0.0006 (stat) ± 0.0019 (syst)	
		e_4	-0.0032 ± 0.0007 (stat) ± 0.0022 (syst)	
7d1^{+}	1	A	0.0537 ± 0.0004 (stat) ± 0.0006 (syst)	13.14
		a_1	-0.1990 ± 0.0276 (stat) ± 0.0442 (syst)	
7d1^{+}	3	A	0.0484 ± 0.0004 (stat) ± 0.0005 (syst)	10.27
		a_1	-0.0042 ± 0.0314 (stat) ± 0.0539 (syst)	
^{6}Li	1	A	0.0290 ± 0.0032	
^{6}Li	3	A	0.0264 ± 0.0029	

Table 10.7: Associated Legendre function coefficient fitting results for ^{7}Li at a photon energy of 13 MeV. The orientation signifies which detector in the most upstream ring was on top of the array. The reaction channel 7d1 was used to fit to data but in reality the data contains contributions from 7n2 and 7n3 as well. Table continues in table 10.8.

Channel	Orientation	Coefficient	Fit Result	Reduced χ^2
7n0	1	A	0.1355 ± 0.0005 (stat) ± 0.0017 (syst)	0.25
		a_1	-0.0471 ± 0.0065 (stat) ± 0.0221 (syst)	
		a_2	-0.2224 ± 0.0110 (stat) ± 0.0370 (syst)	
		a_3	0.0313 ± 0.0124 (stat) ± 0.0389 (syst)	
		a_4	-0.0100 ± 0.0159 (stat) ± 0.0557 (syst)	
		e_2	0.0635 ± 0.0024 (stat) ± 0.0088 (syst)	
		e_3	-0.0030 ± 0.0012 (stat) ± 0.0024 (syst)	
		e_4	-0.0006 ± 0.0008 (stat) ± 0.0023 (syst)	
7n0	3	A	0.1094 ± 0.0004 (stat) ± 0.0014 (syst)	0.34
		a_1	-0.0400 ± 0.0074 (stat) ± 0.0228 (syst)	
		a_2	-0.2162 ± 0.0124 (stat) ± 0.0376 (syst)	
		a_3	0.0403 ± 0.0130 (stat) ± 0.0503 (syst)	
		a_4	-0.0427 ± 0.0178 (stat) ± 0.0623 (syst)	
		e_2	0.0632 ± 0.0026 (stat) ± 0.0088 (syst)	
		e_3	-0.0023 ± 0.0013 (stat) ± 0.0044 (syst)	
		e_4	-0.0034 ± 0.0009 (stat) ± 0.0029 (syst)	
7n1	1	A	0.0199 ± 0.0001 (stat) ± 0.0001 (syst)	25.26
		a_1	0.4569 ± 0.0085 (stat) ± 0.0140 (syst)	
		a_2	-0.2608 ± 0.0123 (stat) ± 0.0181 (syst)	
		e_2	-0.1541 ± 0.0035 (stat) ± 0.0054 (syst)	
		e_3	-0.0271 ± 0.0019 (stat) ± 0.0030 (syst)	
7n1	3	A	0.0184 ± 0.0001 (stat) ± 0.0001 (syst)	14.63
		a_1	0.3371 ± 0.0092 (stat) ± 0.0146 (syst)	
		a_2	0.0375 ± 0.0136 (stat) ± 0.0196 (syst)	
		e_2	-0.2129 ± 0.0035 (stat) ± 0.0044 (syst)	
		e_3	0.0041 ± 0.0019 (stat) ± 0.0028 (syst)	

Table 10.8: Associated Legendre function coefficient fitting results for ^{7}Li at a photon energy of 13 MeV. Table continues from table 10.7.

Channel	Orientation	Coefficient	Fit Result	Reduced χ^2
7d1$^+$	1	A	0.0705 ± 0.0002 (stat) ± 0.0005 (syst)	29.96
		a_1	0.3111 ± 0.0184 (stat) ± 0.0476 (syst)	
7d1$^+$	3	A	0.0627 ± 0.0002 (stat) ± 0.0004 (syst)	17.74
		a_1	0.0000 ± 0.0197 (stat) ± 0.0432 (syst)	
^{6}Li	1	A	0.0287 ± 0.0032	
^{6}Li	3	A	0.0266 ± 0.0029	

Table 10.9: Associated Legendre function coefficient fitting results for ^{7}Li at a photon energy of 15 MeV. The orientation signifies which detector in the most upstream ring was on top of the array. The reaction channel 7d1 was used to fit to data but in reality the data contains contributions from 7n3, 7n4 and 7n5 as well. Table continues in table 10.10.

Channel	Orientation	Coefficient	Fit Result	Reduced χ^2
7n0	1	A	0.0864 ± 0.0004 (stat) ± 0.0012 (syst)	0.31
		a_1	0.0075 ± 0.0078 (stat) ± 0.0236 (syst)	
		a_2	-0.2927 ± 0.0141 (stat) ± 0.0362 (syst)	
		a_3	0.0154 ± 0.0193 (stat) ± 0.0435 (syst)	
		a_4	-0.0500 ± 0.0220 (stat) ± 0.0580 (syst)	
		e_2	0.1395 ± 0.0032 (stat) ± 0.0080 (syst)	
		e_3	-0.0036 ± 0.0017 (stat) ± 0.0045 (syst)	
		e_4	0.0017 ± 0.0011 (stat) ± 0.0029 (syst)	
7n0	3	A	0.1262 ± 0.0005 (stat) ± 0.0017 (syst)	0.17
		a_1	0.0251 ± 0.0077 (stat) ± 0.0238 (syst)	
		a_2	-0.2644 ± 0.0123 (stat) ± 0.0371 (syst)	
		a_3	0.0729 ± 0.0160 (stat) ± 0.0511 (syst)	
		a_4	-0.0246 ± 0.0191 (stat) ± 0.0613 (syst)	
		e_2	0.1307 ± 0.0028 (stat) ± 0.0091 (syst)	
		e_3	0.0015 ± 0.0010 (stat) ± 0.0046 (syst)	
		e_4	-0.0013 ± 0.0007 (stat) ± 0.0029 (syst)	

Table 10.10: Associated Legendre function coefficient fitting results for ^{7}Li at a photon energy of 15 MeV. Table continues from table 10.9.

Channel	Orientation	Coefficient	Fit Result	Reduced χ^2
7n1	1	A	0.0647 ± 0.0002 (stat) ± 0.0004 (syst)	1.97
		a_1	0.1010 ± 0.0055 (stat) ± 0.0124 (syst)	
		a_2	-0.1285 ± 0.0084 (stat) ± 0.0187 (syst)	
		e_2	-0.0056 ± 0.0022 (stat) ± 0.0049 (syst)	
		e_3	-0.0093 ± 0.0012 (stat) ± 0.0027 (syst)	
7n1	3	A	0.0903 ± 0.0002 (stat) ± 0.0005 (syst)	2.82
		a_1	0.1127 ± 0.0046 (stat) ± 0.0123 (syst)	
		a_2	-0.1613 ± 0.0069 (stat) ± 0.0180 (syst)	
		e_2	-0.0016 ± 0.0019 (stat) ± 0.0051 (syst)	
		e_3	-0.0112 ± 0.0010 (stat) ± 0.0027 (syst)	
7n2	1	A	0.0250 ± 0.0001 (stat) ± 0.0002 (syst)	15.07
		a_1	0.0739 ± 0.0083 (stat) ± 0.0110 (syst)	
		a_2	-0.7512 ± 0.0126 (stat) ± 0.0163 (syst)	
		e_2	0.0477 ± 0.0037 (stat) ± 0.0056 (syst)	
		e_2	0.0067 ± 0.0019 (stat) ± 0.0026 (syst)	
7n2	3	A	0.0349 ± 0.0001 (stat) ± 0.0002 (syst)	17.67
		a_1	0.1290 ± 0.0071 (stat) ± 0.0118 (syst)	
		a_2	-0.5825 ± 0.0109 (stat) ± 0.0178 (syst)	
		e_2	0.0410 ± 0.0032 (stat) ± 0.0058 (syst)	
		e_2	0.0119 ± 0.0016 (stat) ± 0.0027 (syst)	
7d1^{+}	1	A	0.0468 ± 0.0002 (stat) ± 0.0003 (syst)	24.25
		a_1	1.0199 ± 0.0230 (stat) ± 0.0371 (syst)	
7d1^{+}	3	A	0.0762 ± 0.0003 (stat) ± 0.0005 (syst)	20.34
		a_1	0.8923 ± 0.0187 (stat) ± 0.0387 (syst)	
^{6}Li	1	A	0.0257 ± 0.0028	
^{6}Li	3	A	0.0320 ± 0.0035	

to take care in interpreting the results. Figure 10.6 shows the results of a fit where we have fixed the 7n0 reaction channel using the isolated method results and fit the $7d1^+$ channel to the data. The light-output cut used to fit the $7d1^+$ data is 400 keV_{ee} and the results of the fit can be found in table 10.6. From the A values we can find

$$\frac{\sigma[7n0]}{\sigma[7n0 + 7d1^+]} = 0.688 \pm 0.009 \text{ and } \frac{\sigma[7d1^+]}{\sigma[7n0 + 7d1^+]} = 0.312 \pm 0.011.$$

The weighted averages for the associated Legendre function coefficients are reported in table 10.11. While the a_1 value for the $7d1^+$ reaction channel has little physical meaning, it is useful as an input to the simulation and is found to be $a_1 = -0.11 \pm 0.14$, which is indistinguishable from zero.

Reaction channels we must consider for the 13 MeV data include 7n1, 7n2, 7n3, 7d0 and 7d1, which have simulated neutron kinetic energy spectra shown in figure 10.5. Notice how the 7n1 and 7d1 reaction channels have higher neutron kinetic energies than the other channels. We will fit the 7n1 and 7d1 reaction channels to the spectrum. For 7n1 this will be an approximation, but a fairly good one as none of the ignored reaction channels contribute substantially above kinetic energy 2.5 MeV. The results for 7d1 will contain contributions from 7n2, 7n3 and 7d1 and we will again refer to this reaction channel as $7d1^+$. A cut of 250 keV_{ee} was used for the non-isolatable reaction channels. Figure 10.6 shows an example fit and the numerical results from the fit are reported in table 10.7. The 7n1 and $7d1^+$ reaction channels appear to explain the data well and we are even able to extract information about the dependence of 7n1 on the polarisation of the photon beam. As was the case for 6n0, we are able to reliably find values for a_1, a_2, e_1 and e_2 for 7n1. From the A values we find

$$\begin{aligned}
\frac{\sigma[7n0]}{\sigma[7n0 + 7n1 + 7d1^+]} &= 0.5853 \pm 0.0080, \\
\frac{\sigma[7n1]}{\sigma[7n0 + 7n1 + 7d1^+]} &= 0.0927 \pm 0.0023 \text{ and} \\
\frac{\sigma[7d1^+]}{\sigma[7n0 + 7n1 + 7d1^+]} &= 0.3228 \pm 0.0085.
\end{aligned}$$

The weighted averages for the associated Legendre function coefficients can be found in table 10.11 for 7n0 and table 10.12 for 7n1. The a_1 value for the $7d1^+$ reaction channel is useful as an input to the simulation and is found to be $a_1 = 0.11 \pm 0.16$, which is indistinguishable from zero.

For the data taken with a 15 MeV photon beam we must consider the non-isolatable reaction channels 7n1, 7n2, 7n3, 7n4, 7n5, 7d0 and 7d1. The simulated neutron kinetic energy spectra of the non-isolatable reaction channels are shown in figure 10.5. While the 7n1 reaction channel is not isolatable, it is very prominent and stands out from the others. The 7n2 also has a sharp, distinct spectrum that we are able to observe in the data. The rest of the reaction channels have either low energies or broad spectra and we cannot separate them. We will use the 7d1 reaction channel as it seems to explain the data well within the assumption that the spectrum contains neutrons from the

7n3, 7n4, 7n5 and 7d0 reaction channels as well, again referring to it at $7d1^+$. A cut of 420 keV_{ee} was used for the non-isolatable reaction channels. Figure 10.6 shows an example detected neutron kinetic energy spectra and the related simulations. The fit results are reported in table 10.9. From the A values we can find

$$\begin{aligned}
\frac{\sigma[7n0]}{\sigma[7n0 + 7n1 + 7n2 + 7d1^+]} &= 0.3863 \pm 0.0049, \\
\frac{\sigma[7n1]}{\sigma[7n0 + 7n1 + 7n2 + 7d1^+]} &= 0.2826 \pm 0.0029, \\
\frac{\sigma[7n2]}{\sigma[7n0 + 7n1 + 7n2 + 7d1^+]} &= 0.1085 \pm 0.0025 \text{ and} \\
\frac{\sigma[7d1^+]}{\sigma[7n0 + 7n1 + 7n2 + 7d1^+]} &= 0.2217 \pm 0.0059.
\end{aligned}$$

The weighted averages for the associated Legendre function coefficients can be found in table 10.11 for 7n0, table 10.12 for 7n1 and table 10.13 for 7n2. The a_1 value for the $7d1^+$ reaction channel is useful as an input to the simulation and is found to be $a_1 = 0.95 \pm 0.14$. This value is non-zero and may represent other reaction channels having a greater influence.

It may be noted that the reduced χ^2 values for the 7n0 reaction channel are much smaller than unity, while the reduced χ^2 values for all other reaction channels are much greater than one. This is because the 7n0 reaction channel is isolatable while the others are not. The low reduced χ^2 values for 7n0 indicate that we are either overestimating our systematic uncertainties or the systematic uncertainties in the neutron yields are not independent. The high χ^2 for the other reaction channels results from uncertainties introduced by the method of separating non-isolatable reaction channels discussed in section 7.2.2.

We can use the A values, which have the three-paddle photon flux monitor as a dominant source of uncertainty, and the isotope neutron yield comparison method, which has the light-output cut as the dominant source of uncertainty, to compute cross sections for reaction channels of ^{7}Li relative to the observed reaction channels of ^{6}Li. The results for the 12, 13 and 15 MeV data are listed in tables 10.14, 10.15 and 10.16 respectively. In order to isolate the ^{6}Li contribution, a cut of 1900 keV_{ee} was used for the 12 MeV data, while a cut of 2600 keV_{ee} was used for the 13 MeV data and a cut of 3600 keV_{ee} was used for the 15 MeV data. Since the 7n0 reaction channel is isolatable we present two quantities: The first is the relative cross section of 7n0 to the observable reaction channels of ^{6}Li. The second is the relative cross section of all observable reaction channels of ^{7}Li to those of ^{6}Li. These relative cross sections are especially useful when adding the ^{6}Li contribution into the simulation that uses the natural lithium target.

Table 10.11: Final associated Legendre function coefficient values for ^{7}Li at photon energies of 12, 13 and 15 MeV for the reaction channel 7n0

Energy	Coefficient	Fit Result
12 MeV	a_1	-0.018 ± 0.013
	a_2	-0.081 ± 0.023
	a_3	0.043 ± 0.027
	a_4	-0.031 ± 0.037
	e_2	0.0121 ± 0.0050
	e_3	-0.0010 ± 0.0015
	e_4	-0.0018 ± 0.0016
13 MeV	a_1	-0.044 ± 0.017
	a_2	-0.219 ± 0.028
	a_3	0.035 ± 0.032
	a_4	-0.025 ± 0.043
	e_2	0.0634 ± 0.0065
	e_3	-0.0028 ± 0.0023
	e_4	-0.0017 ± 0.0019
15 MeV	a_1	0.016 ± 0.018
	a_2	-0.279 ± 0.028
	a_3	0.041 ± 0.036
	a_4	-0.038 ± 0.045
	e_2	0.1355 ± 0.0064
	e_3	-0.0010 ± 0.0034
	e_4	0.0001 ± 0.0022

Table 10.12: Final associated Legendre function coefficient values for ^{7}Li at photon energies of 13 and 15 MeV for the reaction channel 7n1

Energy	Coefficient	Fit Result
13 MeV	a_1	0.384 ± 0.051
	a_2	-0.084 ± 0.070
	e_2	-0.195 ± 0.018
	e_3	-0.007 ± 0.010
15 MeV	a_1	0.106 ± 0.014
	a_2	-0.143 ± 0.022
	e_2	-0.0040 ± 0.0058
	e_3	-0.0101 ± 0.0031

Table 10.13: Final associated Legendre function coefficient values for ^{7}Li at the photon energy of 15 MeV for the reaction channel 7n2

Energy	Coefficient	Fit Result
15 MeV	a_1	0.099 ± 0.039
	a_2	-0.675 ± 0.059
	e_2	0.045 ± 0.019
	e_3	0.009 ± 0.009

Table 10.14: Calculation of cross sections relative to ^{6}Li cross sections for the data with 12 MeV photons using the A values computed from the fits and the isotope neutron yield comparison method. The numbers 1 and 3 signify the orientation of the array and identify which detector was on top.

	$\frac{\sigma[7n0]}{\sigma[6n0 + 6n1 + 6p1]}$	$\frac{\sigma[7n0 + 7d1^{+}]}{\sigma[6n0 + 6n1 + 6p1]}$
From A Values; 1	0.335 ± 0.001 (stat) ± 0.037 (syst)	0.487 ± 0.006 (stat) ± 0.054 (syst)
From A Values; 3	0.332 ± 0.001 (stat) ± 0.037 (syst)	0.482 ± 0.006 (stat) ± 0.053 (syst)
Isotope Method; 1	0.310 ± 0.005 (stat) ± 0.064 (syst)	0.445 ± 0.007 (stat) ± 0.083 (syst)
Isotope Method; 3	0.320 ± 0.006 (stat) ± 0.067 (syst)	0.454 ± 0.007 (stat) ± 0.087 (syst)
Weighed Average	0.329 ± 0.023	0.474 ± 0.032

Table 10.15: Calculation of cross sections relative to ^{6}Li cross sections for the data with 13 MeV photons using the A values computed from the fits and the isotope neutron yield comparison method. The numbers 1 and 3 signify the orientation of the array and identify which detector was on top.

	$\frac{\sigma[7n0]}{\overline{\sigma[6n0 + 6n1 + 6p1]}}$	$\frac{\sigma[7n0 + 7n1 + 7d1^+]}{\overline{\sigma[6n0 + 6n1 + 6p1]}}$
From A Values; 1	0.388 ± 0.001 (stat) ± 0.043 (syst)	0.646 ± 0.004 (stat) ± 0.072 (syst)
From A Values; 3	0.338 ± 0.001 (stat) ± 0.037 (syst)	0.588 ± 0.003 (stat) ± 0.065 (syst)
Isotope Method; 1	0.325 ± 0.008 (stat) ± 0.080 (syst)	0.54 ± 0.01 (stat) ± 0.12 (syst)
Isotope Method; 3	0.340 ± 0.008 (stat) ± 0.084 (syst)	0.58 ± 0.01 (stat) ± 0.12 (syst)
Weighed Average	0.354 ± 0.025	0.601 ± 0.042

Table 10.16: Calculation of cross sections relative to ^{6}Li cross sections for the data with 15 MeV photons using the A values computed from the fits and the isotope neutron yield comparison method. The numbers 1 and 3 signify the orientation of the array and identify which detector was on top.

	$\frac{\sigma[7n0]}{\overline{\sigma[6n0 + 6n1 + 6p1]}}$	$\frac{\sigma[7n0 + 7n1 + 7n2 + 7d1^+]}{\sigma[6n0 + 6n1 + 6p1]}$
From A Values; 1	0.276 ± 0.001 (stat) ± 0.031 (syst)	0.712 ± 0.004 (stat) ± 0.078 (syst)
From A Values; 3	0.324 ± 0.001 (stat) ± 0.036 (syst)	0.841 ± 0.003 (stat) ± 0.092 (syst)
Isotope Method; 1	0.35 ± 0.01 (stat) ± 0.10 (syst)	0.93 ± 0.03 (stat) ± 0.24 (syst)
Isotope Method; 3	0.36 ± 0.01 (stat) ± 0.12 (syst)	0.97 ± 0.03 (stat) ± 0.30 (syst)
Weighed Average	0.301 ± 0.022	0.782 ± 0.057

10.7 Absolute Cross Section Determination

As was done for the ^{6}Li data, we apply the Compton scattering comparison method of section 7.4.1 to determine the absolute cross sections of the photodisintegration of ^{7}Li. We emit $N_{sim} = 5 \times 10^7$ neutrons and $\Phi^s = 5 \times 10^8$ photons in the respective simulations. Table 10.17 reports the computed ratios. Since the 7n0 reaction channel is isolatable we have done the analysis of the neutron spectra with two distinct light-output cuts for beam energies of 12, 13 and 15 MeV. The higher cut gives us the ratio for the 7n0 reaction channel only and the lower cut gives us the ratio for all observable reaction channels. Unfortunately, due to limited amounts of beam-time, we were not able to take data in order to use this method with the natural lithium target at a beam energy of 11 MeV.

Table 10.17: Ratios of simulated and measured yields used to determine the absolute cross section of ^{7}Li photodisintegration through the Compton scattering comparison method. The first uncertainty is statistical and the second is systematic.

Beam Energy	Orient-ation	$\left\langle N^s_{d,\gamma}/N_{d,\gamma} \right\rangle$	$\left\langle N_{d,n}/N^s_{d,n} \right\rangle$ 7n0 only ($\times 10^{-3}$)	$\left\langle N_{d,n}/N^s_{d,n} \right\rangle$ all ^{7}Li channels ($\times 10^{-3}$)
10 MeV	1	1.394 ± 0.002 ± 0.034	1.49 ± 0.05 ± 0.14	n/a
12 MeV	3	0.979 ± 0.001 ± 0.024	3.16 ± 0.05 ± 0.22	4.25 ± 0.05 ± 0.14
13 MeV	1	1.456 ± 0.002 ± 0.036	2.23 ± 0.06 ± 0.19	3.70 ± 0.05 ± 0.11
13 MeV	3	1.570 ± 0.003 ± 0.039	2.10 ± 0.05 ± 0.18	3.39 ± 0.04 ± 0.10
15 MeV	1	2.261 ± 0.005 ± 0.055	1.12 ± 0.05 ± 0.13	3.07 ± 0.04 ± 0.08
15 MeV	3	2.293 ± 0.005 ± 0.056	1.07 ± 0.05 ± 0.13	2.96 ± 0.04 ± 0.07

Because the natural lithium target contains some ^{6}Li, we must take this contribution into account in our calculations. It is easy to produce a simulation that can emit neutrons from both ^{6}Li and ^{7}Li photodisintegration events. In order to get the correct contribution from each isotope we need to simulate $N_{sim,7}$ photodisintegration of ^{7}Li events and $N_{sim,6}$ photodisintegration of ^{6}Li events. These numbers will depend on the relative atomic densities and cross sections of the isotopes.

One method to find σ_7/σ_6 is to use equation (10.3) and compute it from the A values of a fit. We can invert this technique and the required number of simulated events can be found by

modifying equation (10.3) to read[2]

$$\frac{\sigma_7}{\sigma_6} = \frac{0.0759}{0.9241}\frac{N_{sim,7}}{N_{sim,6}}. \tag{10.4}$$

Since the total number of simulated photodisintegration events is $N_{sim} = N_{sim,7} + N_{sim,6}$, we can find the fractional number of simulated events for each isotope:

$$\frac{N_{sim,6}}{N_{sim}} = \frac{1}{1 + \frac{0.9241}{0.0759}\frac{\sigma_7}{\sigma_6}} \text{ and } \frac{N_{sim,7}}{N_{sim}} = \frac{\frac{0.9241}{0.0759}\frac{\sigma_7}{\sigma_6}}{1 + \frac{0.9241}{0.0759}\frac{\sigma_7}{\sigma_6}}. \tag{10.5}$$

Figure 10.7 shows the results of a simulation of a photodisintegration experiment using the natural lithium target. In this simulation, both ^{6}Li and ^{7}Li photodisintegration events were produced in

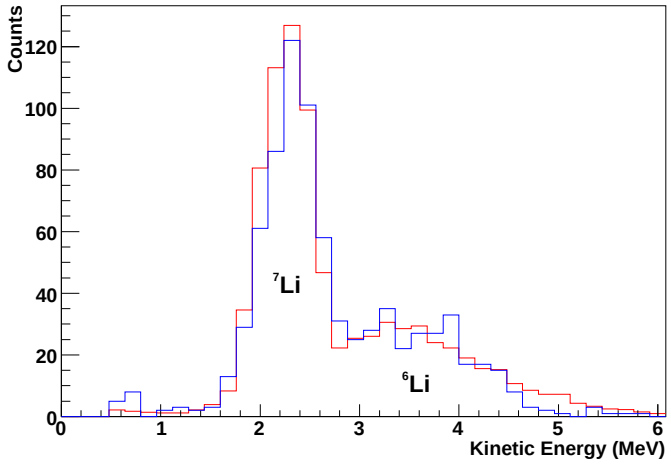

Figure 10.7: Neutron kinetic energy spectra for a detector in the centre ring with the natural lithium target and a photon beam energy of 10 MeV. Notice that the simulated spectrum (red) agrees with the measured spectrum (blue) in both the high energy end due to ^{6}Li photodisintegration and the low energy end due to ^{7}Li photodisintegration.

the ratios given by equation (10.5). Notice how both the high-energy neutrons from the photodisintegration of ^{6}Li, and the low-energy neutrons from the photodisintegration of ^{7}Li, appear in the correct proportions.

Because of the ^{6}Li contribution, we must make some slight modifications to the Compton scattering comparison method of section 7.4.1. Nothing changes in terms of the gamma-ray portion of the calculation. However, we must make some alteration to our calculations of the neutron portion.

[2]Don't be confused by the definition of A in section 7.3. The N_{sim} in that section refers to the number of simulated photodisintegration events used to determine A. The N_{sim} in this section refers to the number of simulated photodisintegration events used to reconstruct the observed spectra given the relative cross sections we determined in our analysis.

First, we look at the contributions of the two isotopes to the measured spectra. Equation (7.12) becomes

$$\begin{aligned} N_{d,n} &= \epsilon_{n,7}\Phi N_7 \ell\sigma_7 \int_{\Omega_d} G\left[\rho_7(\cos\theta,\phi)\right] d\Omega + \epsilon_{n,6}\Phi N_6 \ell\sigma_6 \int_{\Omega_d} G\left[\rho_6(\cos\theta,\phi)\right] d\Omega \\ &= \epsilon_{n,7}\Phi N \ell\sigma_7 \left[(0.9241)\int_{\Omega_d} G\left[\rho_7(\cos\theta,\phi)\right] d\Omega \right. \\ &\quad \left. + \frac{\epsilon_{n,6}\sigma_6}{\epsilon_{n,7}\sigma_7}(0.0759)\int_{\Omega_d} G\left[\rho_6(\cos\theta,\phi)\right] d\Omega\right]. \end{aligned} \tag{10.6}$$

Here we have number densities $N_7 = 0.9241N$ and $N_6 = 0.0759N$, where N is the atomic density of the target. There is also an angular distribution for each isotope, $\rho_7(\cos\theta,\phi)$ and $\rho_6(\cos\theta,\phi)$. The cross sections σ_7 and σ_6 are the total photoneutron cross sections for the observable reaction channels of ^{7}Li and ^{6}Li respectively. We also define $\epsilon_{n,7}$ to be the detector efficiency for the spectrum emitted by the photodisintegration of ^{7}Li, while $\epsilon_{n,6}$ is the efficiency for the spectrum emitted by the photodisintegration of ^{6}Li. Notice that these two numbers are different due to the different energy distributions of the two spectra.

We also need to make a modification to the equation for the simulated spectra. We can use relationships for $N_{sim,7}$ and $N_{sim,6}$, found in equation (10.5), to modify equation (7.15) to read

$$\begin{aligned} N^s_{d,n} &= \epsilon^s_{n,7} N_{sim,7} \int_{\Omega_d} G\left[\rho_7(\cos\theta,\phi)\right] d\Omega + \epsilon^s_{n,6} N_{sim,6} \int_{\Omega_d} G\left[\rho_6(\cos\theta,\phi)\right] d\Omega \\ &= \frac{\frac{\sigma_7}{\sigma_6}}{0.0759 + 0.9241\frac{\sigma_7}{\sigma_6}} \epsilon^s_{n,7} N_{sim} \left[(0.9241)\int_{\Omega_d} G\left[\rho_7(\cos\theta,\phi)\right] d\Omega \right. \\ &\quad \left. + (0.0759)\frac{\epsilon^s_{n,6}}{\epsilon^s_{n,7}}\frac{\sigma_6}{\sigma_7}\int_{\Omega_d} G\left[\rho_6(\cos\theta,\phi)\right] d\Omega\right]. \end{aligned} \tag{10.7}$$

If we assume equality of the simulation and actual efficiencies, $\epsilon^s_{n,6}/\epsilon^s_{n,7} = \epsilon_{n,6}/\epsilon_{n,7}$, we can continue our analysis similarly to that done in section 7.4.1 to obtain a modified version of equation (7.20),

$$\sigma_7 = (170\bar{0}\text{ mb})\left(\frac{\frac{\sigma_7}{\sigma_6}}{0.0759 + 0.9241\frac{\sigma_7}{\sigma_6}}\right)\frac{N_{sim}}{\Phi^s}\frac{N_{d,n}}{N^s_{d,n}}\frac{N^s_{d,\gamma}}{N_{d,\gamma}}. \tag{10.8}$$

We perform the same averaging discussed in section 8.6 so that our final equation is

$$\sigma_7 = (170\bar{0}\text{ mb})\, C_{76}\frac{N_{sim}}{\Phi^s}\left\langle\frac{N_{d,n}}{N^s_{d,n}}\right\rangle\left\langle\frac{N^s_{d,\gamma}}{N_{d,\gamma}}\right\rangle \tag{10.9}$$

where

$$C_{76} \equiv \left(\frac{\frac{\sigma_7}{\sigma_6}}{0.0759 + 0.9241\frac{\sigma_7}{\sigma_6}}\right) \tag{10.10}$$

and the uncertainty in C_{76} can be computed by

$$\delta C_{76} = \frac{0.0759}{\left(0.0759 + 0.9241\frac{\sigma_7}{\sigma_6}\right)^2}\delta\left(\frac{\sigma_7}{\sigma_6}\right). \tag{10.11}$$

The factor C_{76} is not completely intuitive, so it may be helpful to look at some limiting cases. In the limit that $\sigma_7 = 0$ we have $C_{76} = 0$, while in the limit of $\sigma_6 = 0$ we have $C_{76} = 1/0.9241$, which is essentially a correction for the atomic density of ^{7}Li being lower. The case $\sigma_7/\sigma_6 = 1$ can be a bit tricky since $C_{76} = 1$ and equation (10.9) is returned to the single-isotope case. This is explained because the simulation only simulates $N_{sim,7}$ photodisintegration of ^{7}Li events and the correction due to the ^{6}Li contribution is already built into $N_{d,n}/N^s_{d,n}$. It is also interesting to look at the uncertainty in C_{76}. If we approximate $\sigma_7/\sigma_6 \sim 1$, then

$$\frac{\delta C_{76}}{C_{76}} = 0.0759 \times \frac{\delta\left(\sigma_7/\sigma_6\right)}{\sigma_7/\sigma_6}. \tag{10.12}$$

The relative uncertainty in C_{76} is only $\sim 8\%$ the relative uncertainty in σ_7/σ_6. The measured ratios σ_7/σ_6 can be found in tables 10.4, 10.14, 10.15, and 10.16.

After taking into account the ^{6}Li contribution, we can compute the absolute cross sections and they are reported in table 10.18. The absolute cross sections for 7n0 are computed for all energies.

Table 10.18: Absolute cross sections for the observable photonuclear reaction channels of ^{7}Li. For 12 MeV all = 7n0 + 7d1$^+$, for 13 MeV all = 7n0 + 7n1 + 7d1$^+$ and for 15 MeV all = 7n0 + 7n1 + 7n2 + 7d1$^+$.

Beam Energy (MeV)	σ[7n0] (mb)	σ[all] (mb)
10	0.297 ± 0.031	n/a
12	0.455 ± 0.035	0.652 ± 0.029
13	0.488 ± 0.032	0.867 ± 0.025
15	0.361 ± 0.033	1.142 ± 0.031

The absolute cross sections for all reaction channels are computed for 12, 13 and 15 MeV as only these energies have more than one observable reaction channel. The cross sections for the individual reaction channels will be separated and discussed further in chapter 13.

Chapter 11

Data Analysis for ^{6}Li With Photon Energies Above 16 MeV

11.1 Introduction

Our observations of the photodisintegration of ^{6}Li with photon energies below 16 MeV cover the energy range of 8 to 15.6 MeV, a range of 7.6 MeV. Our measurements of the photodisintegration of ^{6}Li above 16 MeV cover the energy spread of 20 to 35 MeV. This span is twice as large as the lower energy measurements and we have data at only four energies, compared with eight for the lower energy range. This span presents additional challenges but we will continue our data analysis in a principled way using the same techniques and some additional reaction channels.

One major difference between the analysis done in this chapter and that done with lower energy photons is the polarisation of the photons. Before, we had linearly polarised photons and were able to obtain values for the e_2, e_3, and sometimes e_4, associated Legendre coefficients. Now we have circularly polarised photons and are unable to obtain values for these coefficients.

There are a number of new excited states of importance and these are listed in table 11.1. Taking these new states into account, we have a number of new reaction channels to consider and these are listed in table 11.2. It is important to note that the states of ^{5}Li and ^{5}He are not from experimental observations but the results of a theoretical calculation [Til02]. Since they have shown promise in our analysis of the data at lower energies, we will continue to use them as the model of our photodisintegration reactions at higher energies.

There is an excited state of ^{5}He with excitation energy 16.84 MeV and an excited state of ^{5}Li with excitation energy 16.87 MeV [Til02]. These states are responsible for the reaction channels 6p2 and 6n2 listed in table 11.2. Note that, compared with other states of ^{5}He and ^{5}Li, these states have narrow decay widths. The neutron kinetic energy spectra due to 6n2 and 6p2 will be much sharper than those due to 6n1 and 6p1.

The review [Til02] reports a huge number of states for each of ^{5}He and ^{5}Li. For ^{5}He, there are seven states listed between 19.14 and 21.64 MeV. Obviously we cannot consider all of these states in our analysis as their neutron kinetic energy spectra are all overlapping. We will use a subset of

Table 11.1: Excited states considered in the analysis of the ^{6}Li data with photon beam energies above 16 MeV in addition to those listed in table 1.4 [Til02]. There are no uncertainties given in the reference. Decay widths for ^{5}Li are the total widths while those for ^{5}He are the neutron partial widths.

Isotope	Excitation Energy (MeV)	Spin/Parity	Decay Width (MeV)
^{5}He	16.84	$\frac{3}{2}^+$	0.040
^{5}He	19.14	$\frac{5}{2}^+$	0.003
^{5}He	21.25	$\frac{3}{2}^+$	0.098
^{5}Li	16.87	$\frac{3}{2}^+$	0.267
^{5}Li	19.28	$\frac{3}{2}^-$	0.959
^{5}Li	22.06	$\frac{5}{2}^-$	15.5

Table 11.2: Reaction channels to consider in the analysis of the ^{6}Li data above 16 MeV in addition to those listed in table 9.1

Label	Reaction	Threshold (MeV)
6p2	$^6\mathrm{Li} + \gamma \rightarrow p + {}^5\mathrm{He}(16.8) \quad \rightarrow n + p + {}^4\mathrm{He}(\mathrm{g.s.})$	21.4
6n2	$^6\mathrm{Li} + \gamma \rightarrow n + {}^5\mathrm{Li}(16.9)$	22.6
6p3	$^6\mathrm{Li} + \gamma \rightarrow p + {}^5\mathrm{He}(19.1) \quad \rightarrow n + p + {}^4\mathrm{He}(\mathrm{g.s.})$	23.7
6n3	$^6\mathrm{Li} + \gamma \rightarrow n + {}^5\mathrm{Li}(19.3)$	25.0
6p4	$^6\mathrm{Li} + \gamma \rightarrow p + {}^5\mathrm{He}(21.3) \quad \rightarrow n + p + {}^4\mathrm{He}(\mathrm{g.s.})$	25.9
6n4	$^6\mathrm{Li} + \gamma \rightarrow n + {}^5\mathrm{Li}(22.1)$	27.8

these states to represent the whole.

In order to construct the 6n3 and 6p3 reaction channels we use the states in this range with lowest excitation energy. These are the 19.14 MeV state of ^{5}He and the 19.28 MeV state of ^{5}Li [Til02].

In order to construct the 6n4 and 6p4 reaction channels we use the states in this range with the largest decay widths: namely the 22.06 MeV state of ^{5}Li, with a decay width of 15.5 MeV, and the 21.25 MeV state of ^{5}He, with a neutron partial decay width of 0.098 MeV.

We must take a moment to consider three-body decays. The quasideuteron reaction becomes important at higher energies so we must quantify it. Wade *et al.* have studied the onset of the quasideuteron reaction on ^{6}Li. At 30 MeV the cross section of this reaction is less than 10% the cross section of the photodisintegration of the deuteron, giving a value of 35 μb if we take the deuteron cross section to be 350 μb [Ber86]. At 50 MeV the ^{6}Li quasideuteron cross section is about 30% that of the deuteron giving about 51 μb for the deuterons 170 μb. Even at these higher energies the quasideuteron contribution is small for the photodisintegration of ^{6}Li.

We continue to neglect the three-body decays as they are not necessary to explain the data. We do not include any reaction channels that lead to excited states of ^{4}He. Such states exist but are not particle stable [Til92].

11.2 Background Contribution from Atmospheric Nitrogen

In section 8.6 we examined the relative contributions of gamma rays scattered from the air and a lithium target. We computed the length of the natural lithium target in mass thickness units to be 6.78 g/cm^2 while the same quantity for the air is approximately 0.36 g/cm^2. We concluded that the effects of the photons Compton scattering from the air was not negligible. However, we were still able to ignore the effects of photodisintegration reactions from the air by direct examination of the measured data obtained with with the empty target.

At energies above 16 MeV the situation is different. Figure 11.1 shows the total ^{14}N photoneutron cross section as reported in the review of Berman and Fultz [Ber75]. This cross section is fairly low below 16 MeV. However at-and-above 20 MeV, the cross section is much larger. We may need to perform a subtraction of the background neutrons due to the photodisintegration of atmospheric nitrogen.

In a run with the empty target and a beam energy of 20 MeV, the five-paddle flux monitor recorded 252 million events after correcting for dead time. We see about 85 neutron events in each detector for a light-output cut of 1100 keV$_{ee}$, giving us 0.34 neutrons per million flux monitor counts. In a run using the ^{6}Li target, we have 628 million flux monitor counts and we see on average 8800 neutron events in each detector for the same cuts. This gives us 14.0 neutrons per million

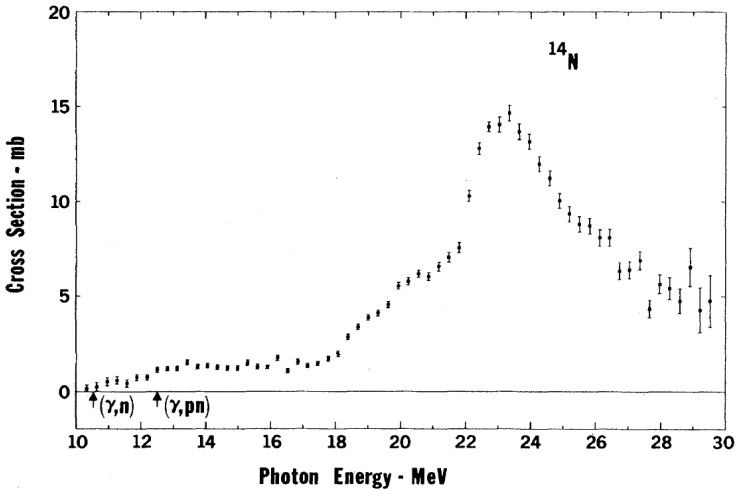

Figure 11.1: The total photoneutron cross section for ^{14}N reported by the review of Berman and Fultz [Ber75]

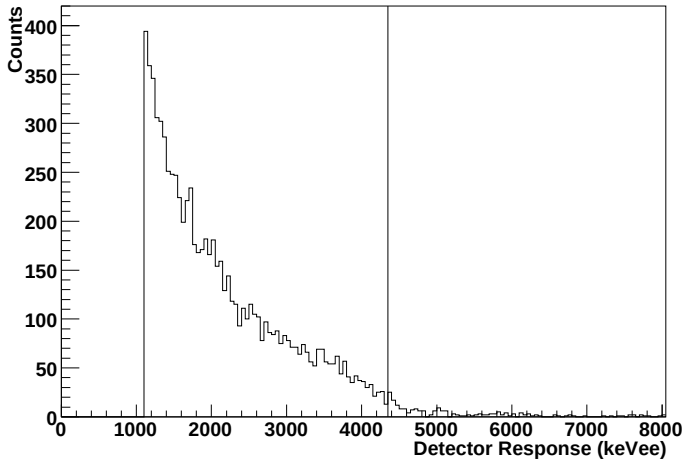

Figure 11.2: Light output spectrum for all detectors summed with the empty target and a beam energy of 20 MeV. PSD and time-of-flight cuts have been applied to eliminate gamma-ray events. The line indicates a light output of 4350 keV$_{ee}$ which is approximately the highest light-output possible for the $^{14}\mathrm{N}+\gamma \rightarrow {}^{13}\mathrm{N}+n$ reaction.

flux monitor counts. Thus the background contribution is 2.4%, and we need to consider it in our analysis.

It will be useful to examine the spectrum of neutrons emitted from the photodisintegration of atmospheric nitrogen. The isotope ^{14}N has a binding energy of 104.66 MeV, while ^{13}N has a binding energy of 94.11 MeV [Aud03], giving a threshold of 10.55 MeV for the $^{14}\mathrm{N} + \gamma \rightarrow {}^{13}\mathrm{N} + n$ reaction. Since the nitrogen nucleus is much heaver than the neutron, conservation of energy and momentum demand that the neutron takes most of the remaining energy away as kinetic energy.

For the 20 MeV data, we expect to see neutrons with around 8.7 MeV kinetic energy. These are observed in the kinetic-energy spectra. However, since these spectra are computed from time-of-flight, there is significant smearing due to the uncertainty in where the reaction occurs. The light-output spectrum is based on the energy each neutron deposits in the detector so it will not be influenced by where the reaction occurs. We expect to see a maximum light-output at about 4800 keV$_{ee}$ (about 4350 keV$_{ee}$ after correcting for the QDC gain anomaly). Since there are so few counts in each detector, we add up all the light-output spectra from all detectors and present these in figure 11.2. Notice that the light-output cutoff in this figure agrees well with our prediction, indicating that the observed neutrons in the background spectra are from the reaction $^{14}\mathrm{N} + \gamma \rightarrow {}^{13}\mathrm{N} + n$ occurring due to the photodisintegration of atmospheric nitrogen.

11.3 Analysis for the Photon Energy of 20 MeV

Since there are no new reaction channels available for photon energies of 20 MeV, the analysis of this data process similarly to that of the below 16 MeV data except that we are not able to obtain values for any of the e_k coefficients because circularly polarised photons were used. The neutron kinetic energy distributions for the 6n0 and 6n1 reaction channels are very similar. We will not be able to treat these channels separately and will only be able to find results for their sums as we did for 6n1 and 6p1 at energies between 10 and 13 MeV. It is important to note that the 6n0 reaction channel is still required in order to get good agreement with the data.

We use a light output cut of 1100 keV$_{ee}$ to ensure good separations between gamma-rays and neutrons using PSD. An example detected neutron kinetic energy spectrum can be seen in figure 11.3. Notice how the narrower 6n0 reaction channel is contained within the broader 6n1 reaction channel, making them impossible to separate.

Assuming charge independence of the nuclear force we expect the contribution from 6p0 to be about 3.0% the contribution from 6n0. These neutrons have low energies and will affect mainly the computed neutron yield of the 6p1 reaction channel.

The associated Legendre function coefficient fit results are reported in table 11.3. From the A

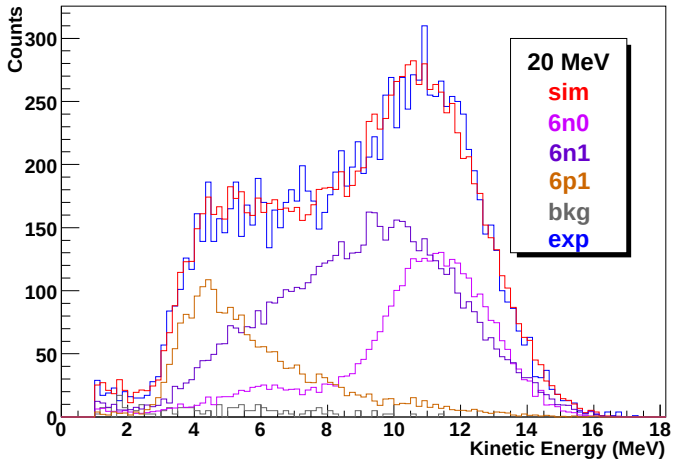

Figure 11.3: The neutron kinetic energy spectra for a beam energy of 20 MeV for a detector in the centre ring. Shown are the simulation of the 6n0, 6n1 and 6p1 reaction channels, the measured empty-target background (bkg; gray) and the measured spectrum (blue). The red histogram is the sum of the simulation histograms.

Table 11.3: Associated Legendre function coefficient fitting results for ^{6}Li at a photon energy of 20 MeV. The orientation signifies which detector in the most upstream ring was on top of the array.

Channel	Orientation	Coefficient	Fit Result	Reduced χ^2
6n0	1	A	0.1896 ± 0.0004 (stat) ± 0.0008 (syst)	3.91
		a_1	0.1765 ± 0.0035 (stat) ± 0.0079 (syst)	
		a_2	-0.3836 ± 0.0053 (stat) ± 0.0119 (syst)	
6n0	3	A	0.1142 ± 0.0003 (stat) ± 0.0005 (syst)	1.94
		a_1	0.1919 ± 0.0045 (stat) ± 0.0079 (syst)	
		a_2	-0.3832 ± 0.0069 (stat) ± 0.0119 (syst)	
6n1	1	A	0.1892 ± 0.0004 (stat) ± 0.0008 (syst)	3.46
		a_1	0.1694 ± 0.0036 (stat) ± 0.0081 (syst)	
		a_2	-0.3819 ± 0.0054 (stat) ± 0.0122 (syst)	
6n1	3	A	0.1138 ± 0.0003 (stat) ± 0.0005 (syst)	1.70
		a_1	0.1887 ± 0.0046 (stat) ± 0.0082 (syst)	
		a_2	-0.3812 ± 0.0070 (stat) ± 0.0122 (syst)	
6p1	1	A	0.4313 ± 0.0010 (stat) ± 0.0029 (syst)	7.64
		a_1	0.5507 ± 0.0086 (stat) ± 0.0239 (syst)	
6p1	3	A	0.2224 ± 0.0008 (stat) ± 0.0015 (syst)	11.14
		a_1	0.6041 ± 0.0120 (stat) ± 0.0244 (syst)	

values we can compute the relative cross sections of the three reaction channels:

$$\frac{\sigma[6n0 + 6n1]}{\sigma[6n0 + 6n1 + 6p1]} = 0.503 \pm 0.007 \text{ and } \frac{\sigma[6p1]}{\sigma[6n0 + 6n1 + 6p1]} = 0.510 \pm 0.011.$$

As we have had to take the sum of the 6n0 and 6n1 reaction channels in order to get any results from the method of separating non-isolatable reaction channels, we cannot make any conclusions based on the coefficients a_k listed in table 11.3. However, these coefficients are useful as input to the simulation and are listed here. For 6n0 we have $a_1 = 0.186 \pm 0.010$ and $a_2 = -0.383 \pm 0.015$, while for 6n1 we have $a_1 = 0.182 \pm 0.010$ and $a_2 = -0.381 \pm 0.015$; for 6p1 we have $a_1 = 0.571 \pm 0.056$.

11.4 Analysis for the Photon Energies of 25 and 30 MeV

The analysis of the ^{6}Li data with photon beam energies of 25 and 30 MeV will proceed differently than the analysis at lower beam energies. Table 11.2 shows that we have additional reaction channels to contend with: 6n2, 6p2 and 6p3 at both energies and 6n3, 6n4 and 6p4 at 30 MeV. We will need to make a small change in how we view the process of data analysis.

Up until now, we have looked at the 6n0, 6n1 and 6p1 reaction channels, keeping in mind that 6p0 is also present but with neutrons that have too little kinetic energy to be detected. Now the number of reaction channels has exploded and we must reconsider how we model the photodisintegration of ^{6}Li. We recall that we encountered a similar problem with our analysis of the photodisintegration of ^{7}Li in that we had many reaction channels which emitted neutrons with similar energy distributions. This led us to create the 7d1$^+$ pseudo-reaction channel to describe a number of reaction channels collectively. For ^{6}Li we will not place a '+' marker on all our reaction channels, but rather we will just understand that we have had to make some assumptions in order to describe the data; we simply cannot separate all the reaction channels involved.

To describe our data we will follow two simple rules. First, we will use the minimum number of reaction channels needed to describe the data. Second, we will give preference to reaction channels with final products in lower energy states. Based on these two rules, we will not need the 6n4 and 6p4 reaction channels to describe our data and we no longer discuss them.

For the case of 25 MeV, the 6n2 and 6p0 reaction channels produces neutrons with too low an energy to survive the light-output cut. Since the neutron's kinetic energy actually comes from the decay of the ^{5}He nucleus for 6p2 and 6p3, these reaction channels will produce neutrons with sufficient energy to be detected. For the case of 30 MeV, we must consider all reaction channels except 6p0.

All reaction channels of relevance are shown in figure 11.4. For 25 MeV notice that the 6n0, 6n1, 6p2, and 6p3 reaction channels all produce neutrons with about the same energies, with peaks between 13 and 17 MeV. On the low energy end, the 6p1 reaction channel dominates and there

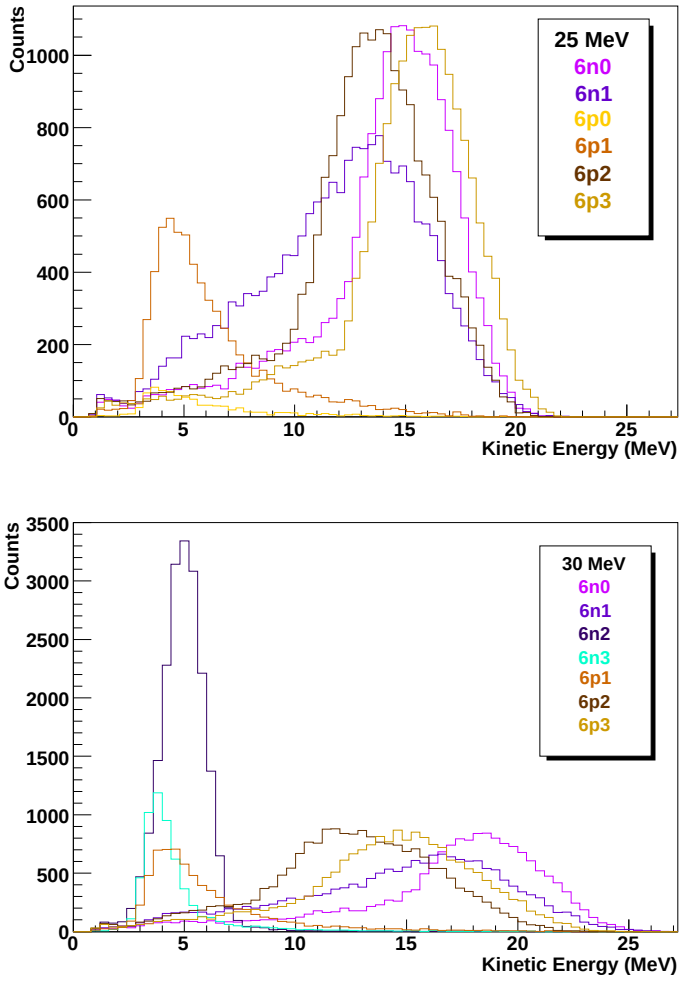

Figure 11.4: Two-body reaction channels with simulated neutron kinetic energies for a detector in the centre ring with photon beams of 25 and 30 MeV. Each histogram is the result of 50 million simulated photodisintegration events for that reaction channel. The light-output threshold is 1100 keV_{ee}.

is a tiny contribution from 6p0. For 30 MeV we see a grouping of reaction channels with neutron energies greater than 8 MeV and a second grouping with neutron energies lower than 8 MeV.

The neutron time-of-flight spectra lead us to an interesting observation. We can describe the data with photon beam energies of 25 and 30 MeV quite well without the 6n0 reaction channel. This does not mean the reaction does not occur; rather it is being dominated by the 6n1 reaction channel. We will no longer include the 6n0 reaction channel in our fit in order to allow us to separate the rest of the reaction channels.

For the 25 MeV data, the only reaction channel in addition to 6n1 that is required to describe the data is 6p1. For the 35 MeV data, the 6n1 and 6p1 reaction channels are required but are not sufficient to describe the data. We must also include the 6n2 and 6p2 reaction channels. While we have typically shown only the neutron kinetic energy spectra, for these two energies we show both the time-of-flight and neutron kinetic energy spectra. This is because the energy resolution of our detectors worsens as the neutron's kinetic energy increases. The time-of-flight spectra, shown in figure 11.5, is a better representation of the agreement, while the neutron kinetic energy spectra, shown in figure 11.6, is more intuitive.

We will also take a slightly different approach to fitting our simulation spectra to the measured spectra. The sharp peaks in the time-of-flight spectra tend to confuse the fitting algorithms. For the 25 MeV data we fit to the light-output spectra instead, using a light-output cut of 1100 keV_{ee}. For the 30 MeV data, we fit the 6n1 reaction channel using the light-output spectra with a cut of 8000 keV_{ee}, and then fit the 6p1, 6n2 and 6p2 reaction channels using the time-of-flight spectra with a cut of 1100 keV_{ee}.

The associated Legendre function coefficients computed from the fits are reported in table 11.4 for 25 MeV and 11.5 for 30 MeV. The raw values of tables 11.4 and 11.5 are converted to final values and presented in table 11.6. The relative cross sections for the data taken with a photon beam of 25 MeV are

$$\frac{\sigma[\text{6n1}]}{\sigma[\text{6n1 + 6p1}]} = 0.4328 \pm 0.0034 \text{ and } \frac{\sigma[\text{6p1}]}{\sigma[\text{6n1 + 6p1}]} = 0.5676 \pm 0.0060.$$

The relative cross sections for the data taken with a photon beam of 30 MeV are

$$\begin{aligned}
\frac{\sigma[\text{6n1}]}{\sigma[\text{6n1 + 6p1 + 6n2 + 6p2}]} &= 0.338 \pm 0.007, \\
\frac{\sigma[\text{6n2}]}{\sigma[\text{6n1 + 6p1 + 6n2 + 6p2}]} &= 0.094 \pm 0.004, \\
\frac{\sigma[\text{6p1}]}{\sigma[\text{6n1 + 6p1 + 6n2 + 6p2}]} &= 0.497 \pm 0.021 \text{ and} \\
\frac{\sigma[\text{6p2}]}{\sigma[\text{6n1 + 6p1 + 6n2 + 6p2}]} &= 0.070 \pm 0.002.
\end{aligned}$$

It is interesting to note that for both energies, we find the cross section of 6p1 to be larger than that of 6n1. For the 30 MeV data we find the situation reversed for 6n2 and 6p2; the cross section

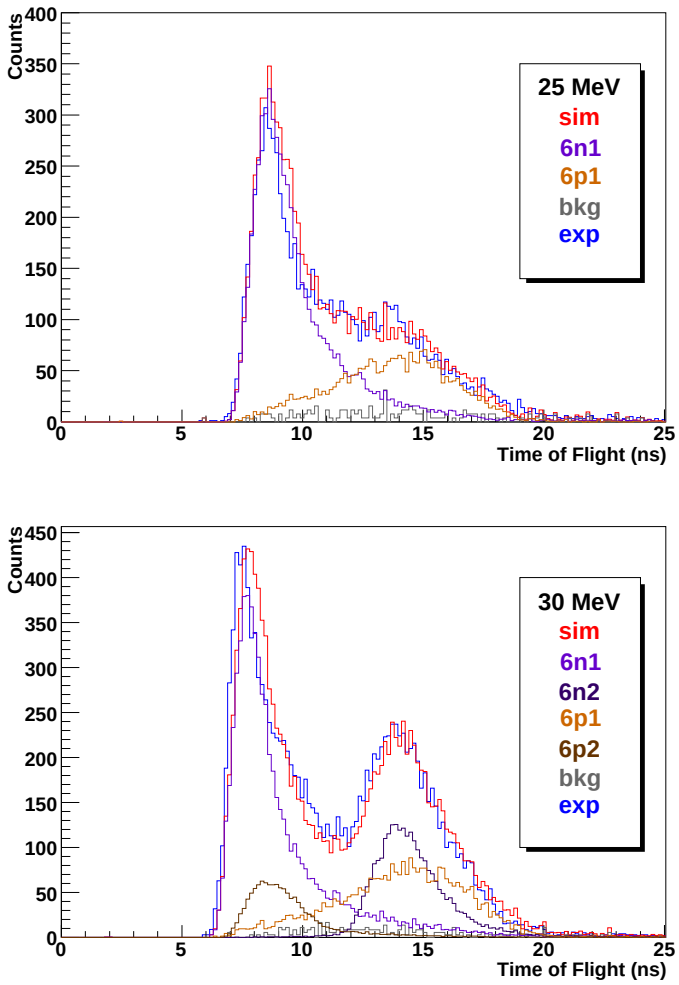

Figure 11.5: The neutron time-of-flight spectra for beam energies of 25 and 30 MeV for a detector in a centre ring. Shown are the simulation of the 6n1, 6p1, 6n2 and 6p2 reaction channels, the measured empty-target background (bkg; gray) and the measured spectrum (blue). The red histogram is the sum of the simulation histograms and the background.

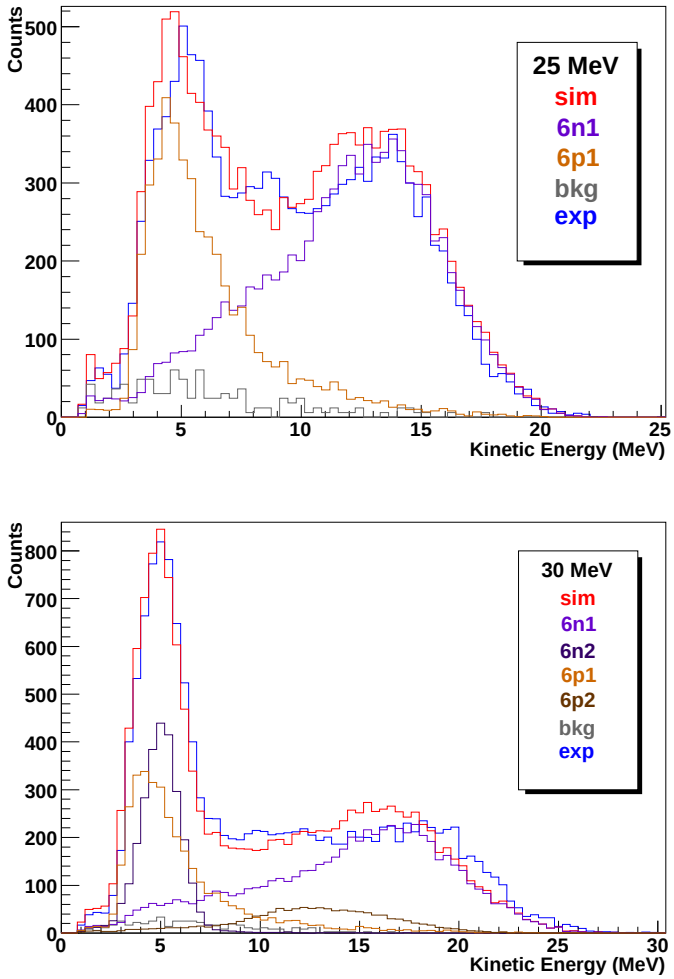

Figure 11.6: The neutron kinetic energy spectra for beam energies of 25 and 30 MeV for a detector in a centre ring. Shown are the simulation of the 6n1, 6p1, 6n2 and 6p2 reaction channels, the measured empty-target background (bkg; gray) and the measured spectrum (blue). The red histogram is the sum of the simulation histograms and the background.

Table 11.4: Associated Legendre function coefficient fitting results for ^{6}Li at a photon energy of 25 MeV. The orientation signifies which detector in the most upstream ring was on top of the array.

Channel	Orientation	Coefficient	Fit Result	Reduced χ^2
6n1	1	A	0.2472 ± 0.0004 (stat) ± 0.0010 (syst)	1.43
		a_1	0.1060 ± 0.0032 (stat) ± 0.0084 (syst)	
		a_2	-0.4406 ± 0.0048 (stat) ± 0.0124 (syst)	
6n1	3	A	0.3860 ± 0.0005 (stat) ± 0.0017 (syst)	6.42
		a_1	0.1323 ± 0.0026 (stat) ± 0.0084 (syst)	
		a_2	-0.5383 ± 0.0038 (stat) ± 0.0120 (syst)	
6p1	1	A	0.3232 ± 0.0008 (stat) ± 0.0021 (syst)	3.67
		a_1	0.3820 ± 0.0087 (stat) ± 0.0216 (syst)	
		a_2	-0.7483 ± 0.0276 (stat) ± 0.0692 (syst)	
6p1	3	A	0.5086 ± 0.0010 (stat) ± 0.0032 (syst)	3.11
		a_1	0.3812 ± 0.0070 (stat) ± 0.0217 (syst)	
		a_2	-0.7690 ± 0.0223 (stat) ± 0.0700 (syst)	

Table 11.5: Associated Legendre function coefficient fitting results for ^{6}Li at a photon energy of 30 MeV. The orientation signifies which detector in the most upstream ring was on top of the array.

Channel	Orientation	Coefficient	Fit Result	Reduced χ^2
6n1	3	A	0.2872 ± 0.0005 (stat) ± 0.0027 (syst)	0.537
		a_1	0.1050 ± 0.0034 (stat) ± 0.0172 (syst)	
		a_2	-0.4392 ± 0.0053 (stat) ± 0.0269 (syst)	
6n2	3	A	0.0799 ± 0.0002 (stat) ± 0.0005 (syst)	37.38
		a_1	0.9829 ± 0.0049 (stat) ± 0.0087 (syst)	
		a_2	-0.6512 ± 0.0100 (stat) ± 0.0227 (syst)	
6p1	3	A	0.4220 ± 0.0010 (stat) ± 0.0029 (syst)	26.16
		a_1	1.0213 ± 0.0063 (stat) ± 0.0202 (syst)	
6p2	3	A	0.0598 ± 0.0002 (stat) ± 0.0002 (syst)	34.79
		a_1	-1.3976 ± 0.1298 (stat) ± 0.1612 (syst)	

Table 11.6: Final associated Legendre function coefficient values for ^{6}Li at photon energies of 25 and 30 MeV.

Reaction Channel	Coefficient	$E_\gamma = 25$ MeV	$E_\gamma = 30$ MeV
6n1	a1	0.111 ± 0.010	0.105 ± 0.018
	a2	-0.460 ± 0.014	-0.439 ± 0.027
6n2	a1	n/a	0.983 ± 0.061
	a2	n/a	-0.65 ± 0.15
6p1	a1	0.382 ± 0.030	1.02 ± 0.11
	a2	-0.760 ± 0.096	n/a
6p2	a1	n/a	-1.4 ± 1.2

for 6n2 is larger than that of 6p2.

There are some interesting points to be made about the associated Legendre function coefficient values found in table 11.6. The coefficients for 6n1 are consistent between the two energies but this is not true for 6p1. Given the large values for the a_1 coefficients for the 6p1 and 6p2 reaction channels at 30 MeV, it is likely that these values are not physically meaningful. However, they are useful as inputs to the simulation.

11.5 Analysis for the Photon Energy of 35 MeV

The analysis of the data taken with a 35 MeV photon beam will proceed similarly to that of the 30 MeV beam except we will be forced to consider even more reaction channels. We will again consider the 6n1, 6n2, 6p1 and 6p2 reaction channels, but these are not sufficient to describe the data. We will need to consider the 6n3 reaction channel in order to describe the observed low energy neutrons. Given that we are including 6n3, we will also include 6p3. Unfortunately, because the energy resolution of our detectors decreases as the energy increases, the 6p3 reaction channel will have very similar neutron kinetic energy spectra to the 6p2 reaction channel. We therefore are forced to consider only the sum of 6p2 and 6p3. The neutron kinetic energy spectra for these reaction channels can be seen in figure 11.7.

In the analysis of the 30 MeV data we used two cuts. The first effectively isolated the 6n1 reaction channel, while the second allowed us to separate the 6n2, 6p1 and 6p2 reaction channels. In order to separate the reaction channels for the 35 MeV data, we use three cuts. The first light-output cut varies from 14500 to 16000 keV$_{ee}$ depending on the ring. We fit the light-output spectra of the 6n1 reaction channel to the measured spectra. The second light-output cut varies from 5000 to 6500 keV$_{ee}$ depending on the ring. We fit our simulated time-of-flight spectra for the reaction

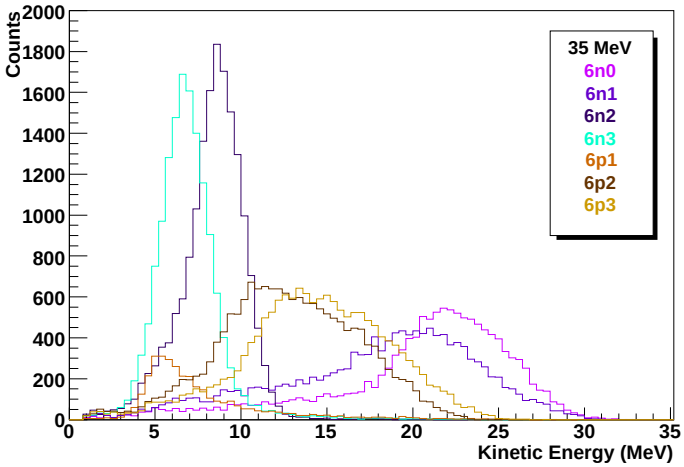

Figure 11.7: Two-body reaction channels with simulated neutron kinetic energies for a detector in the centre ring with a photon beam energy of 35 MeV. Each histogram is the result of 50 million simulated photodisintegration events for that reaction channel. The light-output threshold is 1500 keV_{ee}.

channels 6p2 and 6p3 to the measured spectra. The third light-output cut is set to 1500 keV_{ee} for all detectors. This light output cut is quite low and we suffer from increasing systematic uncertainties due to PSD being less than 100% efficient. This low light output cut lets us separate the 6n2, 6n3 and 6p1 reaction channels. It may be somewhat surprising to note that we get better results when we use the light-output spectra to separate these last three reaction channels, rather than the time-of-flight spectra. An example of these three fits can be seen in figure 11.8, which shows us the resulting neutron kinetic energy spectra. The quantities computed from these fits are listed in table 11.7.

In section 5.6 we discussed the physics lists used in our simulations and how the high-precision neutron physics list ends at neutron kinetic energies of 20 MeV. In this section, we saw how the LHEP_PRECO_HP physics list was unsuitable above 20 MeV but the QGSP_BERT_HP physics list offered what appeared to be acceptable results. We see from figure 11.9 that the QGSP_BERT_HP physics list may be breaking down for neutron energies above 20 MeV. Notice the extra tail on the simulation time-of-flight spectrum with times larger than 8 ns. We do not expect to see this tail. We expect that, since the light-output cut is so high, the only neutrons that can pass the cut are those that are emitted from the target and interact only with the detector; they are not scattered by any other piece of matter and their time-of-flight spectrum should be very sharp. This is what is seen in the measured data. Even so, we feel that the simulation is sufficient for the study of the lithium isotopes. In order to ensure that we are not underestimating our uncertainties, we will take the simple and ad-hoc action of multiplying the uncertainties associated with the 6n1 reaction channel by a factor of 2. This seems reasonable as the height of the simulated time-of-flight peak

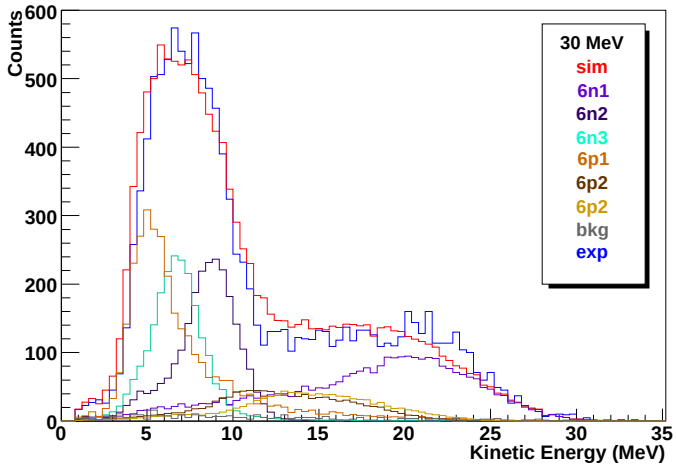

Figure 11.8: The neutron kinetic energy spectra for a beam energy of 35 MeV for a detector in a centre ring. Shown are the simulation of the 6n1, 6p1, 6n2, 6p2, 6n3 and 6p3 reaction channels, the measured empty-target background (bkg; gray) and the measured spectrum (blue). The red histogram is the sum of the simulation histograms and the background.

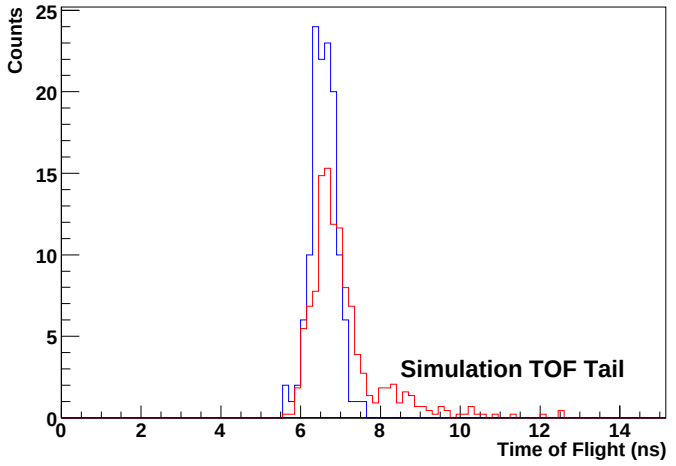

Figure 11.9: Simulation (red) and experimental (blue) time-of-flight spectra with a photon beam energy of 35 MeV and a light-output cut of 15200 keV_{ee}

Table 11.7: Associated Legendre function coefficient fitting results for ^{6}Li at a photon energy of 35 MeV. The orientation signifies which detector in the most upstream ring was on top of the array. Continued in table 11.8.

Channel	Orientation	Coefficient	Fit Result	Reduced χ^2
6n1	1	A	0.1743 ± 0.0005 (stat) ± 0.0062 (syst)	0.40
		a_1	0.2045 ± 0.0051 (stat) ± 0.0705 (syst)	
		a_2	-0.2683 ± 0.0079 (stat) ± 0.1062 (syst)	
6n1	3	A	0.1704 ± 0.0005 (stat) ± 0.0061 (syst)	0.85
		a_1	0.2721 ± 0.0050 (stat) ± 0.0694 (syst)	
		a_2	-0.1732 ± 0.0076 (stat) ± 0.1035 (syst)	
6n2	1	A	0.0754 ± 0.0003 (stat) ± 0.0004 (syst)	33.27
		a_1	0.4724 ± 0.0063 (stat) ± 0.0086 (syst)	
		a_2	-0.7028 ± 0.0094 (stat) ± 0.0110 (syst)	
6n2	3	A	0.0734 ± 0.0002 (stat) ± 0.0004 (syst)	84.27
		a_1	0.5969 ± 0.0060 (stat) ± 0.0051 (syst)	
		a_2	-0.7507 ± 0.0085 (stat) ± 0.0063 (syst)	
6n3	1	A	0.1126 ± 0.0003 (stat) ± 0.0006 (syst)	13.94
		a_1	-0.0123 ± 0.0052 (stat) ± 0.0096 (syst)	
		a_2	-0.9030 ± 0.0079 (stat) ± 0.0132 (syst)	
6n3	3	A	0.1269 ± 0.0003 (stat) ± 0.0006 (syst)	14.48
		a_1	-0.0748 ± 0.0050 (stat) ± 0.0098 (syst)	
		a_2	-0.7259 ± 0.0078 (stat) ± 0.0146 (syst)	
6p1	1	A	0.5217 ± 0.0013 (stat) ± 0.0035 (syst)	10.82
		a_1	0.2933 ± 0.0078 (stat) ± 0.0210 (syst)	
		a_2	-0.7816 ± 0.0232 (stat) ± 0.0618 (syst)	
6p1	3	A	0.5307 ± 0.0013 (stat) ± 0.0034 (syst)	15.31
		a_1	0.2441 ± 0.0076 (stat) ± 0.0196 (syst)	
		a_2	-0.9811 ± 0.0226 (stat) ± 0.0588 (syst)	

Table 11.8: Associated Legendre function coefficient fitting results for ^{6}Li at a photon energy of 35 MeV. Continued from table 11.7.

Channel	Orientation	Coefficient	Fit Result	Reduced χ^2
6p2	1	A	0.0255 ± 0.0002 (stat) ± 0.0002 (syst)	45.94
		a_1	3.4129 ± 0.2014 (stat) ± 0.3903 (syst)	
6p2	3	A	0.0305 ± 0.0002 (stat) ± 0.0002 (syst)	50.30
		a_1	3.9234 ± 0.2053 (stat) ± 0.4501 (syst)	
6p3	1	A	0.0256 ± 0.0002 (stat) ± 0.0001 (syst)	53.32
		a_1	4.6722 ± 0.2654 (stat) ± 0.4125 (syst)	
6p3	3	A	0.0303 ± 0.0002 (stat) ± 0.0002 (syst)	56.89
		a_1	3.8512 ± 0.2554 (stat) ± 0.3896 (syst)	

Table 11.9: Final associated Legendre function coefficient values for ^{6}Li at a photon energy of 35 MeV.

Reaction Channel	a_1	a_2
6n1	0.24 ± 0.10	-0.22 ± 0.15
6n2	0.525 ± 0.047	-0.723 ± 0.063
6n3	-0.043 ± 0.029	-0.823 ± 0.042
6p1	0.271 ± 0.055	-0.87 ± 0.16
6p2	3.6 ± 2.3	n/a
6p3	4.2 ± 2.5	n/a

tends to be approximately half that of the measured peak. A study requiring higher precision may need an improved physics list for neutrons with kinetic energies above 20 MeV.

We take the raw results of table 11.7, average them and produce the final associated Legendre function coefficients found in table 11.9. Since it was not possible to separate the 6p2 and 6p3 reaction channels, their coefficients should not be considered to have physical meaning but are only useful as inputs to the simulation. Taking the A values from table 11.7, we are able to compute the relative cross sections,

$$\begin{aligned}
\frac{\sigma[\text{6n1}]}{\sigma[\text{6n1} + \text{6p1} + \text{6n2} + \text{6p2} + \text{6n3} + \text{6p3}]} &= 0.181 \pm 0.011, \\
\frac{\sigma[\text{6n2}]}{\sigma[\text{6n1} + \text{6p1} + \text{6n2} + \text{6p2} + \text{6n3} + \text{6p3}]} &= 0.0790 \pm 0.0027, \\
\frac{\sigma[\text{6n3}]}{\sigma[\text{6n1} + \text{6p1} + \text{6n2} + \text{6p2} + \text{6n3} + \text{6p3}]} &= 0.1204 \pm 0.0024, \\
\frac{\sigma[\text{6p1}]}{\sigma[\text{6n1} + \text{6p1} + \text{6n2} + \text{6p2} + \text{6n3} + \text{6p3}]} &= 0.555 \pm 0.012 \text{ and} \\
\frac{\sigma[\text{6p2} + \text{6p3}]}{\sigma[\text{6n1} + \text{6p1} + \text{6n2} + \text{6p2} + \text{6n3} + \text{6p3}]} &= 0.0583 \pm 0.0029.
\end{aligned}$$

Since the separation of the individual reaction channels was very difficult for the data with a 35 MeV photon beam, the uncertainties on these quantities are likely unreasonably small. In other words, the algorithm is being confused by the washed-out spectrum in a systematic way that we are not able to account for in our uncertainties. It is easy to see from figure 11.8 that we have excellent qualitative agreement between our model and the data. However, our methods for quantitative analysis do not work as well at this photon energy, with its multitude of reaction channels with similar energy distributions, as it does at lower photon energies.

11.6 Absolute Cross Section Determination

For the data with photon energies above 16 MeV, we are able to determine the absolute cross sections using two methods: the Compton scattering comparison method used previously and the photon flux monitor method. Both methods are described in chapter 7.

In order to determine the absolute cross section using the Compton scattering comparison method, described in section 7.4.1, we follow a very similar procedure as we did when analysing the below 16 MeV data in section 9.9. The only difference here is that we must now account for neutrons from the photodisintegration of atmospheric nuclei. These are taken into account by making a simple background subtraction on a detector-by-detector basis. Table 11.10 contains the ratios required to compute the cross sections. For the neutron spectra, light-output cuts of 1100 keV_{ee} were used for the data at 20, 25 and 30 MeV, while a cut of 1800 keV_{ee} was used at 35 MeV due to the higher gain value. These cuts ensure excellent pulse-shape discrimination.

Table 11.10: Ratios of simulated and measured yields used to determine the absolute cross section of ^{6}Li photodisintegration through the Compton scattering comparison method for the data with photon energies above 16 MeV. The first uncertainty is statistical and the second is systematic. Subtraction of atmospheric neutrons has already been performed.

Beam Energy	Orientation	$\left\langle N^s_{d,\gamma}/N_{d,\gamma} \right\rangle$	$\left\langle N_{d,n}/N^s_{d,n} \right\rangle$
20 MeV	1	$0.525 \pm 0.001 \pm 0.015$	$(17.26 \pm 0.14 \pm 0.61) \times 10^{-3}$
20 MeV	3	$0.491 \pm 0.001 \pm 0.014$	$(18.55 \pm 0.14 \pm 0.59) \times 10^{-3}$
25 MeV	1	$0.456 \pm 0.001 \pm 0.011$	$(20.17 \pm 0.16 \pm 0.77) \times 10^{-3}$
25 MeV	3	$0.472 \pm 0.001 \pm 0.011$	$(19.55 \pm 0.15 \pm 0.62) \times 10^{-3}$
30 MeV	3	$0.400 \pm 0.001 \pm 0.011$	$(23.55 \pm 0.17 \pm 0.71) \times 10^{-3}$
35 MeV	1	$0.366 \pm 0.001 \pm 0.012$	$(28.63 \pm 0.22 \pm 0.99) \times 10^{-3}$
35 MeV	3	$0.392 \pm 0.001 \pm 0.013$	$(26.83 \pm 0.21 \pm 0.87) \times 10^{-3}$

We are also able to determine cross section by explicitly measuring the photon flux using the five-paddle flux monitor described in section 4.6 and the method described in section 7.4.3. By measuring the flux of the photon beam and the neutron yield, we can determine the absolute cross section. A simulation is still required to account for the effects of the finite geometry on our measurement and we continue to subtract the neutrons resulting from photodisintegration reactions in the atmosphere. However, the calculation of uncertainties will have to proceed in a slightly different way.

Previously, when we have wanted to average measurements taken with two orientations of the Blowfish neutron detector array, we assumed that all the systematic uncertainties were independent, so we added them in quadrature. This is a good approximation since rotating the array is an approximation to having a second, independent array. However, we can not make this simplifying approximation when using the flux monitor because systematic uncertainties in the flux rate and target length will not be independent between the two data acquisition runs with the array in two different orientations. It is helpful to recall equation (7.33), which we reproduce here, and take an average over all detectors,

$$\sigma_n = \frac{N_{sim}}{\Phi N \ell} \left\langle \frac{N_{d,n}}{N^s_{d,n}} \right\rangle . \tag{11.1}$$

The photon flux, Φ, and the target length, ℓ, will not be taken to have independent systematic uncertainties.

The uncertainty in the photon flux will be taken to be 2% [Pyw09b] and the target length will be taken to be 12.5 ± 0.2 cm. The target is certainly not longer than its 12.7 cm container, but it may be a few millimetres shorter. In order to achieve an uncertainty of 2% in the photon flux,

we must perform a correction for count-rate dependent effects [Pyw09b] and the attenuation of the photon beam by the lithium target and the air between the target and the monitor. It is important to note that the flux varies through a run and so we will have to apply a correction each time the flux scaler is read, instead of a single correction for the entire run. We will use the number density $N = 0.0769$ mol/cm^3 and simulations with 50 million neutron events.

The quantities required to find the cross sections using the five-paddle flux monitor are listed in table 11.11. The final cross sections are listed in table 11.12. The observable reaction channels are 6n0, 6n1 and 6p1 for 20 MeV, 6n1 and 6p1 for 25 MeV, 6n1, 6n2, 6p1 and 6p2 for 30 MeV and 6n1, 6n2, 6n3, 6p1, 6p2 and 6p3 for 35 MeV.

Table 11.11: Ratios of simulated and measured yields used to determine the absolute cross section of ^{6}Li photodisintegration using the five-paddle flux monitor for the data with photon energies above 16 MeV. The photon flux is the total number of photons and is not a rate. The subtraction of atmospheric neutrons and the flux monitor rate-dependent correction have already been performed.

Beam Energy	Orientation	Flux, Φ ($\times 10^9$ photons) $\pm$ 2%	$\left\langle N_{d,n}/N^s_{d,n} \right\rangle$
20 MeV	1	41.63	0.804 $\pm$ 0.001 (stat) $\pm$ 0.028 (syst)
20 MeV	3	25.45	0.459 $\pm$ 0.001 (stat) $\pm$ 0.015 (syst)
25 MeV	1	29.40	0.575 $\pm$ 0.001 (stat) $\pm$ 0.022 (syst)
25 MeV	3	46.00	0.900 $\pm$ 0.001 (stat) $\pm$ 0.029 (syst)
30 MeV	3	47.63	0.916 $\pm$ 0.001 (stat) $\pm$ 0.027 (syst)
35 MeV	1	38.04	0.936 $\pm$ 0.002 (stat) $\pm$ 0.032 (syst)
35 MeV	3	41.42	0.993 $\pm$ 0.002 (stat) $\pm$ 0.032 (syst)

Table 11.12: Total cross section for all observable reaction channels for the photodisintegration of ^{6}Li with photon energies above 16 MeV

Beam Energy	Compton Scattering Comparison Method (mb)	Flux Monitor Method (mb)	Weighted Average (mb)
20 MeV	1.544 $\pm$ 0.049	1.613 $\pm$ 0.069	1.567 $\pm$ 0.040
25 MeV	1.567 $\pm$ 0.047	1.690 $\pm$ 0.074	1.602 $\pm$ 0.040
30 MeV	1.601 $\pm$ 0.066	1.661 $\pm$ 0.065	1.631 $\pm$ 0.046
35 MeV	1.785 $\pm$ 0.060	2.098 $\pm$ 0.088	1.884 $\pm$ 0.050

Chapter 12

Data Analysis for ^{7}Li With Photon Energies Above 16 MeV

12.1 Introduction

We continue our study of the photodisintegration of ^{7}Li to higher photon energies. We saw a notable increase in the number of observable reaction channels in our study of the photodisintegration of ^{6}Li with photon energies above 16 MeV. The number of reaction channels for ^{7}Li increases even more due to the more complex structure of the ^{7}Li nucleus. With the exception of 7n0, it will be no longer possible to separate reaction channels from each other, which will greatly limit any conclusions that we may attempt to make.

For our study of the photodisintegration of ^{7}Li at photon energies below 16 MeV, we had the good fortune that most of the excited states under consideration are well understood and their parameters are based on several measurements. The notable exception to this are the states of ^{5}He, for which there is only a calculation of the excitation levels due to this nucleus's highly unstable nature. Now that we are dealing with higher photon energies, more care will be needed in discussing the excited states of the daughter nuclei. While the first excited state of ^{6}He, ^{6}He(1.80), is well founded experimentally, the higher-energy excited states are not. For instance, as of the review of Tilley *et al.* in 2002, the state ^{6}He(5.6) has only been observed in the reaction $^6\mathrm{Li}+^7\mathrm{Li} \rightarrow {}^7\mathrm{Be}+{}^6\mathrm{He}$ [Til02]. The state of ^{6}Li(18.0) and those with higher excitation energies are also not on the best footing. The inclusion of these states in the review is based only on observations of elastic scattering and radiative capture of ^{3}He and ^{3}H with some broad resonances in the correct energy range observed in the elastic scattering of ^{4}He and the deuteron [Til02]. In order to continue our analysis, we will consider all of the states recommended by the review with the understanding that, as the excitation energy increases, some of the states are included on limited evidence. The states to be considered are presented in table 12.1. The two-body reaction channels of interest are listed in table 12.2 and some three-body reaction channels are listed in table 12.3.

It is also quite possible that there are states which are not listed in table 12.1. We will see evidence of such a state when we analyse the data at photon energies of 25, 30 and 35 MeV.

Table 12.1: Excited states considered in the analysis of the ^{7}Li data with photon beam energies above 16 MeV in addition to those listed in table 1.4 [Til02, Til92]. Quantities listed without uncertainties have no uncertainties given in the reference. Decay widths for ^{5}He are the neutron partial widths and no uncertainties are given in the reference for these or the excitation energy.

Isotope	Excitation Energy (MeV)	Spin/Parity	Decay Width (MeV)
^{6}Li	17.985 ± 0.025	2^-	3.012 ± 0.007
^{6}Li	24.779 ± 0.054	3^-	6.754 ± 0.110
^{6}Li	24.890 ± 0.055	4^-	5.316 ± 0.112
^{6}Li	26.590 ± 0.065	2^-	8.684 ± 0.125
^{6}He	5.6 ± 0.3	n/a	12.1 ± 1.1
^{6}He	14.6 ± 0.7	n/a	7.4 ± 1.0
^{6}He	15.5 ± 0.5	n/a	4.0 ± 2.0
^{6}He	23.3 ± 1.0	n/a	14.8 ± 2.3
^{5}He	16.84	$\frac{3}{2}^+$	0.040
^{5}He	19.14	$\frac{5}{2}^+$	0.003
^{5}He	21.25	$\frac{3}{2}^+$	0.098
^{4}He	21.01	0^-	0.20

Table 12.2: Two-body reaction channels to consider in the analysis of the ^{7}Li data above 16 MeV in addition to those listed in table 10.1

Label	Reaction		Threshold (MeV)
7p2	$^7\mathrm{Li} + \gamma \rightarrow p + {}^6\mathrm{He}(5.6)$	$\rightarrow p + 2n + {}^4\mathrm{He}(\mathrm{g.s.})$	15.6
7tα2	$^7\mathrm{Li} + \gamma \rightarrow {}^3\mathrm{H} + {}^4\mathrm{He}(21.0)$	$\rightarrow n + {}^3\mathrm{H} + {}^3\mathrm{He}$	23.5
7p3	$^7\mathrm{Li} + \gamma \rightarrow p + {}^6\mathrm{He}(14.6)$	$\rightarrow p + 2n + {}^4\mathrm{He}(\mathrm{g.s.})$	24.6
7n6	$^7\mathrm{Li} + \gamma \rightarrow n + {}^6\mathrm{Li}(18.0)$		25.3
7p4	$^7\mathrm{Li} + \gamma \rightarrow p + {}^6\mathrm{He}(15.5)$	$\rightarrow p + 2n + {}^4\mathrm{He}(\mathrm{g.s.})$	25.5
7hh	$^7\mathrm{Li} + \gamma \rightarrow {}^3\mathrm{He} + {}^4\mathrm{H}$	$\rightarrow n + {}^3\mathrm{He} + {}^3\mathrm{H}$	25.9
7d2	$^7\mathrm{Li} + \gamma \rightarrow d + {}^5\mathrm{He}(16.8)$	$\rightarrow n + d + {}^4\mathrm{He}(\mathrm{g.s.})$	26.4
7d3	$^7\mathrm{Li} + \gamma \rightarrow d + {}^5\mathrm{He}(19.1)$	$\rightarrow n + d + {}^4\mathrm{He}(\mathrm{g.s.})$	28.7
7d4	$^7\mathrm{Li} + \gamma \rightarrow d + {}^5\mathrm{He}(21.3)$	$\rightarrow n + d + {}^4\mathrm{He}(\mathrm{g.s.})$	30.9
7n7	$^7\mathrm{Li} + \gamma \rightarrow n + {}^6\mathrm{Li}(24.8)$		32.1
7n8	$^7\mathrm{Li} + \gamma \rightarrow n + {}^6\mathrm{Li}(24.9)$		32.2
7p5	$^7\mathrm{Li} + \gamma \rightarrow p + {}^6\mathrm{He}(23.3)$	$\rightarrow p + 2n + {}^4\mathrm{He}(\mathrm{g.s.})$	33.3
7n9	$^7\mathrm{Li} + \gamma \rightarrow n + {}^6\mathrm{Li}(26.6)$		33.9

Table 12.3: Three-body photodisintegration reaction channels for ^{7}Li that produce neutrons and have thresholds above 16 MeV

Reaction		Threshold (MeV)
$^7\mathrm{Li} + \gamma \rightarrow n + {}^3\mathrm{He}(\mathrm{g.s.}) + {}^3\mathrm{H}(\mathrm{g.s.})$		23.0
$^7\mathrm{Li} + \gamma \rightarrow 2n + {}^5\mathrm{Li}(16.9)$	$\rightarrow 2n + p + {}^4\mathrm{He}(\mathrm{g.s.})$	27.3
$^7\mathrm{Li} + \gamma \rightarrow n + p + {}^5\mathrm{He}(16.8)$	$\rightarrow 2n + p + {}^4\mathrm{He}(\mathrm{g.s.})$	28.6
$^7\mathrm{Li} + \gamma \rightarrow n + d + {}^4\mathrm{He}(21.0)$		29.7

12.2 Analysis for the Photon Energy of 20 MeV

For the data taken with the natural lithium target and a 20 MeV photon beam, we can proceed similarly to the below 16 MeV data. The only new reaction channel to be considered is 7p2 and we consider 7n0, 7n1, 7n2, 7n3, 7n4, 7n5, 7p2, 7d0 and 7d1, while neglecting all three-body reaction channels. The reaction channel 7p1 does not produce neutrons with a high enough energy to survive the light-output cut. The 7n0 reaction channel will be isolatable. The kinetic energy spectra for all non-isolatable reaction channels can be seen in figure 12.1. Notice that these reaction channels

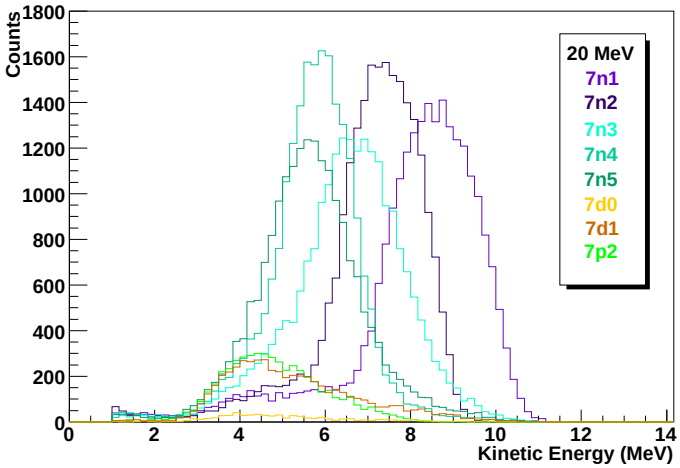

Figure 12.1: Two-body reaction channels with simulated neutron kinetic energies for a detector in the centre ring with a photon beam of 20 MeV. Each histogram is the result of 50 million simulated photodisintegration events for that reaction channel. The light-output threshold is 1100 keV$_{ee}$.

all have very similar energy spectra. One might notice that 7n1 stands out more on the high end and 7d1 and 7p2 appear at the low end. The channels 7n2, 7n3, 7n4 and 7n5 are tightly packed in the middle and cannot be separated from each other. In this analysis, we will model the photodisintegration of ^{7}Li with only four reaction channels: 7n0, 7n1^{+}, 7n3^{+} and 7d1^{+}. Again, the '+' signifies that there are neutron contributions due to other reaction channels and we cannot completely separate them. We use 7d1 rather than 7p2, given the uncertainty in the existence of the ^{6}He(5.6) state and our previous success with 7d1 at lower energies.

The reaction channel 7n0 is isolated with a cut on the light output as was done at lower energies, with one small difference. To isolate the 7n0 channel we use progressive cuts from 5000 keV$_{ee}$ in ring 1 to 5500 keV$_{ee}$ in rings 10 and 11. At lower energies we used a single cut for simplicity. However, at higher energies a progressive cut is required to preserve sufficient numbers of neutrons.

The three non-isolatable reaction channels, 7n1^{+}, 7n3^{+} and 7d1^{+}, were chosen as they cover the required energy range and fit the data well. The light-output cut used is 1100 keV$_{ee}$ as this

Table 12.4: Associated Legendre function coefficient fitting results for ^{7}Li at a photon energy of 20 MeV. The orientation signifies which detector in the most upstream ring was on top of the array. The reaction channels 7n1, 7n3 and 7d1 were used to reconstruct the data for all non-isolatable reaction channels and this is represented by the '+' on their labels. Table continues in table 12.5.

Channel	Orientation	Coefficient	Fit Result	Reduced χ^2
7n0	1	A	0.1262 ± 0.0009 (stat) ± 0.0032 (syst)	0.38
		a_1	-0.0081 ± 0.0091 (stat) ± 0.0285 (syst)	
		a_2	-0.3773 ± 0.0192 (stat) ± 0.0645 (syst)	
		a_3	0.0618 ± 0.0212 (stat) ± 0.0761 (syst)	
		a_4	-0.0765 ± 0.0290 (stat) ± 0.1060 (syst)	
		e_2	-0.0323 ± 0.0044 (stat) ± 0.0166 (syst)	
		e_3	-0.0106 ± 0.0022 (stat) ± 0.0024 (syst)	
		e_4	0.0059 ± 0.0014 (stat) ± 0.0049 (syst)	
7n0	3	A	0.1184 ± 0.0009 (stat) ± 0.0032 (syst)	1.36
		a_1	-0.0647 ± 0.0117 (stat) ± 0.0406 (syst)	
		a_2	-0.4599 ± 0.0197 (stat) ± 0.0668 (syst)	
		a_3	-0.1678 ± 0.0250 (stat) ± 0.0916 (syst)	
		a_4	-0.1615 ± 0.0301 (stat) ± 0.1132 (syst)	
		e_2	-0.0179 ± 0.0049 (stat) ± 0.0129 (syst)	
		e_3	-0.0001 ± 0.0010 (stat) ± 0.0035 (syst)	
		e_4	-0.0010 ± 0.0015 (stat) ± 0.0031 (syst)	
7n1$^+$	1	A	0.1203 ± 0.0003 (stat) ± 0.0005 (syst)	5.55
		a_1	0.1337 ± 0.0043 (stat) ± 0.0078 (syst)	
		a_2	-0.3006 ± 0.0067 (stat) ± 0.0114 (syst)	
7n1$^+$	3	A	0.1340 ± 0.0003 (stat) ± 0.0006 (syst)	22.73
		a_1	0.0470 ± 0.0040 (stat) ± 0.0074 (syst)	
		a_2	-0.5150 ± 0.0062 (stat) ± 0.0110 (syst)	
7n3$^+$	1	A	0.1078 ± 0.0003 (stat) ± 0.0005 (syst)	9.13
		a_1	-0.1617 ± 0.0046 (stat) ± 0.0078 (syst)	
		a_2	-0.3583 ± 0.0072 (stat) ± 0.0121 (syst)	
7n3$^+$	3	A	0.1226 ± 0.0003 (stat) ± 0.0005 (syst)	10.04
		a_1	-0.1559 ± 0.0043 (stat) ± 0.0079 (syst)	
		a_2	-0.3307 ± 0.0070 (stat) ± 0.0127 (syst)	

Table 12.5: Associated Legendre function coefficient fitting results for ^{7}Li at a photon energy of 20 MeV. Table continues from table 12.4.

Channel	Orientation	Coefficient	Fit Result	Reduced χ^2
7d1$^+$	1	A	0.3646 ± 0.0010 (stat) ± 0.0026 (syst)	5.87
		a_1	0.0866 ± 0.0094 (stat) ± 0.0244 (syst)	
7d1$^+$	3	A	0.3897 ± 0.0011 (stat) ± 0.0028 (syst)	7.93
		a_1	0.1399 ± 0.0090 (stat) ± 0.0243 (syst)	
^{6}Li	1	A	0.0394 ± 0.0011	
^{6}Li	3	A	0.0423 ± 0.0012	

cut provides excellent separation of neutrons and gamma-rays through PSD. A lower light-output cut does not allow us to include any more reaction channels. Figure 12.2 shows the neutron kinetic energy spectrum of a detector in the centre ring with the three reaction channels fit to it, along with the 7n0, ^{6}Li and background contributions. Notice that these reaction channels alone are indeed

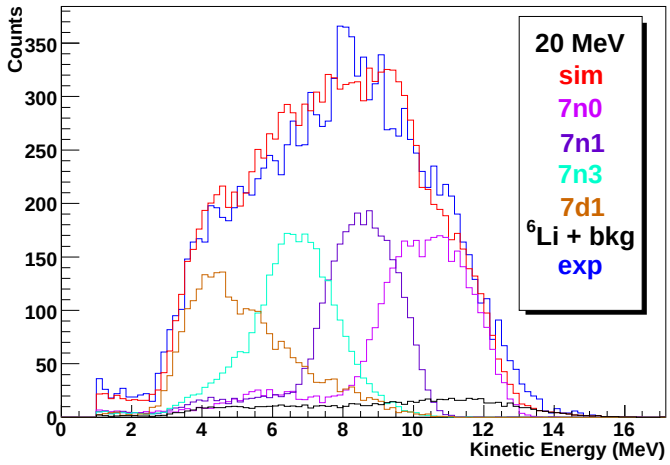

Figure 12.2: The neutron kinetic energy spectra for a beam energy of 20 for a detector in the centre ring. Shown are the simulations of various reaction channels, the ^{6}Li contribution added with the background neutrons (black) and the measured spectrum (blue). The red histogram is the sum of the simulation histograms.

able to reproduce the measured spectra. It is unfortunate that we cannot include the 7n2, 7n4 and 7n5 reaction channels in our fit but the fitting routine is not able to discern between them and the results are essentially meaningless. Careful attention will have to be given in the interpretation of our results.

The background neutrons from the photodisintegration of atmospheric nitrogen do not affect

our analysis of the 7n0 reaction channel. The light-output cut that eliminates the non-isolatable reaction channels also eliminates this background. We do take into account background neutrons in our analysis of the other reaction channels.

It is no longer possible to use the isotope neutron yield comparison method to find the cross section of the photodisintegration of ^{7}Li relative to that of ^{6}Li. As can be seen in figure 12.2, there are insufficient numbers of neutrons due to ^{6}Li with high enough energy to perform such an analysis.

The raw fit results are given in table 12.4 and the uncertainty on the quantities associated with ^{6}Li are now computed based on a five-paddle photon flux monitor uncertainty of 2%. The final associated Legendre function coefficients are given in tables 12.6 and 12.7.

Table 12.6: Final associated Legendre function coefficient values for the reaction channel 7n0 at a photon energy of 20 MeV

Coeff.	Value
a_1	-0.027 ± 0.024
a_2	-0.417 ± 0.048
a_3	-0.032 ± 0.061
a_4	-0.116 ± 0.080
e_2	-0.024 ± 0.011
e_3	-0.0059 ± 0.0024
e_4	0.0012 ± 0.0029

Table 12.7: Final associated Legendre function coefficient values for reaction channels of the photodisintegration of ^{7}Li other than 7n0 at a photon energy of 20 MeV

Reaction Channel	a_1	a_2
7n1^{+}	0.115 ± 0.019	-0.346 ± 0.028
7n3^{+}	-0.160 ± 0.016	-0.331 ± 0.046
7d1^{+}	0.110 ± 0.048	n/a

Notice that the e_2 value for 7n0 may be different from zero. This indicates that the photons may not be 100% circularly polarised as this value would be zero if the beam had no linear components. However, because of the large uncertainties associated with isolating the 7n0 reaction channel, we cannot say that this evidence is even remotely conclusive. Deuterium measurements taken with the same experimental setup may give us a better indication if there is a small linear polarisation component to the photon beam.

Also note that the coefficients in table 12.7 associated with $7n1^+$, $7n3^+$ and $7d1^+$ must be used with great care. These coefficients are useful inputs to the simulation and we can reproduce the measured spectra. However, the 7n2, 7n4 and 7n5 reaction channels have been completely neglected and their contributions will greatly influence these coefficients.

Using the A values of table 12.4 we are able to determine a number of relative cross sections:

$$\begin{aligned}
\frac{\sigma[7n0]}{\sigma[7n0 + 7n1^+ + 7n3^+ + 7d1^+]} &= 0.1647 \pm 0.0035, \\
\frac{\sigma[7n1^+]}{\sigma[7n0 + 7n1^+ + 7n3^+ + 7d1^+]} &= 0.1692 \pm 0.0023, \\
\frac{\sigma[7n3^+]}{\sigma[7n0 + 7n1^+ + 7n3^+ + 7d1^+]} &= 0.1546 \pm 0.0021, \\
\frac{\sigma[7d1^+]}{\sigma[7n0 + 7n1^+ + 7n3^+ + 7d1^+]} &= 0.5082 \pm 0.0083, \\
\frac{\sigma[7n0]}{\sigma[6n0 + 6n1 + 6p1]} &= 0.2448 \pm 0.0068 \text{ and} \\
\frac{\sigma[7n0 + 7n1^+ + 7n3^+ + 7d1^+]}{\sigma[6n0 + 6n1 + 6p1]} &= 1.492 \pm 0.053.
\end{aligned}$$

12.3 Analysis for the Photon Energies of 25, 30 and 35 MeV

The isotope ^{7}Li has turned out to be a proverbial dark horse. Looking at our analysis for the data at 20 MeV, we may postulate that the analysis at 25, 30 and 35 MeV will proceed similarly. We expect to be able to isolate the 7n0 reaction channel with increasing difficulty and to have a cocktail of other reaction channels that are not separable but can describe the measured spectrum well. For the most part this is the case. However, a careful analysis of the data shows neutrons with spectra that cannot be explained by any of the reaction channels listed in tables 10.1, 12.2 and 12.3.

These neutrons can most clearly be seen in the data taken with a photon beam of energy 30 MeV, but are certainly observable in the data at photon energies of 25 and 35 MeV. A sample time-of-flight spectrum is provided in figure 12.3. This spectrum compares measured data to simulated data containing a representative sample of reaction channels. None of the two-body reaction channels in tables 10.1 and 12.2 are able to describe the anomalous peak. There are three possible origins for these neutrons: a two-body reaction channel $^7\text{Li} + \gamma \rightarrow n + {}^6\text{Li(X)}$, where ^{6}Li(X) is an excited state of ^{6}Li not in the standard tables of the reference [Til02], a three-body reaction channel such as 7nd, 7nn0 or 7np0 or the four-body reaction channel $^7\text{Li} + \gamma \rightarrow 2n + p + {}^4\text{He}$. The neutrons cannot be due to a reaction where the neutrons are produced in the decay of an unstable daughter nucleus; the variation of neutron kinetic energy with photon energy does not support such a proposition.

We can eliminate the four-body reaction channel first by using a simple kinematics argument. The threshold for this reaction is 10.9 MeV, from table 1.3. We expect the neutrons and proton to take nearly all of the kinetic energy and for them to take away about a third of the energy each

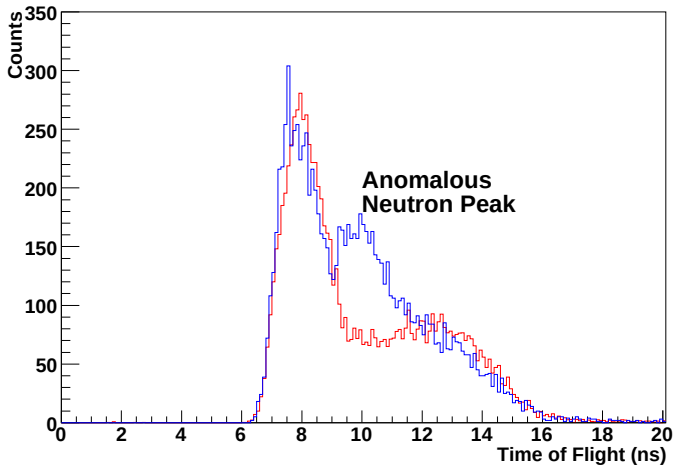

Figure 12.3: Time-of-flight spectra for detector 49 with the natural lithium target and a photon beam energy of 30 MeV. The measured spectrum is blue and the simulated spectrum is red. Notice the anomalous neutron peak at a time-of-flight of 10 ns.

on average. For the data with a photon energy of 35 MeV, the neutron peak is observed to have energy between 10 and 16 MeV, depending on the ring. However, the reaction products have only 24.1 MeV available to them, meaning that they would take, on average, 8.0 MeV of kinetic energy away with them; this is insufficient to explain the data at 35 MeV.

Because we have data at three photon energies we should be able to determine if the neutrons are from a two-body reaction or a three-body reaction by their time-of-flight spectra. Figure 12.4 shows the time-of-flight spectra of two three-body reactions, 7nd and 7np0, compared with a two-body reaction with excitation energy of 10 MeV. Two-body reactions that produce either a neutron and a proton or two neutrons can be excluded based on the plots. Because the kinetic energy must be split between two particles of equal or near-equal mass, the peak is not narrow enough to explain the data and it does not have the correct energy dependence. There are two three-body reaction channels that have sharper peaks and energy dependence that is more like the experimental data, $^{7}\mathrm{Li} + \gamma \rightarrow n + d + {}^{4}\mathrm{He}$, labelled 7nd, and $^{7}\mathrm{Li} + \gamma \rightarrow n + {}^{3}\mathrm{H} + {}^{3}\mathrm{He}$, which was never given a label. These reaction channels produce a single neutron plus two heavier daughter nuclei, meaning that the neutron carries away most of the kinetic energy. The reaction channel $^{7}\mathrm{Li} + \gamma \rightarrow n + d + {}^{4}\mathrm{He}$(g.s.) can be excluded based on its kinetic energy being greater than the measured data, while the threshold for $^{7}\mathrm{Li} + \gamma \rightarrow n + d + {}^{4}\mathrm{He}(21.0)$ is too high. From table 1.3 the reaction channel $^{7}\mathrm{Li} + \gamma \rightarrow n + {}^{3}\mathrm{H} + {}^{3}\mathrm{He}$ has a threshold of 23.0 MeV, which is much too high to explain the data.

By a process of elimination we find that the data is best explained by a two-body reaction channel with an excited state of ^{6}Li not in the standard tables. In determining the excitation

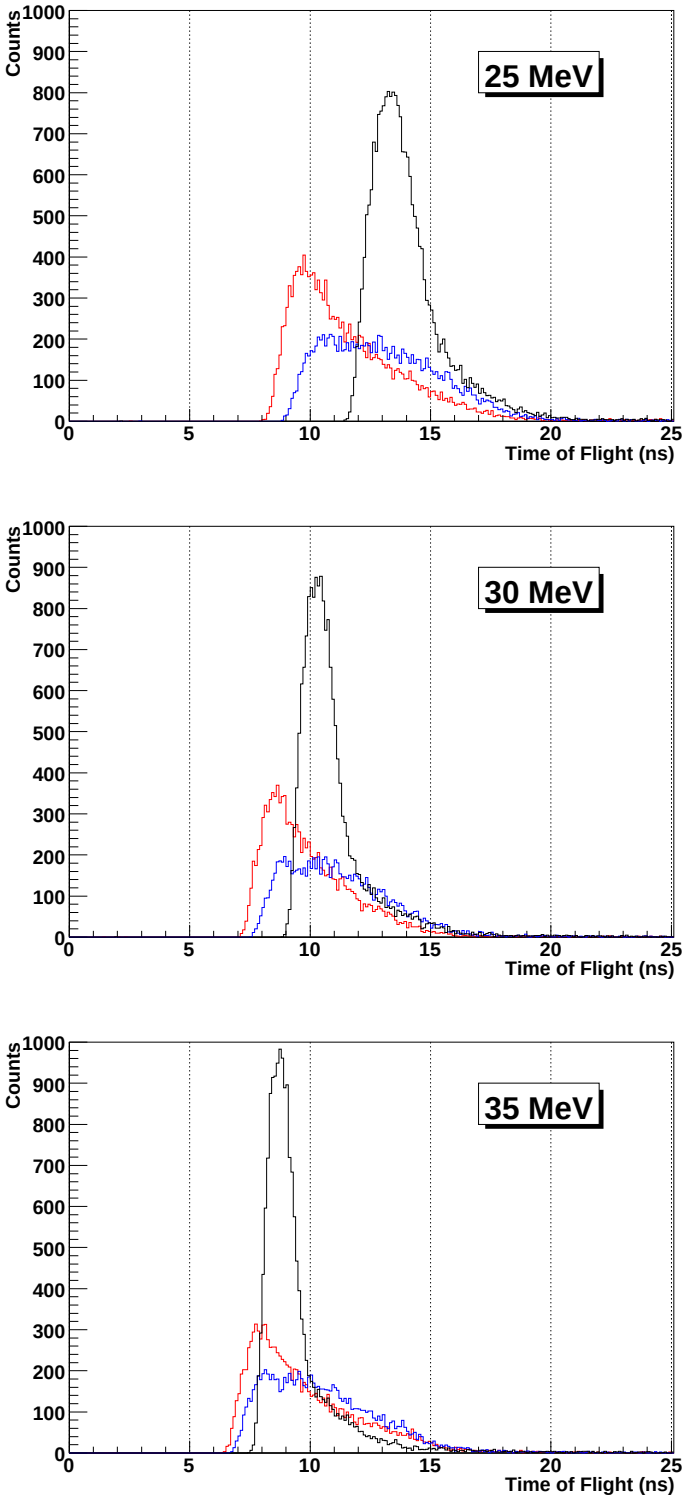

Figure 12.4: Simulated time-of-flight spectra for a detector in the centre ring with a photon beam of 25, 30 and 35 MeV. The black spectra correspond to the 2-body decay with an excited state of ^{6}Li with excitation energy of 10 MeV while the blue spectra are 7np0 and the red spectra are 7nd. Each histogram is the result of 50 million simulated photodisintegration events for that reaction channel.

energy we assume the state has zero decay width, $\Gamma = 0$. We do not have sufficient resolution to determine the decay width based on our measurements. By adjusting the excitation energy of the reaction in our simulation and fitting the resulting spectra to the data we see that it has an excitation energy of 10.0 ± 0.5 MeV. We will label this reaction channel as 7nX and its long form is written $^7\mathrm{Li} + \gamma \rightarrow n + {}^6\mathrm{Li}(10.0)$. The uncertainty in the excitation energy was determined by varying the excitation energy in the simulation. It was found that excitation energies from 9.5 to 10.5 MeV fit the measured data.

The idea that there is an excited state of ^{6}Li between 5.7 and 18.0 MeV is not new. Duĭsebaev *et al.* claimed to have observed an excited state of ^{6}Li with energy 14.0 MeV and a width that does not exceed several dozen keV [Duĭ74]. They studied the reaction $^9\mathrm{Be} + p \rightarrow \alpha + {}^6\mathrm{Li}$. Grüebler *et al.* saw evidence for a new state with excitation energy between 11 and 15 MeV while studying the reaction $^4\mathrm{He} + \vec{d} \rightarrow d + {}^4\mathrm{He}$ [Grü75]. Delbar *et al.* suggest there is evidence for a state with excitation energy $E_x = 8.2 \pm 0.2$ MeV with a decay width of $\Gamma = 2.2 \pm 0.2$ MeV while studying the reaction $^9\mathrm{Be} + p \rightarrow \alpha + {}^6\mathrm{Li}$ [Del76]. Later, they would again find evidence of an anomaly that could correspond to an excited state of ^{6}Li [Del83]. This observation was made with both the reactions $^9\mathrm{Be} + p \rightarrow \alpha + {}^6\mathrm{Li}$ and $^9\mathrm{Be} + {}^3\mathrm{He} \rightarrow 2{}^6\mathrm{Li}$ and suggests an excited state with energy 8 to 12 MeV. These measurements are based on hadronic processes and all report possible states between 8 and 15 MeV. However, the measured excitation energies are not consistent, so no such state is included in the standard tables. We must wonder if some, or all, of these measurements are indeed observing the excited state of ^{6}Li that we believe we are observing in our photodisintegration data.

In order to isolate the 7n0 reaction channel we will use light-output cuts from 8200 to 9200 keV$_{ee}$ for a photon energy of 25 MeV, 11500 to 13000 keV$_{ee}$ at 30 MeV and 15000 to 16800 keV$_{ee}$ at 35 MeV. In order to observe the other reaction channels we will use a light-output cut of 1100 keV$_{ee}$ at 25 MeV while we use a light output cut of 1800 keV$_{ee}$ at 30 and 35 MeV. An astute reader may wonder why we use different minimum light-output cuts for ^{6}Li and ^{7}Li at 30 MeV. It is because these data collection runs were performed with different detector gains since the ^{6}Li was done during an evening and the ^{7}Li was done the next morning on the say day as the 35 MeV runs, which required a different gain setting.

Figure 12.5 shows the neutron kinetic energy spectra, while figure 12.6 shows the time-of-flight spectra comparing the measured data with the simulations. Since it is not possible to separate all of the reaction channels, we use a representative sample and add on the '+' designation. At all photon energies we fit the 7n0, 7n3$^+$ and 7nX$^+$ reaction channels. For the data with a photon energy of 25 MeV, we also include 7n1$^+$ to better describe the high-energy peak. For photon energies of 25 and 30 MeV we will use 7d1$^+$ to describe the low energy neutrons, while at 30 MeV we will use 7n6$^+$ which appears to become dominant.

The raw results of the data analysis can be found in tables 12.8, 12.10 and 12.11 which are

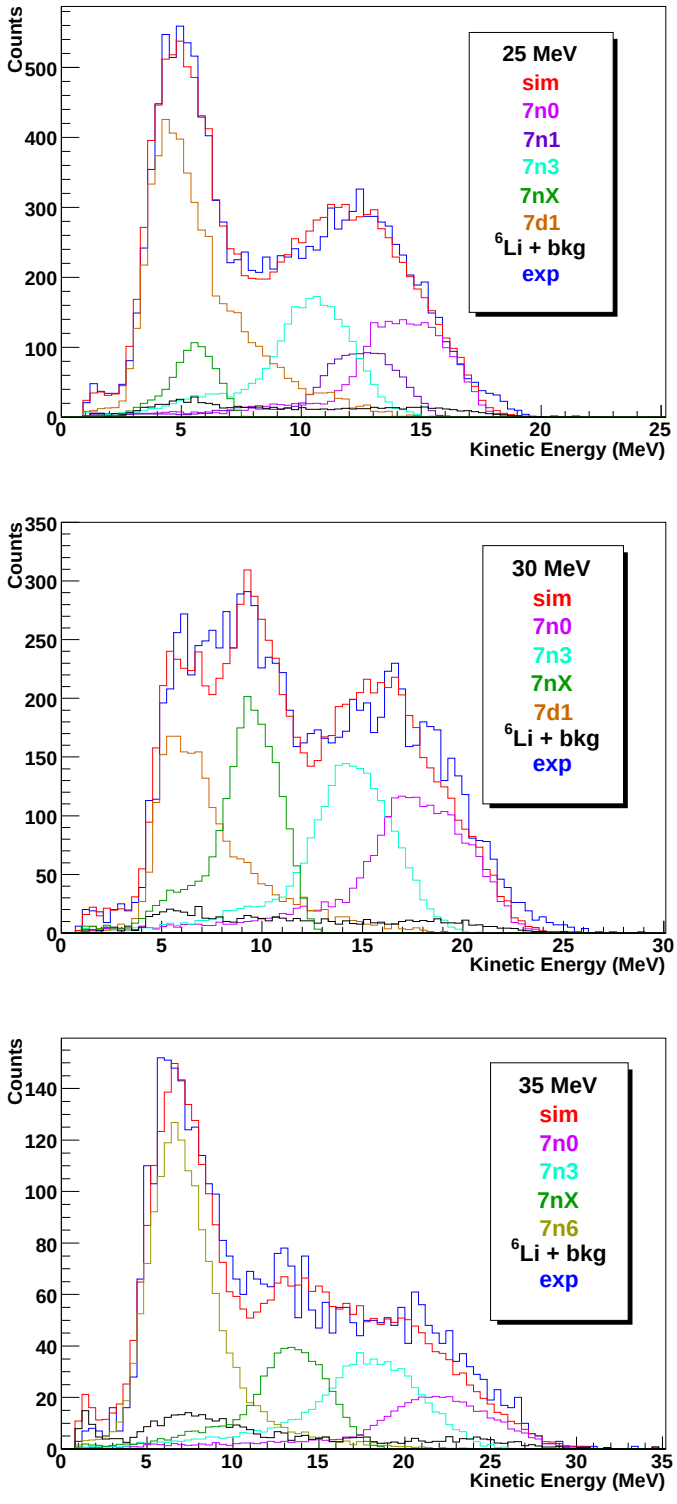

Figure 12.5: The neutron kinetic energy spectra for beam energies of 25, 30 and 35 MeV for a detector in a centre ring. Shown are the simulations of various reaction channels, the ^{6}Li contribution added with the background neutrons (black) and the measured spectrum (blue). The red histogram is the sum of the simulation histograms.

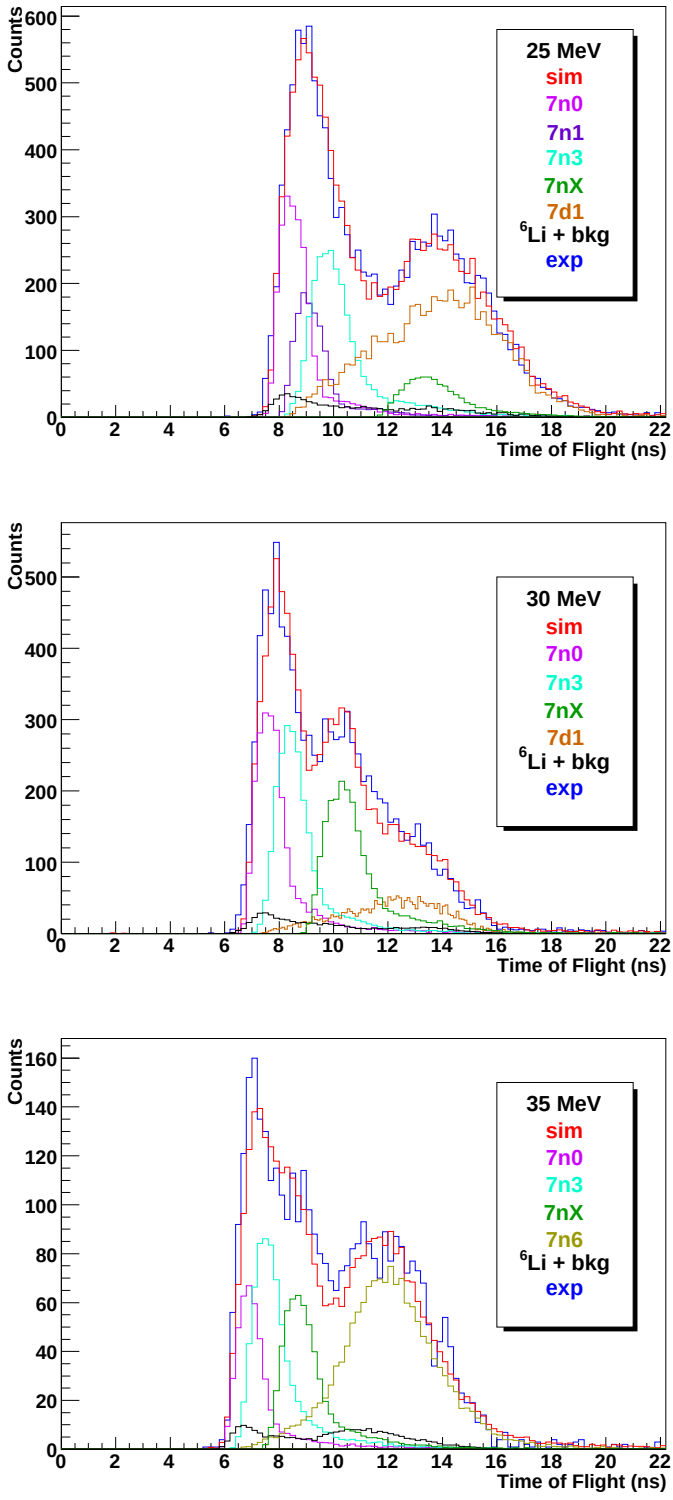

Figure 12.6: The time-of-flight spectra for beam energies of 25, 30 and 35 MeV for a detector in a centre ring. Shown are the simulations of various reaction channels, the ^{6}Li contribution added with the background neutrons (black) and the measured spectrum (blue). The red histogram is the sum of the simulation histograms.

Table 12.8: Associated Legendre function coefficient fitting results for ^{7}Li at a photon energy of 25 MeV. The orientation signifies which detector in the most upstream ring was on top of the array. The reaction channels 7n1, 7n3, 7nX and 7d1 were used to reconstruct the data for all non-isolatable reaction channels and this is represented by the '+' on their labels. Table continues in table 12.9.

Channel	Orientation	Coefficient	Fit Result	Reduced χ^2
7n0	1	A	0.0716 ± 0.0011 (stat) ± 0.0036 (syst)	0.50
		a_1	-0.1250 ± 0.0247 (stat) ± 0.0866 (syst)	
		a_2	-0.4798 ± 0.0384 (stat) ± 0.1371 (syst)	
		a_3	0.1925 ± 0.0489 (stat) ± 0.1938 (syst)	
		a_4	0.0191 ± 0.0566 (stat) ± 0.2328 (syst)	
7n0	3	A	0.0885 ± 0.0012 (stat) ± 0.0041 (syst)	0.16
		a_1	-0.0696 ± 0.0217 (stat) ± 0.0854 (syst)	
		a_2	-0.4345 ± 0.0331 (stat) ± 0.1315 (syst)	
		a_3	0.1636 ± 0.0427 (stat) ± 0.1914 (syst)	
		a_4	-0.1534 ± 0.0521 (stat) ± 0.2347 (syst)	
7n1$^+$	1	A	0.0332 ± 0.0002 (stat) ± 0.0002 (syst)	67.48
		a_1	0.0816 ± 0.0086 (stat) ± 0.0100 (syst)	
		a_2	-0.4144 ± 0.0137 (stat) ± 0.0172 (syst)	
7n1$^+$	3	A	0.0528 ± 0.0002 (stat) ± 0.0003 (syst)	42.65
		a_1	0.2047 ± 0.0063 (stat) ± 0.0082 (syst)	
		a_2	-0.7593 ± 0.0094 (stat) ± 0.0116 (syst)	
7n3$^+$	1	A	0.0793 ± 0.0002 (stat) ± 0.0004 (syst)	11.43
		a_1	0.2053 ± 0.0057 (stat) ± 0.0100 (syst)	
		a_2	-0.3101 ± 0.0085 (stat) ± 0.0146 (syst)	
7n3$^+$	3	A	0.1062 ± 0.0003 (stat) ± 0.0005 (syst)	7.67
		a_1	0.1668 ± 0.0049 (stat) ± 0.0100 (syst)	
		a_2	-0.1513 ± 0.0075 (stat) ± 0.0152 (syst)	
7nX$^+$	1	A	0.0534 ± 0.0002 (stat) ± 0.0004 (syst)	29.50
		a_1	1.6922 ± 0.0062 (stat) ± 0.0052 (syst)	
		a_2	0.6925 ± 0.0084 (stat) ± 0.0068 (syst)	
7nX$^+$	3	A	0.0637 ± 0.0002 (stat) ± 0.0004 (syst)	77.60
		a_1	1.9838 ± 0.0054 (stat) ± 0.0039 (syst)	
		a_2	1.3582 ± 0.0064 (stat) ± 0.0032 (syst)	

Table 12.9: Associated Legendre function coefficient fitting results for ^{7}Li at a photon energy of 25 MeV. Table continues from table 12.8.

Channel	Orientation	Coefficient	Fit Result	Reduced χ^2
7d1^{+}	1	A	0.3882 ± 0.0009 (stat) ± 0.0028 (syst)	18.52
		a_1	1.2679 ± 0.0060 (stat) ± 0.0153 (syst)	
		a_1	-1.8006 ± 0.0205 (stat) ± 0.0551 (syst)	
7d1^{+}	3	A	0.5360 ± 0.0011 (stat) ± 0.0038 (syst)	12.25
		a_1	1.0942 ± 0.0053 (stat) ± 0.0165 (syst)	
		a_1	-1.7234 ± 0.0181 (stat) ± 0.0595 (syst)	
^{6}Li	1	A	0.0377 ± 0.0011	
^{6}Li	3	A	0.0491 ± 0.0014	

Table 12.10: Associated Legendre function coefficient fitting results for ^{7}Li at a photon energy of 30 MeV. The orientation signifies which detector in the most upstream ring was on top of the array. The reaction channels 7n3, 7nX and 7d1 were used to reconstruct the data for all non-isolatable reaction channels and this is represented by the '+' on their labels.

Channel	Orientation	Coefficient	Fit Result	Reduced χ^2
7n0	3	A	0.0761 ± 0.0017 (stat) ± 0.0050 (syst)	0.28
		a_1	-0.0240 ± 0.0376 (stat) ± 0.1232 (syst)	
		a_2	-0.7630 ± 0.0593 (stat) ± 0.1851 (syst)	
		a_3	-0.2898 ± 0.0671 (stat) ± 0.2808 (syst)	
		a_4	-0.3525 ± 0.0725 (stat) ± 0.3224 (syst)	
7n3^{+}	3	A	0.1443 ± 0.0003 (stat) ± 0.0006 (syst)	8.30
		a_1	0.0824 ± 0.0047 (stat) ± 0.0088 (syst)	
		a_2	-0.3098 ± 0.0070 (stat) ± 0.0122 (syst)	
7nX^{+}	3	A	0.0940 ± 0.0003 (stat) ± 0.0005 (syst)	5.72
		a_1	0.2292 ± 0.0052 (stat) ± 0.0101 (syst)	
		a_2	-0.4982 ± 0.0078 (stat) ± 0.0143 (syst)	
7d1^{+}	3	A	0.6136 ± 0.0016 (stat) ± 0.0048 (syst)	4.58
		a_1	0.4156 ± 0.0074 (stat) ± 0.0234 (syst)	
^{6}Li	3	A	0.0503 ± 0.0014	

Table 12.11: Associated Legendre function coefficient fitting results for ^{7}Li at a photon energy of 35 MeV. The orientation signifies which detector in the most upstream ring was on top of the array. The reaction channels 7n3, 7nX and 7n6 were used to reconstruct the data for all non-isolatable reaction channels and this is represented by the '+' on their labels.

Channel	Orientation	Coefficient	Fit Result	Reduced χ^2
7n0	1	A	0.0138 ± 0.0009 (stat) ± 0.0012 (syst)	0.82
		a_1	0.2755 ± 0.1244 (stat) ± 0.2541 (syst)	
7n0	3	A	0.0314 ± 0.0014 (stat) ± 0.0026 (syst)	1.14
		a_1	0.3067 ± 0.0695 (stat) ± 0.2546 (syst)	
7n3$^+$	1	A	0.0473 ± 0.0003 (stat) ± 0.0002 (syst)	19.56
		a_1	0.2231 ± 0.0089 (stat) ± 0.0095 (syst)	
		a_2	-0.3587 ± 0.0140 (stat) ± 0.0137 (syst)	
7n3$^+$	3	A	0.1249 ± 0.0004 (stat) ± 0.0006 (syst)	48.52
		a_1	0.2878 ± 0.0055 (stat) ± 0.0093 (syst)	
		a_2	-0.6189 ± 0.0085 (stat) ± 0.0139 (syst)	
7nX$^+$	1	A	0.0247 ± 0.0002 (stat) ± 0.0001 (syst)	7.98
		a_1	-0.1239 ± 0.0110 (stat) ± 0.0083 (syst)	
		a_2	-0.6778 ± 0.0180 (stat) ± 0.0133 (syst)	
7nX$^+$	3	A	0.0707 ± 0.0003 (stat) ± 0.0003 (syst)	10.19
		a_1	-0.1238 ± 0.0066 (stat) ± 0.0087 (syst)	
		a_2	-0.4881 ± 0.0105 (stat) ± 0.0136 (syst)	
7n6$^+$	1	A	0.0931 ± 0.0003 (stat) ± 0.0006 (syst)	2.64
		a_1	0.0637 ± 0.0066 (stat) ± 0.0117 (syst)	
		a_2	-0.3868 ± 0.0107 (stat) ± 0.0184 (syst)	
7n6$^+$	3	A	0.2580 ± 0.0005 (stat) ± 0.0015 (syst)	2.23
		a_1	0.0355 ± 0.0039 (stat) ± 0.0116 (syst)	
		a_2	-0.3784 ± 0.0062 (stat) ± 0.0177 (syst)	
^{6}Li	1	A	0.0245 ± 0.0007	
^{6}Li	3	A	0.0662 ± 0.0019	

Table 12.12: Final associated Legendre function coefficient values for ^{7}Li at photon energies of 25, 30 and 35 MeV for the reaction channel 7n0

Energy	Coefficient	Fit Result
25 MeV	a_1	-0.097 ± 0.063
	a_2	-0.456 ± 0.098
	a_3	0.18 ± 0.14
	a_4	-0.07 ± 0.17
30 MeV	a_1	-0.02 ± 0.13
	a_2	-0.76 ± 0.19
	a_3	-0.29 ± 0.29
	a_4	-0.35 ± 0.33
35 MeV	a_1	0.29 ± 0.19

Table 12.13: Final associated Legendre function coefficient values for ^{7}Li at photon energies of 25 MeV for the reaction channel 7n1^{+}

Energy	Coefficient	Fit Result
25 MeV	a_1	0.170 ± 0.057
	a_2	-0.681 ± 0.086

Table 12.14: Final associated Legendre function coefficient values for ^{7}Li at photon energies of 25, 30 and 35 MeV for the reaction channel 7n3^{+}

Energy	Coefficient	Fit Result
25 MeV	a_1	0.182 ± 0.024
	a_2	-0.215 ± 0.036
30 MeV	a_1	0.082 ± 0.029
	a_2	-0.310 ± 0.041
35 MeV	a_1	0.247 ± 0.046
	a_2	-0.454 ± 0.069

Table 12.15: Final associated Legendre function coefficient values for ^{7}Li at photon energies of 25, 30 and 35 MeV for the reaction channel 7nX^{+}

Energy	Coefficient	Fit Result
25 MeV	a_1	1.797 ± 0.035
	a_2	1.002 ± 0.043
30 MeV	a_1	0.229 ± 0.027
	a_2	-0.498 ± 0.039
35 MeV	a_1	-0.124 ± 0.026
	a_2	-0.570 ± 0.041

Table 12.16: Final associated Legendre function coefficient values for ^{7}Li at photon energies of 25 and 30 MeV for the reaction channel 7d1^{+}

Energy	Coefficient	Fit Result
25 MeV	a_1	1.168 ± 0.046
	a_2	-1.76 ± 0.17
30 MeV	a_1	0.416 ± 0.053

Table 12.17: Final associated Legendre function coefficient values for ^{7}Li at photon energies of 35 MeV for the reaction channel 7n6^{+}

Energy	Coefficient	Fit Result
35 MeV	a_1	0.047 ± 0.014
	a_2	-0.382 ± 0.022

respectively the results for photon energies of 25, 30 and 35 MeV. The final values for the associated Legendre function coefficients are given in tables 12.12 for 7n0, 12.13 for 7n1, 12.14 for 7n3, 12.15 for 7nX, 12.16 for 7d1 and 12.17 for 7n6. Using the A values of our fits we can find relative cross sections. For a photon energy of 25 MeV, we find

$$\begin{aligned}
\frac{\sigma[7n0]}{\sigma[7n0+7n1^{+}+7n3^{+}+7nX^{+}+7d1^{+}]} &= 0.1085 \pm 0.0042, \\
\frac{\sigma[7n1^{+}]}{\sigma[7n0+7n1^{+}+7n3^{+}+7nX^{+}+7d1^{+}]} &= 0.0589 \pm 0.0024, \\
\frac{\sigma[7n3^{+}]}{\sigma[7n0+7n1^{+}+7n3^{+}+7nX^{+}+7d1^{+}]} &= 0.1259 \pm 0.0023, \\
\frac{\sigma[7nX^{+}]}{\sigma[7n0+7n1^{+}+7n3^{+}+7nX^{+}+7d1^{+}]} &= 0.0808 \pm 0.0032, \\
\frac{\sigma[7d1^{+}]}{\sigma[7n0+7n1^{+}+7n3^{+}+7nX^{+}+7d1^{+}]} &= 0.628 \pm 0.015, \\
\frac{\sigma[7n0]}{\sigma[6n1+6p1]} &= 0.1515 \pm 0.0062 \text{ and} \\
\frac{\sigma[7n0+7n1^{+}+7n3^{+}+7nX^{+}+7d1^{+}]}{\sigma[6n1+6p1]} &= 1.390 \pm 0.035.
\end{aligned}$$

For a photon energy of 30 MeV, we find

$$\begin{aligned}
\frac{\sigma[7n0]}{\sigma[7n0+7n3^{+}+7nX^{+}+7d1^{+}]} &= 0.0820 \pm 0.0058, \\
\frac{\sigma[7n3^{+}]}{\sigma[7n0+7n3^{+}+7nX^{+}+7d1^{+}]} &= 0.1555 \pm 0.0029, \\
\frac{\sigma[7nX^{+}]}{\sigma[7n0+7n3^{+}+7nX^{+}+7d1^{+}]} &= 0.1013 \pm 0.0020, \\
\frac{\sigma[7d1^{+}]}{\sigma[7n0+7n3^{+}+7nX^{+}+7d1^{+}]} &= 0.661 \pm 0.015, \\
\frac{\sigma[7n0]}{\sigma[6n1+6p1+6n2+6p2]} &= 0.1243 \pm 0.0093 \text{ and} \\
\frac{\sigma[7n0+7n3^{+}+7nX^{+}+7d1^{+}]}{\sigma[6n1+6p1+6n2+6p2]} &= 1.515 \pm 0.047.
\end{aligned}$$

For a photon energy of 35 MeV, we find

$$\begin{aligned}
\frac{\sigma[7n0]}{\sigma[7n0+7n3^{+}+7nX^{+}+7n6^{+}]} &= 0.0689 \pm 0.0050, \\
\frac{\sigma[7n3^{+}]}{\sigma[7n0+7n3^{+}+7nX^{+}+7n6^{+}]} &= 0.2614 \pm 0.0072, \\
\frac{\sigma[7nX^{+}]}{\sigma[7n0+7n3^{+}+7nX^{+}+7n6^{+}]} &= 0.1426 \pm 0.0026, \\
\frac{\sigma[7n6^{+}]}{\sigma[7n0+7n3^{+}+7nX^{+}+7n6^{+}]} &= 0.5268 \pm 0.0064, \\
\frac{\sigma[7n0]}{\sigma[6n1+6p1+6n2+6p2+6n3+6p3]} &= 0.0415 \pm 0.0031 \text{ and} \\
\frac{\sigma[7n0+7n3^{+}+7nX^{+}+7n6^{+}]}{\sigma[6n1+6p1+6n2+6p2+6n3+6p3]} &= 0.601 \pm 0.013.
\end{aligned}$$

It is unfortunate that the only reaction channel that we are able to definitively separate is 7n0. The rest of the reaction channels are not separable and we must use a representative sample of reaction channels. One possible exception is the 7nX reaction channel at a photon energy of 30 MeV. Since this reaction channel is so prominent in the time-of-flight spectra, it may be separable. The a_k values and relative cross section we find may be an accurate representation of the actual values. However, it is difficult to say for certain. At photon energies of 25 and 35 MeV, it is not possible to separate 7nX from the other reaction channels well enough to say anything definitive about the extracted values.

12.4 Absolute Cross Section Determination

As was done for ^{6}Li with photon energies above 16 MeV, we can find the absolute cross sections of the photodisintegration of ^{7}Li using both the Compton scattering comparison and flux monitoring methods. Recall that in section 10.7 we had to modify our method to account for the ^{6}Li concentration in our natural lithium target. We did this by finding a factor C_{76} such that

$$C_{76} \equiv \left(\frac{\frac{\sigma_7}{\sigma_6}}{0.0759 + 0.9241\frac{\sigma_7}{\sigma_6}} \right) \tag{12.1}$$

and the modified equation for the Compton scattering comparison method is

$$\sigma_7 = (170\bar{0}\text{ mb})\, C_{76} \frac{N_{sim}}{\Phi^s} \left\langle \frac{N^s_{d,\gamma}}{N_{d,\gamma}} \right\rangle \left\langle \frac{N_{d,n}}{N^s_{d,n}} \right\rangle . \tag{12.2}$$

The argument works the same for the flux monitoring method and its equation can be modified to read

$$\sigma_7 = C_{76} \frac{N_{sim}}{\Phi N \ell} \left\langle \frac{N_{d,n}}{N^s_{d,n}} \right\rangle . \tag{12.3}$$

The values for the Compton scattering comparison method are presented in table 12.18, while the values for the explicit flux monitoring method with the five-paddle monitor are presented in table 12.19. The cross sections found with the two different methods are presented in table 12.20 for 7n0 and table 12.21 for all observable reaction channels. Since we are unable to separate the reaction channels of the photodisintegration of ^{7}Li at these energies, the absolute cross sections for all observable reaction channels requires some interpretation. These values are for all reaction channels we are able to observe in our data, as modelled by our simulations. For instance, at 35 MeV, we use only the 7n6$^+$ reaction channel to model the low-energy neutrons and neglect 7d1$^+$. However, we can detect neutrons from 7n6$^+$ with more efficiency than 7d1$^+$ because of a more favourable neutron kinetic energy spectrum. Therefore, our choice of reaction channel has influenced the results of table 12.21. Furthermore we have no way of estimating a cross section for reaction channels that produce neutrons with too little energy to be detected. An example of such

a reaction channel is 7d0. Neither of these effects are taken into account in table 12.21 but will be discussed further in section 13.6.

It is not understood why the cross sections determined with the Compton scattering comparison method and the photon flux monitor method differ outside of experimental uncertainties in table 12.21. Possible reasons include unaccounted for rate dependent effects when high photon fluxes are used with the five-paddle monitor and should be investigated further. Like the analysis for ^{6}Li, the result using the flux monitoring method typically exceeds that of the Compton scattering comparison method.

Table 12.18: Ratios of simulated and measured yields used to determine the absolute cross section of ^{7}Li photodisintegration through the Compton scattering comparison method for photon energies greater than 16 MeV. The first uncertainty is statistical and the second is systematic.

Beam Energy	Orient-ation	$\left\langle N^s_{d,\gamma}/N_{d,\gamma} \right\rangle$	$\left\langle N_{d,n}/N^s_{d,n} \right\rangle$ 7n0 only ($\times 10^{-3}$)	$\left\langle N_{d,n}/N^s_{d,n} \right\rangle$ all ^{7}Li channels ($\times 10^{-3}$)
20 MeV	1	0.525 ± 0.001 ± 0.014	3.66 ± 0.15 ± 0.75	19.99 ± 0.15 ± 0.74
20 MeV	3	0.480 ± 0.001 ± 0.013	3.64 ± 0.15 ± 0.88	21.96 ± 0.15 ± 0.73
25 MeV	1	0.544 ± 0.001 ± 0.013	3.88 ± 0.27 ± 1.08	25.50 ± 0.17 ± 0.84
25 MeV	3	0.463 ± 0.001 ± 0.011	3.94 ± 0.26 ± 1.10	29.49 ± 0.19 ± 0.97
30 MeV	3	0.345 ± 0.001 ± 0.009	5.81 ± 0.62 ± 2.19	34.91 ± 0.25 ± 1.08
35 MeV	3	0.358 ± 0.001 ± 0.012	8.36 ± 3.18 ± 3.28	20.90 ± 0.15 ± 0.83

Table 12.19: Ratios of simulated and measured yields used to determine the absolute cross section of ^{7}Li photodisintegration using the five-paddle flux monitor for the data with photon energies above 16 MeV. The photon flux is the total number of photons and is not a rate. The subtraction of atmospheric neutrons and the flux monitor rate-dependent correction have already been performed. The first uncertainty is statistical and the second is systematic.

Beam Energy	Orient-ation	Flux, Φ ($\times 10^9$ photons) ± 2%	$\left\langle N_{d,n}/N^s_{d,n} \right\rangle$ 7n0 only	$\left\langle N_{d,n}/N^s_{d,n} \right\rangle$ all ^{7}Li channels
20 MeV	1	34.27	0.166 ± 0.001 ± 0.034	0.797 ± 0.001 ± 0.022
20 MeV	3	39.77	0.167 ± 0.001 ± 0.040	0.885 ± 0.001 ± 0.024
25 MeV	1	23.29	0.103 ± 0.001 ± 0.029	0.723 ± 0.001 ± 0.024
25 MeV	3	30.37	0.135 ± 0.002 ± 0.038	0.944 ± 0.001 ± 0.031
30 MeV	3	35.07	0.128 ± 0.002 ± 0.048	1.036 ± 0.002 ± 0.032
35 MeV	1	12.46	0.050 ± 0.002 ± 0.020	0.224 ± 0.001 ± 0.009
35 MeV	3	35.15	0.102 ± 0.004 ± 0.040	0.613 ± 0.001 ± 0.025

Table 12.20: Total cross section for the reaction channel 7n0 with photon energies above 16 MeV

Beam Energy	Compton Scattering Comparison Method (mb)	Flux Monitor Method (mb)	Weighted Average (mb)
20 MeV	0.254 ± 0.041	0.317 ± 0.071	0.270 ± 0.036
25 MeV	0.233 ± 0.048	0.269 ± 0.076	0.243 ± 0.041
30 MeV	0.222 ± 0.087	0.205 ± 0.078	0.213 ± 0.058
35 MeV	0.18 ± 0.10	0.109 ± 0.036	0.120 ± 0.040

Table 12.21: Total cross section for all observable reaction channels for the photodisintegration of ^{7}Li with photon energies above 16 MeV

Beam Energy	Compton Scattering Comparison Method (mb)	Flux Monitor Method (mb)	Weighted Average (mb)
20 MeV	1.834 ± 0.058	2.016 ± 0.074	1.903 ± 0.046
25 MeV	2.391 ± 0.070	2.74 ± 0.11	2.492 ± 0.059
30 MeV	2.102 ± 0.087	2.62 ± 0.11	2.301 ± 0.068
35 MeV	1.211 ± 0.064	1.456 ± 0.070	1.323 ± 0.047

Chapter 13

Discussion

13.1 Introduction

In our analysis of the photodisintegration of the lithium isotopes we have extracted a great number of quantities from our measured data. Chapters 7, 8, 9, 10, 11 and 12 each dealt with a different aspect of the analysis. The content of these chapters is presented from the data analysis point of view. In this chapter, we take the final results of this analysis and present them in a logical manner from a physics point of view. We take the physically meaningful quantities found in the analysis and redistribute them into five conceptual units represented by the five following sections.

First, we look at the photodisintegration of ^{6}Li in section 13.2. In this section we will examine how cross sections evolve over the entire photon energy interval of 8 MeV to 35 MeV. We find that with only a few reaction channels we can qualitatively describe the data very well and we can extract some very interesting quantitative results.

The photodisintegration of ^{7}Li has been broken up into four conceptual units as the spectra found for these neutrons provide interesting and distinct insights into nuclear physics. We begin our study of the ^{7}Li data by examining the reaction channel $^7\mathrm{Li} + \gamma \rightarrow {}^6\mathrm{Li(g.s.)} + n$, which we have labelled 7n0, in section 13.3. We are able to isolate this reaction channel from all others by placing cuts on the light-output spectra. This data provides a very clear insight into the evolution of the photodisintegration cross section as the photon energy increases from 10 MeV to 35 MeV.

Section 13.4 looks at the reaction channels $^7\mathrm{Li} + \gamma \rightarrow {}^6\mathrm{Li}(2.19) + n$ and $^7\mathrm{Li} + \gamma \rightarrow {}^6\mathrm{Li}(3.56) + n$, which we have labelled 7n1 and 7n2. At photon energies of 13 and 15 MeV these reaction channels are easy to separate using time-of-flight spectra and we are able to investigate their cross sections.

An unexpected reaction channel, $^7\mathrm{Li} + \gamma \rightarrow n + {}^6\mathrm{Li}(10.0)$, labelled 7nX, presents itself in our data at photon energies of 25, 30 and 35 MeV. Extra peaks in our neutron time-of-flight spectra bring us to the conclusion that this reaction channel exists, necessitating an excited state of ^{6}Li with excitation energy $E_x = 10.0 \pm 0.5$ MeV. This state is discussed in section 13.5.

While we are not able to separate all the reaction channels for the photodisintegration of ^{7}Li at all energies, we can estimate the total photoneutron cross section. This is discussed in section 13.6.

The historic experimental data in this chapter are taken from the Experimental Nuclear Reaction

Data (EXFOR/CSISRS) database. This data is checked against the relevant publications to ensure that it is the same. The EXFOR/CSISRS database is provided through the National Nuclear Data Center (NNDC) and is available at www.nndc.bnl.gov/exfor/.

13.2 The Photodisintegration of ^{6}Li

13.2.1 Introduction

We have studied the photodisintegration of ^{6}Li at photon energies of 8, 9, 10, 11, 12, 13, 15, 15.6, 20, 25, 30 and 35 MeV. The neutron spectra have a feature-full and consistent qualitative structure; above 9 MeV there is always a feature with higher energy and one with lower energy. For the energies of 8 to 15.6 MeV, where we are able to observe the effects of a polarised photon beam, we see that the high energy feature has a dependence on the beam polarisation while the low energy feature has no such dependence. This leads us to postulate a model that we can use to take our qualitative data analysis to a quantitative analysis.

We model the photodisintegration of ^{6}Li by using two competing processes. The first is the photoneutron reaction which produces a highly unstable ^{5}Li nucleus and a neutron. The ^{5}Li nucleus is assumed to decay into a proton and an alpha particle, neither of which can reach our detectors. The second is the photoproton reaction which produces a highly unstable ^{5}He nucleus and a proton. The proton cannot reach our detectors, but the ^{5}He nucleus is assumed to decay into a neutron and an alpha particle. That neutron can reach our detectors and will be detected if it has sufficient kinetic energy.

This simple model of the photodisintegration of ^{6}Li immediately explains the qualitative features of our analysis. The high-energy feature has dependence on polarisation because the photoneutron reaction has dependence on polarisation. The low-energy feature does not appear to have dependence on polarisation because the spectra of neutrons emitted by the decaying ^{5}He nucleus have nearly no dependence on polarisation.

In our model we have made the implicit assumption that any three-body decays of ^{6}Li are negligible. We know this to be true for the correlated quasideuteron interaction from experimental measurements [Pro60, Wad84]. These measurements do not preclude an uncorrelated or weakly correlated $^6\mathrm{Li}+\gamma \rightarrow n+p+^4\mathrm{He}$ reaction. We find that when we model such an uncorrelated reaction channel and simulate its spectra, it is neither necessary nor sufficient to explain our measured spectra. Therefore, we do not consider it. We do not consider any type of weakly correlated reaction channels as they are not necessary in explaining our data.

The intermediate states ^{5}Li and ^{5}He have a number of excited states that are necessary in describing our data. The parameters for these states are taken from the TUNL nuclear data project [Til02]. Once a state's excitation energy and decay width are known, we model the decay using

relativistic kinematics. When modelling the decay of ^{5}He, we assume that the neutron is emitted isotropically in the rest frame of the ^{5}He nucleus. For two-body reactions and the associated decays, this leaves us with no free parameters in determining the neutron kinetic energy spectra.

We are able to adequately explain all the ^{6}Li data with photon energies between 8 and 35 MeV using only seven two-body reaction channels. At-and-below 25 MeV, we need only three.

13.2.2 Angular Dependence of the Cross Sections

By fitting the results of simulations generated with each of the associated Legendre function polynomials, we are able to compare the simulated neutron yields to the experimental yields and obtain the expansion coefficients for several reaction channels. Because of degeneracies in the simulated neutron yields and some difficulties in separating spectra, the quantitative values obtained are not always physically meaningful. Instead they are useful as inputs to the simulation in order to qualitatively reproduce the experimental spectra. Using these coefficients allows us to produce light-output and time-of-flight spectra that are very good representations of the measured spectra. Such unphysical coefficients are not discussed here but can be found for reference in chapters 9 and 11.

The most meaningful associated Legendre function coefficients obtained are those of the reaction channel 6n0 with photon energies from 8 to 15.6 MeV. These are listed in table 13.1 and plotted in figure 13.1. Notice that we are able to obtain values for all coefficients with $k \leq 3$ for the

Table 13.1: Associated Legendre function coefficients for the reaction channel 6n0

Photon Energy (MeV)	a_1	a_2	a_3	e_2	e_3
8	0.070 ± 0.017	-0.199 ± 0.026	0.082 ± 0.036	0.1266 ± 0.0061	-0.0039 ± 0.0033
9	0.067 ± 0.011	-0.171 ± 0.018	0.036 ± 0.024	0.0953 ± 0.0044	-0.0043 ± 0.0023
10	0.195 ± 0.030	-0.445 ± 0.043	n/a	0.144 ± 0.013	0.0019 ± 0.0063
11	0.223 ± 0.028	-0.389 ± 0.040	n/a	0.237 ± 0.011	0.0015 ± 0.0052
12	0.399 ± 0.035	-0.348 ± 0.049	n/a	0.213 ± 0.013	-0.0094 ± 0.0063
13	0.270 ± 0.033	-0.311 ± 0.046	n/a	0.226 ± 0.011	0.0017 ± 0.0058
15	0.293 ± 0.036	-0.310 ± 0.051	n/a	0.194 ± 0.012	0.0023 ± 0.0068
15.6	0.264 ± 0.032	-0.206 ± 0.046	n/a	0.191 ± 0.011	0.0122 ± 0.0064

data at 8 and 9 MeV. This is because we are able to obtain these values without separating this

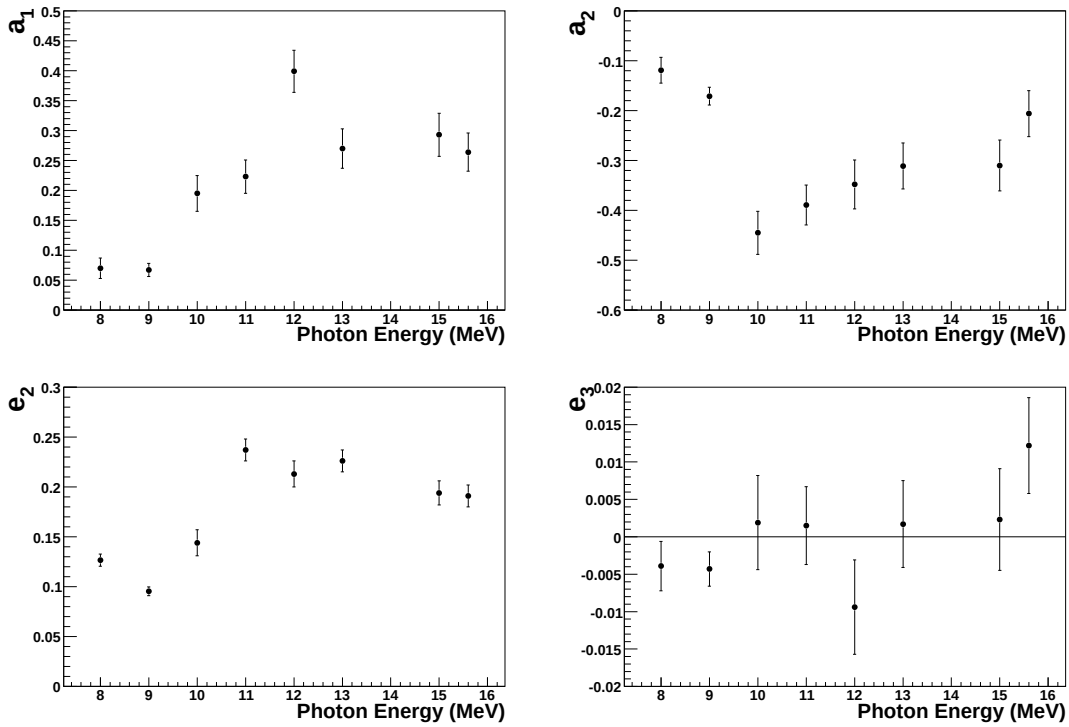

Figure 13.1: Associated Legendre function coefficients for 6n0

reaction channel from the 6n1 and 6p1 reaction channels. At higher photon energies, the algorithm we use to separate the reaction channels is easily confused when we try to obtain values for a_3, so we eliminate this distribution from our fitting procedure. This is equivalent to forcing it to be zero, which is a good approximation as the value is small at 8 and 9 MeV. We are still able to reliably find values for e_3 as the polarisation dependence of P_3^2 tends to less confuse the separation algorithm than the polar dependence introduced by P_3^0.

We show graphically the effect these coefficients have on the angular distributions of the emitted neutrons in figure 13.2. These plots are for the centre-of-momentum frame and red represents more neutrons with blue representing fewer neutrons. Notice that the polarisation of the photon beam has a strong effect, connected with the e_2 coefficient. This effect grows as the energy of the photon beam increases from 8 to 11 MeV and then declines as the energy of the photon beam decreases from 11 MeV to 15.6 MeV. It is also interesting to note that the a_1 and a_2 coefficients similarly grow and decline with peaks at 12 and 10 MeV respectively.

The number of other reaction channels for which we can produce meaningful associated Legendre function coefficients is quite limited. Typically we find coefficients that qualitatively reproduce the data well in our simulations, but may not be physically meaningful.

The coefficients for 6n1 at 25, 30 and 35 MeV appear to be consistent and physically meaningful. These are listed in table 13.2.

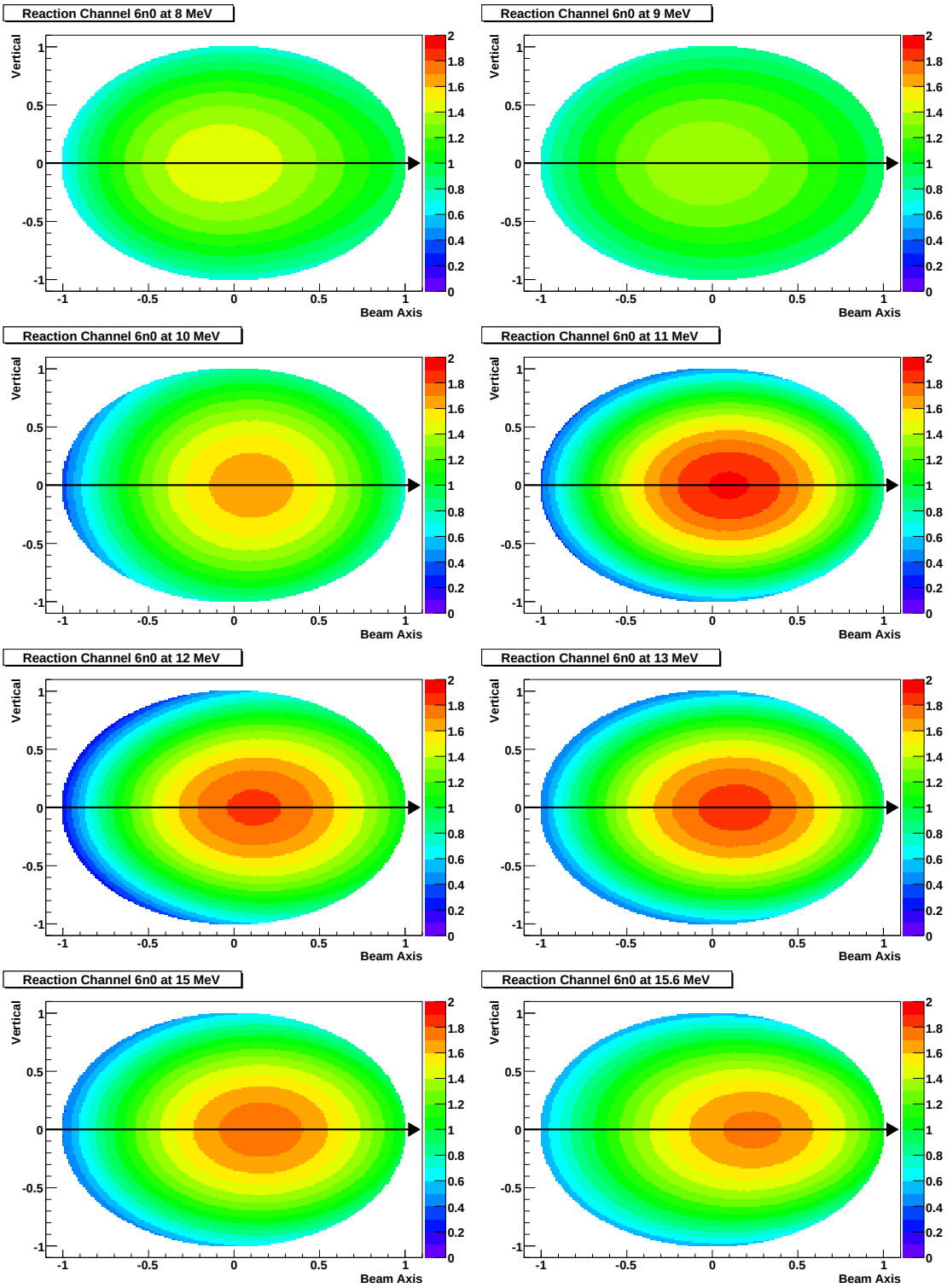

Figure 13.2: The quantity $\frac{4\pi}{\sigma}\frac{d\sigma}{d\Omega}(\theta,\phi)$ as seen in the experimental setup in the centre-of-momentum frame for reaction channel 6n0. This quantity gives us a normalised, relative cross section and allows us to see the angular dependence. The beam axis is the horizontal line with the arrow showing the beam direction. The vertical axis is shown and the projection eliminates the horizontal axis.

Table 13.2: Associated Legendre function coefficients for the reaction channel 6n1

Photon Energy (MeV)	a_1	a_2
25	0.111 ± 0.010	-0.460 ± 0.014
30	0.105 ± 0.018	-0.439 ± 0.027
35	0.24 ± 0.10	-0.22 ± 0.15

13.2.3 Absolute Cross Sections

We are also able to find absolute cross sections for the various reaction channels under discussion. We compute the relative cross sections between reaction channels by examining the A values we generate when finding the associated Legendre function coefficients. Using the methods of Compton scattering comparison and explicit flux monitoring with the five-paddle flux monitor, we can extract the absolute cross sections for all observable reaction channels. By multiplying the two, we can find the absolute cross section for each reaction channel and these results are presented in table 13.3 with selected data appearing in figure 13.3. It is important to note that we have subtracted off any possible contributions by the 6p0 reaction channel from the cross sections for individual reaction channels and we discuss our method for doing so later in this section.

Before continuing with a discussion of how to account for the 6p0 reaction channel, let us notice some of the features present in table 13.3 and figure 13.3. The abnormally high value for σ[6n0] at a photon energy of 9 MeV probably indicates that there is a contribution from 6n1 and 6p1 at this energy that we are not taking into account. After 20 MeV, no correction is needed for the 6p0 reaction channel as we assume it disappears along with the 6n0 reaction channel. Because of the difficulty in separating six reaction channels for the 35 MeV data, the absolute cross sections for the individual reaction channels must be taken as suspect. It is possible that the separation algorithm suffers from unaccounted for uncertainties when separating this large a number of reaction channels from reasonably smooth spectra.

Since we have not measured the 6p0 reaction channel, we must discuss how to do a correction for it, as we have done for the data in table 13.3. While there are many studies of the reaction $^6\mathrm{Li} + \gamma \rightarrow p + {}^5\mathrm{He}$ [Baz60, Pro60, Vol62, Kom64, Den67b, Man65, Won70, Gar73, Mat76, Jun79, Gan87, Car88, Nil94, Dia95] most of these study the reaction at either energies which are not of interest to us or have measured other quantities than absolute cross sections. There are a limited number of papers which may be able to help us quantify the 6p0 reaction channel so that we may subtract it from our data.

The results of Denisov *et al.* [Den67b] appear promising at first, but they are incompatible

Table 13.3: Cross sections for the various observable reaction channels for the photodisintegration of ^{6}Li. Split columns represent reaction channels that could not be separated and the cross section is a sum for both channels. Estimated contributions from the 6n0 reaction channel have been taken into account. The 'Observable' column represents the sum of the 6n0, 6n1, 6n2, 6n3, 6p1, 6p2 and 6p3 reaction channels (excluding 6p0).

Photon Energy (MeV)	Observable (mb)	6n0 (mb)	6n1 (mb)	6p1 (mb)
8	0.499 ± 0.098	0.499 ± 0.098	n/a	
9	0.646 ± 0.071	0.646 ± 0.071	n/a	
10	0.955 ± 0.097	0.517 ± 0.028	0.438 ± 0.089	
11	1.254 ± 0.070	0.470 ± 0.022	0.786 ± 0.058	
12	1.416 ± 0.062	0.535 ± 0.023	0.881 ± 0.047	
13	1.448 ± 0.048	0.545 ± 0.017	0.903 ± 0.039	
15	1.558 ± 0.067	0.505 ± 0.018	0.438 ± 0.018	0.612 ± 0.055
15.6	1.534 ± 0.073	0.538 ± 0.023	0.422 ± 0.023	0.573 ± 0.052
20	1.555 ± 0.042	0.788 ± 0.023		0.787 ± 0.029
25	1.602 ± 0.040	n/a	0.693 ± 0.018	0.909 ± 0.025
30	1.631 ± 0.046	n/a	0.551 ± 0.019	0.811 ± 0.041
35	1.884 ± 0.050	n/a	0.341 ± 0.023	1.046 ± 0.036

Photon Energy (MeV)	6n2 (mb)	6p2 (mb)	6p3 (mb)	6n3 (mb)
30	0.153 ± 0.008	0.114 ± 0.005	n/a	
35	0.149 ± 0.006	0.110 ± 0.006		0.227 ± 0.008

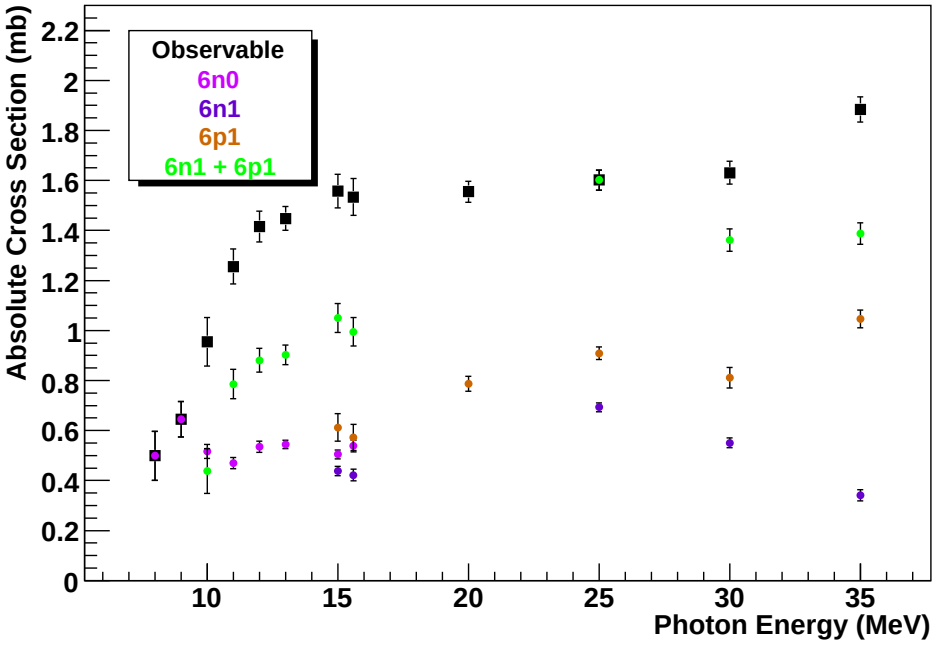

Figure 13.3: Cross sections for the various observable reaction channels for the photodisintegration of ^{6}Li. The 'Observable' points represents the sum of the 6n0, 6n1, 6n2, 6n3, 6p1, 6p2 and 6p3 reaction channels (excluding 6p0).

with our own results. They suggest that, at 10 MeV, the absolute cross section for 6p0 is greater than our measured absolute cross section for the sum of 6n0, 6n1 and 6p1, an unlikely result. One interesting point that we can take from Denisov *et al.* is that the cross section for the 6p0 reaction channel goes to zero at ∼25 MeV. This is consistent with our observation that the 6n0 reaction channel goes to zero at this same energy.

The results of Junghans *et al.* [Jun79] are also interesting, but it is not clear which reaction channels are producing the protons that they detect.

Since there is a lack of historic data to help us with the 6p0 reaction channel, we will use

$$\sigma[6p0] = \sigma[6n0] \pm 100\% \tag{13.1}$$

which seems reasonable given our examination of the 6n1 and 6p1 reaction channels. The large error bounds may appear overly conservative given that there are historic measurements of this cross section and we know it is not zero. However, we have not directly measured it in our analysis and the measurements we have for the 6n1 and 6p1 cross sections are systematically different with $\sigma[6p1] > \sigma[6n1]$.

Although we can't separate the 6p0 contribution in our spectra, it can contribute neutrons that we detect but are not able to identify as being from 6p0. These neutrons can pollute the neutron yields of reaction channels that produce low energy neutrons. We estimate a correction to the cross

sections of reaction channels which may have some neutrons from 6p0 mixed into their experimental data by

$$\sigma[\text{corrected}] = \sigma[\text{uncorrected}] - f \times \sigma[\text{6p0}] \tag{13.2}$$

where σ[uncorrected] are the uncorrected absolute cross sections, which are the quantities reported in tables 9.21 and 11.12, and f is the estimated contribution of 6p0 to the neutron yields relative to the 6n0 contribution. Values for f are reported in chapters 10 and 12. We can then estimate a total photoneutron cross section using

$$\begin{aligned}\sigma[\text{6n0} + \text{6n1} + \ldots + \text{6p0} + \text{6p1} + \ldots] &= \sigma[\text{6n0} + \text{6n1} + \ldots + \text{6p1} + \ldots] + \sigma[\text{6p0}] \\ &= \sigma[\text{all, uncorrected}] \times \left(1 + (1-f) \times \frac{\sigma[\text{6p0}]}{\sigma[\text{all, uncorrected}]}\right)\end{aligned} \tag{13.3}$$

and these are reported in table 13.4. The values 'all, uncorrected' are the value reported in tables

Table 13.4: Estimate of the total photoneutron cross section for ^{6}Li, including all observed reaction channels reported in table 13.3, plus an estimate for 6p0. Note that the large errors on the data at-and-below 20 MeV are due to our inference of the 6p0 reaction channel that we are not able to directly measure.

Photon Energy (MeV)	Cross Section (mb)	Photon Energy (MeV)	Cross Section (mb)
8	1.07 ± 0.51	15	2.06 ± 0.46
9	1.34 ± 0.65	15.6	2.07 ± 0.50
10	1.47 ± 0.44	20	1.95 ± 0.38
11	1.72 ± 0.43	25	1.602 ± 0.040
12	1.95 ± 0.51	30	1.631 ± 0.046
13	1.99 ± 0.52	35	1.884 ± 0.050

9.21 and 11.12 for all observable reaction channels before the correction for 6p0 is performed. The value for $\frac{\sigma[\text{6p0}]}{\sigma[\text{all, uncorrected}]}$ can be estimated from $\frac{\sigma[\text{6n0}]}{\sigma[\text{all, uncorrected}]}$ which we calculated from the A values when determining the associated Legendre polynomial coefficients. It should be obvious that the 6p0 contribution is the largest source of uncertainty since we are adding in a quantity on inference that has not been directly measured. However, we proceed in this way as we desire to compare our measurements with other measurements and the theoretical predictions of the Lorentz integral transform.

We will first compare our measurement with that of the Livermore group [Ber65a] in figure 13.4. These cross sections represent all reaction channels that produce neutrons. We notice that our data follows that of the Livermore group very well from 8 to 11 MeV. At 12 MeV some discrepancy arises

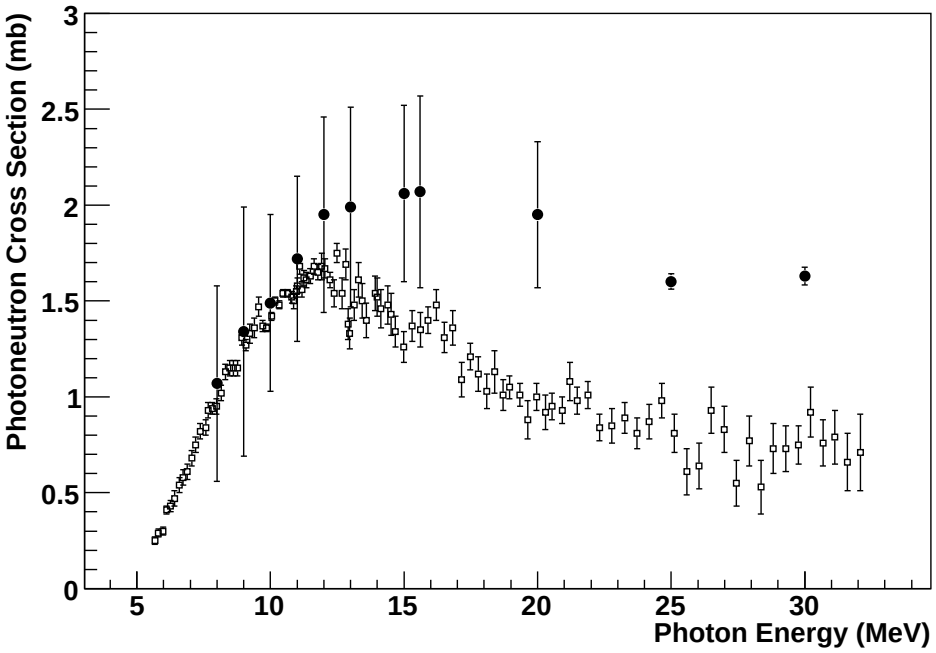

Figure 13.4: The photoneutron cross section for ^{6}Li from our data (closed circles) compared with that of the Livermore group [Ber65a] (open squares). Note that the large error bars on the data at-and-below 20 MeV are due to our inference of the 6p0 reaction channel that we are not able to directly measure.

and by 15 MeV our cross sections are higher than those of the Livermore group. We now turn our attention to a comparison with the Lorentz integral transform prediction.

13.2.4 Comparison with the Lorentz Integral Transform

In order to make a comparison with the ^{6}Li Lorentz integral transform calculation of Bacca *et al.* [Bac04a], we must include reaction channels that we cannot measure as not all reaction channels produce neutrons. Three such reaction channels are the two-body reaction channel $^6\mathrm{Li} + \gamma \rightarrow {}^3\mathrm{He} + {}^3\mathrm{H}$ and the three-body reaction channels $^6\mathrm{Li} + \gamma \rightarrow p + d + {}^3\mathrm{H}$ and $^6\mathrm{Li} + \gamma \rightarrow 3d$. We can immediately disregard $^6\mathrm{Li} + \gamma \rightarrow 3d$ as this is not an electric dipole reaction [She68].

The reaction channel $^6\mathrm{Li} + \gamma \rightarrow p + d + {}^3\mathrm{H}$ has been studied by a number of authors [Mur68, Mur70, Vol78, Kot85, Ryc94]. The measurement of Marakami [Mur68, Mur70] is not consistent with our measurements as this author finds a maximum cross section of this reaction channel of 6 mb at a photon energy of 25 MeV. This cross section is far too large and is possibly affected by uncertainties in the normalisation with the $^{12}\mathrm{C} + \gamma \rightarrow 3\ {}^4\mathrm{He}$ reaction channel to obtain the flux. It is not clear that the results of Volkov *et al.* are model independent and the final cross sections may assume an α-particle photodisintegration process model [Vol78]. Kotikov and Makhnovskiĭ present another interesting work but their cross sections are based on only 18 measured photodisintegration

events [Kot85]. Between these poor statistics and questions about systematic uncertainties, we cannot use these cross sections to aid us. The results of Rychbosch *et al.* give a cross section of about 300 μb at a photon energy of 48 MeV [Ryc94], which is too high of an energy for our use but indicates that the cross section is fairly small at higher energies.

It is interesting to note that both the work of Kotikov and Makhnovskiĭ and the work of Marakami measure similar energy dependences of the $^6\mathrm{Li} + \gamma \rightarrow p + d + {}^3\mathrm{H}$ cross section. The cross section rises quickly from its threshold at 21.3 MeV and peaks between photon energies of 24 and 25 MeV. Unfortunately, the absolute values of the cross sections disagree with each other by more than a factor of two and neither are consistent with our observations based on other reaction channels. If this reaction channel does have an effect on our data, it will be on the data with a photon energy of 25 MeV. Given that we have not yet included any three body reaction channels and there is not a satisfactory measurement of the cross section of $^6\mathrm{Li} + \gamma \rightarrow p + d + {}^3\mathrm{H}$, we will neglect it.

There are a large number of studies of the $^6\mathrm{Li} + \gamma \rightarrow {}^3\mathrm{He} + {}^3\mathrm{H}$ reaction channel [Tit54a, Kom64, Man65, She66b, Den67b, Mur68, She68, Mur70, Won70, Shi75, Vol78, Jun79, Bur89, Den93, Bur95, Dia97] and its inverse reaction [Koh63, Bla68, You70b, Ven71, Ven73]. A number of these studies are at photon energies outside of our range or study quantities we are not interested in.

Komar and Makhnovskiĭ found a cross section which peaks at 8 mb at a photon energy of 21 MeV [Kom64]. Murakami found a cross section which peaks at 5 mb at a photon energy of 21 MeV [Mur68, Mur70]. Because these authors have measured cross sections that are so large, we will not include them in our analysis because their absolute normalisations likely suffer difficulties. However, we find the fact that they both observe peaks at 21 MeV useful.

Titterton and Brinkley do not observe the reaction at a photon energy of 17.6 MeV [Tit54a], which indicates that the cross section is near zero at this energy which is close to the threshold of 15.8 MeV. Manuzio *et al.* found the cross section for this reaction channel from 25.2 to 30 MeV [Man65]. Sherman *et al.* found the cross section from a photon energy of 19 to 35 MeV [She66b, She68]. Shin, Skopik and Murphy found the differential cross section at 90° for photon energies from 23.1 MeV to 68.2 MeV [Shi75] while Junghans *et al.* supply the same quantity with the angular distributions required to convert it into an absolute cross section [Jun79]. We use the Legendre function coefficient values $a_0 = 0$ and $a_1 = -1$ suggested by Junghans *et al.* to convert differential cross sections into absolute cross sections using $\sigma = \frac{8\pi}{3}\frac{d\sigma}{d\Omega}(\theta = 90°)$. These results are plotted in figure 13.5.

Since these values are not in agreement, we construct composite values using the average as our recommended value, with the difference between the highest and lowest as the uncertainty. Our composite values are also shown in figure 13.5 and listed in table 13.5, along with the total absolute cross sections for the photodisintegration of $^6\mathrm{Li}$ that we have constructed for photon energies 20

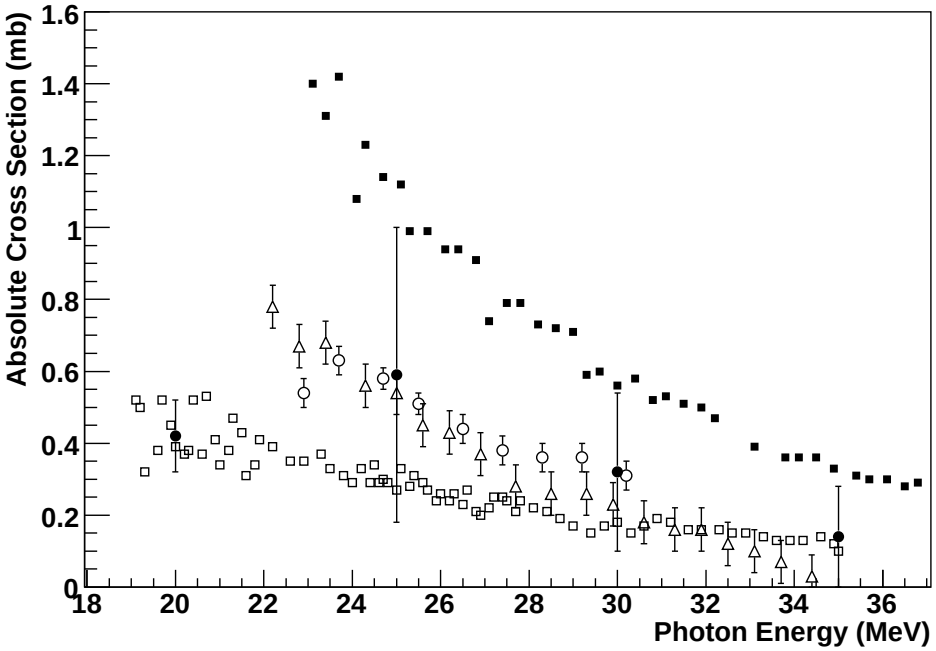

Figure 13.5: Absolute cross section for the reaction channel $^6\mathrm{Li} + \gamma \rightarrow {}^3\mathrm{He} + {}^3\mathrm{H}$ from Manuzio *et al.* (open circles) [Man65], Sherman *et al.* (open squares) [She66b, She68], Shin, Skopik and Murphy (closed squares) [Shi75] and Junghans (open triangles) [Jun79] with our composite values (closed circles)

Table 13.5: Cross sections for our composite value for the $^6\mathrm{Li} + \gamma \rightarrow {}^3\mathrm{He} + {}^3\mathrm{H}$ reaction channel and the total cross section for the photodisintegration of ^{6}Li

Photon Energy (MeV)	$^6\mathrm{Li} + \gamma \rightarrow {}^3\mathrm{He} + {}^3\mathrm{H}$ (mb)	Total ^{6}Li (mb)
20	0.42 ± 0.10	2.37 ± 0.39
25	0.59 ± 0.41	2.19 ± 0.41
30	0.32 ± 0.22	1.95 ± 0.22
35	0.14 ± 0.14	2.02 ± 0.15

to 35 MeV. These cross sections are plotted against the Lorentz integral transform prediction in figure 13.6. Our measurements are in excellent agreement with the calculation below 25 MeV. The

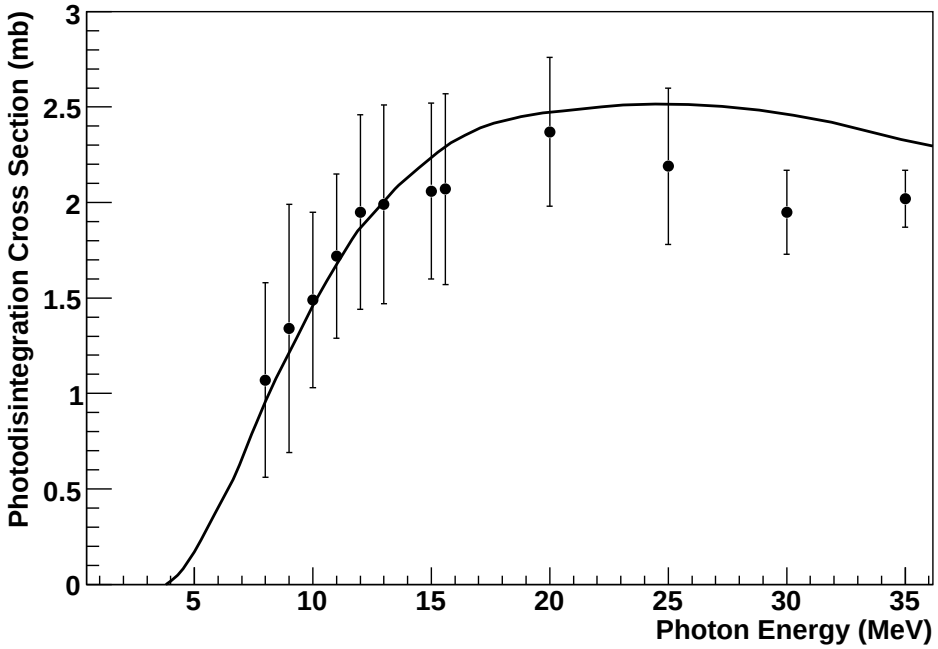

Figure 13.6: Our constructed total ^{6}Li photodisintegration cross section for all reaction channels (closed circles) compared with the prediction of the Lorentz integral transform using the AV4' model (line) [Bac04a]

uncertainties on the data from 8 to 15.6 MeV have error bars that are obviously overestimated. This is due to our inability to observe the 6p0 reaction channel and needing to compensate by approximating it with the 6n0 reaction channel, assuming that the two cross sections are the same but giving 6p0 100% uncertainty. Our measurement at 25 MeV is still in good agreement but our measurements at 30 and 35 MeV are lower than the calculation. The highest two energies are the ones that involve the most fitting of reaction channels to the spectra. The low values could be the results of improperly distributing detected neutrons between the reaction channels which could cause the efficiency of our simulated neutron detectors to be incorrect. Also, we could simply be missing neutrons from reaction channels such as 6p0, which we have neglected at 25 to 35 MeV, or reactions of the form $^6\mathrm{Li} + \gamma \rightarrow n + {}^5\mathrm{He}$ with excited states of ^{5}He which leave too little energy for the neutron's kinetic energy. The three-body reaction $^6\mathrm{Li} + \gamma \rightarrow p + d + {}^3\mathrm{H}$ may also be playing a role since we cannot detect it due to its lack of neutrons.

Even with the disagreement at 30 and 35 MeV, which can easily be justified by unquantifiable uncertainties, we feel that our measurement strongly supports the LIT calculation. Certainly our measurement is in far better agreement with the LIT than that of the Livermore group.

13.3 The Reaction Channel $^7\mathrm{Li} + \gamma \rightarrow {}^6\mathrm{Li(g.s.)} + n$

The reaction channel $^7\mathrm{Li} + \gamma \rightarrow {}^6\mathrm{Li(g.s.)} + n$, referred to in this work as 7n0, is special in that it is isolatable. This makes it different from all other reaction channels studied because we do not need to fit to the time-of-flight spectra in order to separate this reaction channel from others. This has the consequence that our systematic uncertainties are not influenced by the separation algorithm, which makes these uncertainties smaller and easier to quantify.

For the reaction channel 7n0 at photon energies of 10, 11, 12, 13 and 15 MeV, we employed linearly polarised photons and are able to find the associated Legendre coefficients a_k and e_k up to and including $k = 4$. For photon energies of 20, 25 and 30 MeV, we used circularly polarised photons and were able to find the associated Legendre coefficients a_k up to and including $k = 4$. Our data with a photon energy of 35 MeV had too large uncertainties to allow us to find reliable a_k values.

We were able to extract absolute cross sections for this reaction for all energies from 10 MeV to 35 MeV. For photon energies 10, 12, 13, 15, 20, 25, 30 and 35 MeV, we were able to use the Compton scattering comparison method in order to measure the flux of the photon beam. For photon energies of 20, 25, 30 and 35 MeV, we were able to also employ the five-paddle flux monitor to determine the flux.

Unfortunately, due to limited beam time, we were not able to take the data required for us to obtain the absolute cross section for this reaction channel at a photon energy of 11 MeV using the Compton scattering comparison method. However, we can use the cross section obtained for all observable reaction channels of ^{6}Li and the ratio of σ[7n0] to this cross section. These values can be found in tables 9.21 and 10.4 respectively, but are reproduced here:

$$\sigma[\mathrm{6n0 + 6n1 + 6p1}] = 1.298 \pm 0.055 \text{ mb and } \frac{\sigma[\mathrm{7n0}]}{\sigma[\mathrm{6n0 + 6n1 + 6p1}]} = 0.308 \pm 0.029.$$

Multiplying them together we see that the cross section for 11 MeV photons is 0.400 ± 0.041 mb.

The associated Legendre polynomial coefficient values and the absolute cross sections are listed in tables 13.6 and 13.7. The coefficients are plotted as functions of energy in figure 13.7 and the angular distributions are plotted in figure 13.8. The absolute cross section is plotted as a function of energy in figure 13.9.

We see a number of interesting features in these plots. The a_1, a_3, a_4, e_3 and e_4 coefficients are indistinguishable from zero at all photon energies except possibly 10 MeV. The a_2 and e_2 values have definite dependence on energy and both cross zero. This causes the cross section to be peaked toward the backward direction, while its dependence on polarisation changes from being peaked at 90° from the polarisation axis to being peaked on the polarisation axis. Unfortunately, we are not able to determine the effect of polarisation on the cross section above photon energies of 15 MeV due to the fact that we could not use linearly polarised photons.

Table 13.6: Absolute cross section and associated Legendre polynomial expansion a_k coefficient values for the reaction channel $^7\mathrm{Li} + \gamma \rightarrow {}^6\mathrm{Li}(\mathrm{g.s.}) + n$

Energy (MeV)	Cross Section (mb)	a_1	a_2	a_3	a_4
10	0.297 ± 0.031	-0.330 ± 0.038	0.084 ± 0.055	0.191 ± 0.067	-0.001 ± 0.091
11	0.400 ± 0.041	-0.043 ± 0.017	0.013 ± 0.027	0.068 ± 0.034	-0.014 ± 0.041
12	0.455 ± 0.035	-0.018 ± 0.013	-0.081 ± 0.023	0.043 ± 0.027	-0.031 ± 0.037
13	0.488 ± 0.032	-0.044 ± 0.017	-0.219 ± 0.028	0.035 ± 0.032	-0.025 ± 0.043
15	0.361 ± 0.033	0.016 ± 0.018	-0.279 ± 0.028	0.041 ± 0.036	-0.038 ± 0.045
20	0.270 ± 0.036	-0.027 ± 0.024	-0.417 ± 0.048	-0.032 ± 0.061	-0.116 ± 0.080
25	0.243 ± 0.041	-0.097 ± 0.063	-0.456 ± 0.098	0.18 ± 0.14	-0.07 ± 0.17
30	0.213 ± 0.058	-0.02 ± 0.13	-0.76 ± 0.19	-0.29 ± 0.29	-0.35 ± 0.33
35	0.120 ± 0.040	n/a	n/a	n/a	n/a

Table 13.7: Associated Legendre polynomial expansion e_k coefficient values for the reaction channel $^7\mathrm{Li} + \gamma \rightarrow {}^6\mathrm{Li}(\mathrm{g.s.}) + n$

Energy (MeV)	e_2	e_3	e_4
10	-0.082 ± 0.012	-0.0114 ± 0.0066	0.0037 ± 0.0043
11	-0.0714 ± 0.0054	-0.0019 ± 0.0030	-0.0027 ± 0.0020
12	0.0121 ± 0.0050	-0.0010 ± 0.0015	-0.0018 ± 0.0016
13	0.0634 ± 0.0065	-0.0028 ± 0.0023	-0.0017 ± 0.0019
15	0.1355 ± 0.0064	-0.0010 ± 0.0034	0.0001 ± 0.0022

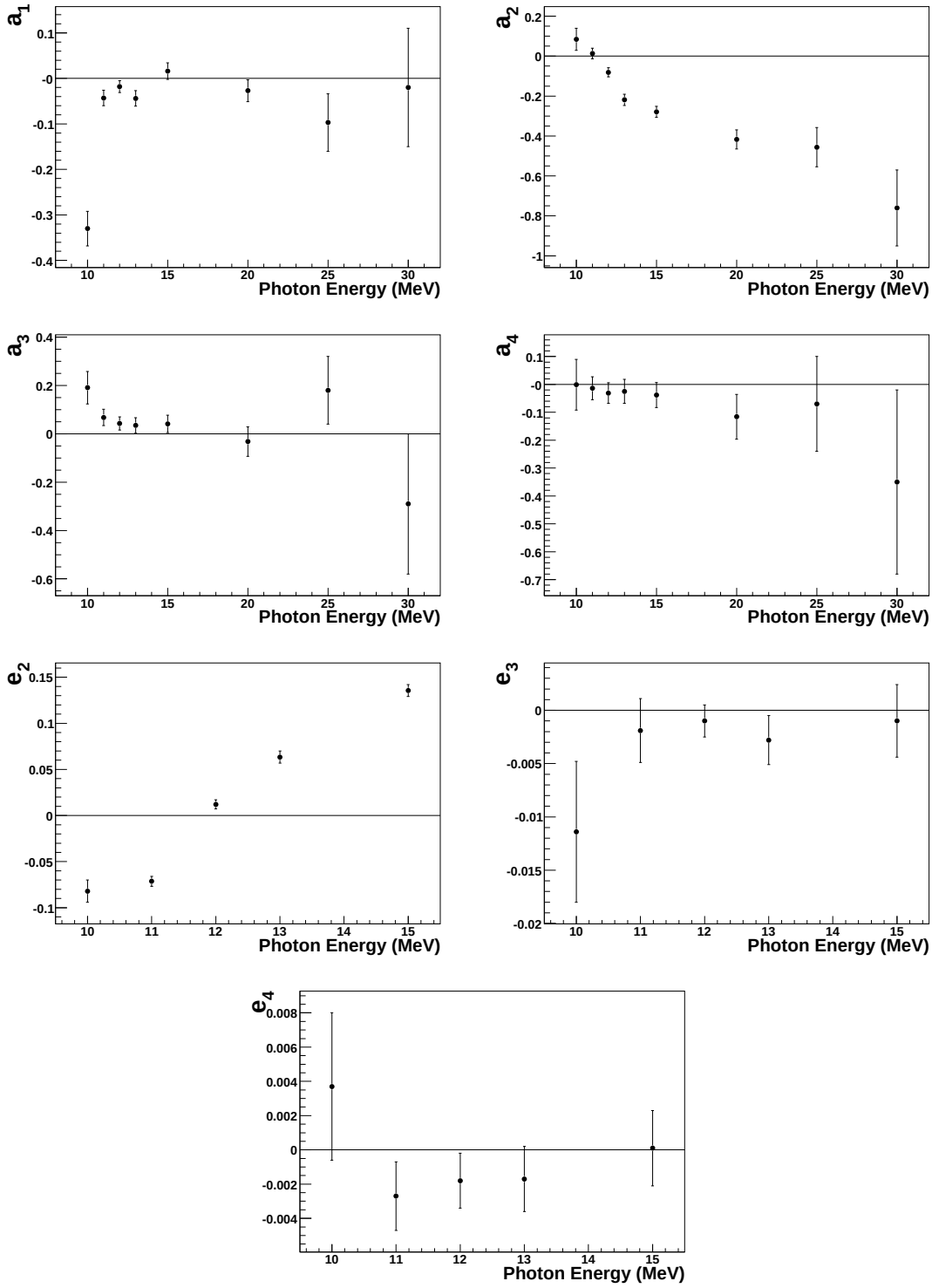

Figure 13.7: The associated Legendre function coefficients for the reaction channel $^{7}\mathrm{Li} + \gamma \rightarrow {}^{6}\mathrm{Li}(\mathrm{g.s.}) + n$, also labelled 7n0

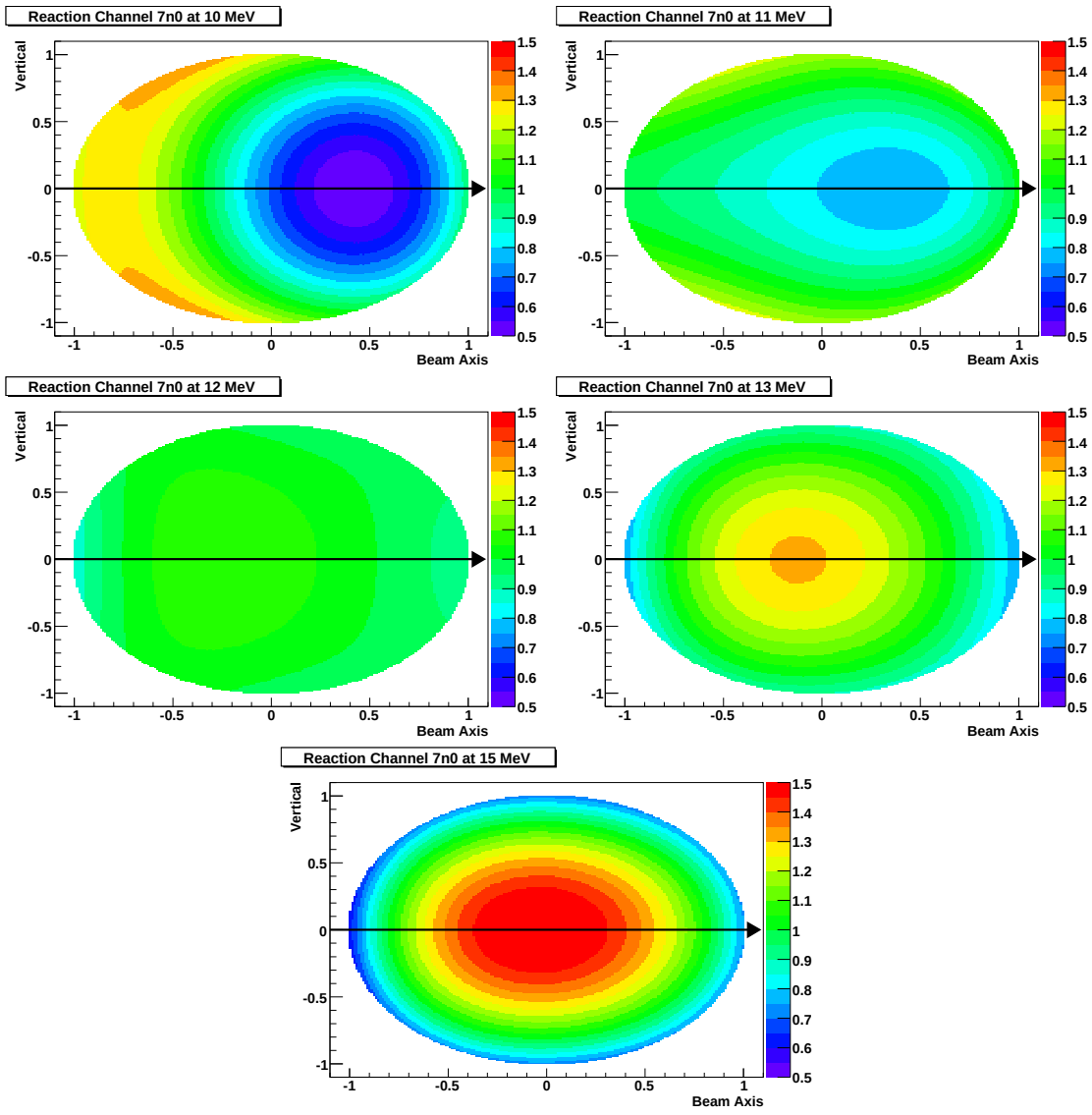

Figure 13.8: The quantity $\frac{4\pi}{\sigma}\frac{d\sigma}{d\Omega}(\theta,\phi)$ as seen in the experimental setup in the centre-of-momentum frame for reaction channel 7n0. This quantity gives us a normalised, relative cross section and allows us to see the angular dependence. The beam axis is the horizontal line with the arrow showing the beam direction. The vertical axis is shown and the projection eliminates the horizontal axis.

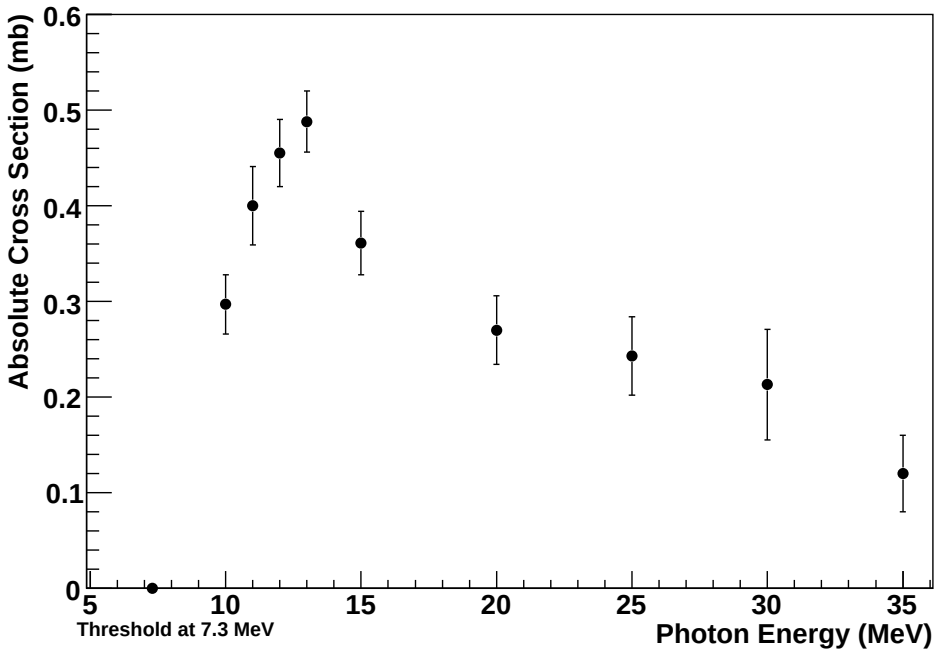

Figure 13.9: The absolute cross section for $^7\mathrm{Li} + \gamma \rightarrow {}^6\mathrm{Li}(\mathrm{g.s.}) + n$, also labelled 7n0

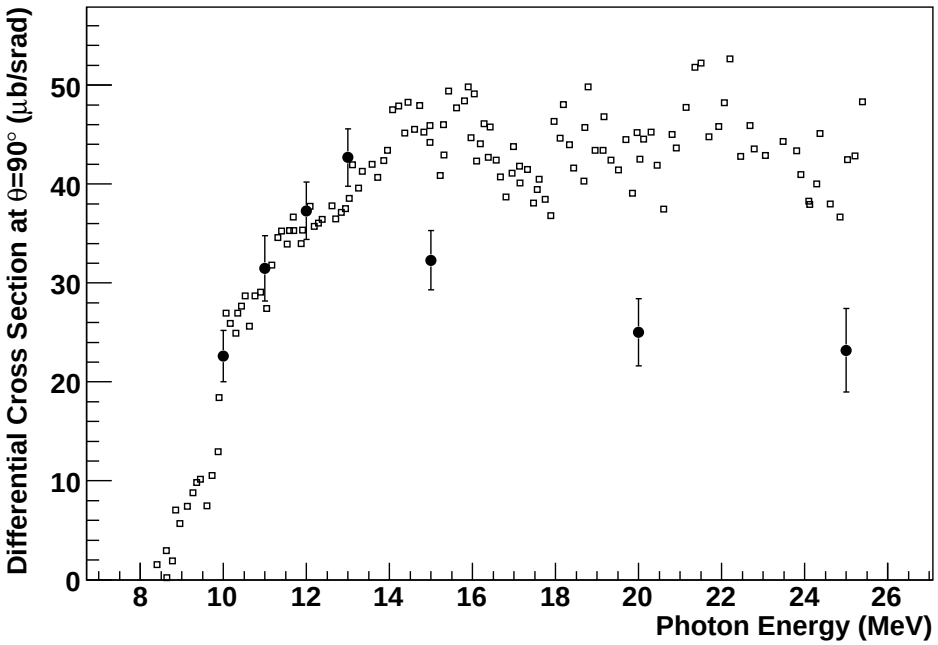

Figure 13.10: The differential cross section for 7n0 at $\theta = 90°$ from our data (closed circles) compared with that of Ferdinande *et al.* [Fer77] (open squares)

The absolute cross section plotted in figure 13.9 shows a sharp increase after the threshold, a peak between photon energies of 12 and 15 MeV, and then a long, declining tail up to 35 MeV where our data ends. It is our hope that this data will be matched by a theoretical calculation using the Lorentz integral transform.

There is one previous experimental result that can provide an interesting comparison with our measurements. Ferdinande *et al.* [Fer77] measured the differential cross section of the 7n0 reaction channel at $\theta = 90^\circ$ for photon energies from threshold up to 25 MeV. We can easily obtain comparison values from our data using

$$\frac{d\sigma}{d\Omega}(\theta = 90^\circ) = \frac{\sigma}{4\pi}\left(1 - \frac{1}{2}a_2 + \frac{3}{8}a_4\right) \tag{13.4}$$

and plot these against the data of Ferdinande *et al.* in figure 13.10. Notice that the agreement between the two datasets is excellent from 10 MeV to 13 MeV but the agreement is poor from 15 MeV to 25 MeV. This poor agreement on the high energy data is not unexpected due to the large uncertainties in the data points of Ferdinande *et al.* and the fact that they used a polychromatic bremsstrahlung photon source. Since Ferdinande *et al.* do not publish explicit uncertainties, we take the scatter in their data points to be statistical uncertainties. In the region where the two measurements agree, the measurements of Ferdinande *et al.* have much smaller uncertainties.

13.4 The Photodisintegration of ^{7}Li through Reaction Channels with Excited States

We discuss the reaction channels $^7\mathrm{Li}+\gamma \rightarrow {}^6\mathrm{Li}(2.19)+n$ and $^7\mathrm{Li}+\gamma \rightarrow {}^6\mathrm{Li}(3.56)+n$, which we have labelled 7n1 and 7n2, at photon energies of 13 and 15 MeV. It is only at these two energies that we can separate these reaction channels from all other reaction channels by fitting time-of-flight spectra. At lower photon energies these reaction channels do not produce neutrons with sufficiently high energy. At higher photon energies, there are too many reaction channels with neutrons energies close enough that they cannot be separated using any spectra that we are able to measure with the resolution of the Blowfish Neutron Detector Array.

We also include the 7d1$^+$ pseudo-reaction channel in our discussion. This pseudo-reaction channels contains neutrons primarily from the $^7\mathrm{Li} + \gamma \rightarrow {}^6\mathrm{He}(1.27) + d$ reaction channel, labelled 7d1, but also contains neutrons from other reaction channels. The 7d1$^+$ pseudo-reaction channel contains the low-energy neutrons from a medley of reaction channels. We observe 7d1$^+$ at photon energies of 12, 13 and 15 MeV.

The reaction channel $^7\mathrm{Li} + \gamma \rightarrow {}^6\mathrm{Li}(\mathrm{g.s.}) + n$, labelled 7n0, can be isolated from all other reaction channels by applying a light-output cut. This reaction channel was discussed in section 13.3 and is crucial in our separation of the 7n1, 7n2 and 7d1$^+$ reaction channels. We obtain angular

distributions for 7n1 and 7n2 by fitting the time-of-flight spectra for our simulations of the 7n0, 7n1, 7n2 and 7d1 reaction channels to the measured spectra. The angular distribution and neutron yield for 7n0 is already fixed by the results of section 13.3, making it easier to extract the other reaction channels. At 12 MeV, we fit only the 7n0 and 7d1 reaction channels but since the spectra also contain contributions from 7n1 and 7d0 which we cannot account for, we denote the second reaction channel $7d1^{+}$. At 13 MeV we are able to fit 7n0, 7n1 and 7d1 to the measured data where 7n2, 7n3 and 7d0 cannot be separated from 7d1, so we again denote it $7d1^{+}$. At 15 MeV we are able to fit 7n0, 7n1, 7n2 and 7d1 to the measured data where 7n3, 7n4, 7n5 and 7d0 cannot be separated from 7d1.

The measured associated Legendre function coefficients for 7n1 and 7n2 are reported in tables 10.12 and 10.13 and are re-listed here in table 13.8. The angular distributions are represented graphically in figure 13.11.

Table 13.8: Measured associated Legendre function coefficient values for reaction channels 7n1 and 7n2 at photon energies of 13 and 15 MeV

Energy	Coefficient	7n1	7n2
13 MeV	a_1	0.384 ± 0.051	n/a
	a_2	-0.084 ± 0.070	n/a
	e_2	-0.195 ± 0.018	n/a
	e_3	-0.007 ± 0.010	n/a
15 MeV	a_1	0.106 ± 0.014	0.099 ± 0.039
	a_2	-0.143 ± 0.022	-0.675 ± 0.059
	e_2	-0.0040 ± 0.0058	0.045 ± 0.019
	e_3	-0.0101 ± 0.0031	0.009 ± 0.009

Since the 7n1 reaction channel can be observed at two energies, we can observe some progression of the associated Legendre function coefficients. At 13 MeV we have a large, positive a_1 coefficient making the cross section forward peaked and a large, negative e_2 coefficient making the cross section peaked at 90° to the plane of polarisation. The angular distribution is quite different at 15 MeV and one may think from figure 13.11 that all coefficients are nearly zero. This is not quite the case as we have moderate a_1 and a_2 coefficients which are distinguishable from zero. The e_2 coefficient has been reduced dramatically and is indistinguishable from zero at 15 MeV. The e_3 coefficient was indistinguishable from zero at 13 MeV but is different than zero at 15 MeV, even if it is very small. There is almost no polarisation dependence for the angular distribution of 7n1 at a photon energy of 15 MeV. The angular distribution is close to, but distinct from, the uniform distribution.

We can only observe the 7n2 reaction channel at one photon energy, 15 MeV. We see only a

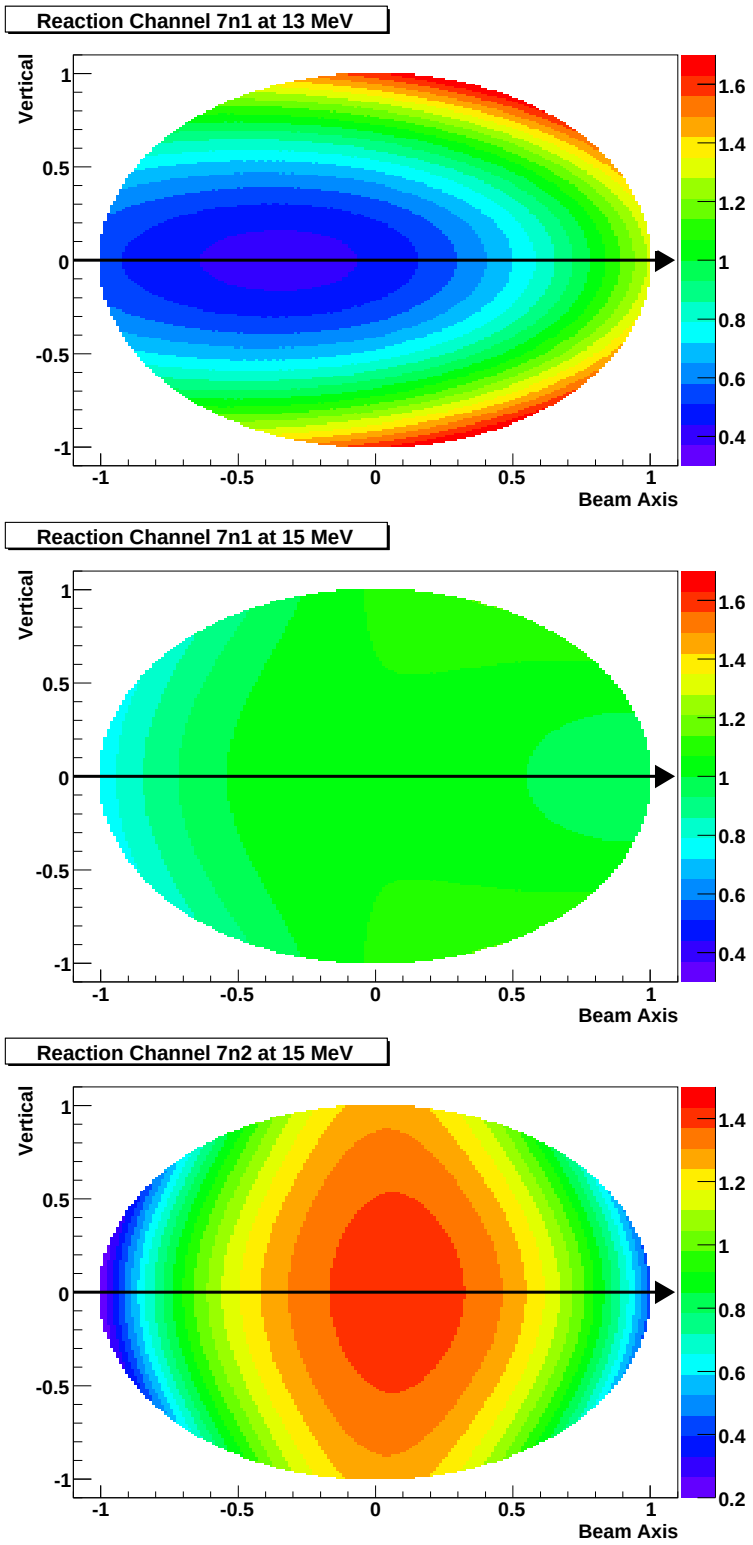

Figure 13.11: The quantity $\frac{4\pi}{\sigma}\frac{d\sigma}{d\Omega}(\theta,\phi)$ as seen in the experimental setup in the centre-of-momentum frame for reaction channels 7n1 and 7n2. This quantity gives us a normalised, relative cross section and allows us to see the angular dependence. The beam axis is the horizontal line with the arrow showing the beam direction. The vertical axis is shown and the projection eliminates the horizontal axis. Notice the colour indices for the two 7n1 plots are the same but the 7n2 plot has a different colour index.

slight dependence on polarisation. The a_1 coefficient is small but the a_2 coefficient is quite large and negative. This means that the cross section is peaked at 90° to the beam axis.

Physically meaningful angular distributions for the reaction channel 7d1 could not be found due to the influence of other reaction channels on the pseudo-reaction channel $7d1^+$.

We can now find the absolute cross sections for the 7n1, 7n2 and $7d1^+$ reaction channels. In section 10.6 we determined the cross section of each reaction channel relative to the sum of the cross sections for all observable reaction channels. In section 10.7 we found the absolute cross section for all observable reaction channels and reported them in table 10.18. We can simply multiply these quantities together to obtain the absolute cross sections for each reaction channel and these results are reported in table 13.9. We see that the cross section of the 7n1 reaction channel increases with

Table 13.9: Absolute cross sections for the reaction channels 7n1, 7n2 and $7d1^+$ at photon energies of 12, 13 and 15 MeV

Beam Energy (MeV)	$\sigma[7d1^+]$ (mb)	σ[7n1] (mb)	σ[7n2] (mb)
12	0.203 ± 0.012	n/a	n/a
13	0.280 ± 0.011	0.0804 ± 0.0031	n/a
15	0.253 ± 0.010	0.3227 ± 0.0094	0.1239 ± 0.0044

energy, which is the expected behaviour near threshold. The 7n2 reaction channel has only one point so we can't see any trends but its value seems consistent with the 7n1 reaction channel given that their thresholds differ by 1.4 MeV. The $7d1^+$ cross section for the reaction channel remains fairly level but not constant. Since the cross sections of 7n1 at 13 MeV and 7n2 at 15 MeV are small, it is likely that these cross sections are even smaller at 12 MeV and 13 MeV respectively. Likewise, we expect the contribution to $7d1^+$ from the 7n3, 7n4 and 7n5 reaction channels to also be small. While it would be irresponsible to suggest that we could assume their contributions are negligible, we believe that the cross sections listed in table 13.9 for the pseudo-reaction channel $7d1^+$ make excellent upper bounds for the cross section of the reaction channel 7d1.

We have been able to measure the cross section of the 7n1 reaction channel with photon beams of 13 and 15 MeV and the 7n2 reaction channel with a photon beam of 15 MeV. We have been able to measure both the angular dependence of the cross sections and their absolute values. For the 7d1 reaction channel we have been able to determine an upper bound on its cross section at photon energies of 12, 13 and 15 MeV. We were not able to obtain any physically meaningful values for the angular dependence of its cross section.

13.5 The Photodisintegration of ^{7}Li and the State ^{6}Li(10.0)

The existence of an excited state of ^{6}Li with excitation energy $E_x = 10.0 \pm 0.5$ MeV is a serendipitous find. We have discussed in detail the evidence for this state in section 12.3, so we will provide only a summary of the discussion here.

The first hints of this state come from unexplained peaks in the neutron time-of-flight spectra for the photodisintegration of ^{7}Li with photon energies 25, 30 and 35 MeV. These peaks are most pronounced at 30 MeV. There are no such unexplained peaks in the data with photon energy 20 MeV. No two-body reaction channel using the states found in [Til02] can explain these peaks, so we require an alternative explanation.

Neutrons from the mystery reaction channel appear at three energies and for each energy can be easily observed in a number of different detector rings. We not only have the dependence of these neutrons' kinetic energies on the photon energy, but also on the polar angle. Immediately we can eliminate any secondary decay of a daughter nucleus, such as ^{5}He, as the source. The kinematics simply do not agree as the neutron kinetic energies increase too much with increasing photon energy. We can eliminate the four-body reaction based on kinematics; the neutrons and proton do not have the correct dependence on photon energy. Similarly we can neglect three-body reactions with two light products and one heavy one. It may be possible for a three-body reaction with two heavier products and one neutron to produce a neutron kinetic energy spectra with similar dependence on photon energy as a two-body reaction. However, there is no good candidate when we enumerate all such reactions.

We are therefore left with the conclusion that the neutrons must be from a two body decay. By simple kinematics we find that the decay $^7\mathrm{Li} + \gamma \rightarrow n + {}^6\mathrm{Li}(10.0)$ describes the data very well. This leads to two possible conclusions: there exists an excited state of ^{6}Li with excitation energy $E_x = 10.0 \pm 0.5$ MeV or there exists a reaction channel completely different than those that we have been using with good success. Occam's razor would certainly have us choose the first option. In our discussion of section 12.3, we reviewed a number of results of hadronic studies which suggest an excited state of ^{6}Li in a surrounding energy range. We therefore conclude that there exists an excited state of ^{6}Li with excitation energy $E_x = 10.0 \pm 0.5$ MeV.

13.6 The Photoneutron Cross Section of ^{7}Li

Our discussions of the reaction channels 7n0, 7n1, 7n2 and 7d1$^+$ in sections 13.3 and 13.4 give a thorough presentation of the photoneutron results found for the data with photon energies of 10 to 15 MeV. Unfortunately, for the data with photon energies of 20 to 35 MeV we cannot separate the data into reaction channels other than 7n0 as there are simply too many and their neutron kinetic

energy spectra are too similar. However, we can use a representative sample of reaction channels in order to reconstruct the measured spectra and compare with the experimental data. The result is a photodisintegration cross section for the observed reaction channels and these are reported in table 13.10.

Table 13.10: Estimate of the total photoneutron cross section for ^{7}Li including all observed reaction channels

Photon Energy (MeV)	Cross Section (mb)
10	0.297 ± 0.031
11	0.400 ± 0.041
12	0.652 ± 0.029
13	0.867 ± 0.025
15	1.142 ± 0.031
20	1.903 ± 0.046
25	2.492 ± 0.059
30	2.301 ± 0.068
35	1.323 ± 0.047

There are a few issues that must be addressed concerning these cross sections. Because we are using a representative sample of reaction channels, our choice of sample can affect our results. For instance, for the 35 MeV data we chose to use the 7n6 reaction channel to represent our low-energy data and neglected the 7d1 reaction channel that we had used up to that point. Since there are, in reality, neutrons being produced by both 7n6 and 7d1, this is an approximation. Since the neutrons produced by 7n6 and 7d1 are detected with different efficiencies, our modelling the reaction with one-channel-or-another will cause the efficiencies of the simulated detectors to differ from those of the real detectors. This will have an effect on the final results.

Another problem comes from our neglect of any two-body reaction channels that produce two neutrons, such as 7p2. For example, the reaction channels 7d1 and 7p2 produce neutrons with similar kinetic energy spectra for photon energies of 20 MeV. If we substitute 7p2 for 7d1, we need half as many photodisintegration events to make up for the same number of detected neutrons.

The most serious issue in trying to estimate a total photoneutron cross section from our data is reaction channels that produce neutrons with too little energy to be detected. In order to separate the gamma-ray background from the neutron spectra, we need to use pulse-shape discrimination. This requires us to impose a cut on the light-output spectra and any neutrons depositing too little energy to pass this cut are missed. An example of such a reaction channel is 7d0, which we are

unable to observe in our data.

Even with these issues, we feel that it is worthwhile comparing our cross sections with historic measurements. These measurements used BF_3 proportional counters with moderators that reduced the neutron's kinetic energy and then detected the neutrons through capture reactions. Such slow neutron detectors can give a better picture for all reaction channels but cannot separate the reaction channels as we can with our fast neutron detectors.

Figure 13.12 shows our data compared with that of Bramblett *et al.* [Bra73] from the Livermore measurements. The agreement from 11 to 15 MeV is not good, but the two datasets follow the

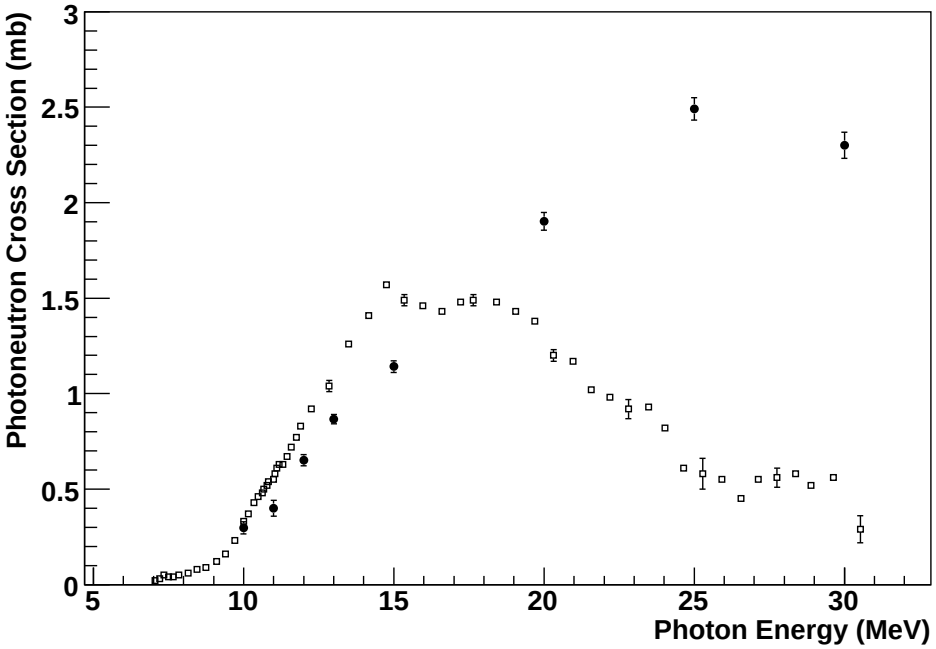

Figure 13.12: The estimated ^{7}Li photoneutron cross section from our data (closed circles) compared with the data from the Livermore measurements [Bra73] (open squares)

same trend. Likely our data is lower due to our neglecting the contribution of the 7d0 reaction channel. The data at 20, 25 and 30 MeV do not agree at all.

We see a similar trend when we compare with the data of Siddiqui *et al.* [Sid86] in figure 13.13. Our data is below theirs, likely due to our inability to detect the 7d0 reaction channel. However, our data agrees with theirs much better at 20 MeV, meaning that the reaction which produce two-neutrons might be less important at 20 MeV than suggested by the Livermore data.

It is important to note that our measurement at a photon energy of 10 MeV agrees very well with both historic datasets. We note in table 10.1 that the threshold for the 7d0 reaction channel is 9.6 MeV, so we expect its cross section to be negligibly small at 10 MeV.

Although our cross sections do not agree with the historic measurements, we have a good

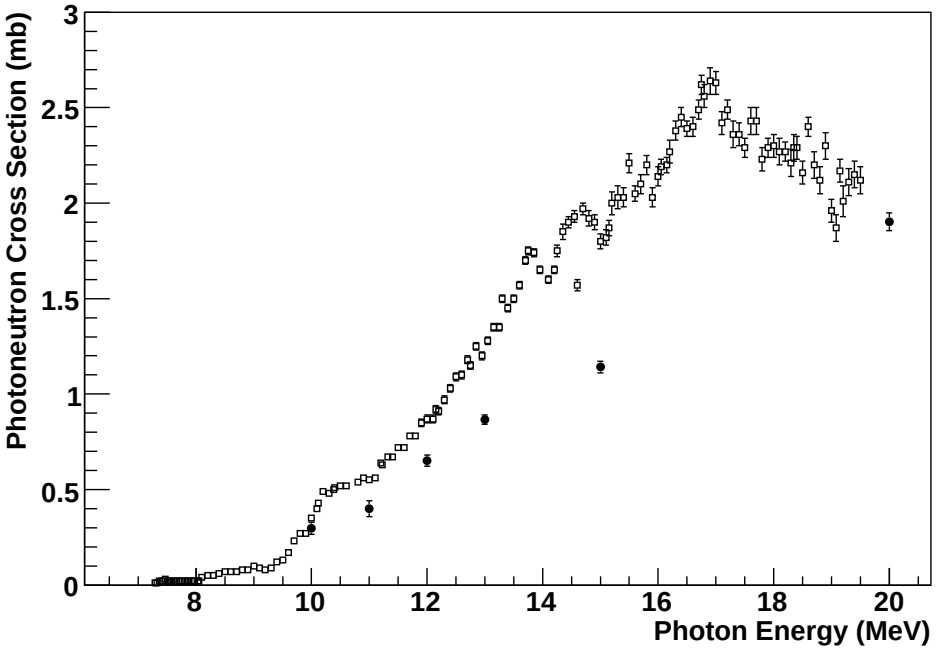

Figure 13.13: The estimated ^{7}Li photoneutron cross section from our data (closed circles) compared with the data from the measurements of Siddiqui *et al.* [Sid86] (open squares)

understanding of the disagreement. Because of the fundamentally different methods for measuring cross sections, we are not comparing similar quantities. Our use of fast neutron detectors is more suited to obtaining cross sections of individual reaction channels. Because we cannot observe the 7d0 reaction channel and we have not taken into account the effects of reaction channels that produce two neutrons, we do not expect our data to agree with the measurements of Bramblett *et al.* or Siddiqui *et al.* However, the comparison has still proven enlightening.

Chapter 14

Conclusions and Future Work

14.1 Conclusion

We have studied the photodisintegration of the lithium isotopes, ^{6}Li and ^{7}Li, using polarised, monochromatic photons from the High Intensity Gamma-Ray Source (HIGS) and detected neutrons using the Blowfish Neutron Detector Array. The photons produced by HIGS were incident upon our lithium targets in order to produce neutrons through the process of nuclear photodisintegration. These neutrons were detected by our neutron detectors and we were able to construct three principle spectra: time-of-flight, scintillator light-output and pulse-shape discrimination. Using these spectra we are able to divide our data into distinct reaction channels. Unfortunately, because we are not able to utilise events with low scintillator light-output, we are not able to observe all reaction channels that produce neutrons. However, we are able to make conclusions based on the reaction channels we do observe.

Our motivation for studying ^{6}Li is to make a measurement to compare with an existing theoretical prediction found using the Lorentz integral transform (LIT) method [Efr94, Bac04a]. Comparison between the LIT prediction and the cross section found by the Livermore group [Ber65a] is good at low photon energies but poor at higher energies. Our goal is to provide new data for comparison. We performed measurements from a photon energies from 8 to 35 MeV. Below 16 MeV, we were able to use linearly polarised photons, while above 16 MeV we were forced to use circularly polarised photons due to the method of photon production.

We are able to qualitatively model the photodisintegration spectra of ^{6}Li very well using two competing processes, $^{6}\mathrm{Li} + \gamma \rightarrow n + {}^{5}\mathrm{Li}$ and $^{6}\mathrm{Li} + \gamma \rightarrow p + {}^{5}\mathrm{He}$, where the highly unstable ^{5}He nucleus immediately decays into a neutron and an alpha particle. The analysis is complicated by the fact that both ^{5}Li and ^{5}He have excited states, and all states are highly unstable, meaning that they have large decay widths. We are able to model our data at, and below, the photon energy of 25 MeV by using only the ground states of ^{5}Li and ^{5}He and their first excited states. We use two additional excited states from each of ^{5}Li and ^{5}He to model our data up to a photon energy of 35 MeV.

While the model reproduces the qualitative data very well, there were further complications in

obtaining quantitative agreement. Since many of the neutron kinetic energy spectra for many of the reaction channels are very similar, we could not separate all reaction channels at all photon energies. Therefore, we had to take combinations of reaction channels and make a number of approximations in order to obtain quantitative results. We were also hampered by the algorithm used to separate reaction channels. This algorithm itself is the dominant source of uncertainties in our measurements. While we believe that we are doing well in separating reaction channels, there are a number of indications that there may be unaccounted for uncertainties. The most blatant of these is the large difference in the cross sections of the $^6\mathrm{Li} + \gamma \rightarrow n + {}^5\mathrm{Li}(1.49)$ and $^6\mathrm{Li} + \gamma \rightarrow p + {}^5\mathrm{He}(1.27)$ reaction channels, which we label 6n1 and 6p1 respectively. We do not know whether this difference is physical or simply an artifact of our analysis.

We present our angular distributions and cross sections with a thorough discussion of the issues involved in obtaining them. We then present our comparison with the historic data of the Livermore group in figure 13.4 and the LIT in figure 13.6. We agree well with the Livermore group for photon energies 8 to 13 MeV but do not agree with their measurements at higher energies. We agree well with the LIT prediction from 8 to 25 MeV and have some disagreement at 30 and 35 MeV. This disagreement can easily be explained by uncertainties that we are unable to quantify. We conclude that our measurement of the photodisintegration of ^{6}Li supports the LIT calculation.

The goal for our measurements on ^{7}Li is to produce data for comparison with future LIT calculations. There exists a calculation of the total photodisintegration cross section of ^{7}Li [Bac04b]. Since the photodisintegration of ^{7}Li involves many processes that do not produce neutrons, we cannot measure the total cross section. However, we are able to study individual reaction channels. We took data with photon energies from 10 to 35 MeV at the same time as our ^{6}Li measurements.

We can measure the cross sections of individual reaction channels, especially $^7\mathrm{Li}+\gamma \rightarrow {}^6\mathrm{Li}(\mathrm{g.s.})+ n$, which we label 7n0. Neutrons from this reaction channel can be isolated from all other reaction channels by making cuts on the light-output spectra. This reduces our uncertainties and gives us greater confidence in this result in comparison to our results obtained for ^{6}Li, where we separated reaction channels by fitting to spectra. There is no calculation of the $^7\mathrm{Li} + \gamma \rightarrow {}^6\mathrm{Li}(\mathrm{g.s.}) + n$ cross section yet, but the technique for performing such a calculation on an individual reaction channel has already been demonstrated for ^{4}He [Qua04]. There does exist a measurement by Ferdinande *et al.* [Fer77] for comparison. These researchers measured the differential cross section of this reaction channel at an angle of 90° to the beam axis. Our data agree well with theirs at photon energies 10 to 13 MeV. The agreement from 15 to 25 MeV is not as good but the results of Ferdinande *et al.* suffer from large uncertainties in this range.

We were able to obtain results for other reaction channels in the photodisintegration of ^{7}Li by fitting spectra. These results give us cross sections for $^7\mathrm{Li} + \gamma \rightarrow {}^6\mathrm{Li}(2.19) + n$ and $^7\mathrm{Li} + \gamma \rightarrow {}^6\mathrm{Li}(3.56) + n$, labelled 7n1 and 7n2, at photon energies of 13 and 15 MeV. These reaction channels

produce peaks in our time-of-flight spectra that make them easier to fit than the comparatively smooth ^{6}Li data. Above 15 MeV, we were not able to obtain any such results because of the proliferation of reaction channels that could not be separated due to their similar neutron kinetic energy spectra.

A surprise result is the discovery of an excited state of ^{6}Li by studying the photodisintegration of ^{7}Li. We observed neutrons which we concluded could only be from the reaction channel $^7\text{Li}+\gamma \rightarrow n+^6\text{Li}(10.0)$, which necessitates an excited state of ^{6}Li with excitation energy $E_x = 10.0 \pm 0.5$ MeV.

Through our analysis of the photodisintegration of the lithium isotopes, we have been able to make a number of conclusions. Our comparisons with experimental data and theoretical calculations have provided interesting discussion. We hope that our measurements will spawn future calculations, based on the LIT or another method, in order to better understand the structure of few-body nuclei and the forces that hold them together. A physicist's work is never done and we now turn our attention to other possible projects that build upon the base we have created here.

14.2 Future Work

The study of the photodisintegration of lithium isotopes has provided us with insight into the photodisintegration process. Using this insight, we are able to conceive of future projects and experiments related to the Blowfish Neutron Detector Array. Such projects and experiments are described here.

14.2.1 Separating Non-Isolatable Reaction Channels

In section 7.2.2 we discussed our technique for separating non-isolatable reaction channels. Typically we used the time-of-flight spectra but we occasionally used the light-output spectra for our separation algorithm. This technique has proven to be somewhat successful as we are able to qualitatively describe all of our data by breaking it into reaction channels. However, sometimes we are not able to adequately separate our data for a more quantitative analysis. A future project aimed at improving this method might be of interest. Such a project may be a simple study of how to use both the time-of-flight and light-output spectra at the same time during a fit, as they have different resolutions and uncertainties. A more detailed study might consider redesigning an experiment so that it is easier to separate non-isolatable reaction channels.

Also of interest is a new method for determining the uncertainties resulting from our separation algorithm itself. In this work we took the semi ad-hoc step of multiplying uncertainties by the square root of the reduced χ^2. While it seems that this method may have sufficed for the present work, a more rigorous method for finding uncertainties would be a welcome addition to the algorithm.

14.2.2 Lithium

We believe that this thesis has presented a reasonably thorough analysis of the existing photodisintegration of lithium data. However, it is conceivable that there is yet more interesting physics to be extracted from our data. Also, our analysis has shown areas where future experiments may be of interest. In this section, we suggest some areas where exploration of the existing lithium data may be possible, and also some future experiments.

One further area for future analysis of the existing data is an examination of the data where two detectors detect neutrons, events that have a multiplicity greater than one. One could search for a three body decay such as $^7\mathrm{Li} + \gamma \rightarrow 2n + {}^5\mathrm{Li}$ or the 2-body reaction $^7\mathrm{Li} + \gamma \rightarrow p + {}^6\mathrm{He} \rightarrow 2n + p + {}^4\mathrm{He}$. Some challenges in such a search include less-useful PSD, one neutron being detected in two neighbouring detectors after scattering and multiple single-neutron reactions occurring at the same time.

An interesting project could arise if a better understanding of the structures of the A=5 nuclei, ^{5}Li and ^{5}He, arises. In this work we relied heavily on the results of the reference [Til02] to obtain the energies and widths of the states of ^{5}Li and ^{5}He. If future theoretical or experimental work produces new estimates of these properties, the analysis of the lithium data can be redone by changing the appropriate parameters in the Geant4 simulation and rerunning the existing analysis code. This may be of particular interest to the ^{6}Li data. While the current scheme of states describes this data qualitatively very well, modifications or refinements to the scheme could produce interesting results.

It is always possible to perform experiments with the Blowfish Neutron Detector Array at photon energies not covered in this thesis. However, this may be of limited use. It would be difficult to detect neutrons produced by photons with energy less than the minimum energies presented in this analysis. It may be of interest to look at photon energies between the energies used in this thesis, such as 14, 17 and 18 MeV. However, by good planning and a little luck it seems that the energies we have already studied make a good representative sample. It certainly would be possible to extend the data to higher photon energies, but this may also be of limited use. First, our modelling of our detectors at the photon energies of 30 and 35 MeV is already pushing the limits of what we can say is reasonably validated. Second, it is not likely that we would see much interesting structure but rather a great number of reaction channels that are inseparable. Having said that, our accidental discovery of an excited state of ^{6}Li with an excitation energy of 10.0 ± 0.5 MeV shows that interesting things can be found in the most unlikely places.

Should there become a way to produce linearly polarised photons beyond the energy of 16 MeV, some measurements could be repeated in order to obtain the dependence of the cross section on polarisation.

It is more likely that future experiments should concentrate on increasing the energy resolution

of our detectors. This means increasing the resolution of our time-of-flight spectra by moving the detectors further from the target. Moving the detectors would also have the effect of decreasing our angular coverage to something much less than $\frac{1}{4}$ of 4π srad.

One interesting experiment would be to observe the 7nX reaction channel with better energy resolution. This would likely be done at a photon energy near 30 MeV but simulations using the results from the existing data could be performed to further optimise the photon energy. It may be possible to extract not only a precision measurement of the state's excitation energy but also to make a measurement of its decay width.

A longer time-of-flight experiment could be performed to get a better measurement of the $^7\mathrm{Li} + \gamma \rightarrow n + {}^6\mathrm{Li}$(g.s.) reaction channel's cross section. By moving the detectors further away, and by increasing the threshold on the discriminators, we could reduce the dead time of our system to nearly zero. The longer time-of-flight could be used to increase the energy resolution to a point where we could separate this reaction channel from the others by use of the time-of-flight spectra alone.

Clearly, there are some future avenues for studying the photodisintegration of the lithium isotopes. There are many other isotopes that deserve study and we turn our attention to some of these.

14.2.3 Deuterium

Deuterium is the isotope that inspired the creation of the Blowfish Neutron Detector Array. Blowfish was built to study the Gerasimov-Drell-Hearn (GDC) sum rule [Ger65, Dre66] on deuterium. The GDH sum rule for the deuteron states that

$$\int_0^\infty \frac{\sigma_P(E_\gamma) - \sigma_A(E_\gamma)}{E_\gamma} dE_\gamma = \frac{2\pi^2\alpha}{m_d^2}\kappa_d^2 \tag{14.1}$$

where σ_P and σ_A are the cross section with photon and deuteron spins parallel and anti-parallel, m_d is the deuteron mass, α is the fine-structure constant and κ_d is the anomalous magnetic moment of the deuteron. What is important about the GDH sum rule is that if we integrate the difference of the two cross sections over all energies, we obtain a value which has dependence on a small number of physical constants which have been well measured. If the GDH integral were measured and found to be any value other than this collection of constants, it would signal the need for new physics. Since there is a factor of $1/E_\gamma$ in the integral, measurements at lower energies are weighted heavier. These energies are easily produced by HIGS. With the OK-5 helical wiggler, HIGS can produce circularly polarised photons which have a definite helicity state. With the completion of the polarised target drawing near, we will soon be able to use Blowfish to measure the GDH integral.

Two PhDs have already been awarded for deuterium measurements using Blowfish. B. Sawatzky

measured the neutron asymmetry and normalised differential cross section for the photodisintegration of deuterium at photon energies 3.5, 4, 6 and 10 MeV [Swa05]. This experiment served as Blowfish's commissioning experiment. M. Blackston measured the same quantities at 14 and 16 MeV and performed a transition matrix element analysis on the data [Bla07, Bla08]. S. Kucuker performed a measurement on deuterium at higher energies. This measurement was performed immediately before the lithium measurements above 16 MeV and were thus performed under the same experimental conditions.

Deuterium is the simplest of possible nuclei and is to nuclear physics what the hydrogen atom is to atomic physics. There will always be interest in this nucleus and its properties. Because of a lack of flux monitoring, there have been no absolute cross sections produced for the deuterium measurements and this is also an area for future work.

While deuterium is of great interest, tritium is not being considered for experiments using Blowfish due to the hazards of working with the radioactive gas.

14.2.4 Helium

The photodisintegration of ^{4}He is more controversial than the photodisintegration of lithium isotopes, mainly because of a larger body of recent theoretical and experimental work done in the giant-dipole resonance region. A consensus value for the photoneutron cross section, as a function of energy, was forged by Calarco, Berman and Donnelly [Cal83] in 1983. LIT calculations would call this consensus into question. The total photodisintegration cross section was calculated [Efr97]. This calculation shows a prominent peak to the photodisintegration cross section, opposed to the consensus value's reduced peak. A few years later, the photoneutron and photoproton cross section were calculated [Qua04]. These results also showed a prominent peak. Two recent experimental results have not been able to resolve the discrepancy. A measurement of the photoneutron cross section from MAX-lab [Nil07] agrees well with the trend of the LIT calculation, but not its exact value. The prominent peak is evident in the MAX-lab data. On the other hand, a recent measurement from Japan [Shi05] agrees with neither the prediction nor the consensus value.

The Blowfish Neutron Detector Array could be used to make a high-precision measurement of the photoneutron cross section of ^{4}He. As demonstrated in this thesis, HIGS can produce circularly polarised photons above the ^{4}He photoneutron threshold, 20.6 MeV. A target is required for such an experiment. With helium, there are two options for targets: liquid and gas. A liquid, cryogenic target has the advantage of higher density but the disadvantage that it requires a cryogenic system to operate. A gas target requires no cryogenic system but has the disadvantage of lower density. A high-pressure gas target would have disadvantages of a thick target container but a low-pressure gas target would require a lighter container. A low-pressure target could also be made into an active target. For instance, the production of ions by charged radiation can be used to detect a

photodisintegration event. In the case of the photodisintegration of ^{4}He, the (γ,n) reaction will leave a ^{3}He ion that could be detected by such a scheme. A report has been written which describes the preliminary design of the Helium Target Ionisation Chamber, HeTIC [Wur08a]. HeTIC is based on a segmented ionisation chamber that runs the length of Blowfish. This will allow for measurements at a wide variety of angles, including angles very close to 0° and 180°.

The options for working with ^{3}He are much more limited due to its prohibitively high costs. An additional point of interest in ^{3}He is that only the complete three-body breakup produces neutrons, meaning that neutrons arriving at any one detector will be completely polychromatic. Currently, B. Perdue from Duke University is studying the photodisintegration of ^{3}He with data obtained from an experiment using Blowfish.

14.2.5 Beryllium

The photodisintegration of beryllium has applications in astrophysics. Since the reaction $\alpha + d \rightarrow {}^6\text{Li} + 1.2$ MeV cannot proceed by the electric dipole process, one must consider other ways of generating nuclei heaver than the alpha particle. Essentially, the reaction responsible for all heavier matter is $2\alpha + n \rightarrow {}^9\text{Be}$ which is followed by ${}^9\text{Be} + \alpha \rightarrow n + {}^{12}\text{C}$. This reaction is favoured over the $3\alpha \rightarrow {}^{12}$C reaction [Uts00]. By studying the inverse reaction, the photodisintegration of ^{9}Be, we can learn much about the astrophysical origins of heavier matter. For example, see [Uts00] for a recent measurement of the photoneutron cross section of ^{9}Be using gamma rays generated by Compton backscattering laser light from a conventional laser off electrons in a storage ring. The neutrons in this experiment were detected using BF_3 proportional counters.

There are a number of reaction channels involved in the photodisintegration of ^{9}Be and we must examine them in a similar way as we did those of the lithium isotopes. Table 14.1 lists the isotopes of interest and table 14.2 lists a few states of practical interest to photoneutron measurements. We can enumerate a few of the reaction channels in table 14.3 but do not enumerate them all as was done with lithium. What is important in table 14.3 is that the final products of all reactions below 16.88 MeV are a neutron and two alpha particles. Below the photoproton threshold there are three types of reaction channels: the three-body decay, the single-neutron knockout reactions and the single-alpha knockout reactions. It is generally assumed that the reaction ${}^9\text{Be}+\gamma \rightarrow n+{}^8\text{Be(g.s.)} \rightarrow n+2\alpha$ dominates based on the relatively long life time of ^{8}Be(g.s.), which has a decay width on the order of eV rather than MeV [Til04, Uts00]. However, there is interest in the three-body decay and searches have been performed to measure it near threshold [Alb04].

Notice that the three basic types of decays can be described by the relativistic two-body photodisintegration of section 5.3.1, relativistic two-body decay of section 5.3.2 and semi-relativistic three-body photodisintegration of section 5.3.3. Thus, a measurement of the neutron kinetic energy spectrum could provide useful information about these reaction channels and their relative rates.

Table 14.1: Isotopes of interest to the photodisintegration of beryllium in addition to those of table 1.1. Only ground states are considered. Binding energies listed without error are known to more decimal places than recorded here. Half lives are reported as they appear in the references. [Aud03, Til02, Til04]

Isotope	Binding Energy	Spin/Parity	Half Life or Decay Width	Decay Mode
^{9}Be	58.165 MeV	$\frac{3}{2}^-$	stable	
^{8}Be	56.500 MeV	0^+	5.57 ± 0.25 eV	alpha decay
^{8}Li	41.28 MeV	2^+	839.9 ± 0.9 ms	beta decay
^{7}Be	37.60 MeV	$\frac{3}{2}^-$	53.22 ± 0.06 d	electron capture
^{7}Li	39.24 MeV	$\frac{3}{2}^-$	stable	
^{7}He	28.83 ± 0.02 MeV	$\frac{3}{2}^-$	150 ± 20 keV	neutron emission
^{6}Be	26.92 MeV	0^+	92 ± 6 keV	proton emission
^{6}Li	31.99 MeV	1^+	stable	
^{6}He	29.27 MeV	0^+	806.7 ± 1.5 ms	beta decay
^{6}H	5.76 ± 0.24 MeV	n/a	1.6 ± 0.4 MeV	^{3}He + 3n

Table 14.2: States of interest to the photodisintegration of ^{9}Be [Til04].

Isotope	Excitation Energy (MeV)	Spin/Parity	Decay Width or Half Life	Decay Mode
^{8}Be	0.0	0^+	5.57 ± 0.25 eV	2α
^{8}Be	3.03 ± 0.10	2^+	1.513 ± 0.015 MeV	2α
^{8}Be	11.4 ± 1.5	4^+	∼ 3.5 MeV	2α
^{5}He	0.0	$\frac{3}{2}^-$	0.648 MeV	n, α
^{5}He	1.27	$\frac{1}{2}^-$	5.57 MeV	n, α

Table 14.3: Selected photodisintegration reactions for ^{9}Be and their thresholds.

Reaction	Threshold (MeV)
$^9\mathrm{Be} + \gamma \rightarrow n + 2\alpha$	1.573
$^9\mathrm{Be} + \gamma \rightarrow n + {}^8\mathrm{Be}$(g.s.) $\rightarrow n + 2\alpha$	1.665
$^9\mathrm{Be} + \gamma \rightarrow \alpha + {}^5\mathrm{He}$(g.s.) $\rightarrow n + 2\alpha$	2.465 ± 0.050
$^9\mathrm{Be} + \gamma \rightarrow \alpha + {}^5\mathrm{He}(1.27) \rightarrow n + 2\alpha$	3.74
$^9\mathrm{Be} + \gamma \rightarrow n + {}^8\mathrm{Be}(3.03) \rightarrow n + 2\alpha$	4.70 ± 0.10
$^9\mathrm{Be} + \gamma \rightarrow n + {}^8\mathrm{Be}(11.35) \rightarrow n + 2\alpha$	13.0 ± 1.5
$^9\mathrm{Be} + \gamma \rightarrow p + {}^8\mathrm{Li}$	16.88
$^9\mathrm{Be} + \gamma \rightarrow d + {}^7\mathrm{Li}$	16.70
$^9\mathrm{Be} + \gamma \rightarrow {}^3\mathrm{H} + {}^6\mathrm{Li}$	17.33
$^9\mathrm{Be} + \gamma \rightarrow {}^3\mathrm{He} + {}^6\mathrm{He}$	21.17

This would require performing measurements very similar to the ones described in this thesis. All that needs to be done in order to perform such an experiment is to locate or create a suitable target, select the optimal photon energies and schedule accelerator time. An experiment studying this reaction channel would also provide valuable experience of using Blowfish with low photon energies. This experience could be very valuable when performing the GDH measurements.

The photodisintegration of beryllium is a project that could easily be studied using Blowfish and would produce very interesting results relevant to astrophysics. It is also hoped that the Lorentz integral transform method may be applied to ^{9}Be, as it was to ^{7}Li. A measurement with high accuracy, as could be done with Blowfish, would provide incentive for such a calculation.

14.2.6 Other Nuclei

While this report has emphasised the few-body nuclei, any nucleus can be studied with Blowfish. The theoretical basis for studying other nuclei will be different but the array can be used for any target. So far, only data for oxygen have been taken.

Data for oxygen were taken at energies of 20, 25 and 30 MeV and are currently being analysed by S. Kucuker at the University of Virginia. These data were taken under the same conditions as the lithium data at these energies as they measurements were performed just prior to or consecutive with the lithium measurements.

Since Blowfish has a large infrastructure already set up, including detectors, hardware, data acquisition and software, the time is right to explore photoneutron reactions of the table of nuclides.

Many person hours have been put into making Blowfish work and we should try to reap maximum benefit from this work.

References

[Ada91] F. V. Adamian, A. Yu. Buniatian, G. S. Frangulian, P. I. Galumian, V. H. Grabsky, A. V. Hairapetian, H. H. Hakopian, V. K. Hoktanian, G. V. Karapetian, V. V. Karapetian, A. H. Vartapetian and V. G. Volchinsky, J. Phys. G **17**, 1657 (1991).

[Ahr74] J. Ahrens, H. B. Eppler, H. Gimm, M. Kröning, P. Riehn, A. Zieger and B. Ziegler, Phys. Lett. **52B**, 43 (1974).

[Ahr75] J. Ahrens, H. Borchert, K. H. Czock, H. B. Eppler, H. Gimm, H. Gundrum, M. Kröning, P. Riehn, G. Sita Ram, A. Zieger and B. Ziegler, Nucl. Phys. **A251**, 479 (1975).

[Alb04] D. E. Alburger, R. E. Chrien, R. J. Sutter and J. F. Wishart, Phys. Rev. C **70**, 064611 (2004).

[All64] F. R. Allum, G. M. Crawley and B. M. Spicer, Nucl. Phys. **51**, 177 (1964).

[Ant72a] Yu. N. Antuf'ev, V. L. Agranovich, V. S. Kuz'menko, I. I. Miroshnichenko and P. V. Sorokin, JETP Lett. **16**, 52 (1972); translation of ZhETF Pis. Red. **16**, 77 (1972).

[Ant72b] Yu. N. Antuf'ev, V. L. Agranovich, V. S. Kuz'menko and P. V. Sorokin, JETP Lett. **16**, 240 (1972); translation of ZhETF Pis. Red. **16**, 339 (1972).

[Ant72c] Yu. N. Antoufiev, V. L. Agranovich, V. S. Kuzmenko and P. V. Sorokin, Phys. Lett. **42B**, 347 (1972).

[Ant73] Yu. P. Antuf'ev, V. L. Agranovich, V. S. Kuz'menko and P. V. Sorokin, JETP Lett. **18**, 294 (1973); translation of ZhETF Pis. Red. **18**, 501 (1973).

[Ant75] Yu. P. Antuf'ev, V. L. Agranovich, V. S. Kuz'menko and P. V. Sorokin, Sov. J. Nucl. Phys. **21**, 622 (1976); translation of Yad. Fiz. **21**, 1206 (1975).

[Apo08] J. Apostolakis, G. Folger, V. Grichine, A. Howard, V. Ivanchenko, M. Kosov, A. Ribon, V. Uzhinsky, D. H. Wright, *2008 IEEE Nuclear Science Symposium Conference Record*, 833 (2008).

[Asa80] J. Asai, J. J. Murphy II and D. M. Skopik, Phys. Rev. C **21**, 469 (1980).

[Aud03] G. Audi, A. H. Wapstra and C. Thibault, Nucl. Phys. **A729**, 337 (2003).

[Bac04a] S. Bacca, N. Barnea, W. Leidemann, G. Orlandini, Phys. Rev. C **69**, 057001 (2004).

[Bac04b] S. Bacca, H. Arenhövel, N. Barnea, W. Leidemann and G. Orlandini, Phys. Lett B **603**, 159 (2004).

[Bar54] M. Q. Barton and J. H. Smith, Phys. Rev. **95**, 573 (1954).

[Bar58] M. Q. Barton and J. H. Smith, Phys. Rev. **110**, 1143 (1958).

[Bar09] J. Barlow *et al.*, Can. J. Earth Sci. **46**, 181 (2009).

[Baz60] E. B. Bazhanov and L. A. Kul'chitskiĭ, Soviet Physics–JETP **11**, 1215 (1960); translation of J. Exptl. Theoret. Phys. (U.S.S.R.) **38**, 1685 (1960).

[Baz64] E. B. Bazhanov, A. P. Komar and A. V. Kulikov, Soviet Physics–JETP **19**, 1014 (1964); translation of J. Exptl. Theoret. Phys. (U.S.S.R.) **46**, 1497 (1964).

[Baz65] E. B. Bazhanov, A. P. Komar, A. V. Kulikov and E. D. Makhnovsky, Nucl. Phys. **68**, 191 (1965).

[Baz66] E. B. Bazhanov, A. P. Komar and A. V. Kulikov, Soviet Physics–Doklady **11**, 953 (1967); translation of Doklady Akademii Nauk SSSR **171**, 549 (1966).

[Bec47] R. A. Becker, A. O. Hanson and B. C. Diven, Phys. Rev. **71**, 466 (1947).

[Ber63a] M. Bernheim and G. R. Bishop, Phys. Lett. **5**, 270 (1963).

[Ber63b] M. Bernheim and G. R. Bishop, Phys. Lett. **5**, 294 (1963).

[Ber65a] B. L. Berman, R. L. Bramblett, J. T. Caldwell, R. R. Harvey and S. C. Fultz, Bull. Am. Phys. Soc. **10**, 541 (1965).

[Ber65b] B. L. Berman, R. L. Bramblett, J. T. Caldwell, R. R. Harvey and S. C. Fultz, Phys. Rev. Lett. **15**, 727 (1965).

[Ber75] B. L. Berman and S. C. Fultz, Rev. Mod. Phys. **47**, 713 (1975).

[Ber86] R. Bernabei, A. Incicchitti, M. Mattioli, P. Picozza, D. Prosperi, L. Casano, S. d'Angelo, M. P. De Pascale, C. Schaerf, G. Giordano, G. Matone, S. Frullani and B. Girolami, Phys. Rev. Lett. **57**, 1542 (1986).

[Ber99] J. C. Bergstrom, R. Igarashi and J. M. Vogt, Phys. Rev. C **59**, 2588 (1999).

[Bev69] P. R. Bevingtron, *Data Reduction and Error Analysis for the Physical Sciences*. McGraw-Hill, New York (1969). Pages 168-171.

[Bew05] B. E. Bewer, *Development of a Gain Monitoring System for a Neutron Detector Array*. MSc Thesis, University of Saskatchewan, Unpublished (2005). (Available at: http://nucleus.usask.ca/technical_reports/report_index.html)

[Bew09] B. E. Bewer, R.E. Pywell, R. Igarashi and W. A. Wurtz, Nucl. Instr. and Meth. **A608**, 417 (2009).

[Bir51] J. B. Birks, Proc. Phys. Soc. A **64**, 874 (1951).

[Bir64] J. B. Birks, *The Theory and Practice of Scintillation Counting*. Pergamon Press, Oxford (1964).

[Bis63] G. R. Bishop and M. Bernheim, Phys. Lett. **5**, 140 (1963).

[Bis64] G. R. Bishop and M. Bernheim, Phys. Lett. **8**, 48 (1964).

[Bix68] M. Bixon and J. Jortner, J. Chem. Phys. **48**, 715 (1968).

[Bla68] S. L. Blatt, A. M. Young, S. C. Ling, K. J. Moon and C. D. Poterfield, Phys. Rev. **176**, 1147 (1968).

[Bla07] M. Blackston, *Precision Measurements of Deuteron Photodisintegration Using Linearly Polarized Photons of 14 and 16 MeV*. PhD Thesis, Duke University, Unpublished (2007).

[Bla08] M. A. Blackston, M. A. Ahmed, B. A. Perdue, H. R. Weller, B. Bewer, R. E. Pywell, W. A. Wurtz, R. Igarashi, S. Kucuker, B. Norum, K. Wang, J. Li, S. F. Mikhailov, V. G. Popov, Y. K. Wu, B. D. Sawatzky, Phys. Rev. C **78**, 034003 (2008).

[Bra66] R. L. Bramblett, B. L. Berman, M. A. Kelly, J. T. Caldwell and S. C. Fultz, Bull. Am. Phys. Soc. **11**, 367 (1966).

[Bra73] R. L. Bramblett, B. L. Berman, M. A. Kelly, J. T. Caldwell and S. C. Fultz, in *International Conference on Photonuclear Reactions and Applications*, ed. B. L. Berman, p 175, University of California, Livermore (1973).

[Bru97] R. Brun and F. Rademakers, Nucl. Inst. and Meth. **A389**, 81 (1997). See also http://root.cern.ch/.

[Bur89] N. A. Burkova, Yu. V. Vladimirov, V. B. Ganenko, V. A. Gushchin, I. G. Evseev, Yu. V. Zhebrovskij M. A. Zhusupov, L. Ya. Kolesnikov, V. P. Likhachev, S. A. Pashchuk, A. L. Rubashkin, G. A. Savitskij, P. V. Sorokin, V. M. Khvastunov and R. A. Ehramzhyan, Phys. Lett. B **223**, 136 (1989).

[Bur95] N. A. Burkova, V. V. Denyak, R. A. Ehramzhyan, I. G. Evseev, V. M. Khvastunov, V. P. Likhachev, S. A. Pashchuk, M. A. Zhusupov, Nucl. Phys. **A586**, 293 (1995).

[Cal83] J. R. Calarco, B. L. Berman and T. W. Donnelly, Phys. Rev. C **27**, 1866 (1983).

[Car88] P. J. Carlos, Ph. Bourgeois, J. Fagot, J. L. Fallou, P. Garganne, J. M. Laget, A. Lepretre, A. de Miniac, A. Veyssiere, J. Jury and D. Ryckbosch, Phys. Lett. B **203**, 33 (1988).

[Cec96] F. E. Cecil, J. Yan and C. S. Galovich, Phys. Rev. C **53**, 1967 (1996).

[Cha04] D. Chabot, A. Del Frari, R. Igarashi, T. Regier, D. Murray, E. Norum, T. Wilson and G. Wright *LUCID User's Guide, Ed. 3.0.* Unpublished (2004). (Available at: http://nucleus.usask.ca/technical_reports/report_index.html)

[Chi62] V. P. Chizhov, A. P. Komar, L. A. Kulchitsky, A. V. Kulikov, E. D. Makhnovsky and Yu. M. Volkov, Nucl. Phys. **34**, 562 (1962).

[Cho52] C. N. Chou, Phys. Rev. **87**, 904 (1952).

[Cli63] F. M. Clikeman, A. J. Bureau, J. R. McConnell, M. G. Stewart and D. A. Tripp, Bull. Am. Phys. Soc. **8**, 290 (1963).

[Con98] J. P. Connelly, B. L. Berman, W. J. Briscoe, K. S. Dhuga, A. Mokhtari, D. Zubanov, H. P. Blok, R. Ent, J. H. Mitchell and L. Lapikás, Phys. Rev. C **57**, 1569 (1998).

[Cos63] S. Costa, S. Ferroni, V. Wataghin and R. Malvano, Phys. Lett. **4**, 308 (1963).

[Cos66] S. Costa, F. Ferrero, C. Manfredotti, L. Pasqualini and L. Roasio, Nuovo Cimento **42 B**, 382 (1966).

[Czi64] J. B. Czirr, D. R. Nygren, C. D. Zafiratos, Nucl. Instr. and Meth. **31**, 226 (1964).

[Dal65] P. J. Dallimore, K. S. Lam and H. H. Thies, Aust. J. Phys. **18**, 389 (1965).

[Del76] T. Delbar, G. Grégoire, J. Lega, G. Paic and P. Wastyn, Phys. Rev. C **14**, 1659 (1976).

[Del83] Th. Delbar, Gh. Grégoire, P. Belery and G. Paić, Phys. Rev. C **27**, 1876 (1983).

[DeL03] J. R. De Laeter, J. K. Böhlke, P. De Bièvre, H. Hidaka, H. S. Peiser, K. J. R. Rosman and P. D. P. Taylor, Pure Appl. Chem. **75**, 683 (2003).

[Den67a] V. P. Denisov and L. A. Kul'chitskiĭ, Soviet J. Nucl. Phys. **5**, 344 (1967); translation of J. Nucl. Phys. (U.S.S.R.) **5**, 490 (1967).

[Den67b] V. P. Denisov, A. P. Komar, L. A. Kul'chitskiĭ and E. D. Makhnovskiĭ, Soviet J. Nucl. Phys. **5**, 349 (1967); translation of J. Nucl. Phys. (U.S.S.R.) **5**, 498 (1967).

[Den69] V. P. Denisov, A. P. Komar, L. A. Kul'chitskiĭ and I. Ya. Chubukov, Soviet J. Nucl. Phys. **10**, 635 (1970); translation of Yad. Fiz. **10**, 1116 (1969).

[Den74] V. P. Denisov and I. Ya. Chubukov, Sov. J. Nucl. Phys. **20**, 579 (1975); translation of Yad. Fiz. **20**, 1106 (1974).

[Den75] V. P. Denisov and I. Ya. Chubukov, Sov. J. Nucl. Phys. **22**, 466 (1976); translation of Yad. Fiz. **22**, 897 (1975).

[Den78] V. P. Denisov and I. Ya. Chubukov, Sov. J. Nucl. Phys. **27**, 469 (1978); translation of Yad. Fiz. **27**, 882 (1978).

[Den82] V. P. Denisov and I. Ya. Chubukov, Sov. J. Nucl. Phys. **35**, 6 (1982); translation of Yad. Fiz. **35**, 11 (1982).

[Den93] V. V. Denyak, I. G. Evseev, V. P. Likhachev, S. A. Pashchuk and V. M. Khvastunov, Phys. At. Nucl. **56**, 14 (1993); translation of Yad. Fiz. **56**, 26 (1993).

[Dia95] J. F. Dias, D. Ryckbosch, R. Van de Vyver, C. Van den Abeele, G. De Meyer, L. Van Hoorebeke, J.-O. Adler, K. I. Blomqvist, D. Nilsson, H. Ruijter and B. Schröder, Nucl. Phys. **A587**, 434 (1995).

[Dia97] J. F. Dias, D. Ryckbosch, R. Van de Vyver, C. Van den Abeele, G. De Meyer, L. Van Hoorebeke, J.-O. Adler, K. I. Blomqvist, D. Nilsson, H. Ruijter and B. Schröder, Phys. Rev. C **55**, 942 (1997).

[Dre66] S. D. Drell and A. C. Hearn, Phys. Rev. Lett. **16**, 908 (1966).

[Duĭ74] A. D. Duĭsebaev, G. N. Ivanov, É. I. Kébin, Yu. I. Nechaev, Yu. V. Solov'ev, V. G. Sukharevskiĭ and V. A. Khaĭmin, JETP Lett. **19**, 280 (1974); translation of ZhETF Pis. Red. **19**, 531 (1974).

[Dyt84] N. Dytlewski, S. A. Siddiqui and H. H. Thies, Nucl. Phys. **A430**, 214 (1984).

[Edg56] R. D. Edge, Aust. J. Phys. **9**, 429 (1956).

[Efr94] V. D. Efros, W. Leidemann and G. Orlandini, Phys. Lett. B **338**, 130 (1994).

[Efr97] V. D. Efros, W. Leidemann and G. Orlandini, Phys. Rev. Lett. **78**, 4015 (1997).

[Efr07] V. D. Efros, W. Leidemann, G. Orlandini and N. Barnea, J. Phys. G **34**, R459 (2007).

[Eig69] F. Eigenbrod, Z. Physik **228**, 337 (1969).

[Ent86] R. Ent, H. P. Blok, J. F. A. van Hienen, G. van der Steenhoven, J. F. J. van den Brand, J. W. A. den Herder, E. Jans, P. H. M. Keizer, L. Lapikás, E. N. M. Quint, P. K. A. de Witt Huberts, B. L. Berman, W. J. Briscoe, C. T. Christou, D. R. Lehman, B. E. Norum and A. Saha, Phys. Rev. Lett. **57**, 2367 (1986).

[Ent94] R. Ent, B. L. Berman, H. P. Blok, J. F. J. van den Brand, W. J. Briscoe, M. N. Harakeh, E. Jans, P. D. Kunz, L. Lapikás, Nucl. Phys. **A578**, 93 (1994).

[Erd54] P. Erdös, P. Stoll, M. Wächter and V. Wataghin, Nuovo Cimento **12**, 639 (1954).

[Fas60] R. W. Fast, P. A. Flournoy, R. S. Tickle and W. D. Whitehead, Phys. Rev. **118**, 535 (1960).

[Fer77] H. Ferdinande, N. K. Sherman, K. H. Lokan and C. K. Ross, Can. J. Phys. **55**, 428 (1977).

[Ful73] S. C. Fultz, B. L. Berman, R. A. Alavarez and P. Meyer, in *International Conference on Photonuclear Reactions and Applications*, ed. B. L. Berman, p 273, University of California, Livermore (1973).

[Gan87] V. B. Ganenko, V. A. Gushchin, Yu. V. Zhebrovskiĭ, L. Ya. Kolesnikov, A. L. Rubashkin and P. V. Sorokin, JETP Lett. **46**, 272 (1987); translation of Pis'ma Zh. Eksp. Teor. Fiz. **46**, 216 (1987).

[Gar73] S. N. Gardiner, J. L. Matthews and R. O. Owens, Phys. Lett. **46B**, 186 (1973).

[Gea03] The Geant4 Collaboration, Nucl. Instr. and Meth. **A506**, 250 (2003).

[Gea06] The Geant4 Collaboration, IEEE Trans. Nucl. Sci. **53**, 270 (2005).

[Gen72] J. P. Genin, J. Julien, R. Letourneau, A. Mougeot, J. Rambaut, C. Samour, in *Nuclear Structure Studies Using Electron Scattering and Photoreaction*, ed. K. Shoda and H. Ui, p 439, Tohoku University, Sendai, Japan (1972).

[Gen74] J. P. Genin, J. Julien, M. Rambaut, C. Samour, A. Palmeri and Vinciguerra, Phys. Lett. **52B**, 46 (1974).

[Ger65] S. B. Gerasimov, Soviet J. Nucl. Phys. **2**, 430 (1966); translation of J. Nucl. Phys. (U.S.S.R.) **2**, 598 (1965).

[Gle52] H. B. Glenn, Phys. Rev. **88**, 418 (1952).

[Glö83] W. Glöckle, *The Quantum Mechanical Few-Body Problem.* Springer-Verlag, Berlin (1983).

[Gol53] J. Goldemberg and L. Katz, Bull. Am. Phys. Soc. **28**, 16 (1953).

[Gol54a] J. Goldemberg and L. Katz, Can. J. Phys. **32**, 49 (1954).

[Gol54b] J. Goldemberg and L. Katz, Phys. Rev. **95**, 471 (1954).

[Gre62] A. G. Gregory, T. R. Sherwood and E. W. Titterton, Nucl. Phys. **32**, 543 (1962).

[Gre64] L. Green and D. J. Donahue, Phys. Rev. **135**, B701 (1964).

[Gri61] G. M. Griffiths, R. A. Morrow, P. J. Riley and J. B. Warren, Can. J. Phys. **39**, 1397 (1961).

[Grü75] W. Grüebler, P. A. Schmelzbach, V. König, R. Risler and D. Boerma, Nucl. Phys. **A242**, 265 (1975).

[Hei55] F. Heinrich and R. Rubin, Helv. Phys. Acta **28**, 185 (1955).

[Hei74] F. H. Heimlich, E. Rössle, M. Köbberling, J. Moritz, K. H. Schmidt, D. Wegener, D. Zeller, J. K. Bienlein, J. Bleckwenn and H. Dinter, Nucl. Phys. **A228**, 478 (1974).

[Hir73] H. Hiramatsu, T. Kamae, H. Muramatsu, K. Nakamura, N. Izutsu and Y. Watase, Phys. Lett. **44B**, 50 (1973).

[Hol59] H. D. Holmgren and R. L. Johnston, Phys. Rev. **113**, 1556 (1959).

[How65] E. Hayward and T. Stovall, Nucl. Phys. **69**, 241 (1965).

[Hut67] R. M. Hutcheon, T. E. Drake, V. Stobie, G. Beer and H. S. Caplan, Bull. Am. Phys. Soc. **11**, 632 (1967).

[Hut68] R. M. Hutcheon, T. E. Drake, V. W. Stobie, G. A. Beer and H. S. Caplan, Nucl. Phys. **A107**, 266 (1968).

[Hut69] R. M. Hutcheon and H. S. Caplan, Nucl. Phys. **A127**, 417 (1969).

[Iga08] R. Igarashi, Private Communication (2008).

[Iga10] R. Igarashi, Private Communication (2010).

[Ish80] B. S. Ishkhanov, V. I. Mokeev, Yu. A. Novikov and I. M. Piskarëv, Sov. J. Nucl. Phys. **32**, 5 (1980); translation of Yad. Fiz. **32**, 11 (1980).

[Ive03] J. Ives, *Simulation and Measurement of the Response of the Blowfish Detector to Low-Energy Neutrons.* MSc Thesis, University of Saskatchewan, Unpublished (2003). (Available at: http://nucleus.usask.ca/technical_reports/report_index.html)

[Jac99] J. D. Jackson, *Classical Electrodynaics, 3rd Ed.* John Wiley & Sons, Inc., Hoboken, NJ (1999).

[Jod92] M. Jodice, S. Frullani, F. Garibaldi, F. Ghio, G. P. Capitani, E. De Sanctis, M. Bernheim, A. Gerard, A. Magnon, C. Marchand, J. Morgenstern, J. Picard, P. Vernin, A. Zghiche, J. Mougey and M. Brussel, Phys. Lett. B **282**, 31 (1992).

[Jul73] J. Julien, C. Samour, G. Bianchi, P. Duval, J. P. Génin, R. Letourneau, A. Mougeot, M. Rambaut, A. Palmeiri and D. Vinciguerra, in *International Conference on Photonuclear Reactions and Applications*, ed. B. L. Berman, p 1061, University of California, Livermore (1973).

[Jun77] G. Junghans, K. Bangert, U. E. P. Berg, N. Lemmer, G. Schmidt, R. Stock, K. Wienhard, in *Proceedings of the International Conference on Nuclear Structure*, p 143, Tokyo (1977).

[Jun79] G. Junghans, K. Bangert, U. E. P. Berg, R. Stock and K. Wienhard, Z. Phys. A **291**, 353 (1979).

[Kar89] S. Karataglidis, D. Zubanov, P. D. Harty and M. N. Thompson, Nucl. Phys. **A501**, 108 (1989).

[Kno00] G. F. Knoll, *Radiation Detection and Measurement 3rd Ed.* John Wiley & Sons, Inc., New York (2000).

[Koh63] D. Kohler and S. M. Austin, Bull. Am. Phys. Soc. **8**, 290 (1963).

[Kom60] A. P. Komar and E. D. Makhnovskii, Soviet Physics–Doklady **135**, 1229 (1960); translation of Doklady Akademii Nauk SSSR **135**, 52 (1960).

[Kom64] A. P. Komar and E. D. Makhnovskii, Soviet Physics–Doklady **9**, 463 (1964); translation of Doklady Akademii Nauk SSSR **156**, 774 (1964).

[Kor99] E. Korkmaz, G. V. O'Rielly, D. A. Hutcheon, G. Feldman, D. Jordan, N. R. Kolb, R. E. Pywell, G. A. Retzlaff, B. D. Sawatzky, D. M. Skopik, J. M. Vogt, E. Cairns, U. Giesen, L. Holm, A. K. Opper, F. M. Rozon, J. Souku, Nucl. Instr. and Meth. **A431**, 446 (1999).

[Kot73] E. A. Kotikov and E. D. Makhnovskiĭ, Sov. J. Nucl. Phys. **18**, 125 (1974); translation of Yad. Fiz. **18**, 245 (1973).

[Kot85] E. A. Kotikov and E. D. Makhnovskiĭ, Sov. J. Nucl. Phys. **41**, 183 (1985); translation of Yad. Fiz. **41**, 289 (1985).

[Kot87] E. A. Kotikov and E. D. Makhnovskiĭ, Sov. J. Nucl. Phys. **46**, 579 (1987); translation of Yad. Fiz. **46**, 1009 (1987).

[Kul63] L. A. Kul'chitskiĭ and Yu. M. Volkov, Soviet Physics–JETP **17**, 780 (1963); translation of J. Exptl. Theoret. Phys. (U.S.S.R.) **44**, 1153 (1963).

[Kus80] M. Kusuhara, Phys. Rev. C **21**, 1165 (1980).

[Lan89a] J. B. J. M. Lanen, A. M. van den Berg, H. P. Blok, J. F. J. van den Brand, C. T. Christou, R. Ent, A. G. M. van Hees, E. Jans, G. J. Kramer, L. Lapikás, D. R. Lehman, W. C. Parke, E. N. M. Quint, G. van der Steenhoven, and P. K. A. de Witt Huberts, Phys. Rev. Lett. **62**, 2925 (1989).

[Lan89b] J. B. J. M. Lanen, R. G. Lovas, A. T. Kruppa, H. P. Blok, J. F. J. van den Brand, R. Ent, E. Jans, G. J. Kramer, L. Lapikás, E. N. M. Quint, G. van der Steenhoven, P. C. Tiemeijer and P. K. A. de Witt Huberts, Phys. Rev. Lett **63**, 2793 (1989).

[LaP00] A. La Piana, W. Leidemann, Nucl. Phys. **A677**, 423 (2000).

[Leo94] W. R. Leo, *Techniques for Nuclear and Particle Physics Experiments*. Springer-Verlag, Berlin (1994).

[Leu77] M. K. Leung, J. J. Murphy, II, Y. M. Shin and D. M. Skopik, Can. J. Phys. **55**, 252 (1977).

[Lev51] J. S. Levinger, Phys. Rev. **84**, 43 (1951).

[Lik99] V. P. Likhachev, M. N. Martins, M. T. F. da Cruz, J. D. T. Arruda-Neto, L. P. Geraldo, R. Semmler and J. F. Dias, Phys. Rev. C **59**, 525 (1999).

[Lit96] V. N. Litvinenko, B. Burnham, J. M. J. Madey, S. H. Park and Y. Wu, Nucl. Instr. and Meth. **A375**, 46 (1996).

[Lit97] V. N. Litvinenko, B. Burnham, M. Emamian, N. Hower, J. M. J. Madey, P. Morcombe, P. G. O'Shea, S. H. Park, R. Sachtschale, K. D. Straub, G. Swift, P. Wang, Y. Wu, R. S. Canon, C. R. Howell, N. R. Roberson, E. C. Schreiber, M. Spraker, W. Tornow, H. R. Weller, I. V. Pinayev, N. G. Gavrilov, M. G. Fedotov, G. N. Kulipanov, G. Y. Kurkin, S. F. Mikhailov, V. M. Popik, A. N. Skrinsky, N. A. Vinokurov, B. E. Norum, A. Lumpkin and B. Yang, Phys. Rev. Lett. **78**, 4569 (1997).

[Lit01] V. N. Litvinenko, S. F. Mikhailov, O. A. Shevchenko, N. A. Vinokurov, N. G. Gavrilov, G. N. Kulipanov, T. V. Shaftan, P. D. Vobly and Y. Wu, Nucl. Instr. and Meth. **A475**, 407 (2001).

[Mad78] R. Madey, F. M. Waterman, A. R. Baldwin, J. N. Knudson, Nucl. Instr. and Meth. **151**, 445 (1978).

[Mak64] E. D. Makhnovskiĭ, Soviet Physics–JETP **19**, 769 (1964); translation of J. Exptl. Theoret. Phys. (U.S.S.R.) **46**, 1136 (1964).

[Mal69] R. A. Malfliet and J. A. Tjon, Nucl. Phys. **A127**, 161 (1969).

[Man65] G. Manuzio, R. Malvano, G. Ricco and M. Sanzone, Nuovo Cimento **40 B**, 300 (1965).

[Man66] G. E. Manuzio, G. Ricco and M. Sanzone, Nuovo Cimento **42 B**, 348 (1966).

[Mat68] J. L. Matthews, W. Bertozzi, S. Kowalski, C. P. Sargent and W. Turchinetz, Nucl. Phys. **A112**, 654 (1968).

[Mat76] J. L. Matthews, D. J. S. Findlay, S. N. Gardiner and R. O. Owens, Nucl. Phys. **A267**, 51 (1976).

[Mit91] J. H. Mitchell, H. P. Blok, B. L. Berman, W. J. Briscoe, M. A. Daman, R. Ent, E. Jans, L. Lapikas and J. J. M. Steijger, Phys. Rev. C **44**, 2002 (1991).

[Miw55] M. Miwa, J. Phys. Soc. Japan **10**, 173 (1955).

[Miw60] M. Miwa and M. Yamanouchi, J. Phys. Soc. Japan **15**, 947 (1960).

[Moh94] P. Mohr, V. Kölle, S. Wilmes, U. Atzrott, G. Staudt, J. W. Hammer, H. Krauss and H. Oberhummer, Phys. Rev. C **50**, 1543 (1994).

[Mur68] A. Murakami, Nuovo Cimento **55 B**, 604 (1968).

[Mur70] A. Murakami, J. Phys. Soc. Japan **28**, 1 (1970).

[Nab52] H. Nabholz, P. Stoll and H. Wäffler, Helv. Phys. Acta **25**, 701 (1952).

[Nak78] K. Nakamura, S. Hiramatsu, T. Kamae, H. Muramatsu, N. Izutsu and Y. Watase, Nucl. Phys. **A296**, 431 (1978).

[Neu69] R. Neuhausen, Z. Physik **220**, 456 (1969).

[Neu71] R. Neuhausen and R. M. Hutcheon, Nucl. Phys. **A164**, 497 (1971).

[Nil90] D. Nilsson, J.-O. Adler, B.-E. Andersson, K. I. Blomqvist, L. Isaksson, A. Sandell, B. Schröder, K. Ziakas, L. Van Hoorebeke, D. Rychbosch and R. Van de Vyver, Z. Phys. A **335**, 239 (1990).

[Nil94] D. Nilsson, J-O. Adler, B-E. Andersson, K. I. Blomqvist, L. Isaksson, A. Sandell, B. Schröder, K. Ziakas, L. Van Hoorebeke, D. Rykbosch and R. Van de Vyver, Phys. Scripta **49**, 397 (1994).

[Nil07] B. Nilsson, J.-O. Adler, B.-E. Andersson, J. R. M. Annand, I. Akkurt, M. J. Boland, G. I. Crawford, K. G. Fissum, K. Hansen, P. D. Harty, D. G. Ireland, L. Isaksson, M. Karlsson, M. Lundin, J. C. McGeorge, G. J. Miller, H. Ruijter, A. Sandell, B. Schroder, D. A. Sims and D. Watts, Phys. Rev. C **75**, 014007 (2007).

[Nüs66] F. Nüsslin, H. Werner and J. Zimmerer, Z. Naturforch **21a**, 1195 (1966).

[Odi56] A. C. Odian, P. C. Stein, A. Wattenberg, B. T. Field and R. Weinstein, Phys. Rev. **102**, 837 (1956).

[ORi96] G. V. O'Rielly, N. R. Kolb and R. E. Pywell, Nucl. Instr. and Meth. **A368**, 745 (1996).

[Pao66] G. Paoli, M. Scotto and A. Wataghin, Nuovo Cimento **43 B**, 189 (1966).

[Pho98] Photonis Imaging Sensors, *XP2262 Datasheet*. (1998).

[Pis87] I. M. Piskarëv, Sov. J. Nucl. Phys. **45**, 758 (1987); translation of Yad. Fiz. **45**, 1222 (1987).

[Pro60] D. G. Proctor and W. H. Voelker, Phys. Rev. **118**, 217 (1960).

[Pyw06] R. E. Pywell, B. D. Sawatzky, J. Ives, N. R. Kolb, R. Igarashi and W. A. Wurtz, Nucl. Inst. and Meth. **A565**, 725 (2006).

[Pyw09a] R. Pywell and W. Wurtz, *SPIR-142: Blowfish Gain Analysis for 2008 Runs*, Unpublished (2009). (Available at: http://nucleus.usask.ca/technical_reports/report_index.html)

[Pyw09b] R. E. Pywell, O. Mavrichi, W. A. Wurtz and R. Wilson, Nucl. Instr. and Meth. **A606**, 517 (2009).

[Qua04] S. Quaglioni, W. Leidemann, G. Orlandini, N. Barnea and V. D. Efros, Phys. Rev. C **69**, 044002 (2004).

[Rei70] I. Reichstein and Y. C. Tang, Nucl. Phys. **A158**, 529 (1970).

[Ril58] P. J. Riley, J. B. Warren and G. M. Griffiths, Bull. Am. Phys. Soc. **3**, 330 (1958).

[Rob81] R. G. H. Robertson, P. Dyer, R. A. Warner, R. C. Melin, T. J. Bowles, A. B. McDonald, G. C. Ball, W. G. Davies and E. D. Earle, Phys. Rev. Lett. **47**, 1867 (1981); erratum Phys. Rev. Lett. **75**, 4334 (1995).

[Rom59] T. A. Romanowski and V. H. Voelker, Phys. Rev. **113**, 886 (1959).

[Rud54] R. Rubin and M. Walter, Helv. Phys. Acta **27**, 163 (1954).

[Ryb58] T. W. Rybka and L. Katz, Phys. Rev. **110**, 1123 (1958).

[Ryc94] D. Ryckbosch, L. Van Hoorebeke, R. Van de Vyver, C. Van den Abeele, J. Dias, J-O. Adler, K. I. Blomqvist, D. Nilsson, B. Schröder and K. Ziakas, Nucl. Phys. **A568**, 52 (1994).

[Sai05] Saint-Gobain Ceramics & Plastics, Inc., *BC-505 Liquid Scintillator Datasheet*. (2005).

[Sak67] J. J. Sakurai, *Advanced Quantum Mechanics*. Addison Wesley, New York (1967).

[Sak94] J. J. Sakurai, *Modern Quantum Mechanics Revised Edition*. Addison Wsley, New York (1994).

[San70] M. Sanzone, G. Ricco, S. Costa and L. Ferrero, Nucl. Phys. **A153**, 401 (1970).

[Sen83] M. R. Sené, I. Anthony, D. Brandford, A. G. Flowers, A. C. Shotter, C. H. Zimmerman, J. C. McGeorge, R. O. Owens and P. J. Thorley, Phys. Rev. Lett. **50**, 1831 (1983).

[Sen85] M. R. Sené, I. Anthony, D. Brandford, A. G. Flowers, A. C. Shotter, C. H. Zimmerman, J. C. McGeorge, R. O. Owens and P. J. Thorley, Nucl. Phys. **A442**, 215 (1985).

[Sha62] A. Kh. Shardanov and V. G. Shevchenko, Soviet Physics–JETP **15**, 996 (1962); translation of J. Exptl. Theoret. Phys. (U.S.S.R.) **42**, 1438 (1962).

[She51] R. Sher, J. Halpern and A.K. Mann, Phys. Rev. **84**, 387 (1951).

[She65] N. K. Sherman, R. C. Morrison and J. R. Stewart, Bull. Am. Phys. Soc. **10**, 541 (1965).

[She66a] N. K. Sherman, J. E. E. Baglin and R. O. Owens, Bull. Am. Phys. Soc. **11**, 10 (1966).

[She66b] N. K. Sherman, J. R. Stewart and R. C. Morrison, Phys. Rev. Lett. **17**, 31 (1966).

[She67] N. K. Sherman, J. E. E. Baglin and R. O. Owens, Bull. Am. Phys. Soc. **11**, 632 (1967).

[She68] N. K. Sherman, J. E. E. Baglin and R. O. Owens, Phys. Rev. **169**, 771 (1968).

[Shi75] Y. M. Shin, D. M. Skopik and J. J. Murphy, Phys. Lett. **55B**, 297 (1975).

[Shi05] T. Shima, S. Naito, Y. Nagai, T. Baba, K. Tamura, T. Takahashi, T. Kii, H. Ohgaki and H. Toyokawa, Phys. Rev. C **72**, 044004 (2005).

[Sid86] S. A. Siddiqui, N. Dytlewski and H. H. Thies, Nucl. Phys. **A458**, 387 (1986).

[Sko76] D. M. Skopik, E. L. Tomusiak, E. T. Dressler, Y. M. Shin and J. J. Murphy, II, Phys. Rev. C **14**, 789 (1976).

[Sko79a] D. M. Skopik, J. Asai, E. L. Tomusiak and J. J. Murphy II, Phys. Rev. C **20**, 2025 (1979).

[Sko79b] D. M. Skopik, J. J. Murphy II and J. Asai, Phys. Rev. C **19**, 1144 (1979).

[Sto53] P. Stoll and M. Wächter, Nuovo Cimento **10**, 347 (1953).

[Sto54] P. Stoll, Helv. Phys. Acta **27**, 395 (1954).

[Swa99] B. D. Sawatzky, *Calibration of a BC-505 Segmented Neutron Detector Over the Energy Range 0-15 MeV*. MSc Thesis, University of Saskatchewan, Unpublished (1999).

[Swa05] B. D. Sawatzky, *A Measurement of the Neutron Asymmetry in $d(\vec{\gamma}, n)p$ Near Threshold*. PhD Thesis, University of Virginia, Unpublished (2005).

[Tan77] H. Taneichi, H. Ueno and K. Shoda, in *Proceedings of the International Conference on Nuclear Structure*, p 141, Tokyo (1977).

[Tho77] D. R. Thompson, M. Lemere and Y. C. Tang, Nucl. Phys. **A286**, 53 (1977).

[Til87] D. R. Tilley, H. R. Weller and H. H. Hasan, Nucl. Phys. **A474**, 1 (1987).

[Til92] D. R. Tilley, H. R. Weller and G. M. Hale, Nucl. Phys. **A541**, 1 (1992).

[Til02] D. R. Tilley, C. M. Cheves, J. L. Godwin, G. M. Hale, H. M. Hofmann, J. H. Kelley, C. G. Sheu and H. R. Weller, Nucl. Phys. **A708**, 3 (2002).

[Til04] D.R. Tilley, J.H. Kelley, J.L. Godwin, D.J. Millener, J.E. Purcell, C.G. Sheu and H.R. Weller, Nucl. Phys. **A745**, 155 (2004).

[Tit50a] E. W. Titterton, Proc. Phys. Soc. A **63**, 915 (1950).

[Tit50b] E. W. Titterton, Proc. Phys. Soc. A **63**, 1297 (1950).

[Tit51] E. W. Titterton and T. A. Brinkley, Proc. Phys. Soc. A **64**, 212 (1951).

[Tit52] E. W. Titterton and T. A. Brinkley, Proc. Phys. Soc. A **65**, 1052 (1952).

[Tit53a] E. W. Titterton and T. A. Brinkley, Proc. Phys. Soc. A **66**, 194 (1953).

[Tit53b] E. W. Titterton and T. A. Brinkley, Proc. Phys. Soc. A **66**, 579 (1953).

[Tit54a] E. W. Titterton and T. A. Brinkley, Aust. J. Phys. **7**, 350 (1954).

[Tit54b] E. W. Titterton and T. A. Brinkley, Proc. Phys. Soc. A **67**, 469 (1954).

[Tit55] E. W. Titterton, Prog. Nucl. Phys. **4**, 32 (1955).

[Tuc53] B. L. Tucker and E. C. Gregg, Phys. Rev. **91**, 1579 (1953).

[Uts00] H. Utsunomiya, Y. Yonezawa, H. Akimune, T. Yamagata, M. Ohta, M. Fujishiro, H. Toyokawa and H. Ohgaki, Phys. Rev. C **63**, 018801 (2000).

[Ven71] E. Ventura, C. C. Chang and W. E. Meyerhof, Nucl. Phys. **A173**, 1 (1971).

[Ven73] E. Ventura, J. R. Calarco, W. E. Meyerhof and A. M. Young, Phys. Lett. **46B**, 364 (1973).

[Vla89] Yu. V. Vladimirov, V. V. Denyak, S. N. Dyukov, I. G. Evseev, V. I. Kasilov, N. I. Lapin, V. P. Likhachev, S. A. Pashchuk, E. V. Pegushin, V. M. Sanin, V. M. Khvastunov, V. B. Shostak and S. F. Shcherbak, JETP Lett. **49**, 155 (1989); translation of Pis'ma Zh. Eksp. Teor. Fiz **49**, 133 (1989).

[Vol62] Yu. M. Volkov and L. A. Kul'chitskii, Soviet Physics–JETP **15**, 77 (1962); translation of J. Exptl. Theoret. Phys. (U.S.S.R.) **42**, 108 (1962).

[Vol78] Yu. M. Volkov, G. A. Kolomenskiĭ, E. F. Lakovichev, E. D. Makhnovskiĭ, A. V. Nadtochiĭ, V. V. Popov, V. P. Fominenko and V. P. Chizhov, Sov. J. Nucl. Phys. **27**, 461 (1978); translation of Yad. Fiz. **27**, 868 (1978).

[Vol86] Yu. M. Volkov, G. A. Kolomenskiĭ, E. F. Lakovichev, E. D. Makhnovskiĭ, V. V. Popov, V. P. Fominenko and V. P. Chizhov, Sov. J. Nucl. Phys. **44**, 747 (1986); translation of Yad. Fiz. **44**, 1153 (1986).

[Wel63] T. A. Welton in *Fast Neutron Physics*, edited by J. B. Marion and J. L. Fowler. Interscience, New York, Vol. II, p. 1317 (1963).

[Wad84] M. W. Wade, M. K. Brussel, L. J. Koester, Jr. and J. H. Smith, Phys. Rev. Lett. **53**, 2540 (1984).

[Wat56] A. Wattenberg, A. C. Odian, P. C. Stein, H. Wilson and R. Weinstein, Phys. Rev. **104**, 1710 (1956).

[Wat65] A. Wataghin, M. Scotto and G. Paoli, Nuovo Cimento **40 B**, 441 (1965).

[Wel92] H. R. Weller, J. Langenbrunner, R. M. Chasteler, E. L. Tomusiak, J. Asai, R. G. Seyler and D. R. Lehman, Atomic Data and Nuclear Data Tables **50**, 29 (1992).

[Wel94] H. R. Weller, R. M. Chasteler, B. S. Marks, R. G. Seyler and D. R. Lehman, Atomic Data and Nuclear Data Tables **58**, 219 (1994).

[Whi58] C. Whitehead, W. R. McMurray, M. J. Aitken, N. Middlemas and C. H. Collie, Phys. Rev. **110**, 941 (1958).

[Wir95] R. B. Wiringa, V. G. J. Stoks and R. Schiavilla, Phys. Rev. C **51**, 38 (1995).

[Wir02] R. B. Wiringa and S. C. Pieper, Phys. Rev. Lett. **89**, 182501 (2002).

[Won70] C. F. Wong, R. M. Hutcheon, Y. M. Shin and H. S. Caplan, Can. J. Phys. **48**, 1917 (1970).

[Wu01] Y. Wu, V. N. Litvinenko, S. F. Mikhailov, O. A. Shevchenko, N. A. Vinokurov, N. G. Gavilov, T. V. Shaftan and D. A. Kairan, Nucl. Instr. and Meth. **A475**, 253 (2001).

[Wu07] Y. K. Wu, *2007 HIGS Performance With 780, 450 and 280 nm FEL Cavity Mirrors*. Presentation (2007).

[Wur07a] W. A. Wurtz, *SPIR 138: Casting Lithium Targets for Use in Photonuclear Physics*. Unpublished (2007). (Available at: http://nucleus.usask.ca/technical_reports/report_index.html)

[Wur07b] W. A. Wurtz, *RLucid Version 0.4*. Unpublished (2007). (Available at: http://nucleus.usask.ca/∼ward/RLucid/index.html)

[Wur08a] W. A. Wurtz, *SPIR 139: Preliminary Design Considerations for HeTIC*, Unpublished (2007). (Available at: http://nucleus.usask.ca/technical_reports/report_index.html)

[Wur08b] W. A. Wurtz, *Blowfish-ROOT Analysis Package Version 0.0*. Unpublished (2008).

[Wur09] M. Wurtz *et al.*, Phys. Rev. D **79**, 074501 (2009).

[You70a] A. M. Young, S. L. Blatt, J. F. Amann and E. M. Diener, Bull. Am. Phys. Soc. **15**, 125 (1970).

[You70b] A. M. Young, S. L. Blatt and R. G. Seyler, Phys. Rev. Lett. **25**, 1764 (1970).

[Zub90] D. Zubanov, B. L. Berman, W. J. Briscoe, K. S. Dhuga, A. Mokhtari, M. F. Taragin, H. P. Blok, R. Ent, Th. S. Bauer, E. Jans, L. Lapikás and P. K. A. de Witt Huberts, Bull. Am. Phys. Soc. **35**, 927 (1990).

Appendix A

Technical Trigger Diagrams

The following trigger diagrams were produced by Dr. Rob Pywell. They detail the electronics configuration for the photodisintegration of lithium isotopes experiments involving energies of 20, 25, 30 and 35 MeV. The electronics configuration for other energies is conceptually similar but no up-to-date diagram was produced. The lack of such a diagram was a major motivating factor for rebuilding the electronics and producing the following diagrams. Elements in the diagrams are listed by electronics bin number, module slot and channel number. For instance, the module in the second slot of the second electronics bin is a quad coincidence module. The first channel is used in the following diagram and it is labeled 2-2-1.

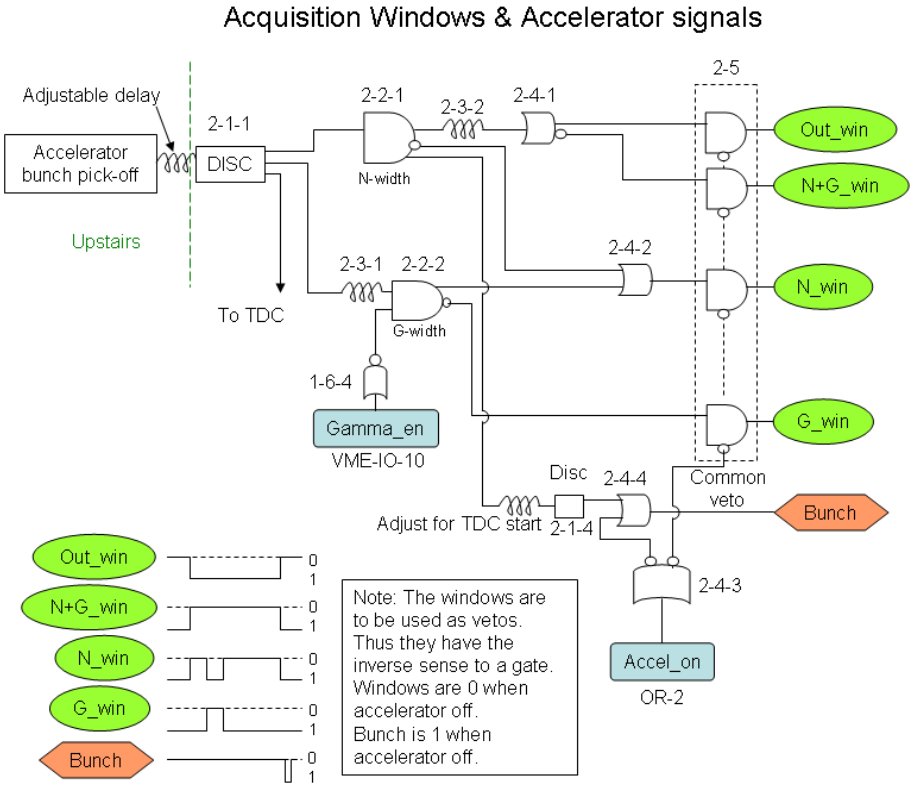

Master Trigger System

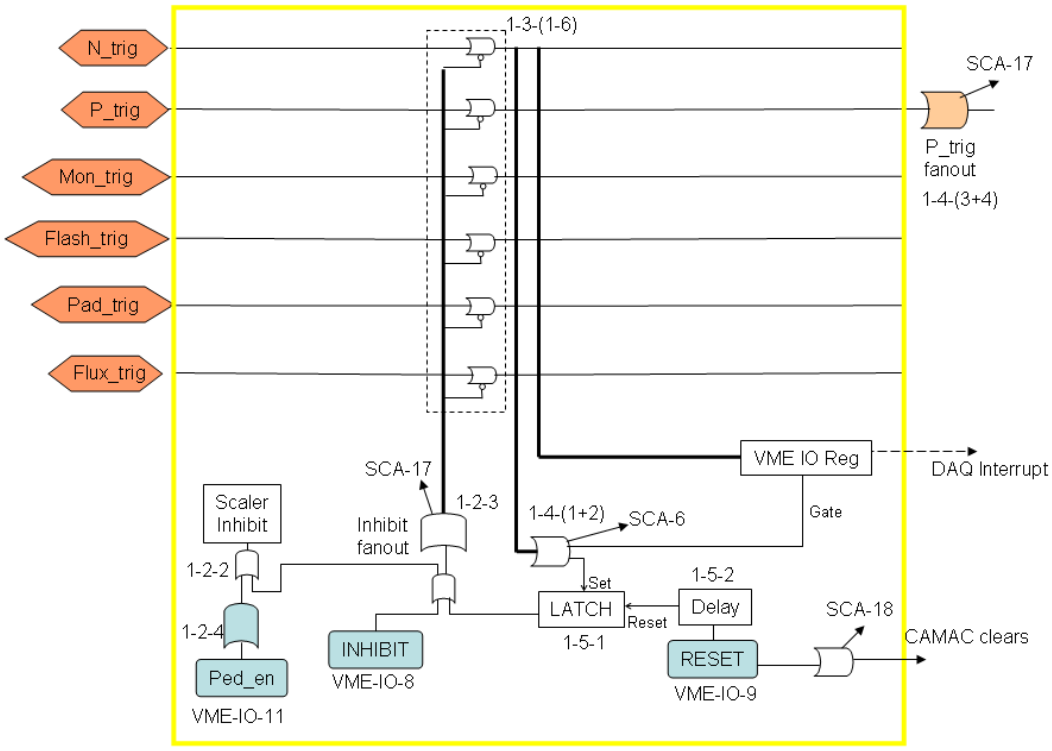

Neutron Cell, Pedestal & Target Triggers

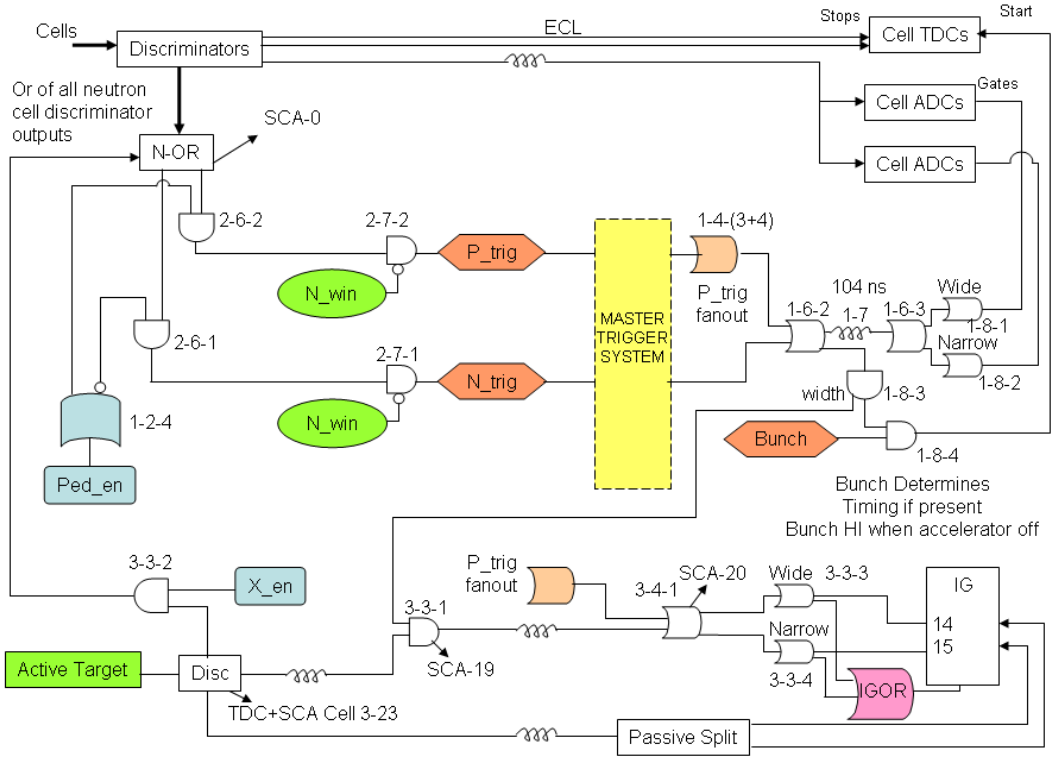

5-Paddle Flux monitor Electronics

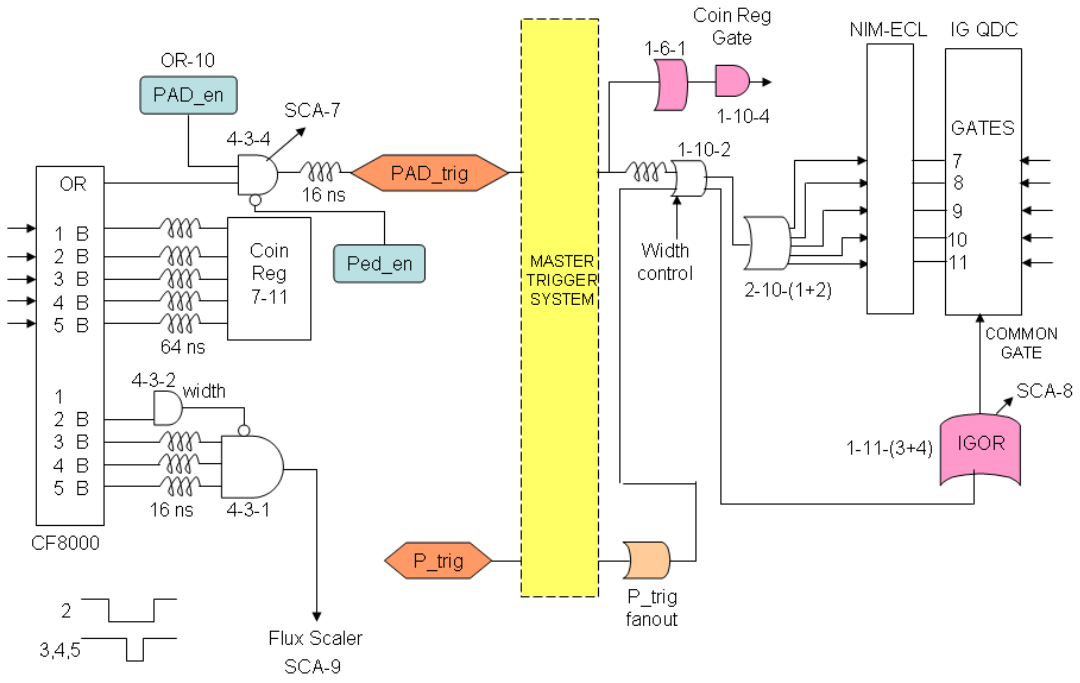

Flasher/Monitor Electronics

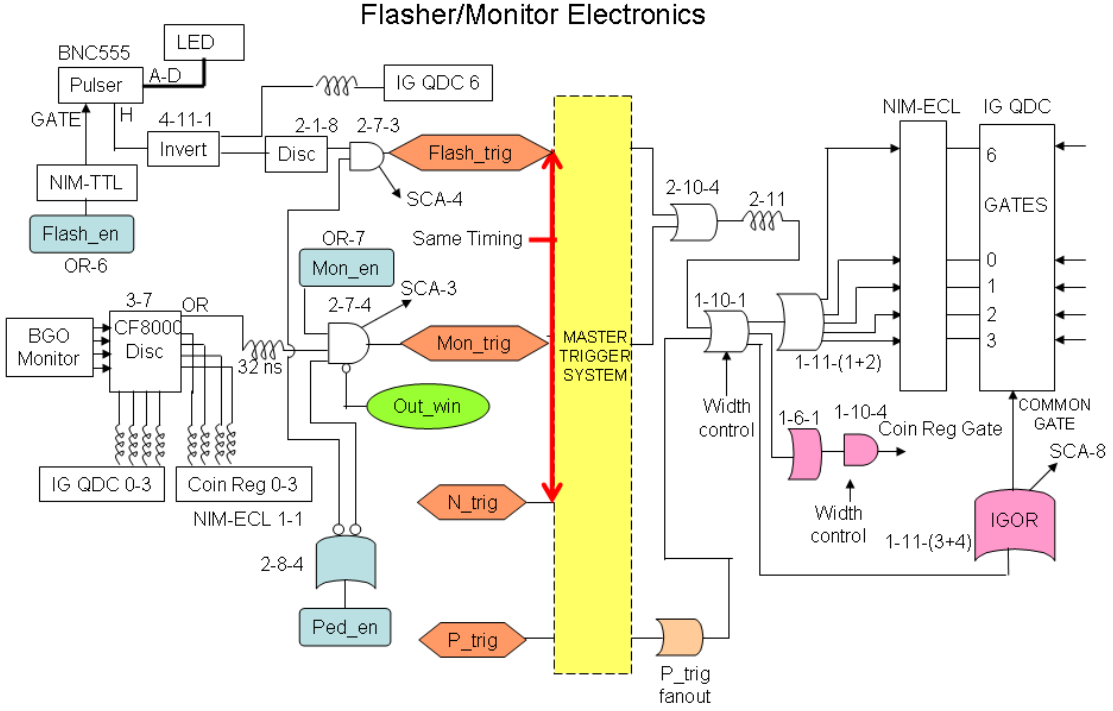

NaI Flux monitor Electronics

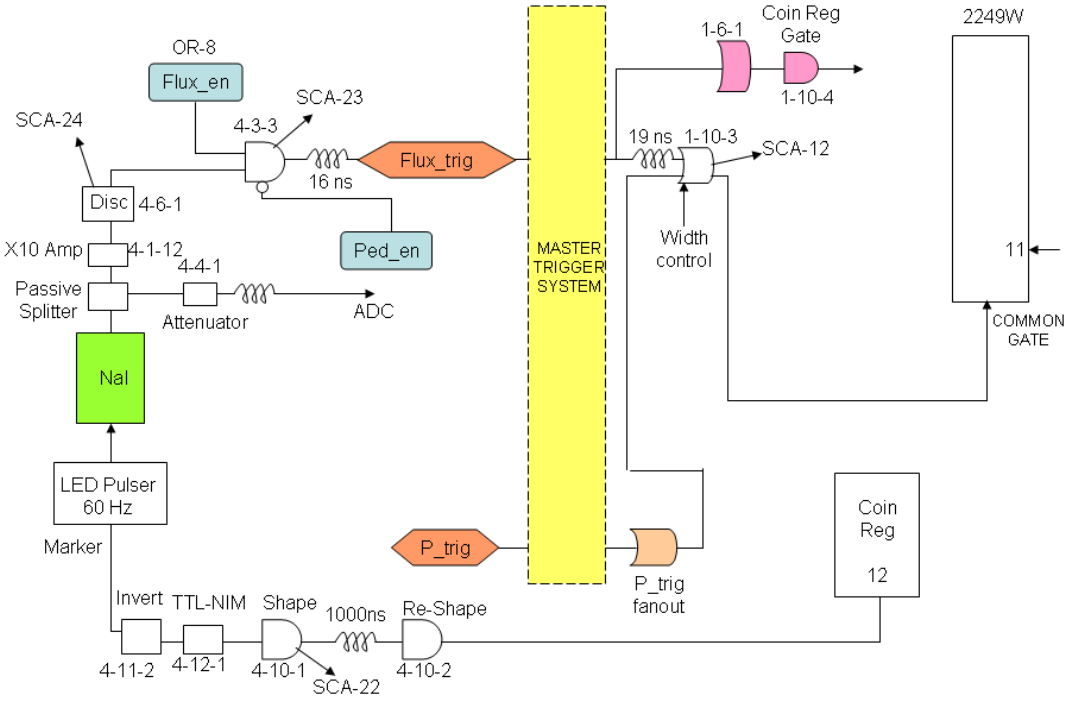

Scaler Map

Channel	From	Signal
0	3-9	N-OR
1	2-7-1	N-trig
2	2-7-2	P-trig
3	2-7-4	Mon-trig
4	2-7-3	Flash-trig
5	2-10-4	Mon+Flash IG starts
6	1-4-(1+2)	Latch Starts
7	4-3-4	Pad-trig
8	1-11-(3+4)	IGOR
9	4-3-1	5-paddle flux
10	upstairs	3-paddle flux
11	1-10-2	Pad gates
12	1-10-3	Flux gates
13	2-1-1	Bunch Raw
14		
15	SAL Clock	1000 Hz clock

2-12 Phillips 726

Channel	From	Signal
16	2-5-1	Out-win (bunch)
17	1-2-3	Inhibit
18	1-2-1	Clear
19		
20		
21		
22	4-10-1	Flux pulser
23	4-3-3	Flux-trig
24	4-6-1	NaI raw
25	3-3-1	X-trig
26	3-4-1	X Gates
27		
28		
29		
30		
31		

1-1 LeCroy 4413

Table A.1: Contents of NIM bin 1

Slot	Manufacturer	Number	Type
1	LeCroy	4616	ECL-NIM-ELC Converter
2	LeCroy	429A	Logic Fan-in/Fan-out
3	Phillips	711	Discriminator
4	LeCroy	429A	Logic Fan-in/Fan-out
5	LeCroy	222	Gate Generator
6	LeCroy	429A	Logic Fan-in/Fan-out
7	Phillips	792	Delay
8	LeCroy		Quad Coincidence
10	LeCroy	622	Quad Coincidence
11	LeCroy	622	Quad Coincidence
12	Phillips	726	Level Converter

Table A.2: Contents of NIM bin 2

Slot	Manufacturer	Number	Type
1	LRS	620BL	Discriminator
2	LeCroy	622	Quad Coincidence
3	Phillips	792	Delay
4	LeCroy	429A	Logic Fan-in/Fan-out
5	LeCroy	4608	Discriminator
6	LeCroy	622	Quad Coincidence
7	Phillips	756	Quad Discriminator
8	LeCroy	429A	Logic Fan-in/Fan-out
9	Phillips	792	Delay
10	LRS	429	Logic Fan-in/Fan-out
11	Phillips	792	Delay
12	Phillips	726	Level Converter

Table A.3: Contents of NIM bin 3

Slot	Manufacturer	Number	Type
3	LeCroy	622	Quad Coincidence
4	LeCroy	429A	Logic Fan-in/Fan-out
7	EG&G-ESN	CF8000	Octal Constant Fraction Discriminator
8	Phillips	777	8-Channel Variable Gain Amplifier
9	LeCroy	729A	Logic Fan-in/Fan-out
10	Phillips	CF8000	Octal Constant Fraction Discriminator
12	Phillips	CF8000	Octal Constant Fraction Discriminator

Table A.4: Contents of NIM bin 4

Slot	Manufacturer	Number	Type
1	LeCroy	612	12-Channel Photomultiplier Amplifier
2	Phillips	CF8000	Octal Constant Fraction Discriminator
3	Phillips	756	Quad Discriminator
4	Phillips	804	Quad Rotary Attenuator
6	LRS	620CL	8-Channel Discriminator
8	Tennelec	TC526	Rate Meter
9	Ortec		Rate Meter
10	LeCroy	622	Quad Coincidence
11	LeCroy	429A	Logic Fan-in/Fan-out
12	Phillips	726	Level Converter

Table A.5: Contents of NIM bin 5

Slot	Manufacturer	Number	Type
1	Phillips	CF8000	Octal Constant Fraction Discriminator
2	Phillips	CF8000	Octal Constant Fraction Discriminator
3	Phillips	CF8000	Octal Constant Fraction Discriminator
4	Phillips	CF8000	Octal Constant Fraction Discriminator
5	Phillips	CF8000	Octal Constant Fraction Discriminator
6	Phillips	CF8000	Octal Constant Fraction Discriminator
7	Phillips	CF8000	Octal Constant Fraction Discriminator
8	Phillips	CF8000	Octal Constant Fraction Discriminator
11	Phillips	CF8000	Octal Constant Fraction Discriminator
12	Phillips	CF8000	Octal Constant Fraction Discriminator

Table A.6: Contents of CAMAC crate

Slot	Manufacturer	Number	Type
1	LeCroy	4448	Coincidence Register
2	Jorway	41	Output Register
4	LeCroy		2249W QDC (Wide Gate)
6	LeCroy	4413	32-Channel Discriminator
7	LeCroy	4434	32-Channel Scaler
8	LeCroy	4434	32-Channel Scaler
9	LeCroy	4434	32-Channel Scaler
17	LeCroy	4434	32-Channel Scaler
18	LeCroy	4434	32-Channel Scaler
19	LeCroy	4434	32-Channel Scaler
20	LeCroy	2132	High Voltage Interface
21	SAL		Clock
22	Jorway		Visual Branch Terminator
24	Jorway		A-2 Crate Controller

Table A.7: Contents of VME crate

Slot	Manufacturer	Number	Type
1	SIS GmBh	SIS 3100	Fiber Optic Interface
2	CAEN	V513	Input/Output Register
3	CAEN	V775	TDC
5	CAEN	V775	TDC
7	CAEN	V775	TDC
9	CAEN	V792	QDC
10	CAEN	V792	QDC
12	CAEN	V792	QDC
13	CAEN	V792	QDC
15	CAEN	V792	QDC
16	CAEN	V792	QDC
18	CAEN	V862	QDC Independent Gate
20	CES	CDB 8210	CAMAC Interface

Appendix B

Design Drawings for the Lithium Targets

This appendix contains the drawings that were used to build the Li target. All lengths in these drawings are given in the units of fractional inches which can be converted into metric units by 2.54 cm = 1 inch. The drawings for the complete apparatus used to cast the lithium targets can be found in reference [Wur07a].

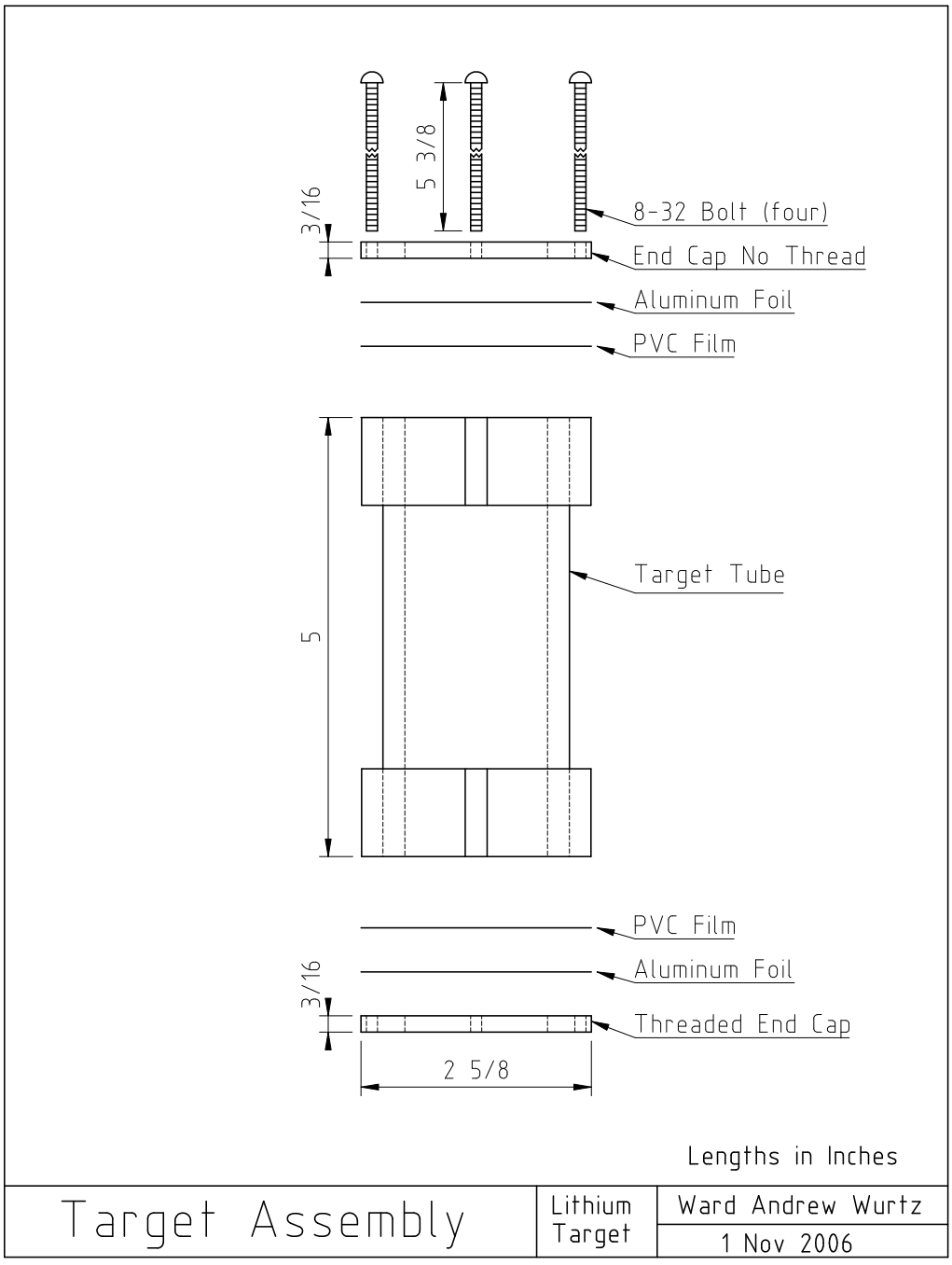
5 3/8
3/16
8-32 Bolt (four)
End Cap No Thread
Aluminum Foil
PVC Film
5
Target Tube
PVC Film
Aluminum Foil
3/16
Threaded End Cap
2 5/8
Lengths in Inches
Target Assembly
Lithium Target
Ward Andrew Wurtz
1 Nov 2006

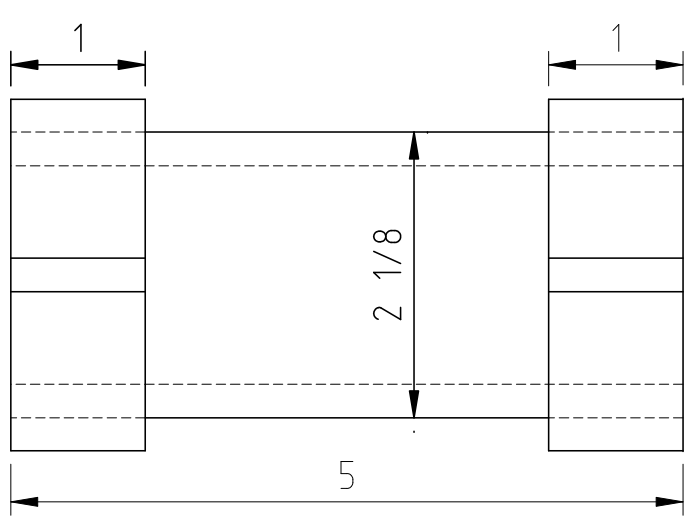

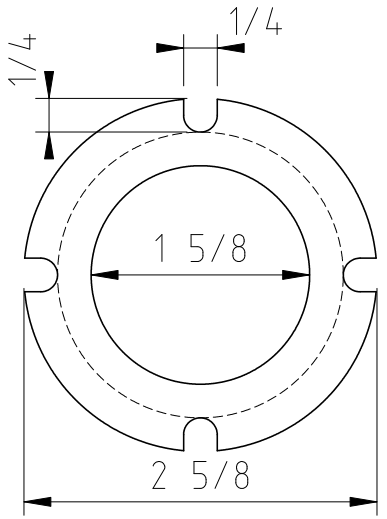

Description: A hollow tube made from a single peice of teflon.
The walls at the centre are 1/4" thick.
The walls at the end are 1/2" thick and have groves to allow the passage of bolts.

Lengths in Inches
Material: Teflon

Target Tube	Lithium Target	Ward Andrew Wurtz
		3 Oct 2006

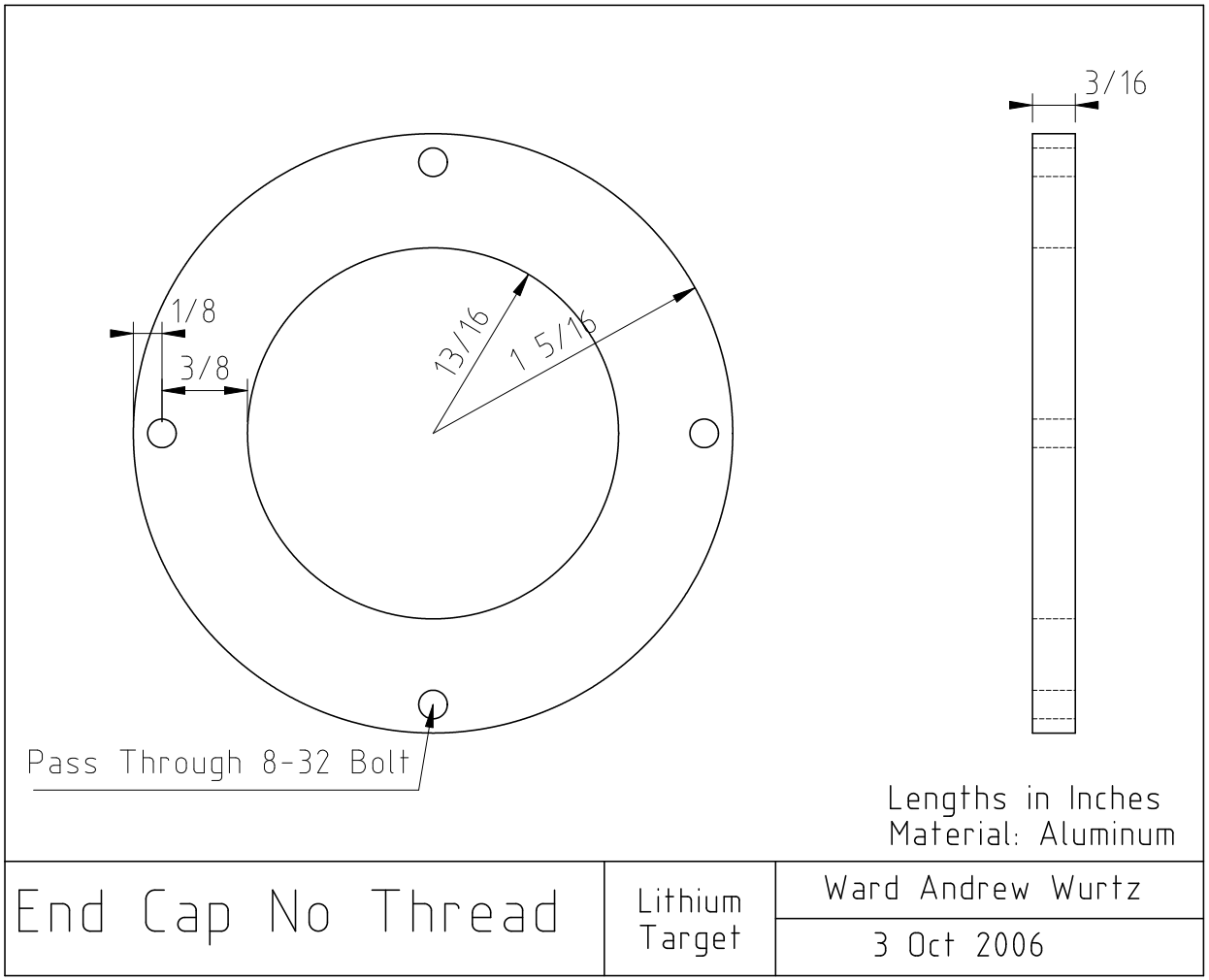
3/16
1/8
3/8
13/16
1 5/16
Pass Through 8-32 Bolt
Lengths in Inches
Material: Aluminum
End Cap No Thread
Lithium Target
Ward Andrew Wurtz
3 Oct 2006

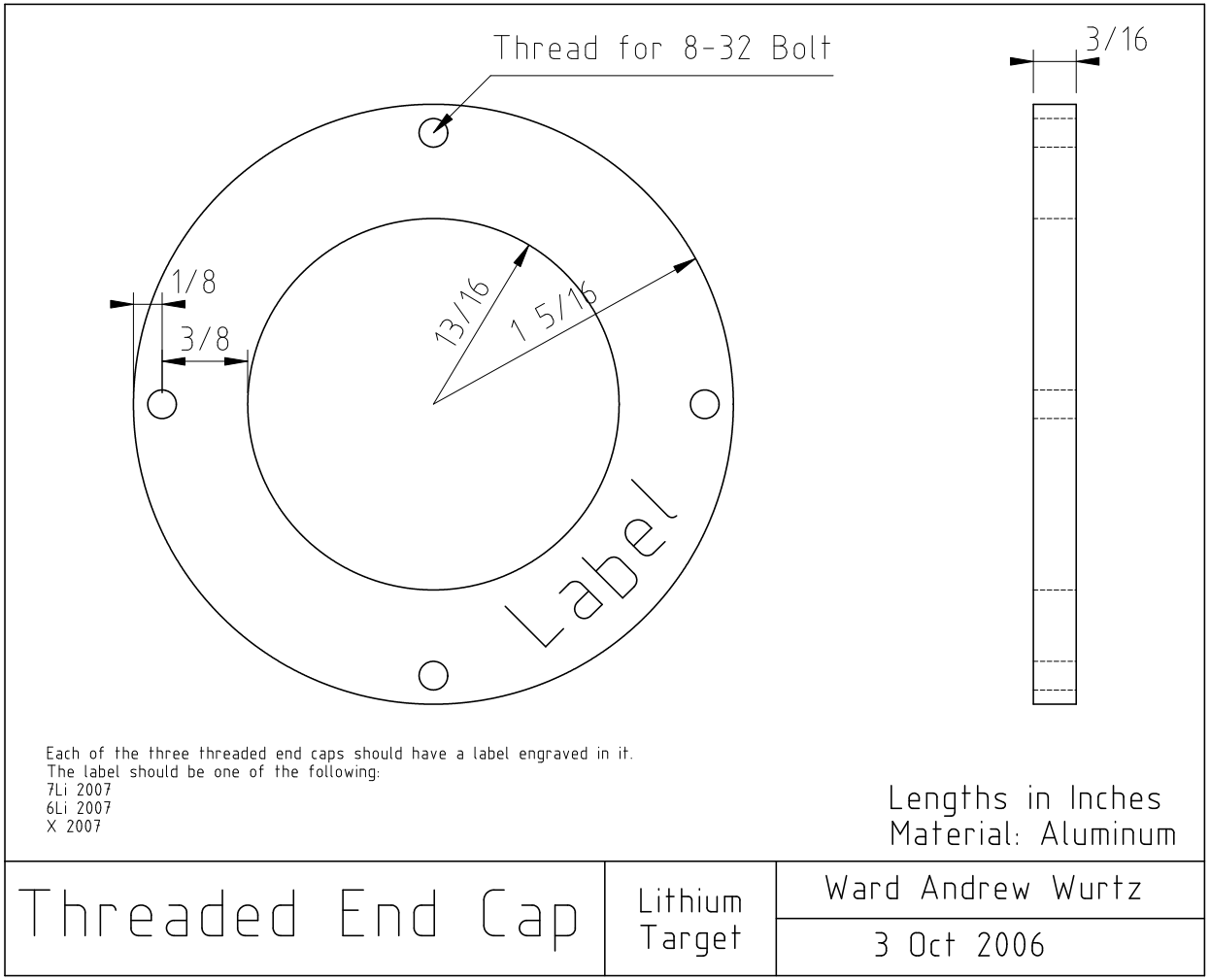
Thread for 8-32 Bolt
3/16
1/8
3/8
13/16
1 5/16
Label
Each of the three threaded end caps should have a label engraved in it.
The label should be one of the following:
7Li 2007
6Li 2007
X 2007
Lengths in Inches
Material: Aluminum
Threaded End Cap
Lithium Target
Ward Andrew Wurtz
3 Oct 2006